Synthesis, Characterisation, and MD Investigation of the Mechanical and Catalytic Properties of Ceria Nanocubes and Ceria-Aerogel Nanocomposites

Lucy M. Morgan

School of Physical Sciences

University of Kent

Supervisory Team

Dr Dean C. Sayle

Prof Anna Corrias

A thesis submitted for the degree of

Doctor of Philosophy

August 2018

Acknowledgements

First and foremost I would like to extend my thanks and appreciation to my supervisors, Dr Dean Sayle and Prof Anna Corrias, for not only accepting me for this PhD, but also for their very different, yet complementary, supervisory styles. This was a unique opportunity to further and explore both experimental and computation chemistry in which I have gained such broad experience and interests from. I cannot exaggerate how infectious Dean's enthusiasm for chemistry is, within 5 minutes of talking to him about a project he seems to inject it with new life and wonder. I can also not emphasize my appreciation for Anna's patience, honesty, and advice as without it I am sure I would not have reached the end of my PhD without struggling to get there.

Special thanks needs to be extended to Dr Shusaku Hayama for his assistance with the XANES experiment we conducted on the I20 at the Diamond Light Source, under the proposal SP-19013. Also to Prof Andrea Falqui, Dr Alberto Casu, and Dr Colm O'Regan, our collaborators in KAUST (Saudi Arabia) for their TEM, AC-TEM, and STEM-EDS characterisation. I would also like to extend my thanks to the various members of both the Sayle and Corrias groups over the years - Francesco Caddeo, Pauline Van Aalderen, Mathew Coomber, Danilo Loche, and Andre Düvel.

Moreover I would like to thank Agata (Makieła) Rożek and Timothy Kinnear ('the fountain of all knowledge') for their exceptional support and advice. For the code was long and full of errors, they were always on hand to help fix it. Without them I would not have such a rounded and well presented thesis.

I also wish to thank all my crazy office cohort for putting up with me the last 3 years. Without them, our random tea parties, chats, and antics, I would not have kept/lost my sanity. In particular Chrissie Rogers, Katy Bruce, Lisa White, Andryj Borys, Leon Schoonderwoerd, and Agata Rożek (again!). Also to all those involved in our department's OUTREACH and the ensuing crayhem; I have not laughed and cried so hard as I have done at our chemistry and forensic residentials.

Finally, thank you to my family for all their love and support.

Abstract

Nanoceria has become a widely used component in catalysis due to its unprecedented ability for oxidation/reduction. Irreversible deformation however plagues the operation of these materials, extinguishing their catalytic properties, and therefore they need protecting from harsh operating conditions. Furthermore, particle agglomeration can cause loss of catalytic activity. Here, two solutions to protecting nanoceria are presented, utilising both experiment analysis and atomistic molecular dynamic (MD) modelling. In particular how the use of sacrificial materials can protect a ceria nanocube, allowing stress of 40 GPa, in comparison to 2.5 GPa unprotected, before plastic deformation occurs, and how encapsulating ceria nanocubes in an aerogel matrix can prevent aggregation, retaining catalytic activity, and also act as a sacrificial material to prevent mechanical wear.

A ceria nanocube synthesis was optimised and Lanthanum introduced as a dopant with the aim of improving the catalytic activity of the ceria nanocubes by promoting the formation of oxygen vacancies (Chapter 3). The resulting nanoparticles were encapsulated in an aerogel host matrix, forming nanocomposites, with the aim of preventing aggregation. L_3 edge HERFD-XANES was used to investigate the oxidation/reduction ability of the ceria nanocubes and nanocomposites under different operating temperatures (Chapter 4).This presented improved catalytic performance in ceria nanoparticles dispersed in an aerogel matrix, with further improvement indicated with the presence of a La-dopant.

An amorphisation-recrystallisation technique was employed for the atomistic MD investigation of sacrificial barriers (Chapter 5), which was further developed to include temperature variations, compression rate, and a calculated dynamic surface area (Chapter 6). This demonstrated that sacrificial barriers can allow for higher applied stress in a system before plastic deformation occurs, preserving the structural integrity. Dynamic surface area calculations presented stress-strain data in high concordance with experiment, whereas increased system temperature presented a reduction of measured stress, and compression rate variation presented further clarity of individual deformation events.

Furthermore, a new technique for the MD simulation of SiO_2 aerogel was developed (Chapter 7), where a seed and cluster growth method was employed to form the aerogel, then uniaxial force was applied to investigate the resulting mechanical properties.

Contents

Publications

Published Articles

- **L.M. Morgan**, M. Molinari, A. Corrias, and D.C. Sayle, *Protecting Ceria Nanocatalysts - The Role of Sacrificial Barriers*, ACS Applied Materials & Interfaces, 2018, 10(38), 32510–32515.

- A. Düvel, **L.M. Morgan**, C. Vinod Chandran, P. Heitjans, and D.C. Sayle, *Formation and Elimination of Anti-site Defects during Crystallization in Perovskite $Ba_{1x}Sr_xLiF_3$*, Crystal Growth & Design, 2018, 18, 2093–2099.

- A. Düvel, **L.M. Morgan**, G. Cibin, D. Pickup, A. Chadwick, P. Heitjans, and D.C. Sayle, *Tuning anti-site defect density in perovskite-$BaLiF_3$ via ball-milling/heating-cycling*, Journal of Physical Chemistry Letters, 2018, 9, 5121–5124.

Publications in Preparation

- **L.M. Morgan**, A. Corrias, R.L. Neale, M. Molinari, and D.C. Sayle, *Nanoceria Ageing; Mechanism and its Prevention.*

- **L.M. Morgan**, R.L. Neale, M. Molinari, and D.C. Sayle, *Surface Mobility of Doped Nanoceria: A liquid surface.*

- **L.M. Morgan** and D.C. Sayle, *Atomistic MD Investigation of Chemical Mechanical Planarization Mechanisms.*

- **L.M. Morgan** and D.C. Sayle, *Atomistic MD Investigation into the Mechanical Properties of Aerogel and Nanocomposite-Aerogel.*

- **L.M. Morgan**, D. Loche, A. Corrias, C. O'Regan, A. Casu, and A. Falqui *Determining the maximum lanthanum incorporation in the fluorite structure of La-doped ceria nanocubes for enhanced redox ability.*

- **L.M. Morgan**, D. Loche, G. Mountjoy, A. Corrias, C. O'Regan, A. Casu, A. Falqui, S. Hayama *Ce^{3+}/Ce^{4+} Ratio in Ceria Based Nanomaterials by In-Situ High-Energy Resolution Fluorescence Detected X-ray Absorption Near Edge Structure.*

- **L.M. Morgan**, D. Loche, G. Mountjoy, A. Corrias, C. O'Regan, A. Casu, A. Falqui, S. Hayama *Stabilisation of ceria nanocubes in an aerogel silica matrix.*

Acronyms and Terms

Chemical Abbreviations and Acronyms

Ceria	Cerium Dioxide, CeO_2
Silica	Silicon Dioxide, SiO_2
EtOH	Ethanol
TEOS	Tetraethyl orthosilicate
TMOS	Tetramethoxysilane
OA	Oleic Acid
PVP	Polyvinylpyrrolidone

Analytical Technique Acronyms

TGA	Thermal Gravimetric Analysis
DSC	Differential Scanning Calorimetry
STA	Simultaneous Thermal Analysis
XRD	X-Ray Diffraction
TEM	Transmission Electron Microscopy
HR AC-TEM	High Resolution Aberration-Corrected TEM
STEM	Scanning Transmission Election Microscopy
STEM-EDS	STEM Energy-Dispersive X-ray Spectroscopy
HAADF-STEM	High-Angle Annular Dark-Field STEM
RIXS	Resonant Inelastic X-ray Scattering
XANES	X-ray Absorption Near Edge Spectroscopy
HERFD-XANES	High Energy Resolution Fluorescence Detection XANES
HT-SD	High Temperature Supercritical Drying

DL_POLY Terms

NVE	Constant number of atoms, volume, and energy
NVT	Constant number of atoms, volume, and temperature
NVP	Constant number of atoms, volume, and pressure
NPH	Constant number of atoms, pressure, and enthalpy
NVT	Constant number of atoms, stress, and temperature

Other Acronyms and Terms

MD	Molecular Dynamics
GULP	General Utility Lattice Program
MSD	Mean Squared Displacement
RDF	Radial Distribution Function
QM	Quantum Mechanics
MM	Molecular Mechanics
DFT	Density Functional Theory
CMP	Chemical Mechanical Planarization
CCD	Charge-Coupled Device
VV	Velocity Verlet
LFV	LeapFrog Verlet
ARC	Amorphisation Re-Crystallisation
RT	Room Temperature
TT	Thermally Treated or Thermal Treatment
SCCM	Standard Cubic Centimetres per Minute

Chapter 1

Introduction to Ceria Nanoparticles, Silica Aerogels, Nanocomposites, and Computational Simulation

1.1 Introduction

The properties of a functional material can be tuned by changing its size and shape (metamaterial sculpting) as an alternative to elemental control [1], which can give great flexibility in the approaches available to researchers. It is therefore unsurprising that reduction in size to the nanoscale can greatly affect the properties the material exhibits. This is partially evidenced by the creation of around 70 new journals which are devoted to nanoscience [2]. It can be argued that a change in scale can itself be considered a change in chemistry, due to the fundamental behaviour changes which are exhibited. For instance, the mechanical [3] and catalytic [4] properties are highly influenced by a reduction in size to the nanoscale. The consequence of traversing to the nanoscale can in fact be quite severe, for example, small forces can translate to considerable pressures when contact areas are reduced to the nanoscale. In particular, when the same force acts upon a contact area that is reduced from 1 cm^2 to 10 nm^2 the pressure increases by 13 orders of magnitude. Nevertheless, with such a dynamic range of possibilities nanomaterials present, their applications span many fields, being utilised in areas such as biomedicine [5], supercapacitor electrodes [6], photodetectors [7], removal of heavy metals from waste water [8], agricultural production and crop protection [9], chemical mechanical planarization [10, 11], catalysis [12], and energy materials, such as batteries [13] and fuel cells [14], among many other applications. Properties of a functional material can therefore be tuned by directly controlling their scale, shape, structure, and microstructure, which can be beneficial compared to altering the elemental composition.

One of the most beneficial effects of nanoscale materials is their comparatively large surface area. Smaller particles, rods, porous materials, etc., have a larger surface area, giving a larger overall contact area for activity to occur. This has particular importance for applications in catalysis, where catalytic reactions rely on the surface activity; therefore the larger surface area of nanomaterials can greatly improve efficiency. For nanoparticles, this is further influenced by tuning the shape, which in turn determines the crystal structure exposed [15], whereby the different surface structures provide varying catalytic potential.

1.1.1 Cerium Dioxide (CeO_2, Ceria)

A catalytically important functional nanomaterial, ceria, CeO_2, has been the subject of intense scrutiny because of its remarkable properties, including surface activity [16], redox and defect chemistry [17], and oxygen transport [18], with application in energy materials (including solid oxide fuel cells [19] and solar cells [20]), catalysis [21], nanomedicine [22], and chemical mechanical planarization [23]. For example, ceria, in nanoform, has been shown to be a highly active catalyst; CeO_2 nanocubes can catalyse CO to CO_2 at room temperature in contrast to the parent bulk material [24], and currently, ceria is used as a component of three-way automobile exhaust catalysts [25].

Nanoceria is unique, unlike most other nano-structure, as the lattice expands with reducing particle size, which sub-sequentially leads to a decrease in oxygen release and absorption [26]. Cerium is the first element in the periodic table to possess a ground state electron in a 4f orbital, which results in ceria possessing excellent reduction/oxidation behaviour between its Ce^{3+} and Ce^{4+} oxidation states. CeO_2 typically crystallises in a fluorite structure, with space group Fm3m [17], and the ideal cell consists of a face-centred cubic (fcc) arrangement of cations with the anions occupying the octahedral interstitials, giving 8-coordinated Ce^{4+} and 4-coordinated O^{2-}. At high temperatures ceria is able to reduce by releasing oxygen, resulting in a non-stoichiometric form which is anion deficient, while still being able to retain the fluorite lattice. The effect of this is the formation of oxygen vacancies within the lattice, which can be re-oxidised/filled with the introduction of heat and oxygen.

Nanoparticles, in general, can be synthesised using a variety of methods which have developed over the years. In 2001 Gonzalez *et al* synthesised nanoparticles using gas evaporation [27] which was introduced previously by Granqvist and Buhrman in 1976 [28]. Thermal evaporation however is known to be limited to metal compounds and therefore a method which replaced the thermal evaporation source with a sputtering source was later developed by Hahn and Averback in 1990 [29]. This method also had its limitations such as the particle size being depended on the gas pressure which could fluctuate. More recently, lime suspension in rotating reactors, high gravity multiphase reactive precipitation, and other methods have been developed, however these methods do not give finer control to the synthesis for manipulating the size and shape of the nanoparticles.

Controlled synthesis of nanoparticles has become a significant subject of colloid and materials chemistry, due to the development and deeper understanding of the effects size and shape have on the properties of the nanoparticles. As the understanding of the nucleation and growth process has become more in-depth, we are able to utilise this knowledge to better control the shape and size of nanoparticles being synthesised [30], tailoring their properties. As the shape of the nanoparticle influences the surface structure, {111}, {110}, and {100}, Figure 1.1, specifically for ceria the {111} surface is the most stable and is also the least reactive. It is therefore necessary to manipulate the surface structure, by tuning the shape, to expose the less stable surfaces, more specifically the {100} surface, which is also the most reactive.

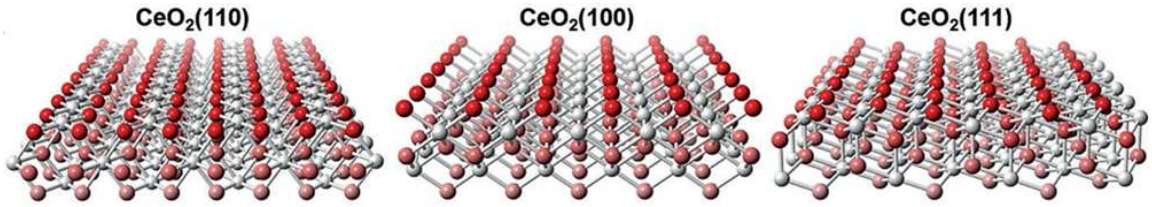

Figure 1.1: Structural models of ceria showing the {110}, {100}, and {111} surface structures, where the white atoms represent Ce and the red atoms represent O [31].

1.1.2 Silica Aerogels

Aerogel is a unique type of solid material comprising of an exceptionally low density, with up to 98% of their volume consisting of air [32]. The structure of an aerogel consists of open pores which results in a very high surface area relative to its size. These properties cause aerogels to have curious physical properties such as low refractive index [33, 34], low thermal conductivity [35], low sound speed [36], high mechanical strength [37, 38], and a low mean free path of diffusion [39].

Silica aerogels were first synthesised in 1931 by S.S. Kistler as, surprisingly, the result of a bet with a colleague as to who could replace the liquid in gels with a gas [40, 41], without destruction of the microstructure or shrinking of the networked solid. This idea lead to the extraction of the solvent while in a supercritical state (supercritical drying), avoiding the destructive nature of a solvent front on the fragile pore network (capillary action), which resulted in what we refer to as aerogels [42]. Kistler's method used a sodium silicate solution reacted with hydrochloric acid, Equation 1.1. To turn this solution into an aerogel, the NaCl needed to first be removed through multiple washing cycles, then the water removed and replaced by another solvent.

$$Na_2SiO_2 + 2HCl \xrightarrow{H_2O} [SiO_2 \cdot xH_2O] + 2NaCl \tag{1.1}$$

Although this was an optimistic and promising area of study, the process was both complicated and time consuming, which lead to very little interest in the field of aerogels until much later on when the synthetic procedure was carefully reconsidered, making it simpler and quicker. The next most notable acceleration in aerogel synthesis research was achieved by Teichner *et al* in 1968 where the use of TMOS (tetramethoxysilane) removed the need for solvent exchange in the sol-gel preparation process [43], Equation 1.2. Since then, further progress in the area of aerogel synthesis has lead to newly developed processes which utilised hydrolysis and condensation reactions of metal alkoxide precursors [44] (such as TEOS) to form the gel, with more readily used solvents such as ethanol.

$$Si(OCH_3)_4 + H_2O \xrightarrow{CH_3OH} [SiO_2 \cdot H_2O] + CH_3OH \tag{1.2}$$

As mentioned, aerogels are formed from their molecular precursor, sol-gels, which consist of an interlinked pore system filled with a liquid solvent. The sol-gel process [45] involves converting a precursor of colloidal particles (usually 1-1000 nm diameter) dispersed in a liquid (*sol*) into a discrete integrated network of pores (*gel*) filled with liquid. Silicate based sol-gels are of particular interest, with applications in areas such as catalytic activity [46], optical properties [47], and antibacterial biomaterials [48]. The sol-gel process has also been considered a useful technique for preparing nanoparticles due to its ability to give good stoichiometric control and produce ultrafine particles with a narrow size distribution at a relatively low temperature in a short time scale [49].

Currently, there is high interest in aerogels, with research and reviews published on the synthesis, properties, and applications of aerogels [50, 51]. Silica aerogels are among the most common, with applications in many fields, including thermal [52]/acoustic [36] insulation, gas-phase purification, sensing, and catalysis [53].

1.1.2.1 Sol-gel Chemistry

From a chemical stand point, the precursors which are generally used in sol-gel syntheses are commonly metal alkoxides, which are metal organic compounds with an organic ligand attached to a metal atom. These possess the general form $M(OR)_n$, and undergo a series of hydrolysis equilibria. A solution containing a catalyst, which aids in accelerating the hydrolysis, and the alkoxide precursor are reacted, resulting in the initial equilibria reaction presented in Equation 1.3, and propagated as presented in Equation 1.4.

$$M(OR)_n + H_2O \rightleftharpoons M(OR)_{n-1}(OH) + ROH \tag{1.3}$$

$$M(OR)_{n-(n-1)}(OH)_{n-1} + H_2O \rightleftharpoons M(OH)_n + ROH \tag{1.4}$$

In a second stage, depending on parameters such as temperature, and with the addition of an alcohol, condensation reactions can occur via a polymerisation mechanism, which subsequently forms M-O-M bonds. This can be between -OH groups (Equation 1.5) or -OH and non-hydrolysed -OR groups (Equation 1.6).

$$2M(OR)_{n-1}(OH) \rightleftharpoons (OR)_{n-1}M(OR)_{n-1} + H_2O \tag{1.5}$$

$$M(OR)_{n-1}(OH) + M(OR)_n \rightleftharpoons (OR)_{n-1}M(OR)_{n-1} + ROH \tag{1.6}$$

The most widely and extensively explored metal alkoxide is tetraethyl orthosilicate (TEOS), which results in silica gels/aerogels, or as a common alternative tetramethoxysilane (TMOS). TEOS and TMOS are popular precursor as they are able to readily react with water to form silanol groups, where M = Si and n = 4 in Equation 1.3. With the addition of alcohol, this can then sub-sequentially undergo an alcohol condensation reaction, forming polysilicates, which can occur between -OH groups (such as in Equation 1.5) and -OH with an non-hydrolysed -OR group (such as in Equation 1.6).

After the sol-gel process is completed the liquid (solvent) needs to be removed from the pores of the wet gel and replaced with gas, which can be achieved through various drying techniques. When the wet gel is left to dry in air the solvent evaporates, however forces at the liquid-vapour interface cause surface tension through capillary pressure (Δp) and result in the deformation and collapse of the porous structure. Capillary pressure is inversely proportional to the pore radius, which can be expressed using the Laplace equation, Equation 1.7.

$$\Delta p = \frac{2\gamma cos\theta}{r} \tag{1.7}$$

Here, γ is the surface tension of the liquid phase, θ is the contact angle of the meniscus at the liquid-vapour interface, and r is the radius of the pore. This interaction can also be represented visually, as given in Figure 1.2. As the pores shrink in size, OH groups at the surface of the gel draw closer together and cause a reaction. For example, in a SiO_2 gel this can form siloxane bridges which further decreases pore size. This would reduce the overall volume and form a dense material known as a xerogel; therefore to avoid the liquid-vapour phase boundary of the solvent and prevent capillary pressure occurring, so a low density aerogel is formed, special drying techniques are employed.

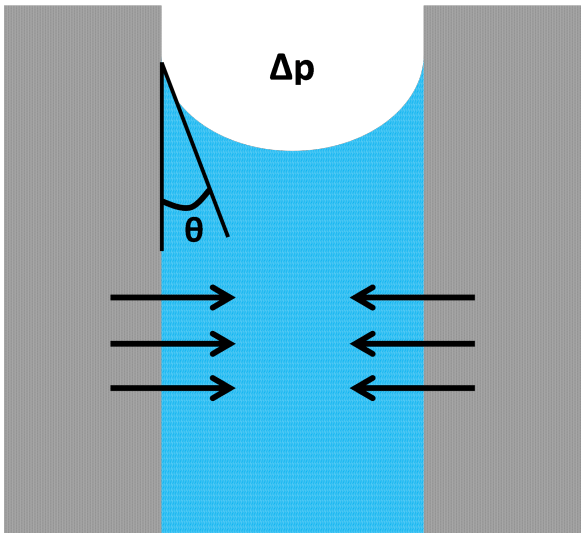

Figure 1.2: Pictographic representation of capillary pressure (Δp) occurring within a pore of a drying gel, propagated by the presence of the meniscus of contact angle θ.

There are many types of drying techniques to obtain aerogels, such as freeze-drying which involves freezing the liquid in the pores and subliming under vacuum [54], ambient-pressure drying using a series of solvent exchanges [55, 56], and supercritical drying of which there are two types: CO_2 (cold) [57] and organic solvent supercritical drying (hot). The latter here is the method employed in this thesis, and will be discussed in further detail.

1.1.2.2 High-Temperature Supercritical Drying (HT-SD)

Organic solvent supercritical drying requires temperatures above 250 °C (T_c) and pressures around 5-8 MPa (P_c) for the alcohol or acetone solvent to achieve a supercritical state. Adversely, high temperatures and pressures give rise to fire risks and a possibility of the vessel exploding if not controlled correctly, therefore many safety precautions must be taken. There is also an additional risk of the gel network rearranging due to the high temperature. The benefit of this drying process however is that there is minimal shrinkage/collapse of the pore network, allowing the formation of very low density aerogels. As the solvent is heated to its supercritical state, the pore structure is held in place as if it still contained a liquid, however there is now an absence of a liquid-vapour interface. The solvent is evacuated slowly under constant high temperature to retain the supercritical state, and is replaced with a gas, forming the low density aerogel.

As mentioned previously, the first occasion where supercritical drying was preformed to extract a solvent from a gel was by Kistler in 1931 [40]. In this instance, Kistler initially used water as a solvent, which resulted in failed extraction attempts. As water approaches its super critical conditions, these conditions induced the network structure of silica to break down and form a colloidal solution with the water. Solvents with lower critical points need to be used, which lead to Kistler performing solvent exchange to remove the water and replace it with a lower critical point counterpart, such as ethanol.

1.1.3 Nanocomposites

Composite materials comprise of multiple phases in order to obtain synergistic properties unattainable by one material alone. Phases usually comprise those termed as a matrix phase and a reinforcement phase. Nanocomposites have at least one phase with a dimension less than 100 nm, or a repeating separation with nanoscale distances between different phases. In mechanical terms, nanocomposites vary from 'conventional' nanocomposites, mainly in the aspect of the reinforcement phase presenting an exceptionally high surface area to volume ratio. For aerogel nanocomposites the aerogel would be the matrix phase and the reinforcement phase could comprise particles, sheets, fibres, etc. The inter-facial area between the matrix and reinforcement phases is therefore an order of magnitude greater than conventional nanocomposites, and the material properties are significantly affected. Due to the sizeable surface area of the reinforcement phase (the nanomaterial), only relatively small quantities are needed to observe an effect in the material properties.

Due to the exceptional nature of nanocomposites there are many different types which span a range of uses, however, the nanocomposite of interest in this research is a dispersion of nanoparticles in a larger host matrix, specifically, silica aerogel. Here, nanoparticles are dispersed in the networked porous silica matrix, which in itself has great interest as it can provide an array of benefits.

1.1.3.1 Silica Aerogel as a Host Matrix

Nanoparticles and nanoscale materials are particularly difficult to manipulate due to their size and chemistry. A main issue facing nanoparticle use is the tendency for particle aggregation, forming larger particles, which can be accentuated by thermal treatment and can lead to an extensive reduction in surface area. This is particularly problematic in catalysis where reduced surface area will significantly reduce the particles reactivity [58]. Using aerogel as a host matrix will allow the nanoparticles to be dispersed into the pores, preventing (at least in part) aggregation and growth of the particles. This allows the nanoparticles to retain their larger surface area and thus their reactivity. As aerogels possess high internal-surface areas, it allows for a high loading of nanoparticles, or other substrates, into the matrix with minimal obstruction to the surface area. This allows high permeability, giving external species good accessibility to the nanoparticles, which is beneficial for applications such as catalysis.

Silica aerogels have been widely used as host matrices due to their unique properties, such as good electrical/acoustic/thermal insulation. Synthesis of their nanocomposites is therefore fairly well explored, with nanoparticle-aerogel composites investigated for their magnetic [59], magneto-optic [60], and catalytic properties [53].

1.1.3.2 Synthesis of Nanocomposite

There are many variables associated with the sol-gel process, so the exact relationship between the synthetic parameter and the resulting microstructural features, such as pore and particle size, homogeneity, and particle distribution is rather challenging to determine. For this reason, the synthetic process and manner in which the nanophase is introduced into the silica aerogel needs careful consideration. There are broadly speaking two methods which can be taken; these are co-gelation and embedment of the nanophase into the pre-formed aerogel. These methods are more fully described by Schubert in 2009 [61], however a brief introduction to the methods is given here.

Co-gelation can be further defined into two categories: co-gelation with the nanophase precursor [62], and co-gelation with the preformed nanophase [63]. In the former, the nanophase is synthesised alongside the silica aerogel, combining the processes, where in the latter, the nanophase is synthesised separately and introduced into the aerogel synthesis to be encapsulated in the matrix as it forms. Co-gelation allows for better control over the dispersion of the nanophase in the matrix, where the loading can be more homogeneous, however, co-synthesis or the presence of a preformed nanophase could have adverse effects on the formation of the silica aerogel.

Introduction of a nanophase directly into pre-formed aerogel, also known as embedment or impregnation, has previously been seen with both the nanophase precursor [64] and pre-formed nanoparticles [65]. This method removes the interference of the nanophase, or precursor, with the synthesis of the aerogel, however there are major limitations associated with this method, the most severe being the poor control of the dispersion/loading of the nanophase into the matrix, and the possibility of damaging the silica aerogel by, for example, introducing the nanophase in liquid phase which can cause capillary action to occur and subsequently collapse the pores.

The nanocomposites produced in this thesis were formed via co-gelation with pre-formed nanoparticles. This method was chosen for its ability to provide good dispersion of the nanoparticles in the silica aerogel matrix and to control the shape of the nanoparticles.

1.1.4 Computational Chemistry

Computational Chemistry uses theoretical chemistry methods, experimentally derived parameters, and computer simulations to calculate the structures and properties of molecules and materials. The data obtained from computational methods usually complement information gained from experimental analysis, and is especially useful for analysing phenomena which is currently not feasible through experimental procedures. It is an effective tool for advances in understanding many-body problems which can not be solved analytically, providing insight into, and predicting, many material properties such as relative energies [66], vibrational frequencies [67], reactivity [68], structure [69], and mechanical properties [70, 71]. Computational chemistry is notably used in industry for the design of new drugs and materials, can be used for biological materials [72], and widely used in research making it a powerful tool for future developments in chemistry.

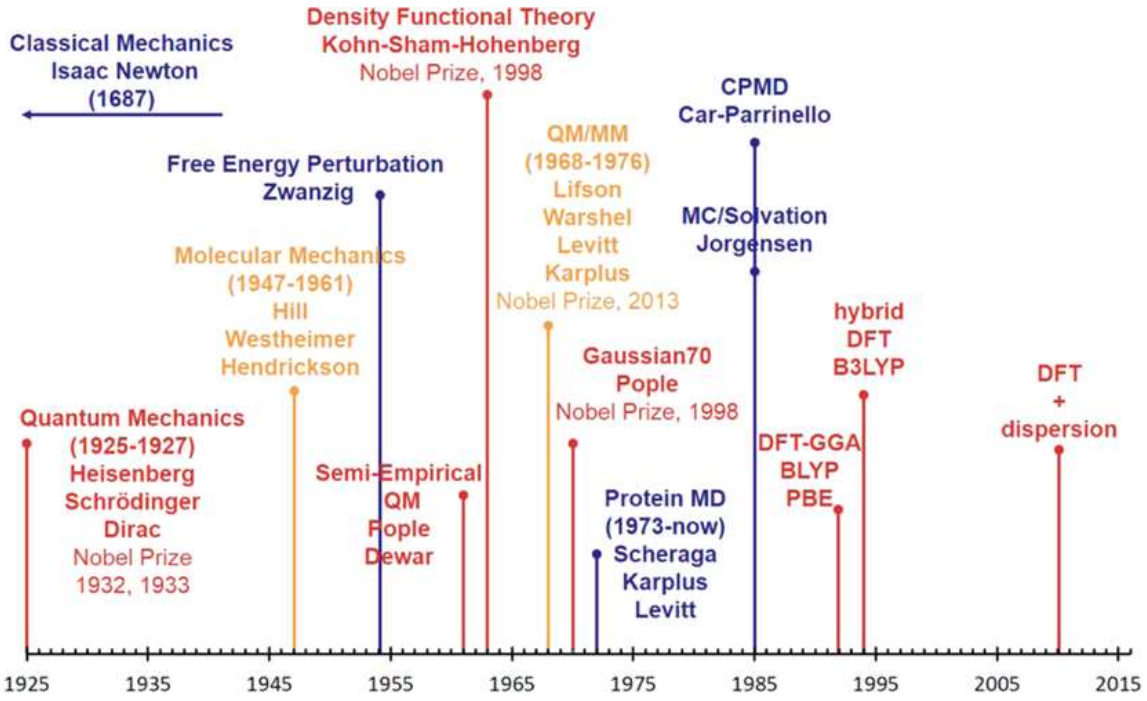

Figure 1.3: A time line presenting some of the milestones achieved in computational chemistry [73]. Red indicated advancements in quantum mechanics (QM), with yellow indicating advancements in molecular mechanics (MM) and QM-MM. Blue indicates developments in molecular dynamics (MD).

Computational chemistry can still be considered in its infancy, with ever growing prospects. In the 1960s computational chemistry was a rarity and had many limitations, however since this time it has rapidly expanded, becoming an alternative/complementary method to experiment. This rapid progress was possible due to the substantial development of computers and technology over a relatively small space of time, concurrently with the development of new mathematics for accurate quantum mechanics (QM) and molecular dynamics (MD) methods. Houk and Liu recently gave an overview of the history of computational chemistry over the last century [73], summarising the milestones as shown in Figure 1.3. These milestones, and the further development of computational techniques has lead to many branches of computational chemistry. Currently, there are many subsections of computational methods, such as Ab initio methods, density functional methods, semi-empirical methods, molecular mechanics, methods for solids, chemical dynamics, molecular dynamics, and quantum mechanics molecular mechanics (QM-MM).

This investigation aims to study the larger scale physical and chemical properties of nanomaterials in order to characterise their behaviours. To do this classical molecular dynamic (MD) atomistic modelling was employed. Out of the many possible methods which could be used, MD was chosen as it has shown to be an effective tool for analysing the dynamic evolution of a system, with focus on the physical movement of atoms [74, 75].

Compared to the 'perfect' or 'ideal' structures used in theoretical studies, models used in computer simulations are able to incorporate abnormalities found to naturally occur experimentally. Atomistic MD simulation therefore is able to capture more realistic structures than, of example QM, as it is able to consider more atoms and thus provide more reliable and comparable results. More specifically an amorphisation recrystallisation technique can be used to allow the microstructural features to evolve in a more natural manner, analogous to experiment [76, 77, 78]. An overview of molecular dynamics is given here, with more specific details of the method described in Chapter 2, Section 2.3.2.

1.1.4.1 Molecular Dynamic Simulations

Molecular Dynamics (MD) is a computational method which studies the physical movements of atoms/molecules, to predict the dynamic evolution of the system over time. The system is comprised of N particles which interact via given interatomic potentials in a classical mechanics framework. This process involves giving each atom an initial location and velocity, then letting them interact over a time period. The trajectories of the atoms over time are determined by numerically solving Newton's equation of motion, Equation 1.8.

$$m_i \vec{r_i} = \vec{f_i}, \vec{f_i} = -\frac{\partial}{\partial \vec{r_i}} u_i \tag{1.8}$$

Here m_i, $\vec{r_i}$, $\vec{f_i}$, and u_i are the mass, coordinates, forces, and potential energy of atom i respectively. In order to conduct an MD simulation, the given system of N atoms, must contain the initial co-ordinates of the atoms and the interatomic potential must be defined.

The interatomic potential describes the interaction between atoms as a function of their position. The potential is chosen depending on the type of study being conducted. There are many inter- and intra- atomic potentials which can be employed by DL_POLY in a classical MD frame work. These include Lennard-Jones, Buckingham, Born-Huggins-Meyer, and Morse potentials. A mixture of potentials can be used to describe the long and short range interactions between atoms and define details such as angular restrictions, multi-body potentials, and tethering forces. A distinction can be made between interactions of the atom as a whole or use of a core-shell model where electrons are treated separately to the core to allow for consideration of polarisation. Here, we are studying ionic solids, metal oxides, where the Coulomb-Buckingham potential [79] has been proven to be particularly effective [80, 81, 82, 83]. This is derived from the Born model of the ionic solid, where the potential energy of the system can be expressed as:

$$E(r_{ij}) = \sum_{ij} \frac{Q_i Q_j}{4\pi\varepsilon_0 r_{ij}} + \sum_{ij} A \exp\left(\frac{-r_{ij}}{\rho}\right) - C r_{ij}^{-6} \tag{1.9}$$

The first term represents the long-range Coulombic interaction between ions, i and j, of charge Q_i and Q_j at a distance of r_{ij}, where ε_0 is the permittivity of free space. The second and third terms represent the short-range Buckingham potential, which describes the Pauli repulsion energy and Van der Waals energy between electron charge clouds. Here A, ρ, and C are constants, which are determined by fitting experimental data for the material.

The basic model for a neutral periodic system is a system of charged point ions mutually interacting via the Coulomb potential. The Ewald Summation [84] can be considered an excellent technique for calculating electrostatic interactions in a periodic system, and the method makes two amendments to the Coulomb potential. Firstly by super-positioning a spherical gaussian cloud of charge, opposite to that of the ion, effectively neutralises the ion at long range, which can then be treated as short ranged. The second amendment superimposes another set of gaussian charges, with the same charge as the ion, which nullifies the effect of the previous gaussian charges. Due to these charges, which are obtained from Poisson's equation, the potential is solved as a Fourier series in *Reciprocal Space* and therefore converges the calculations of $\frac{1}{r}$ much faster, saving computational time. The full Ewald sum needs an additional correction, called the self energy correction, which arises from a gaussian acting on its own site, and is constant. Ewald's method therefore speeds up a slowly converging sum. For molecular systems, as opposed to systems comprised simply of point ions, additional modifications are necessary to correct for the excluded (intra-molecular) Coulombic interactions.

Molecular dynamics simulations have been hailed as an effective tool for the study of physical and chemical behaviours of nanoporous materials [85] among other properties. MD can be used on different scales (i.e. number of atoms in the system) which leads to Quantum-MD (electronic level), classical-MD (atomistic level), and meso-MD (clusters of particles).

1.1.4.2 MD of Mechanical Properties

The mechanical properties of a material are governed by the microstructural features present and are vital to understand and impose limits on the working conditions under which the material can be used without extinguishing desirable properties. A widely studied area of mechanical properties of nanomaterials is on nanoporous metals.

In a review conducted by Xia *et al* in 2015 [86], a range of papers were discussed on the deformation mechanisms of nanoporous metals under uniaxial tension and compression loading. The review found that there was a close agreement between the simulated elastic moduli and constitutive theory. In one of the papers discussed, MD simulations were used to investigate the deformation behaviours and underlying physical mechanisms of nanoporous gold under uniaxial tension [87]. The study found that under tension, and similarly under stress, the dislocations/grain boundaries within the nanoporous structure shift to release energy/pressure from the system, then the ligaments rupture and fully dislocate which leads to a complete plastic deformation.

The deformation mechanism of a nanomaterial depends on multiple structural properties including crystal structures, surface geometry, applied stress state, axial and surface orientation, and exposed transverse surfaces [88].

It has been demonstrated by multiple researchers that the structures and properties of nanomaterials can vary from the bulk material fairly considerably due to the surface effect which can result in different deformation modes. This can be shown both through experiment and molecular dynamic simulation. An example of this is a study by Park where a nanowire with {110} surface type was compressed and it was found that the surfaces prevented slips (on the free surfaces), whereas the higher energy state surfaces of {100} and {110} observed slips occurring and stacking faults appearing [89]. This shows that by simply changing orientation or surface type the mechanical properties can be altered.

In 1999 a study conducted by Ikeda el at using MD simulations focused on the deformation of single crystal Ni and NiCu alloy nanowires, which were subjected to a uniform strain rate [90]. They found that the nanowires are elastic up to 7.5% strain with a yield stress of 5.5 GPa. The transformation from elastic deformation to plastic deformation, where the material suffers irreversible damage, does not occur instantaneously but is a continuous process of slips, twinning, and releases of energy which prolongs the deformation. This phase transformation showed the potential of super plastic behaviour [91].

As previously discussed, ceria nanostructures have been found to have vastly differing physical, chemical, and mechanical properties compared to the bulk equivalent, with a computational comparison of the mechanical properties of nanoceria nanostructures and bulk material well explored, such as by Bresesinski *et al* in 2010 [92]. It is also known that dislocations play a vital role in mechanical strength. However there is a void in the knowledge and understanding of the deformation mechanisms which limits and prevents the ability to form nanomaterials with the desired mechanical properties. This is where atomistic simulations can assist.

The mechanical properties of bulk materials can be determined experimentally, however nanostructures have proven to be more difficult. There has been a fair amount of computational simulations in recent years to aid in understanding these mechanical properties bu in a lot of cases it has been found that the computational models do not entirely predict what is seen experimentally. An example of this would be a study conducted by Agrawal *et al* in 2009 where they found, through simulation, fracture strains to be in the range of 6.5-7.5% in contrast to the experimental observations of 2.4-6% [93]. This is believed to be caused by the 'pristine' structures of

the atomistic models which do not take into account the microstructural features (i.e. voids and grain boundaries etc.) seen experimentally. To address this issue, there are two main driving mechanisms which have been identified which will introduce these microstructural features into the atomistic models. These are crystallisation and the self-assembly of nanoparticles [94]. It hasn't been till more recent years that the inclusion of microstructural features in atomistic models has been considered, with studies conducted on ceria nanoparticles for their relating mechanical properties investigated by Sayle *et al* in 2005 [77], which was further progressed by Caddeo *et al* in 2016 [78]. The work presented in this thesis aims to further progress the amorphisation-recrystallisation used in these studies.

1.1.4.3 MD of Catalytic Properties

Ceria and ceria containing materials have undergone intense scrutiny as heterogeneous catalysts due to their unique properties. The rapid increase in the application and characterisation of ceria catalysts has been highly documented, however despite its obvious importance, a detailed mechanistic understanding of the operation of a ceria catalyst is still somewhat under debate [95]. This is where computational chemistry is a vital tool in examining the mechanistic effects on an atomic scale. Not only does MD provide a visualisation of the atomic interactions, the mechanisms of the catalysis, such as the oxidation and reduction of CO/CO_2 using ceria nanoparticles [96, 97], and the use of ceria as a three way catalyst [98], can be investigated. The analysis of the structures, energies, transport, radial distribution, etc., of MD models of ceria in their role can provide insightful data into the catalytic activity. For example, catalytic activity is highly dependent upon the surface(s) exposed. In particular, ceria {111} surfaces are thermodynamically more stable than {100} surfaces, however, it is more energetically favourable to extract oxygen from the {100} surfaces. Therefore nanoceria, which exposes {100} surfaces is catalytically more active than nanoceria exposing {111}. Oxygen vacancy formation energies reflect the energy required to extract the oxygen and can be gauged by calculating the Madelung energies of the surface oxygen ions. Similarly, calculated mean square displacements (MSD) of oxygen provide insight into oxygen transport within the material. Radial distribution functions (RDF) indicate the order of atoms within a structure and loss in long range order could suggest a change in structure and therefore affect the catalytic activity.

1.1.4.4 MD of Silica Aerogels

MD simulation of aerogels is not a technique which has been widely investigated, in part due to the complex structure of aerogels. With such a low density material and the scale in which MD can operate it is a challenging task to capture the structure in a way which accurately represents the amorphous aerogel structure, specifically the interlinks between the repeating cells. This repeating cell approach in itself will cause some level of order in the aerogel, which is not analogous to the observed structure. That being said, and noted as a limitation, there have been a few different approaches adopted for the formation of the aerogel model. In 1995 Pohl *et al* presented two methods of simulating aerogel using MD [99]. The first method involved hexagonally packing 40 Å silica spheres into a defined space with the aim to study the pore structures. This method is arbitrarily ordered and not a fair representation of the aerogel structure. The second method employed by Pohl *et al* to generate the aerogel model was to take SiO_2 glass and quench it to 300 K after MD at 5000 K, the model cell and atomic coordinates were subsequently expanded by 10% or 20% using the potentials of Fueston and Garofalini [100]. By expanding the glass structure pores were able to form and the string like network was observed. This gave a better representation of the amorphous structure, however it also produced many unconnected ends and some unattached clusters, therefore analysis of mechanical properties, in this case, would not be representative.

In 2010, a different approach to generating an aerogel model was presented by Murillo *et al*, with focus on determining the structure and mechanical properties [101]. Here they used interatomic potentials for amorphous silica developed by Vashishta *et al* [102, 103], with the atomic coordinates for β-crystobalite given by Wyckoff [104]. The model was generated by placing atoms at the β-crystobalite sites, with the desired density. The system was then heated to 3000 K and cooled, transitioning through relaxation steps at several temperatures. The aim was to have a uniform distribution of atoms across the bulk, however in places there was some level of aggregation and others free floating clusters.

In 2012 Ng *et al* used negative pressure rupturing as their approach to forming the aerogel model [105], which followed on from the work of Kieffer and Angell [106]. Here, again, the ideal β-crystobalite structure was used as a base and quenched from 6000 K to 300 K to form a random amorphous silica. This was then expanded uniformly in successive steps, giving the final silica aerogel model. This was a very similar approach to that used by Pohl *et al*, varying mainly in the potentials and temperatures used. This model did appear to contain less free floating clusters.

In the work presented in this thesis, Chapter 7, a new approach was developed. As discussed previously, silica aerogel is formed from SiO_2 seeds, and growth to form the network within a solvent. It is very difficult to capture this experimental formation process in simulation, and resulting frameworks can become branched and flexible. It is also challenging to reproduce a truly random network, interlinking between cells. A more 'natural' approach was taken here, where individual atoms and small seed clusters were placed into a system of specified volume. The Si and O atoms attached to the seeds, forming chains, then bridges between the chains, developing the network. Where atoms and small clusters were unable to attach to the network, due to the limitation in movement without a solvent present, the atoms were removed and randomly replaced into the system for attachment. This process is described in more detail in Chapter 7.

References

[1] Y. Li and W. Shen. Morphology-Dependent Nanocatalysts: Rod-Shaped Oxides. *Chemistry Society Review*, 43:1543, 2014.

[2] A. Rogach. How Many Nano Journals does the World Need? *ACS nano*, 6: 9349, 2012.

[3] D. Guo, G. Xie, and J. Luo. Mechanical Properties of Nanoparticles: Basics and Applications. *Journal of Physics D:Applied Physics*, 47:013001, 2014.

[4] M.J. Climent, A. Corma, S Iborra, and M. Mifsud. MgO Nanoparticle-Based Multifunctional Catalysts in the Cascade Reaction Allows the Green Synthesis of Anti-Inflammatory Agents. *Journal of Catalysis*, 247(2):223–230, 2007.

[5] R. Jayakumar, D. Menon, K. Manzoor, S.V. Nair, and H. Tamura. Biomedical Applications of Chitin and Chitosan Based Nanomaterials A Short Review. *Carbohydrate Polymers*, 82(2):227–232, 2010.

[6] H. Jiang, J. Ma, and Li. C. Mesoporous Carbon Incorporated Metal Oxide Nanomaterials as Supercapacitor Electrodes. *Advanced Materials*, 24(30):4197–4202, 2012.

[7] T. Zhai, X. Fang, M. Liao, X. Xu, H. Zeng, B. Yoshio, and D. Golberg. A Comprehensive Review of One-Dimensional Metal-Oxide Nanostructure Photodetectors. *Sensors*, 9(8):6504–6529, 2009.

[8] M. Hua, S. Zhang, B. Pan, W. Zhang, L. Lv, and Q. Zhang. Heavy Metal Removal from Water/Wastewater by Nanosized Metal Oxides: A Review. *Journal of Hazardous Materials*, 211-212:317–331, 2012. doi: doi.org/10.1016/j.jhazmat.2011.10.016.

[9] L.R. Khot, S. Sankaran, J.M. Maja, R. Ehsani, and E.W. Schuster. Applications of Nanomaterials in Agricultural Production and Crop Protection: A Review. *Crop Protection*, 35:64–67, 2012. doi: doi.org/10.1016/j.cropro.2012.01.007.

[10] G.B. Basim, J.J. Adler, U. Mahajan, R.K. Singh, and B.M. Moudgil. Effect of Particle Size of Chemical Mechanical Polishing Slurries for Enhanced Polishing with Minimal Defects. *Journal of The Electrochemical Society*, 147(9):3523–3528, 2000.

[11] J. Harra, J. Mäkitalo, R. Siikanen, M. Virkki, G. Genty, T. Kobayashi, M. Kauranen, and J.M. Mäkelä. Size-Controlled Aerosol Synthesis of Silver Nanoparticles for Plasmonic Materials. *J. Nanopart. Res.*, 14:1, 2012.

[12] N. Ta, J. Liu, and W. Shen. Tuning the Shape of Ceria Nanomaterials for Catalytic Applications. *Chinese Journal of Catalysis*, 34(5):838–850, 2013.

[13] J.Y. Huang, L. Zhong, C.M. Wang, J.P. Sullivan, W. Xu, L.Q. Zhang, S.X. Mao, N.S. Hudak, X.H. Liu, A. Subramanian, H. Fan, L. Qi, A. Kishima, and J. Li. In Situ Observation of the Electrochemical Lithiation of a Single SnO_2 Nanowire Electrode. *Science*, 330:1515, 2010.

[14] L. Malavasi, C.A.J. Fisher, and M. Saiful Islam. Oxide-Ion and Proton Conducting Electrolyte Materials for Clean Energy Applications: Structural and Mechanistic Features. *Chemical Society Reviews*, 39:4370–4371, 2010.

[15] H.X. Mai, L.D. Sun, Y.W. Zhang, R. Si, W. Feng, H.P. Zhang, H.C. Liu, and C.H Yan. Shape-Selective Synthesis and Oxygen Storage Behaviour of Ceria Nanopolyhedra, Nanorods, and Nanocubes. *Journal of Physical Chemistry B*, 109(751):24380–24385, 2005.

[16] K. Zhou, X. Wang, X. Sun, Q. Peng, and Y. Li. Enhanced Catalytic Activity of Ceria Nanorods from Well-Defined Reactive Crystal Planes. *Journal of Catalysis*, 229(1):206–212, 2005.

[17] M. Mogensen, N.M. Sammes, and G.A. Tompsett. Physical, Chemical and Electrochemical Properties of Pure and Doped Ceria. *Solid State Ionics*, 129 (1-4):63–94, 2000.

[18] A. Holmgren, D. Duprez, and B. Andersson. A Model of Oxygen Transport in Pt/Ceria Catalysts from Isotope Exchange. *Journal of Catalysis*, 182(2): 441–448, 1999.

[19] T.H. Santos, J.P.F. Grilo, F.J.A. Loureiro, D.P. Fagg, F.C. Fonseca, and D.A. Macedo. Structure, Densification and Electrical Properties of Gd^{3+} and Cu^{2+} Co-Doped Ceria Solid Electrolytes for SOFC Applications: Effects of Gd_2O_3 Content. *Ceramics International*, 44(2):2745–2751, 2018.

[20] A. Corma, P. Atienzar, H. Garca, and J. Chane-Ching. Hierarchically Mesostructured Doped CeO_2 with Potential for Solar-Cell Use. *Nature Materials*, 3:394–397, 2004.

[21] S. Liu, X. Wu, D. Weng, and R. Ran. Ceria-Based Catalysts for Soot Oxidation: A Review. *Journal of Rare Earths*, 33(6):567–590, 2015.

[22] C. Walkey, S. Das, S. Seal, J. Erlichman, K. Heckman, L. Ghibelli, E. Traversa, J.F. McGinnis, and W.T. Self. Catalytic Properties and Biomedical Applications of Cerium Oxide Nanoparticles. *Environmental Science: Nano*, 2:33–53, 2015. doi: 10.1039/C4EN00138A.

[23] P.R. Veera Dandu, B.C. Peethala, and S.V. Babu. Role of Different Additives on Silicon Dioxide Film Removal Rate during Chemical Mechanical Polishing Using Ceria-Based Dispersions. *Journal of The Electrochemical Society*, 157(9): 869–874, 2010.

[24] T.X.T. Sayle, M. Cantoni, U.M. Bhatta, S.C. Parker, S.R. Hall, G. Möbus, M. Molinari, D. Reid, S. Seal, and D.C. Sayle. Strain and Architecture-Tuned Reactivity in Ceria Nanostructures; Enhanced Catalytic Oxidation of CO to CO_2. *Chemistry of Materials*, 24(10):1811–1821, 2012.

[25] H.C. Yao and Y.F. Yu Yao. Ceria in Automotive Exhaust Catalysts: I. Oxygen Storage. *Journal of Catalysis*, 86(2):254–265, 1984.

[26] K. Reed, A. Cormack, A. Kulkarmi, M. Mayton, D. Sayle, F. Klaessig, and B. Stadler. Exploring the Properties and Applications of Nanoceria: Is there Still Plenty of Room at the Bottom? *Environment Science: Nano*, 1:390–405, 2014. doi: 10.1039/C4EN00079J.

[27] G. Gonzalez, J. Freites, and C. Rojas. Synthesis and Characterisation of Nanophase Particles Obtained by D.C. Sputtering. *Scripta Materialia*, 44:1883–1887, 2001.

[28] C.G. Granqvist and R.A. Buhrman. Ultrafine Metal Particles. *Journal of Applied Physics*, 47:2200, 1976. doi: doi.org/10.1063/1.322870.

[29] H. Hahn and R. Averback. The Production of Nanocrystalline Powders by Magnetron Sputtering. *Journal of Applied Physics*, 67:1113–1115, 1990.

[30] H. Cölfen, S. Mann, and S. Angew. HigherOrder Organization by Mesoscale SelfAssembly and Transformation of Hybrid Nanostructures. *Angewandte Chemie: International Edition*, 42(21):2350–2365, 2003.

[31] C. Yang, X. Yu, S. Heissler, P.G. Weidler, A. Nefedov, Y. Wang, C. Wöll, T. Kropp, J. Paier, and J. Sauer. O_2 Activation on Ceria Catalysts - The Importance of Substrate Crystallographic Orientation. *Angewandte*, 56:16399–16404, 2017.

[32] M.A. Aegerter, N. Leventis, and M.M. Koebel. *Aerogels Handbook*. Springer, 2011. ISBN 978-1-4419-7589-8.

[33] K. Nanbu, S. Kashiwagi, F. Hinode, Muto. T/, I. Magasawa, Takahashi. K., K. Kanomata, H. Saito, T. Abe, Y. Saito, and H. Hama. Study of Cherenkov Radiation from Thin Silica Aerogel. *International Journal of Magnetics Electromagnetism*, 3(7), 2017.

[34] P. Wang, Beck. A., W. Körner, H. Scheller, and Fricke. J. Density and Refractive Index of Silica Aerogels After Low- and High-Temperature Supercritical Drying and Thermal Treatment. *Journal of Physics D: Applied Physics*, 27:414, 1994.

[35] Y. Xie, Z. Xu, H. Wu, C. Deng, and X. Wang. Interface-Mediated Extremely Low Thermal Conductivity of Graphene Aerogel. *Carbon*, 98:381–390, 2016.

[36] S. Malakooti, H.G. Churu, A. Lee, T. Xu, H. Luo, N. Xiang, C. Sotiriou-Leventis, N.Leventis, and H. Lu. Sound Insulation Properties in Low-Density, Mechanically Strong and Ductile Nanoporous Polyurea Aerogels. *Journal of Non-Crystalline Solids*, 476:36–45, 2017.

[37] A. Simón-Herrero, C. adn Romero, J.L. Valverde, and L. Sánchez-Silva. Hydroxyethyl Cellulose/Alumina-Based Aerogels as Lightweight Insulating Materials with High Mechanical Strength. *Journal of Material Science*, 53(2):1556–1567, 2018.

[38] B. Zhang, J. Zhang, X. Sang, C. Liu, T. Luo, L. Peng, B. Han, X. Tan, X. Ma, D. Wang, and Zhao. N. Cellular Graphene Aerogel Combines Ultralow Weight and High Mechanical Strength: A Highly Efficient Reactor for Catalytic Hydrogenation. *Scientific Reports*, 6(25830), 2016.

[39] V. Kuzmin, K. Safiullin, A. Stanislavovas, and M. Tagirov. Helium-3 Gas Self-Diffusion in a Nematically Ordered Aerogel at Low Temperatures: Enhanced Role of Adsorption. *Physical Chemistry Chemical Physics*, 19:23146–23153, 2017. doi: 10.1039/C7CP03949B.

[40] S.S. Kistler. Coherent Expanded-Aerogels. *Nature*, 127:741, 1931.

[41] S.S. Kistler. Coherent Expanded-Aerogels. *Journal of Physical Chemistry*, 36 (1):52–64, 1932. doi: 10.1021/j150331a003.

[42] N. Hüsing and U. Schubert. Aerogels Airy Materials: Chemistry, Structure, and Properties. *Angewandte Chemie: International Edition*, 37:22–45, 19968.

[43] S.J. Teichner and G.A. Nicolaon. Sur une nouvelle methode de préparation de Xérogels et d'Aerogels de Silice de leurs propriétés texturales. *Bulletin of the French Chemical Society*, pages 1900–1906, 1968.

[44] L.CL Klein, T.A. Gallo, and G.J. Garvey. Transparent Microporous Silica By The Sol-Gel Process. *Advances in Optical Materials*, 505, 1984. doi: 10.1117/12.964629.

[45] L.L. Hench and J.K. West. The Sol-Gel Process. *Chemical Review*, 90(1):33–72, 1990.

[46] J. Yu, XL. Zhao, and Q. Zhao. Effect of Surface Structure on Photocatalytic Activity of TiO_2 Thin Films Prepared by Sol-Gel Method. *Thin Solid Films*, 2379:7–14, 2000.

[47] D. Avnir, V. Kaufam, and R. Reisfeld. Organic Fluorescent Dyes Trapped in Silica and Silica-Titania Thin Films by the Sol-Gel Method. Photophysical, Film and Cage Properties. *Journal of Non-Crystalline Solids*, 74:395–406, 1985.

[48] M. Kawashita, S. Tsuneyama, F. Miyaji, T. Kokubo, H. Kozuka, and K. Yamamoto. Antibacterial Silver-Containing Silica Glass Prepared by Sol-Gel Method. *Biomaterials*, 21:393–398, 2000.

[49] D. Chen and X. He. Synthesis of Nickel Ferrite Nanoparticles by Sol-Gel Method. *Materials Research Bulletin*, 36:1369–1377, 2001.

[50] A.M. Anderson and M.K. Carroll. *Aerogels Handbook - Hydrophobic Silica Aerogels: Review of Synthesis, Properties and Applications*. Springer, 2011.

[51] C. Ziegler, A. Wolf, W. Liu, A. Herrmann, N. Gaponik, and A. Eychmüller. Modern Inorganic Aerogels. *Angewandte Chemie: International Edition*, 56 (43):13200–13221, 2017.

[52] G. Wei, Y. Liu, X. Zhang, F. Yu, and X. Du. Thermal Conductivities Study on Silica Aerogel and its Composite Insulation Materials. *International Journal of Heat and Mass Transfer*, 54(11-12):2355–2366, 2011. doi: 10.1016/j.ijheatmasstransfer.2011.02.026.

[53] J.E. Amonette and J. Matyáš. Functionalized Silica Aerogels for Gas-Phase Purification, Sensing, and Catalysis: A Review. *Microporous and Mesoporous Materials*, 250:100–119, 2017. doi: 10.1016/j.micromeso.2017.04.055.

[54] H. Tamon, H. Ishizaka, T. Yamamoto, and T. Suzuki. Preparation of Mesoporous Carbon by Freeze Drying. *Carbon*, 37(12):2049–2055, 1999.

[55] D. Smith, R. Desphande, and C. Brinker. Better Ceramics Through Chemistry V. *Materials Research Society symposium Proceedings*, 271:567–572, 1992.

[56] S. Prakash, C. Brinker, A. Hurd, and S. Rao. Silica Aerogel Films Prepared at Ambient Pressure by using Surface Derivatization to Induce Reversible Drying Shrinkage. *Nature*, 374:439–443, 1994.

[57] P. Lea and S. Ramjohn. Investigating the Substitution of Ethanol with Liquid Carbon Dioxide During Critical Point Drying. *Micron and Microscopica Acta*, 83:291, 1980.

[58] S. Hoo Joo, J. Young Park, C.K. Tsung, Y. Yamada, P. Yang, and G.A. Somorjai. Thermally Stable Pt Mesoporous Silica CoreShell Nanocatalysts for High-Temperature Reactions. *Nature Materials*, 8:126–131, 2009.

[59] F. Bentivegna, J. Ferré, M. Nývlt, J.P. Jamet, D. Imhoff, M. Canva, A. Brun, P. Veillet, Š. Visšňovský, F. Chaput, and J.P. Boilot. Magnetically Textured γ-Fe_2O_3 Nanoparticles in a Silica Gel Matrix: Structural and Magnetic Properties. *The Journal of Applied Physics*, 83:7776, 1998.

[60] H. Guerrero, G. Rosa, M.P. Morales, F. del Monte, E.M. Moreno, D. Levy, R. Pérez del Real, T. Belenguer, and C.J. Serna. Faraday Rotation in Magnetic γ-Fe_2O_3/SiO_2 Nanocomposites. *Applied Physics Letters*, 71:2698, 1997. doi: 10.1063/1.120181.

[61] U. Schubert. Preparation of Metal Oxide or Metal Nanoparticles in Silica via Metal Coordination to Organofunctional Trialkoxysilanes. *Polymer International*, 58(3):317–322, 2009. doi: 10.1002/pi.2526.

[62] M.F. Casula, A.C. Corrias, and G. Paschina. Fe-Co-SiO_2 Nanocomposite Aerogels by High Temperature Supercritical Drying. *Journal of Materials Chemistry*, 12(5):1505–1510, 2002.

[63] C. Legrand-Buscema, C. Malibert, and S. Bach. Elaboration and Characterization of Thin Films of TiO_2 Prepared by SolGel Process. *Thin Solid Films*, 418(2):79–84, 2002.

[64] L. Casas, A. Roig, E. Molins, J.M. Grenèche, J. Asenjo, and J. Tejada. Iron Oxide Nanoparticles Hosted in Silica Aerogels. *Applied Physics A*, 74(5):591–597, 2002.

[65] M. Popovici, M. Gich, A. Roig, L. Casas, E. Molins, C. Savii, D. Becherescu, J. Sort, S. Suri nach, J.S. Mu noz, M.D. Baró, and J. Nogués. Ultraporous Single Phase Iron OxideSilica Nanostructured Aerogels from Ferrous Precursors. *Langmuir*, 20(4):1425–1429, 2004. doi: 10.1021/la035083m.

[66] B.J. Lynch, Y. Zhao, and G. Truhlar. Effectiveness of Diffuse Basis Functions for Calculating Relative Energies by Density Functional Theory. *Journal of Physical Chemistry A*, 107(9):1384–1388, 2003.

[67] S. Grimme, C. Bannwarth, and P. Shushkov. A Robust and Accurate Tight-Binding Quantum Chemical Method for Structures, Vibrational Frequencies, and Noncovalent Interactions of Large Molecular Systems Parametrized for All spd-Block Elements (Z = 186). *Journal of Chemical Theory and Computation*, 13(3):1989–2009, 2017. doi: 10.1021/acs.jctc.7b00118.

[68] D.J. Tantillo. Faster, Catalyst! React! React! Exploiting Computational Chemistry for Catalyst Development and Design. *Accounts of Chemical Research*, 49(6):1079–1079, 2016.

[69] SM. Chen, X. Lin, W. Zheng, J.N. Onuchic, and P.G. Wolynes. Protein Folding and Structure Prediction from the Ground Up: The Atomistic Associative Memory, Water Mediated, Structure and Energy Model. *Journal of Physical Chemistry B*, 120(33):8557–8565, 2016.

[70] L. He, S. Guo, J. Lei, Z. Sha, and Z. Liu. The Effect of StoneThrowerWales Defects on Mechanical Properties of Graphene Sheets A Molecular Dynamics Study. *Carbon*, 74:124–132, 2014.

[71] R. Darkins, M.L. Sushko, J. Liu, and D.M. Duffy. Stress in Titania Nanoparticles: An Atomistic Study. *Physical Chemistry Chemical Physics*, 16(20):9441–9447, 2014.

[72] D.M. Duffy. Coherent Nanoparticles in Calcite. *Science*, 358(6368):1254–1255, 2017.

[73] K.N. Houk and F. Liu. Holy Grails for Computational Organic Chemistry and Biochemistry. *Accounts of Chemical Research*, 50:539–543, 2017.

[74] P.K. Depa and J.K. Maranas. Dynamic Evolution in Coarse-Grained Molecular Dynamics Simulations of Polyethylene Melts. *The Journal of Chemical Physics*, 126:054903, 2007.

[75] S.D. Feng, K.C. Chan, S.H. Chen, L. Zhao, and R.P. Liu. The Role of Configurational Disorder on Plastic and Dynamic Deformation in $Cu_{64}Zr_{36}$ Metallic Glasses: A Molecular Dynamics Analysis. *Scientific Reports*, 7(40969), 2017.

[76] D.C. Sayle, S.A. Maicaneanu, and G.W. Watson. Atomistic Models for CeO_2 (111), (110), and (100) Nanoparticles, Supported on Yttrium-Stabilized Zirconia. *Journal of the American Chemical Society*, 124(38):11429–11439, 2002.

[77] T.X.T. Sayle, R.A. Catlow, R.R. Maphanga, P.E. Ngoepe, and D.C. Sayle. Generating MnO_2 Nanoparticles using Simulated Amorphization and Recrystallization. *Journal of the American Chemical Society*, 127(37):12828, 2005.

[78] F. Caddeo, A. Corrias, and D.C. Sayle. Tuning the Properties of Nanoceria by Applying Force: Stress-Induced Ostwald Ripening. *Journal of Physical Chemistry C*, 120:14337–14344, 2016.

[79] R.A. Buckingham. The Classical Equation of State of Gaseous Helium, Neon and Argon. *Proceedings of the royal society A*, 168(933):264–283, 1938. doi: 10.1098/rspa.1938.0173.

[80] L. Minervini, M.O. Zacate, and R.W. Grimes. Defect Cluster Formation in M_2O_3-Doped CeO_2. *Solid State Ionics*, 116(3-4):339–349, 1999.

[81] M.O. Zacate and R.W. Grimes. Combined Monte Carlo-energy minimization Analysis of Al-Fe Disorder in Ca_2FeAlO_5 Brownmillerite. *Philosophical Magazine A*, 80(4):797, 2000.

[82] L. Minervini, R.W. Grimes, and Sickafus. K.E. Disorder in Pyrochlore Oxides. *Journal of the American Ceramic Society*, 83(8):1873–1878, 2004.

[83] T.X.T. Sayle, K. Kgatwane, P.E. Ngoepe, and D.C. Sayle. 'Breathing-Crystals' the Origin of Electrochemical Activity of Mesoporous Li–MnO_2. *J. Mater. Chem. A.*, 4:6456, 2016.

[84] M.P. Allen and D.J. Tildesley. *Computer Simulation of Liquids*. Oxford University Press, 1989. ISBN 978-0-19-880319-5.

[85] D. Crowson, D. Farkas, and S. Corcoran. Mechanical Stability of Nanoporous Metals with Small Ligament Sizes. *Scripta Materialia*, 61:497–499, 2009.

[86] R. Xia, R. Wu, Y. Liu, and X. Sun. The Role of Computer Simulation in Nanoporous Metals A Review. *Materials*, 9:5060–5083, 2015.

[87] X. Sun, G. Xu, X. Li, X. Feng, and H. Gao. Mechanical properties and scaling laws of nanoporous gold. *Journal of Applied Physics*, 113(023505), 2013. doi: 10.1063/1.4774246.

[88] H. Li and F. Sun. Recent Advances in Mechanical Properties of Nanowires. *INTECH*, 16:371–394, 2012. doi: 10.5772/52592.

[89] S. Park, K. Gall, and J. Zimmerman. Deformation of FCC Nanowires by Twinning and Slip. *Journal of the Mechanics and Physics of Solids*, 54(9):1862–1881, 2006.

[90] H. Ikeda, Y. Qi, T. Agin, K. Samwer, W. Johnson, and I. Goddard. Strain Rate Induced Amorphization in Metallic Nanowires. *Physical Review Letter*, 82:2900–2903, 1999.

[91] W. Liang and M. Zhou. Size and Strain Rate Effects in Tensile Deformation of Cu Nanowires. *Nanotechnology*, 2:452–455, 2003.

[92] T. Bresesinski, J. Wang, R. Senter, K. Bresesinski, B. Dunn, and S. Tolbert. On the Correlation between Mechanical Flexibility, Nanoscale Structure, and Charge Storage in Periodic Mesoporous CeO_2 Thin Films. *JACS Nano*, 4: 967–977, 2010.

[93] R. Agrawal, B. Peng, and H. Espinosa. Experimental-Computational Investigation of ZnO Nanowires Strength and Fracture. *Nano Letters*, 9:4177–4183, 2009.

[94] D.C. Sayle, X. Feng, Y. Ding, Z. Wang, and T.X.T. Sayle. Simulating Synthesis: Ceria Nanosphere Self-Assembly into Nanorods and Framework Architectures. *Journal of the American Chemical Society*, 129:7924–7935, 2007.

[95] A. Trovarelli. Catalytic Properties of Ceria and CeO_2-Containing Materials. *Catalysis Reviews*, 38(4):439–520, 1996.

[96] T.X.T. Sayle, S.C. Parker, and D.C. Sayle. Oxidising CO to CO_2 using Ceria Nanoparticles. *Physical Chemistry Chemical Physics*, 7(15):2936–2941, 2005.

[97] E. Mamontov and T. Egami. Lattice Defects and Oxygen Storage Capacity of Nanocrystalline Ceria and Ceria-Zirconia. *J. Phys. Chem. B*, 104(47):11110–11116, 2000.

[98] A.F. Diwell, R.R. Rajaram, H.A. Shaw, and T.J. Truex. The Role of Ceria in Three-Way Catalysts. *Studies in Surface Science and Catalysis*, 71:139–152, 1991.

[99] P.I. Pohl, J. Faulon, and D.M. Smith. Molecular Dynamics Computer Simulations of Silica Aerogels. *Journal of Non-Crystalline Solids*, 186:349–355, 1995.

[100] B.P. Feuston and S.H. Garofalini. Oligomerization in Silica Sols. *Journal of Physical Chemistry*, 94(13):5351–5356, 1990.

[101] J.S. Rivas Murillo, M.E. Bachlechner, F.A. Campo, and E.J. Barbero. Structure and Mechanical Properties of Silica Aerogels and Xerogels Modeled by Molecular Dynamics Simulation. *Journal of Non-Crystalline Solids*, 356:1325–1331, 2010.

[102] P. Vashishta, R.K. Kalia, J.P. Rino, and I. Ebbsjö. Interaction Potential for SiO_2: A Molecular Dynamics Study of Structural Correlations. *Physical Review B*, 15:12197–12209, 1990.

[103] P. Vashishta, R.K. Kalia, A. Nakano, W. Li, and I. Ebbsjö. Molecular Dynamics Methods and Large-Scale Simulations of Amorphous Materials. *Amorphous Insulators and Semiconductors, NATO ASI Series*, 23:151–213, 1997.

[104] R.W.G. Wyckoff. *Crystal Structures 2^{nd} Ed.* Intersciense Publishers, 1963.

[105] T.Y. Ng, J.J. Teo, and Z.S. Liu. A Molecular Dynamics Study of the Thermal Conductivity of Nanoporous Silica Aerogel, Obtained through Negative Pressure Rupturing. *Journal of Non-Crystalline Solids*, 358:1350–1355, 2012.

[106] J. Kieffer and C.A. Angell. Generation of Fractal Structures by Negative-Pressure Rupturing of SiO_2 Glass. *Journal of Non-Crystalline Solids*, 106: 336–342, 1988.

Chapter 2

Technical Background: Characterisation Techniques, Experimental Methods, and Simulation Techniques

2.1 Experimental Procedures

2.1.1 Ceria Nanoparticles

As ceria nanoparticles are such important functional nanomaterials their synthesis methods have been developed to provide an array of different shapes and sizes, with targeted uses including nanomedicine [1], surface activity [2], oxygen transport [3], catalysis [4], energy materials [5] and more. The work presented in this thesis aims to optimise the synthesis of cubic ceria nanoparticles, an established synthesis method was sourced from literature [6] and further developed by our group. The original procedure is given in Appendix 1.1, with any alterations discussed in Chapter 3. This is a 'one pot' approach where the finer tuning of the size/shape is controlled by the concentration of the reactants, capping (stabilising) agent, and ratio of organic and aqueous phases. This method requires a cerium precursor to undergo thermal treatment at 180 °C in the presence of an oxidising agent and capping agent. Here, the precursor is introduced in an aqueous phase, where the reaction occurs at the aqueous-organic interface and the nanoparticles migrate into the organic phase, then later precipitate out.

2.1.2 Aerogels

2.1.2.1 Sol-Gel Synthesis

The sol-gel synthesis presented in this thesis has been adapted from a method previously developed by our group [7] and successfully used for the synthesis of silica aerogel composites containing an array of transition metal oxides [8] with a loading of up to 10% in weight. This method is a multi-stage process, where first a two stage sol-gel process is used, utilise hydrolysis and condensation reactions of a metal alkoxide precursor, then supercritical drying is performed to remove the solvent.

The two-stage sol-gel process uses both an acidic and basic catalyst, with urea used in the second stage to ensure a smooth transition of the pH from acid to base. This allows the process to avoid the precipitation of the metal hydroxides from the precursors used to form the transition metal oxide particles. This two-stage process is split into the hydrolysis of an alkoxide precursor (TEOS) in the first step, then heating to 85 °C (condensation) in the second step to promote gelation and form polysilicates. The general form of the overall chemical process is described in Chapter 1, Section 1.1.2.1. A detailed procedure used for the synthesis is given in Appendix 1.2, with the molar ratio of the reactants stated in Table 2.1.

Table 2.1: Molar ratios of the sol-gel reactants in the formation of SiO_2 aerogel.

Hydrolysis			
TEOS	H_2O	EtOH	HNO_3
1.00 ± 0.003	40.9 ± 0.227	6.24 ± 0.042	0.017 ± 0.0005
Condensation			
Urea		EtOH	H_2O
1.78 ± 0.0003		4.70 ± 0.010	8.31 ± 0.034

2.1.2.2 High Temperature Supercritical Drying (HT-SD)

Aerogels were obtained from the SiO_2 gel formed during the sol-gel synthesis via High Temperature Supercritical Drying (HT-SD). This is done by extracting the EtOH whilst in its supercritical state, obtained by use of a 300 mL stainless steel autoclave shown in Figure 2.1, following the temperature program given in Table 2.2. This was done in the presence of 50 mL additional EtOH under an inert N_2 atmospheric conditions. The pressure within the autoclave will increase alongside the temperature, reaching at least the minimum required for EtOH to reach its supercritical state (T_c 241 °C, P_c 63 atm). Once there, or when the pressure has reached 90 atm without reaching the final programmed temperature, the chamber is slowly vented, keeping constant temperature, to remove the EtOH with minimal capillary action occurring. A summary of the HT-SD procedure is given in Appendix 1.3.

Table 2.2: Temperature conditions used for the HT-SD of the aerogels.

Initial Temperature (°C)	Increase rate (°C/min)	Interim Temperature (°C)	Increase rate (°C/min)	Final Temperature (°C)
25 ± 1	5 ± 0.1	250 ± 1	1 ± 0.1	330 ± 1

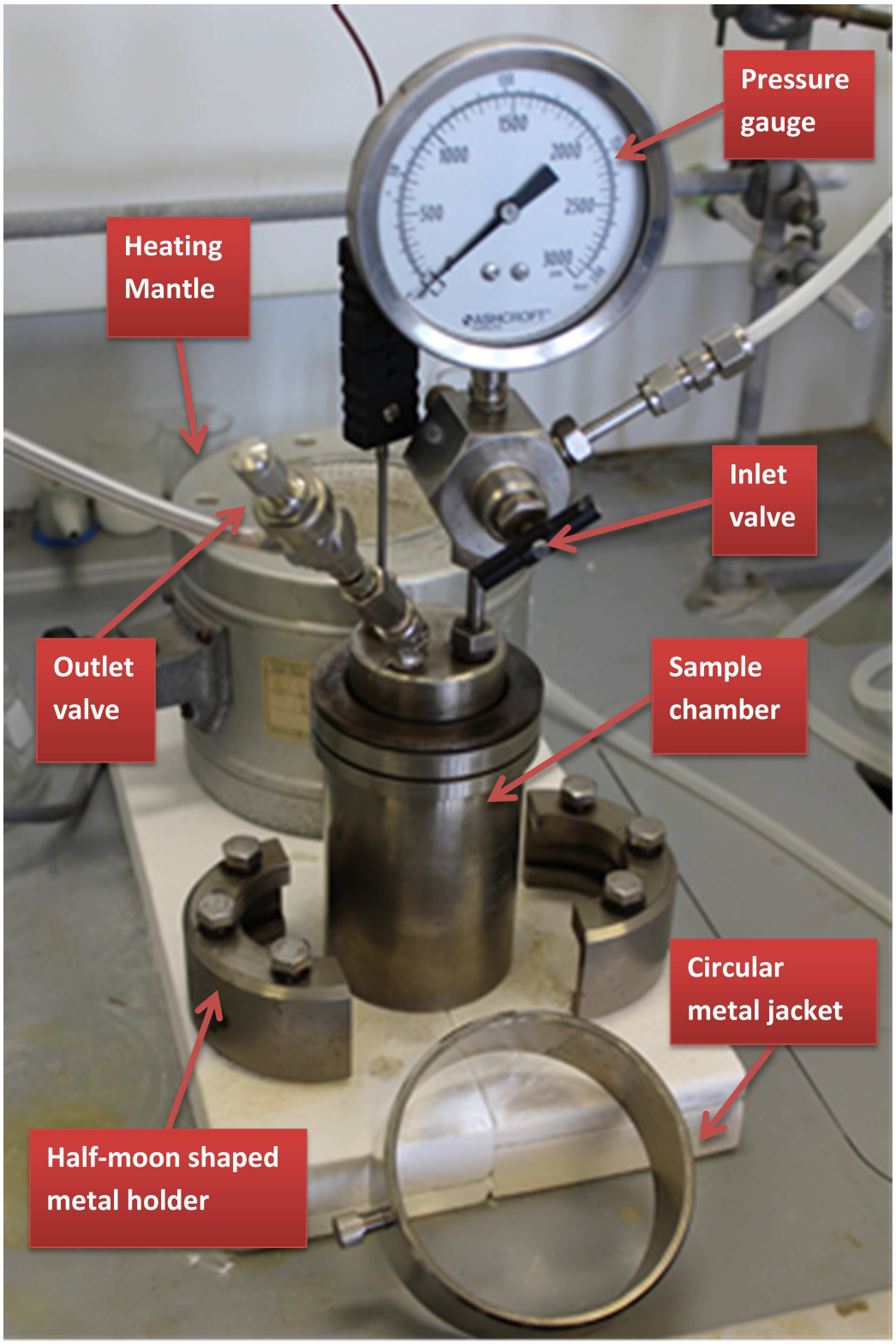

Figure 2.1: Labelled diagram of the autoclave used in the synthesis of all aerogels produced within this work.

2.2 Characterisation Techniques - Theoretical Principles

2.2.1 Thermal Analysis

Thermal analysis is a branch of materials science which investigates the property changes of materials as a function of temperature. There are several thermal analysis methods commonly used, measuring different properties such as thermal decomposition, thermal conductivity, volume changes, or dimensional changes.

2.2.1.1 TGA

Thermal Gravimetric Analysis (TGA) [9] is a technique which investigates the change in mass of a sample, as a function of temperature or time, under controlled temperature environments. Typically the temperature is increased linearly at a set rate to a designated temperature. This type of analysis allows for the examination of certain physical and chemical properties of a material (as a function of temperature) such as thermal decomposition. The results of such analysis appear as a plot of percentage weight loss against time or temperature. This simple concept can be used to quantitatively determine the loss of mass in a material as a result of thermal processes. These processes can be carried out in a range of environments such as vacuum, air, or N_2 (as well as other inert gases).

2.2.1.2 DSC

Differential Scanning Calorimetry (DSC) is a technique which investigates the heat difference required to keep the temperature of a sample and reference the same, measured as a function of temperature, under controlled temperature environments. The temperature program for the DSC is generally designed to produce a linear increase of temperature within the sample chamber. If an endo- or exo- thermal event occurs in the sample cell the heat difference is used to equalise the temperature to that of the reference cell. The enthalpy changes relating to these individual thermal events are measured directly, which makes DSC a suitable technique for quantitative enthalpy measurements.

2.2.1.3 Equipment

All thermal analyses presented within this thesis were conducted on a NETZSCH model STA 409 PC. Here, Simultaneous Thermal Analysis (STA) refers to the simultaneous application of Thermal Gravimetric Analysis (TGA) and Differential Scanning Calorimetry (DSC) to a sample under identical test conditions. The temperature range used in the analysis was 25-600 °C at a heating rate of 10 °C min^{-1}, under N_2 gas (protect) and air (purge).

2.2.2 X-Ray Diffraction (XRD)

Diffraction is a phenomenon which occurs when light is scattered by a periodic array, where the periodicity of the spacing must be similar to the wavelength. This principle produces constructive interference of the monochromatic X-rays and provides information about the atomic arrangement in crystals. The electrons within an atom scatter X-rays coherently, the strength of which is proportional to the number of electrons surrounding the atom. As the atoms within a crystal are arranged in a periodic array, they are able to diffract X-rays, with the distance between the atoms being similar to their wavelength. In fact X-rays were discovered by Wilhelm Röntgen in 1895 and in 1912 Max von Laue learned that crystalline substance act as a three dimensional diffraction grating for X-ray wavelengths, which is similar to the spacing of the planes in a crystal lattice. This was the foundation of the now common technique of XRD for the study of crystal structures and their atomic spacing. This technique is useful for characterising crystalline solids providing information on purity, crystal size, and structure. When X-ray diffraction experiments are carried out on non-crystalline materials, however, as the structures do not possess long range order only diffuse scattering occurs producing very broad peaks, which is the case for oleic acid present within the XRD patterns presented in this thesis.

2.2.2.1 Generation of X-Rays

In a laboratory diffractometer X-rays are generated by a cathode ray tube and filtered to produce monochromatic radiation.The X-ray tube is an evacuated chamber containing a tungsten filament and a target material acting as an anode, most commonly comprising Cu or Mo. The tungsten filament is electrically heated, resulting in the emission of electrons which accelerate towards the Cu or Mo target material. When the electrons collide with the target material, it leads to ionization of the Cu or Mo atom, creating an electronic vacancy in the 1s orbital. Radiation is emitted as a

result of an electron from an outer shell filling the vacancy, and depending which shell this electron comes from, different types of X-rays are produced. When an electron transitions from the 2p orbital to the 1s orbital (L $\rightarrow$ K), K_α radiation is produced, whereas transitions from 3p to 1s (M $\rightarrow$ K) result in K_β radiation. A representation of this can be seen in Figure 2.2(a).

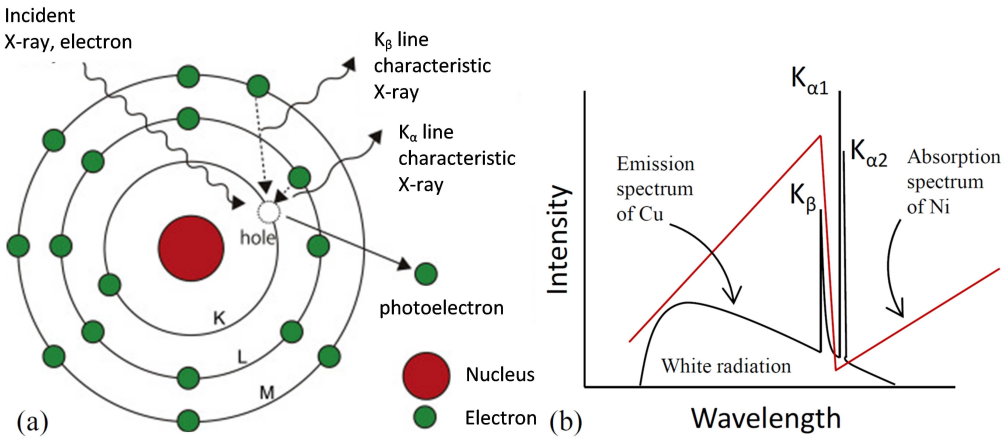

Figure 2.2: X-rays emission from a Cu target, where (a) gives a representation of the mechanism which causes the emission of K_α and K_β radiation and (b) a general emission spectrum of a Cu target with the absorption spectrum of Ni (acting as a filter) imposed over the top.

The K_α radiation is more frequent and therefore more intense, hence they are used in diffraction experiments. To isolate the K_α radiation a monochromator or filter acting as a monochromator is required, such as a Ni foil filter, which is able to absorb the K_β radiation. A typical example of this is given in Figure 2.2(b), where white radiation is also presented. White radiation occurs due to the electrons slowing down when approaching the Cu or Mo target material and in the process there are a few which lose energy and emit X-rays.

2.2.2.2 The Bragg's Law

Crystalline solids are a lattice of repeat units, the smallest of whaich is known as a unit cell. The diffraction pattern shows evidence of a simple set of atomic lattice planes which can be characterised by the Miller indices hkl and the interplanar distance d_{hkl}. According to Braggs approach these planes can be described as semi-transparent mirrors, where some of the X-rays in the incident ray will interact and scatter (or reflect as described by Bragg) from the first array of atoms, and others will penetrate

through this plane and interact with the underlying array of atoms. The interaction angles (θ_{hkl}) and interplanar distance (d_{hkl}) form the basis of Braggs Law for XRD, shown pictorially in Figure 2.3. Braggs equation is given by Equation 2.1.

$$n\lambda = 2d_{hkl}sin\theta_{hkl} \tag{2.1}$$

Where λ is the wavelength of the incident X-ray beam, θ_{hkl} is the angle of incidence/reflection of the X-ray beams with respect to hkl planes (also known as the Bragg angle), and d_{hkl} is the interplanar distance.

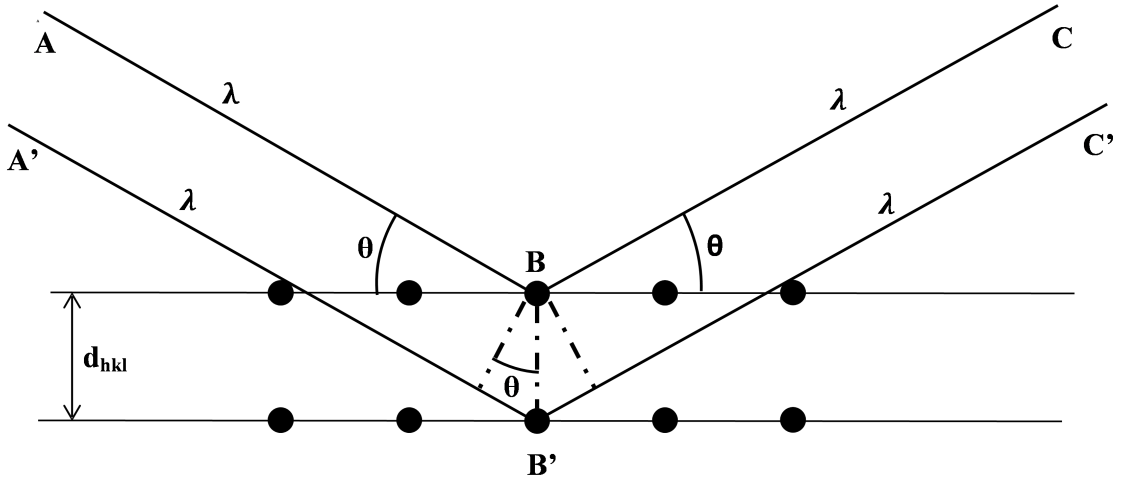

Figure 2.3: Graphical representation of Braggs Law for X-ray diffraction.

The relative intensities of a Bragg peak is, broadly speaking, due to the atom positions within the cell. The atomic planes are described by Miller Indices (hkl) where interceptions with the unit cell faces determine the Miller index i.e. if face parallel the index is 0, and interception through axis centre the index is 2 (Figure 2.4). The interplanar spacing of the cubic unit cell, where a=b=c and all cell angles are 90 °, is related to a simple geometry as given by Equation 2.2.

$$a^2 = {d_{hkl}}^2(h^2 + k^2 + l^2) \tag{2.2}$$

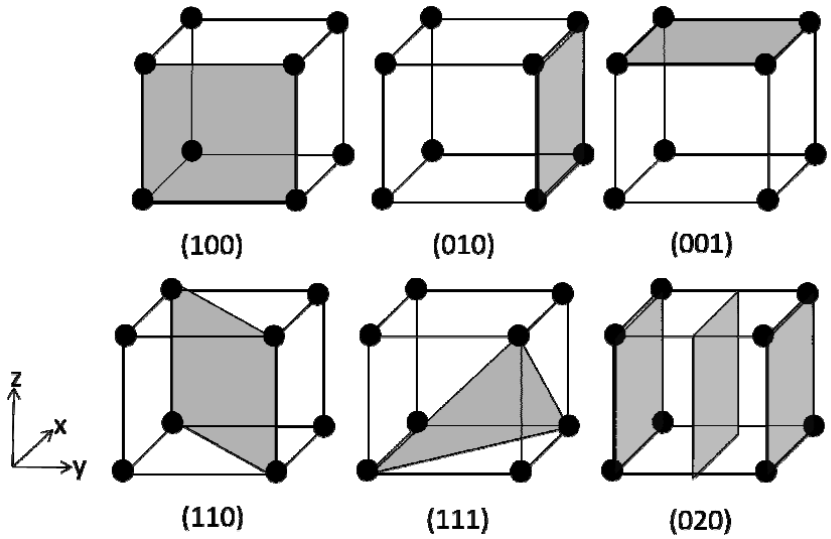

Figure 2.4: Graphical representation of Miller indices.

2.2.2.3 The Powder Method

X-ray diffraction can be used for the characterisation of the powder form of crystalline materials. When finely ground, the powder produces randomly oriented crystallites, where some will be oriented so a specific family of planes will satisfy Bragg conditions, and therefore produce a diffraction pattern. Crystallites can be positioned in all possible directions while maintaining the Bragg conditions, which consequently produce diffracted beams which lie anywhere along the edge of a cone shape (also known as the Debye-Scherrer rings), as represented in Figure 2.5.

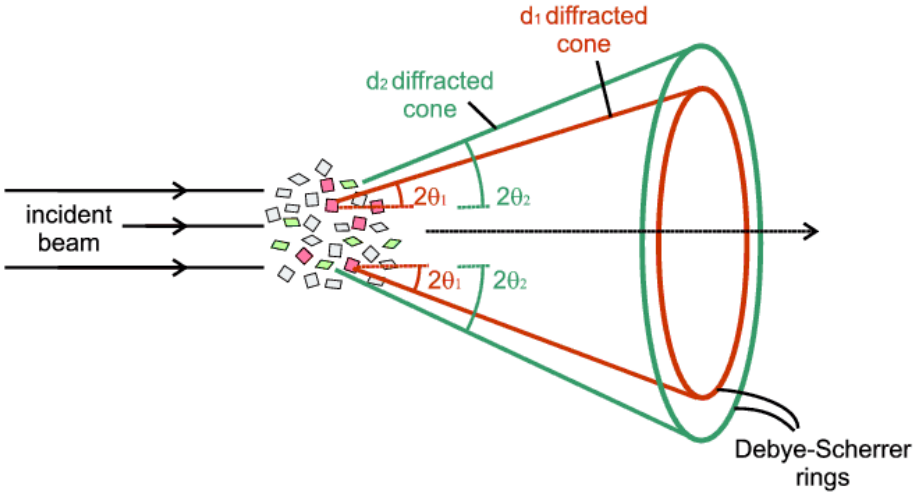

Figure 2.5: Debye-Scherrer diffraction rings produced by powder diffraction. Sourced from http://pd.chem.ucl.ac.uk/pdnn/diff2/cone.gif (11.07.17).

Diffractometers can have two geometries: θ-θ and θ-2θ, which can relate to which part of the diffractometer moves. In a θ-θ system the X-ray tube and the detector move in synchronicity to create a circular movement around the sample stage to form a θ angle with respect to the sample and the detector. In a θ-2θ system the sample stage and detector move to form the θ and 2θ angles, respectively, which is shown pictorially in Figure 2.6.

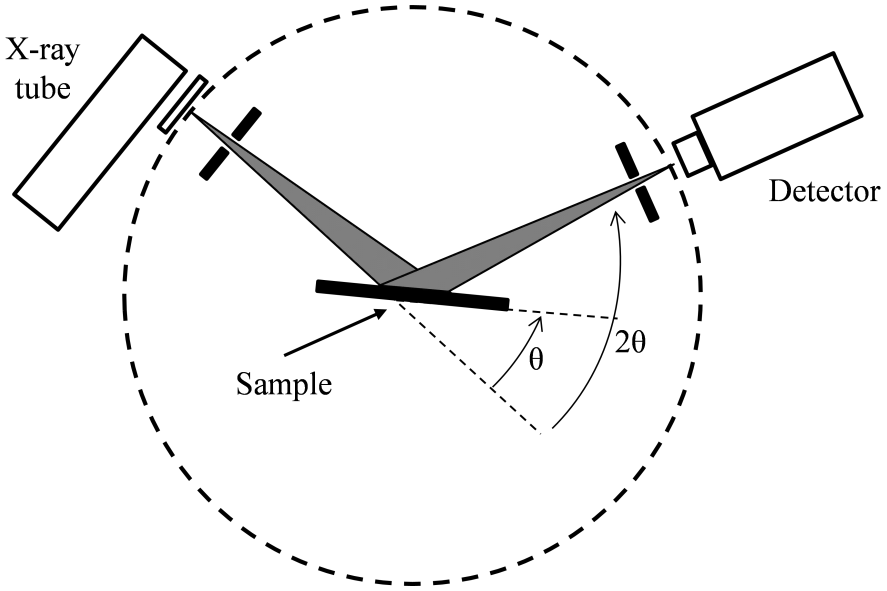

Figure 2.6: Schematic representation of a diffractometer in a θ-2θ geometry. [Copyright ©Taylor and Francis Group LLC Books [10].

2.2.2.4 Equipment

The Wide-Angle XRD conducted on the CeO_2 nanoparticles was done using a Panalytical X'Pert^3 Powder diffractometer or a Rigaku benchtop diffractometer (MiniFlex600), both of which contain a Cu anode (k_α, $\lambda = 1.5426$ Å) with a Ni filter.

2.2.3 HERFD-XANES

X-ray absorption spectroscopy (XAS) is the analysis of X-ray absorptions within the atoms of a material, both near and after the energy required for the ionisation of a core electron [10, 11]. This type of measurement requires an X-ray beam which is intense over a large range of energies, and this is mainly produced by synchrotron facilities. In a synchrotron, electrons are injected and accelerated with kinetic energies above mega electron volts, within a storage ring, giving the electrons a velocity close to the speed of light. Under these conditions the direction in which the electrons can travel is controlled by a series of specially designed magnets. The facility used for the measurements taken in this thesis was the Diamond Light Source facility in Oxfordshire, UK. This facility has a 561 m circumference storage ring capable of accelerating electrons at an energy of 3 GeV, which subsequently emits radiation with wavelengths of 0.04-40 Å. This synchrotron has outlets along the ring, known as beamlines, which are used to conduct different experiments. Here, the I20 beamline was used, which has an energy of 4-34 keV.

The absorption of X-rays follows Beer's law, which can be written in the form given in Equation 2.3, where μ is the absorption coefficient, x is the thickness of the sample, I_0 is the initial intensity, and I the final intensity.

$$\mu(E)x = ln(\frac{I_0}{I}) \tag{2.3}$$

During the analysis the X-ray wavelength is decreased progressively and the results can be presented by a plot of the variation in the absorption coefficient $\mu(E)x$ against the X-ray beam energy (E). With increasing energy there is decreasing absorption coefficient until a critical wavelength is reached, and at this point there is a sudden increase in the absorption coefficient. This rapid increase is known as the *absorption edge* and signifies a point where the X-ray energy is high enough to cause ionisation of the atom via the ejection of a core electron. The type of absorption edge relates to the orbital which an electron transitions from to fill the core hole, for example, in this thesis we are interested in the L-edge, relating to the 2s and 2p orbitals (L-level) which have three quantum energy levels, giving L_1, L_2, and L_3, where L_3 has the lowest energy. Different energies are required to transition electrons from different orbitals therefore the wavelength at which the absorption edge occurs is characteristic of the element.

There are two regions which can be identified using XAS of an element, which are the region close to the characteristic edge (XANES) and the area at slightly higher energies than the characteristic edge (EXAFS). Here, XANES is *X-ray Absorption Near Edge Spectroscopy*, whereas EXAFS is *Extended X-ray Absorption Fine Structure*, and the two techniques contain different information relating to the sample. Within this thesis only XANES have been used, and therefore only XANES and not EXAFS will be discussed further.

The XANES region refers to the area immediately surrounding the absorption edge ($\sim$50 eV depending on edge and element) and is highly influenced by the coordination geometry and oxidation state of the absorbing atom. The oxidation state in particular has the effect of shifting the absorption edge by around 3-5 eV per single increment in oxidation state (depending on the edge), for example $Ce^{3+} \rightarrow Ce^{4+}$ results in a $\sim$5 eV increase in energy. This shift can be used to identify the oxidation state of the subject atoms by comparison to a standard and can also be used to calculate the ratio of different oxidation states within the same target sample.

A feature of a XANES spectrum is the presence, or potential presence, of a small peak very shortly before the absorption edge, which is known as a *pre-peak*. This pre-peak can also give information relating to the oxidation state of the element as well as its coordination geometry. The pre-peak is caused by the excitation of electrons into vacant energy levels, and from ligand-field theory we know that the highest occupied molecular orbital will vary in the number of electrons depending on the oxidation state and coordination geometry of the atom. The pre-peak can provide additional and complementary information to that provided by the absorption edge, where a noticeable shift in the pre-peak may also indicate a change in oxidation state.

Another feature of a XANES spectrum is the presence of 'oscillations' shortly after the absorption edge peak. These are caused by low kinetic energy electrons which have interacted with surrounding atoms as a result of multiple-scattering. These oscillations are able to provide, though not in a easily interpretable way, information regarding the coordination surrounding the atoms.

When an electron transitions from a higher orbital fills a core hole the transition is accompanied by fluorescence or an emission of an Auger electron. The detector type used for collecting the XANES data can therefore be a fluorescence detector. A High-Energy Resolution Fluorescence Detection (HERFD) technique can be employed to overcome some of the main limitations of conventional XAS. The technique measures the XANES by monitoring the intensity of a fluorescence line which corresponds to the specific excited state decay process using a narrow energy resolution [12].

2.2.3.1 Equipment

All HERFD-XANES measurements presented in Chapter 4 were taken at the Diamond Light Source, Figure 2.7, on the I20 beamline, using an emission spectrometer where an energy of 8480.7 eV for the emitted photons was selected, while scanning the incident photon energy close to the Ce L_3 absorption edge.

Figure 2.7: Ariel image of the Diamond Light Source Facility in Oxford, UK.

2.2.4 Transmission Electron Microscopy (TEM)

Electron microscopy gives the possibility of magnifying a specimen though irradiation with an electron beam (of uniform current density). This beam can be focused and orientated by electric and magnetic fields acting as electromagnetic lenses. There are different types of interaction between a specimen and the electron beam, leading to a variety of electron microscopy techniques, where TEM specifically utilises the transmitted beam, which is observed on a fluorescent screen and then either recorded on a photographic film, or acquired via a CCD camera.

There are two main factors to consider when conducting TEM; the thickness and chemical nature of the specimen, as these will greatly affect the intensity of the transmitted beam. The specimen is required to be 'ultrathin' for TEM analysis and cannot exceed 200 nm otherwise an intense transmitted beam cannot be obtained; however the capability of the electron beam in penetrating the specimen also needs to be considered alongside the thickness, as it may allow for thicker specimens to be observed. The quantity of electrons absorbed relates to the atomic number of the

elements within the specimen as well as the specimen thickness. Thicker or denser regions with a higher atomic number will prevent more of the electrons from passing, which will appear darker on the image, while thinner or lower density regions with a lower atomic number will appear brighter. This is determined by considering the wavelength of the electron beam (λ), which is dependent on the accelerating voltage (V) as given by Equation 2.4 [13]. This is the DeBroglie equation which takes into account the mass (m) and charge (e) of the electron along with Planck's constant (h).

$$\lambda = \frac{h}{\sqrt{2meV}} \tag{2.4}$$

The wavelength plays a significant role in the resolution of the produced image (shorter wavelength producing greater resolution), with resolution being the smallest distance between two distinguishable points. This is currently around 0.1 nm in conventional TEM equipment, with high resolution transmission electron microscopy (HR-TEM) able to reach just a few angstroms.

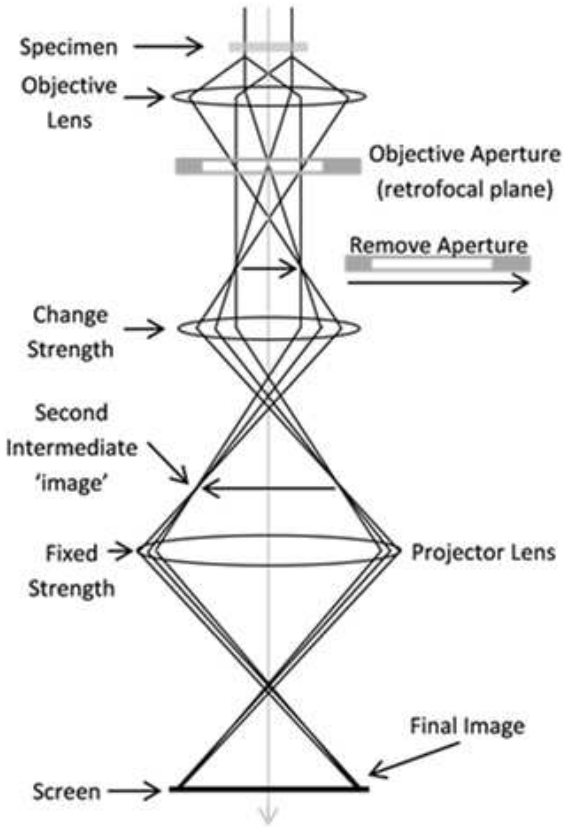

Figure 2.8: The two basic operations of a TEM, with A projecting the diffraction pattern and B the image

The diagram in Figure 2.8 represents the image projection of a specimen observed by a transmitted beam in TEM using an objective aperture. Contrast formation in a TEM is dependent on the mode of operation, each of which can gather differing information about the specimen, including *bright field*, *dark field*, *electron energy loss*, and *phase contrast*. Here bright field, which is one of the most common modes of operation for a TEM, was used. This mode produces the specimen image using the transmitted beam, consisting of dark features on a bright background, which is influenced by the varying specimen thickness or electron density. These dark features are parts of the specimen, where the electrons have been absorbed by the specimen, preventing them from reaching the detector. This therefore makes the assumption of a 2D projection of the specimens thickness and density down the optic axis, where a first model approximation can be made using Beers Law [14], and more complex analysis requiring the addition of phase information [15].

2.2.4.1 Aberration Corrected High Resolution - Transmission Electron Microscopy (AC HR-TEM)

There are different types of aberration corrections (AC) which can be used in TEM allowing for a higher resolution (HR) image to be produced. Aberrations such as *diffraction*, *spherical*, and *chromatic* can occur. Diffraction aberration affects the TEM mode which produces a representative diffraction pattern of the crystal structure while spherical and chromatic aberrations affect the image produced, which is a result of the way the electron beam is transmitted through the lenses. Chromatic aberration relates to the colour (chroma) of the image and is an effect of beam dispersion as the lens becomes unable to focus to the same convergence point. Spherical aberration occurs due to an increase in beam refraction as it hits the lens, caused by intrinsic imperfections, or a reflection of the beam as it hits a mirror near the edge, as opposed to closer to the centre of a mirror. The result is that the beam deviates from the normal pathway and creates imperfections on the image.

The are practical limitations in traditional TEM which allows for energies between $\sim$100-300 eV, corresponding to λ = 3.7-2.0 pm. The resolution of the image is not just limited by the energy but also by intrinsic imperfections in the electron lenses. To prevent or at least reduce the effect of aberration, specially designed auxiliary 'lenses' are installed into the microscope which are known as aberration correctors [16, 17]. With optical microscopy having a resolution range down to $\sim$300 nm and traditional TEM able to achieve a resolution of $\sim$0.2 nm, AC-TEM is able to improve the resolutions below 0.05 nm [18].

2.2.4.2 High-Angle Annular Dark Field - Scanning Transmission Electron Microscopy (HAADF-STEM)

High-Angle Annular Dark Field (HAADF) is a method used in STEM to map samples by collecting incoherently scattered electrons formed at a very high angle with a specific annular dark field detector. The detector collects electrons from an annulus around the beam and is able to sample more scattered electrons that are able to pass through an objective aperture, which is an advantage for signal collection efficiency, and therefore the detector is very sensitive to differences of the element irradiated based on the atomic number (Z-contrast).

2.2.4.3 Scanning Transmission Electron Microscopy - Energy-Dispersive X-ray Spectroscopy (STEM-EDS)

Scanning Transmission Electron Microscopy (STEM) Energy-Dispersive X-ray Spectroscopy (EDS) refers to the combination of a TEM analysis with an EDS detector attached, allowing for elemental analysis. EDS relies on the fundamental principle that each element has a unique atomic structure which produces a unique set of peaks on its electromagnetic spectrum [19]. A function of STEM allows for a narrow incident beam to scan over the grid, performing EDS at each point and build a chemical map of the sample. Using software it is possible to colour the image relative to its elemental characteristics, visually showing the differences in the composition. This is particularly useful for doped materials and nanocomposites, where multiple constituent materials are present, providing analysis of the dispersity and composition, and potentially highlighting areas of agglomeration or homogeneity.

2.2.4.4 Equipment and Characterisation

Nanoparticles dispersed in toluene were prepared for analysis by drop-casting onto carbon-coated copper grids and allowing for the toluene to evaporate. Nanocomposites were ground to a powder and dispersed in toluene, followed by sonication and drop-casting onto carbon-coated copper grids, allowing time for the toluene to evaporate before analysis.

TEM characterisation of nanoparticles and nanocomposites presented within this thesis were performed partly at the University of Kent Bioscience department and partly at the King Abdullah University of Science and Technology (KAUST) in Saudi Arabia. Characterisation conducted at the University of Kent was performed using a Jeol 1230 transmission electron microscope, which operates at an accelerating voltage

of 80 kV, equipped with a Gatan One View 16 MP camera. Characterisation of the nanoparticles conducted at the KAUST was performed using a FEI Titan 80-300 analytical transmission electron microscope, which operates at an accelerating voltage of 300 kV. Selected area electron diffraction patterns (SAEDPs) presented in Chapter 3 were acquired by the same TEM and characterised to match the structure of JCPDS 00-34-0394 (Fm3m, CeO_2).

AC-TEM characterisation was also performed on a FEI Titan 80-300 analytical transmission electron microscope, which operates at an accelerating voltage of 300 kV, which was corrected on the objective lens. This microscope was equipped with an ultra-bright-field emission gun (XFEG), a 2k x 2k CCD camera, and an electron monochromator. The point resolution when corrected was 0.08 nm.

STEM-EDS characterisation was performed at ETH Zürich using a FEI Talos F200X (Chem S/TEM) operating at an accelerating voltage of 200 kV, and equipped with an ultra-bright field emission gun (XFEG), a Super-X EDS detector, and a resolution of 0.16 nm in HAADF-STEM mode. EDS maps were obtained with a scan time of 10 mins for all samples. This allowed for the quantification of La and Ce present within the La-doped ceria nanoparticles.

HAADF-STEM analysis of the nanocomposites were performed using a FEI Titan 80-300 analytical transmission electron microscope, operating at an accelerating voltage of 300 kV, and a camera length of 77 mm, a probe current of 68 pA, a pixel size of 32.5 μs, and a convergence angle of 14.0 mrad. The z-contrast imaging using HAADF-STEM allowed these nanoparticles to be resolved more easily from the SiO_2 host matrix as Ce has a much higher atomic number than Si and O.

2.3 Molecular Dynamic Simulation

2.3.1 Molecular Dynamics

2.3.1.1 Overview

Molecular Dynamics (MD) is a computational method which studies the physical movements of atoms/molecules, to predict the dynamic evolution of the system over time. The system is comprised of N particles which interact via given interatomic potentials, in a classical mechanics framework. The interatomic potential describes the interaction between atoms as a function of their position. The potential is chosen depending on the type of study being conducted. Here the Coulomb-Buckingham potential [20] has been employed, which is derived from the Born model of the ionic solid, where the potential energy of the system can be expressed as:

$$E(r_{ij}) = \sum_{ij} \frac{Q_i Q_j}{4\pi\varepsilon_0 r_{ij}} + \sum_{ij} A \exp\left(\frac{-r_{ij}}{\rho}\right) - C r_{ij}^{-6} \tag{2.5}$$

The first term represents the long-range Coulombic interaction between ions, i and j, of charge Q_i and Q_j at a distance of r_{ij}, where ε_0 is the permittivity of free space. The second and third terms represent the short-range Buckingham potential, which describes the Pauli repulsion energy and Van der Waals energy between electron charge clouds. Here A, ρ, and C are constants, which are determined by fitting experimental data for the material.

Figure 2.9 gives a visual representation of the Coulomb-Buckingham potential given in Equation 2.5. Atoms are either attracted to, or repulsed by, one another which is dependant on their interatomic distance (r), in aid to reduce their potential energy to a minimum (r_{eq}). This is known as a pair-interaction, which can be used to calculate the force ($\vec{F}$) acting on each atom as given by Equation 2.6.

$$\vec{F_i} = \sum_j \vec{\nabla} E(r_{ij}) \tag{2.6}$$

In complex systems, where many atoms are present, there is a 'net effect' of the N surrounding atoms, which can be accounted for by calculating the vector sum of each pair-interaction contribution.

This directional force, $\vec{F}$, along with the atomic mass, m, can be used to determine the acceleration, $\vec{a}$, using Newton's second law (Equation **??**). From this the velocities ($\vec{v}_f$) are derived for a given time-step (t), using Equation 2.7, which allows for a new set of co-ordinates (r_f) to be determined using Equation 2.8.

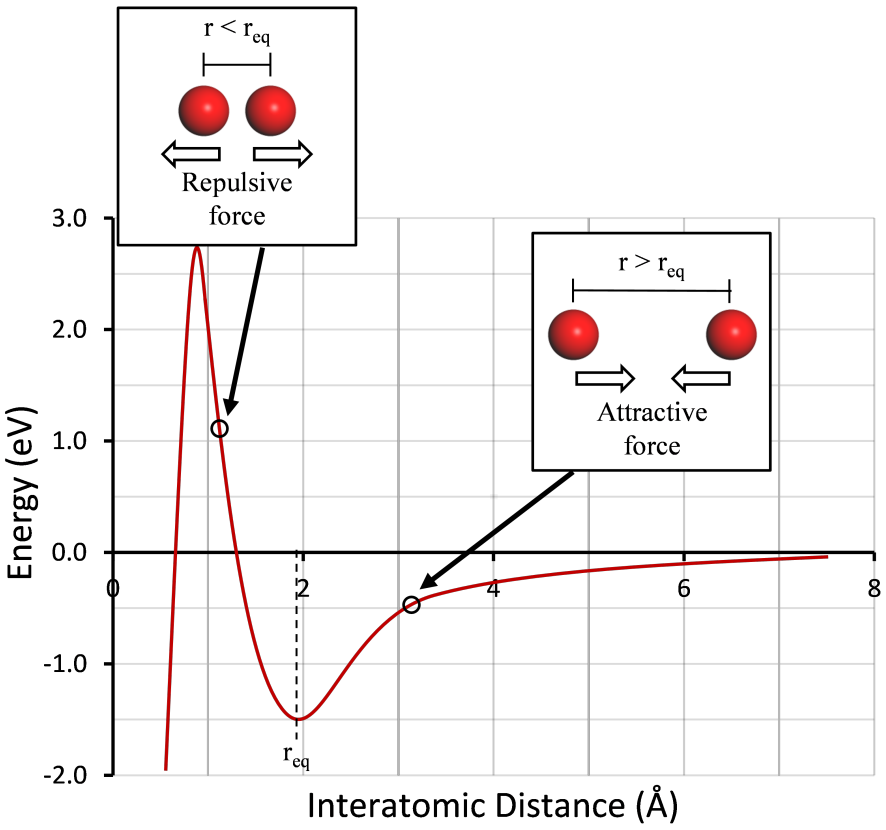

Figure 2.9: Example Coulomb-Buckingham potential, with inserts indicating regions of attraction and repulsion, where r_{eq} is the minimum energy (optimal balanced distance).

$$\vec{v}_f(t) = \int \vec{a}\ dt = \vec{a}t + \vec{v}_i \tag{2.7}$$

$$\vec{r}_f(t) = \int (\vec{a}t + \vec{v}_i)\ dt = \frac{1}{2}\vec{a}t^2 + \vec{v}_i t + \vec{r}_i \tag{2.8}$$

With a new set of co-ordinates calculated for each atom in the system, along with an associated directional velocity, these parameters can be used as a new set of initial conditions and the calculations repeated to form a dynamic evolution of the atoms interacting within the system.

2.3.1.2 Net Effect - The Perfect Lattice

The perfect lattice describes the system as an effectively infinite array of charged, spherical ions. It is derived from the classical born model of solids [21, 22], where the atoms within a structure experience interactions with all other atoms within the structure. These interactions can be expressed in a general form as a series summation:

$$\Psi(r_1...r_n) = \sum_{i,j=1}^{n} \Psi_2(r_{ij}) + \sum_{i,j,k=1}^{n} \Psi_3(r_{ijk}) + \sum_{i,j,k,l=1}^{n} \Psi_4(r_{ijkl}) \tag{2.9}$$

where $\Psi_2(r_{ij})$ is the interaction between pairs of ions {ij}, $\Psi_3(r_{ijk})$ is the interaction between triplets of ions {ijk}, and so on. As pair interactions within ionic materials are dominant, and due to the nature of the expansion, it is computationally tractable to truncate the expression after the first term [23], to give an approximation of the pair potential. This ensures that the interactions between ions can be described via a central force, where the approximate total interactions is expressed as:

$$\Psi(r_1...r_n) = \sum_{i,j=1}^{n} \Psi_2(r_{ij}) \tag{2.10}$$

The term $\Psi_2(r_{ij})$ is the potential energy between ions i and j, which can be expressed as $E(r_{ij})$. The charged nature of the ions form a coulombic interaction, where the relatively slow decay of $\frac{1}{r}$ as r increases, which gives rise to the long range component of the potential. The general term for the total potential can therefore be written as:

$$E(r_{ij}) = \frac{Q_i Q_j}{4\pi\varepsilon_0 r_{ij}} + \Phi_{sr} \tag{2.11}$$

where i and j are ions of charge Q_i and Q_j at a distance of r_{ij}, and ε_0 is the permittivity of free space. Φ_{sr} is used to denote the remaining short-range interactions. These interactions can then be summed to give the lattice energy.

The second term of Equation 2.11, which is used to denote the remaining short-range interactions, can take many forms. It is defined to account for the discrepancy in the long-range interactions caused by the approximation breaking down due to reducing interionic separation. Within this work, this second term takes the form of a Buckingham potential (unless otherwise stated), as discussed in Section 2.3.1.1.

2.3.1.3 Potentials

DL_POLY is the software used to conduct the MD simulations within this thesis. The software has the capability of studying the dynamic progression of many system types, including polymers, silicate glasses and zeolites, and metal alloys. The interactions in a molecular system are defined by a set of functions, known as a force field. As a wide range of forms are possible, DL_POLY does not supply its own force field parameters, but can adapt and draw from sources including the GROMOS [24], Drieding [25], or AMBER [26] forcefield, which share functional forms. Force fields can be broken into six categorises:

- Intramolecular Potential Functions - defining the bond, distance, angle constrictions, and tethering forces.
- Intermolecular Potential Functions - defining the short ranged, metal, tersoff, and three- and four- body potentials
- Long Ranged Electrostatic (coulombic) Potentials - defining the direct or force-shifted sum, distance dependent dielectric, reaction field, and smoothed particle mesh ewald.
- Polarisation Shell Models - Dynamical and Relaxed
- External Fields - such as electric, shear, magnetic, repulsive wall, etc.
- Frozen atoms/Rigid Body/Core-shell Units

2.3.1.4 Integration Algorithms

There are different algorithms for calculating trajectories in MD simulations. These algorithms vary in accuracy, drift, and noise, and should be chosen based on the type of simulation being conducted. Integration algorithms are, by default, based on the Velocity Verlet (VV) scheme [27], which is time reversible. This is the most popular form and generates trajectories in the microcanonical (NVE) ensemble in which the total energy (kinetic and potential) is conserved. This can be described mathematically as given in Equation 2.12, where $\vec{v}$ is velocity, $\vec{r}$ is distance, t is time, and O is error in the approximation of v.

$$\vec{v}(t) = \frac{\vec{r}(t + \Delta t) - \vec{r}(t - \Delta t)}{2\Delta t} + O(\Delta t^2) \tag{2.12}$$

Integration algorithms can also be based on the LeapFrog Verlet (LFV) [27], however this is not time reversible. MD simulations usually require properties which depend on position and velocity simultaneously (i.e sum of potential and kinetic energy), with a range of ensembles available, the most common of which are outlined below.

Simulating at a constant energy (NVE), where N is the number of atoms, and V is system volume, the system follows Newton's equations of motion, and temperature (T) is only considered through velocities, not as an external parameter. The velocities in this case are scaled with a Maxwell distribution to correspond to a given temperature.

Simulating at constant temperature (NVT), the temperature is instantaneous and pushed towards the desired temperatures by scaling the velocities at each step. This is given by Equation 2.13, where E_k is kinetic energy, N is the number of particles, k_B is the Boltzmann constant, T temperature, m mass, and v velocity.

$$E_k = \frac{3}{2} N k_B T = \sum_{i=1}^{N} \frac{1}{2} m_i \vec{v}_i^2 \tag{2.13}$$

Temperature can also be controlled by setting thermostats. A common example is the Nosé-Hoover thermostat, Equation 2.16. where the energy is not conserved.

$$\frac{d\vec{r}(t)}{dt} = \vec{v}(t) \tag{2.14}$$

$$\frac{d\vec{v}(t)}{dt} = \frac{\vec{f}(t)}{m} - \chi(t)\vec{v}(t) \tag{2.15}$$

$$\frac{d\chi}{dt} = \alpha(T(t) - T_{ext}) \tag{2.16}$$

Simulating at a constant pressure (NPT) can be achieved using a barostat, such as the Berendsen barostat. At each designated time step, the system cell and co–ordinates are scaled by a factor of:

$$x = 1 - const(P_{ext} - P) \tag{2.17}$$

Here *const* is dependent on the relaxation constant of the barostat (τ_p).

Barostats and thermostats can be used in conjunction with one another (such as the Berendsen thermo- and baro- stats), where the system is made to obey the equation of motion, as given by Equation 2.18.

$$\frac{dP}{dt} = \frac{(P_{ext} - P)}{\tau_p} \tag{2.18}$$

It is also possible to choose constant enthalpy (H) or constant chemical potential (μ) for a system. A summary of a few common ensembles is given in Table 2.3.

Table 2.3: Summary of some common ensembles in MD simulations

Ensemble	Constants	Summary
NVE	atom number, volume, energy	A micro-canonical ensemble which corresponds to Newtonian mechanics, particularly good for non-equilibrium situations.
NVT	atom number, volume, temperature	A canonical ensemble which allows energy exchange with a heat bath, particularly good for simulating thermal equilibrium, with a choice of different thermostats
NPT	atom number, pressure, temperature	Most physically relevant as the system is connected to a piston and heat bath. Has a choice of thermo- and baro- stats
NPH	atom number, pressure, enthalpy	Has a choice of barostats, where external pressure can be isotropic or anisotropic. Example - Andersen barostat allows for change in cell size isotropically, and Parrinello-Rahman allows shape and size change anisotropically.

2.3.1.5 System Pressure in Molecular Dynamic Calculations

To determine the pressure within a system in equilibrium the virial theorem (Equation 2.19) has been well adapted to molecular dynamical calculations and is employed within DL_POLY. Within this equation P is the pressure, V is the volume of the cell, N is the number of atoms, T is the temperature,k_B is the Boltzmann constant, $\vec{r}_{ij}$ is the distance between i and j, and Φ_{ij} is the interatomic potential between i and j. The angular brackets denote an average over time and ∂ denotes a partial derivative.

$$PV = Nk_BT - 1/3 \left\langle \sum_{i,j<i}^{N} \vec{r}_{ij} \cdot \frac{\partial \Phi_{ij}}{\partial \vec{r}_{ij}} \right\rangle \tag{2.19}$$

Where periodic boundary conditions (PBC) are used to simulate an infinitely extending systems, an assumption is made that the system is unbounded and thus

divided into repeating cells of N atoms each. Within this system the dynamics of the N atoms is identical in each, therefore, the system is considered as one basic period with infinite 'replicated' images. To preserve the physical interactions between the cells the virial theorem is modified to take into account the 'minimum image distance' conventions [28], Equation 2.20. Here v is velocity and $\bar{j}$ refers to the replacement of x_j by its identical image from a neighbouring cell. This is still satisfied even if there is no movement of atoms across the cell boundary, therefore in the case of a system with PBC it is essentially a crystalline solid and the pressure calculated from the virial theorem is the same as that calculated from the interatomic forces.

$$\langle v \rangle = -2N\tau \left\langle \sum_{i,j<i} x_{i\bar{j}} X(i,\bar{j}) \right\rangle - VP \tag{2.20}$$

2.3.1.6 Input files

There are three basic input files used to form the starting configuration for a system to run in DL_POLY, these are the CONTROL file, the CONFIG file, and the FIELD file. For formatting, parameters, and further details on these files, please refer to the DL_POLY manual [29, 30].

The CONTROL file defines the control variables for the system, making use of directives to access the subroutines within DL_POLY. Here, among other parameters, the temperature and pressure of the system are set, alongside the time-step, number of steps, and ensemble configuration. This file also controls how often defined data is printed to the individual output files.

The CONFIG file contains the physical aspects of the system, including the dimensions of the unit cell, the periodic boundary conditions, and the atomic label, co-ordinates, velocities, and forces.

The FIELD file contains the information relating to the force fields, that define the atomic interactions. This includes the number of atoms, their mass and charges, and the potential parameters.

2.3.2 Amorphisation and Re-crystallisation

For an atomistic model to be representative of the real material, it needs to contain the same properties. For metal oxides specifically, the properties of the material are highly depended on the microstructural features which develop naturally as part of the synthetic protocol. These microstructural features include surface abnormalities, such as stepping, point defects, grain boundaries, and dislocations within the structure. For the properties of the material to be more accurately investigated using MD simulation, such as mechanical strength or catalysis, the microstructure features need to be incorporated into the atomistic model. These can be placed artificially, however to better represent the natural development of the microstructure, as developed in the synthetic protocol, an amorphisation and re-crystallisation (ARC) technique can be employed.

The amorphisation and re-crystallisation technique has been extensively used, successfully, to form 'natural' microstructural features [31, 32, 33]. For the amorphisation process to occur, the regular lattice structure of the material, with stoichiometric number of atoms, is generated (as seen for ceria in Figure 2.10 (a)), and MD simulation is conducted at a simulated temperature and duration to produce complete amorphisation (Figure 2.10(b)) of the crystal structure. This is performed under the NVT ensemble, with a Nosé-Hoover thermostat.

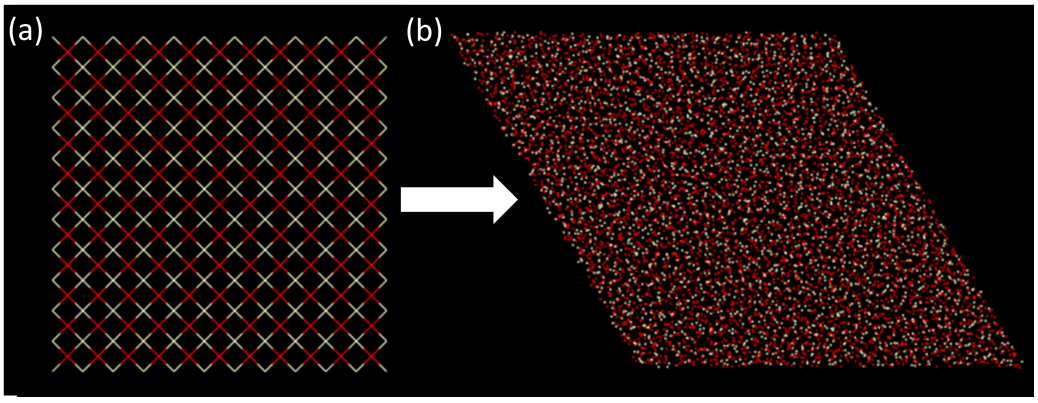

Figure 2.10: (a) Generated regular lattice structure of ceria produced using Materials Studio, and (b) the amorphous ceria structure after melting.

Analogous to experiment, the crystallisation of the material is promoted by the formation of a crystalline seed, evolving naturally due to the random movement of the atoms. The crystalline structure of the seed propagates, until the entire structure is crystalline. This process is performed under NVT ensemble, as before, but at a simulated temperature below the melting point of the material, though high enough

for sufficient mobility of the atoms. The structure is sintered at this temperature for an extended duration, for formation and propagation of the seed/(s) to occur. The temperature is then reduced, cooling the material to 300 K. The sequence of images given in Figure 2.11 shows evidence of this process, with ceria as the material used.

The sintering stage of the recrystallisation process can be extended in duration to reduce the defects within the structure. Where the formation of seeds evolve naturally, more than one may form within the structure with different orientations or grains, leading to the formation of grain boundaries. Extended sintering can be used to allow one crystal grain to propagate into the other, forming a single crystal structure. Shorter sintering durations, before cooling, can result in poly-crystalline materials.

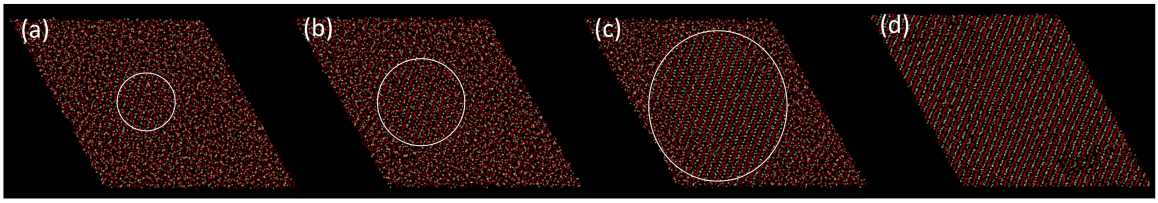

Figure 2.11: The crystallisation process for ceria where (a) shows the initial formation of a crystalline seed (b) the propagation of the crystalline structure, (c) further progression of the crystalline structure, and (d) the fully crystalline ceria structure.

2.3.3 Compression Techniques (PVOIG, Anvils, and Repulsion)

Strain applied to a material can be problematic to simulate, with careful consideration needed to determine the method of application. Experimentally, force is applied to the surface of a material, which transfers to the bulk of the material. However with nanoscale materials this is difficult to achieve.

A method previously developed, involved the modification of the DL_POLY classic source code, to include a parameter which sequentially scales the atom co–ordinates. This parameter was termed 'PVOIG' and could be edited within the CONTROL file. These are performed under the NST ensemble which gives constant stress and temperature, with anisotropic cell shape changes, and can be used in conjunction with a Nosé-Hoover thermostat. One consideration which must be recalled with this method is that the rate of compression scales with parallelisation. Such as increasing the number of processors which the simulation is run, will subsequently increase the compression rate. The limitation of this method is that the strain is applied equally to the entire system, which is not overly representative of the response in the real material. This approach to applying strain has previously been utilised to calculate the mechanical properties of ceria nanorods [34, 35].

An alternative method allowing strain to travel from the surface of a material, to the bulk, which produces a more representative response in accordance with the real material, is the application of strain using repulsive surfaces. This method also allowed for consistent strain to be applied without consideration of the parallelisation. This method is performed under the NVT ensemble, which gives constant volume and temperature, and can be used in conjunction with the Nosé-Hoover thermostat. Although the use of repulsive surfaces, or anvils, give a better representation of the real material response, the repulsion prevents any interaction with the surface of the anvil, which can have an effect on the mechanical properties. Where the mechanical properties of a nanomaterial, are highly dependent on the microstructure of the material, it is also inherent that these properties be applied to the anvils also. Experimentally, it is implausible that anvils would have a perfectly smooth surface, and likely would contain stepping and defects. Repulsive surfaces act as a 'perfect' surface. This approach to applying strain has previously been utilised to calculate the mechanical properties of various nanoceria particles [33].

To better represent the mechanical properties of the nanomaterial, the method of applying strain must consider the anvil structure, as well as the dispersion of the strain

through the particle. Therefore anvils need to be formed with 'realistic' microfeatures, and have the ability to interact with the subject material. This method of compression was developed as part of this research and is described in further detail in Chapter 5. The basic mechanism for applying strain through the anvils was to update the co–ordinates of the atoms at the back end and allowing the material to transfer the strain to the rest of the anvil, then communicate it onto the particle.

2.3.4 GULP

GULP [36] is a program which can be used to perform a variety of simulations on materials using an array of boundary conditions. It focuses on analytical solutions, generally through the use of lattice dynamics. Here, GULP was used to calculate the elastic constants of the anvils used in Chapter 5.

2.3.5 MD and Graphical Software

All simulations presented in this thesis have been conducted using DL_POLY Classic [37] and DL_POLY 4 [38]. Molecular graphics were performed using Materials Studio and VMD [39].

References

[1] S. Das, J.M. Dowding, K.E. Klump, J.F. McGinnis, W. Self, and S. Seat. Cerium Oxide Nanoparticles: Applications and Prospects in Nanomedicine. *Nanomedicine*, 8(9):1483–1508, 2013.

[2] K. Zhou, X. Wang, X. Sun, Q. Peng, and Y. Li. Enhanced Catalytic Activity of Ceria Nanorods from Well-Defined Reactive Crystal Planes. *Journal of Catalysis*, 229(1):206–212, 2005.

[3] A. Holmgren, D. Duprez, and B. Andersson. A Model of Oxygen Transport in Pt/Ceria Catalysts from Isotope Exchange. *Journal of Catalysis*, 182(2):441–448, 1999.

[4] N. Ta, J. Liu, and W. Shen. Tuning the Shape of Ceria Nanomaterials for Catalytic Applications. *Chinese Journal of Catalysis*, 34(5):838–850, 2013.

[5] L. Malavasi, C.A.J. Fisher, and M. Saiful Islam. Oxide-Ion and Proton Conducting Electrolyte Materials for Clean Energy Applications: Structural and Mechanistic Features. *Chemical Society Reviews*, 39:4370–4371, 2010.

[6] S. Yang and L. Geo. Controlled Synthesis and Self-Assembly of CeO_2 Nanocubes. *Journal of American Chemistry Society*, 128:9330–9331, 2006.

[7] M.F. Casula, D. Loche, S. Marras, G. Paschina, and A.C. Corrias. Role of Urea in the Preparation of Highly Porous Nanocomposite Aerogels. *Langmuir*, 23(7): 3509–3512, 2007.

[8] D. Loche, M. Casula, A. Corrias, C. Marras, D. Gozzi, and A. Latini. Catalytic Chemical Vapour Deposition on $MFe_2O_4SiO_2$ (M = Co, Mn, Ni) Nanocomposite Aerogel Catalysts for the Production of Multi Walled Carbon Nanotubes. *Journal of Nanoscience and Nanotechnology*, 16(7):7750–7757, 2016.

[9] A.W. Coats and J.P. Redfern. Thermogravimetric Analysis. A Review. *Analyst*, 88(1053):906–924, 1963.

[10] L.E. Smart and E.A. Moore. *Solid State Chemistry: An Introduction.* CRC press, 2012.

[11] A. Gaur, B.D. Shrivastava, and H. Nigam. X-Ray Absorption Fine Structure (XAFS) Spectroscopy - A Review. *Proceedings of the Indian National Science Academy*, 79(B):921–966, 2013.

[12] Diamond Light Source. HERFD: High Energy Resolution Fluorescence Detected, 2018.

[13] D.B. Williams and C.B. Carter. *Transmission Electron Microscopy*. Plenum Publishing Corporation, New York, 1996.

[14] B. Fultz and J. Howe. *Transmission Electron Microscopy and Diffractometry of Materials*. Springer, 2007. ISBN 3-540-73885-1.

[15] J.M. Cowley. *Diffraction Physics*. Elsevier Science B. V., 1995. ISBN 0-444-82218-6.

[16] H.H. Rose. Optics of High-Performance Electron Microscopes. *Science and Technology of Advanced Materials*, 9:014107, 2008.

[17] N. Tanaka. Present Status and Future Prospects of Spherical Aberration Corrected TEM/STEM for Study of Nanomaterials. *Science and Technology of Advanced Materials*, 9(1):014111, 2008.

[18] S.J. Pennycook, M. Varela, C.J.D. Hetheringtom, and A.I. Kirkland. Materials Advances through Aberration-Corrected Electron Microscopy. *Materials Research Society Bulletin*, 31(1):36–43, 2006.

[19] J. Goldstein. *Scanning Electron Microscopy and X-Ray Microanalysis*. Springer, 2003. ISBN 978-0-306-47292-3.

[20] R.A. Buckingham. The Classical Equation of State of Gaseous Helium, Neon and Argon. *Proceedings of the royal society A*, 168(933):264–283, 1938. doi: 10.1098/rspa.1938.0173.

[21] M. Born and J. Mayer. On the Lattice Theory of Ionic Crystals. *Zeitschrift für Physik*, 75(1–2):1–18, 1932.

[22] J.E. Mayer. Dispersion and Polarizability and the Van der Waals Potential in the Alkali Halides. *The Journal of Chemical Physics*, 1:270, 1932. doi: 10.1063/1.1749283.

[23] J.H. Harding. Computer Simulation of Defects in Ionic Solids. *Reports on Progress in Physics*, 53(11):1403, 1990.

[24] W.F. van Gunsteren and H.J.C. Berendsen. Groningen Molecular Simulation (GROMOS) Library Manual, 1987.

[25] S. Mayo, B. Olafson, and W. Goddard. DREIDING: A Generic Force Field for Molecular Simulations. *Journal of Physical Chemistry*, 94:8897–8909, 1990.

[26] S.J. Weiner, P.A. Kollman, D.T. Nguyen, and D.A. Case. An All Atom Force Field for Simulations of Proteins and Nucleic Acids. *Journal of Computational Chemistry*, 7(2):230–252, 1986. doi: 10.1002/jcc.540070216.

[27] M.P. Allen and D.J. Tildesley. *Computer Simulation of Liquids*. Oxford University Press, 1989. ISBN 978-0-19-880319-5.

[28] D.H. Tsai. The Virial Theorem and Stress Calculation in Molecular Dynamics. *The Journal of Chemical Physics*, 70(3):1375–1382, 1979.

[29] W. Smith, T.R. Forester, and I.T. Todorov. The DL POLY Classic User Manual, 2012.

[30] I.T. Todorov and W. Smith. THE DL POLY 4 USER MANUAL, 2016.

[31] D.C. Sayle, S.A. Maicaneanu, and G.W. Watson. Atomistic Models for CeO_2 (111), (110), and (100) Nanoparticles, Supported on Yttrium-Stabilized Zirconia. *Journal of the American Chemical Society*, 124(38):11429–11439, 2002.

[32] T.X.T. Sayle, R.A. Catlow, R.R. Maphanga, P.E. Ngoepe, and D.C. Sayle. Generating MnO_2 Nanoparticles using Simulated Amorphization and Recrystallization. *Journal of the American Chemical Society*, 127(37):12828, 2005.

[33] F. Caddeo, A. Corrias, and D.C. Sayle. Tuning the Properties of Nanoceria by Applying Force: Stress-Induced Ostwald Ripening. *Journal of Physical Chemistry C*, 120:14337–14344, 2016.

[34] T.X.T. Sayle and D.C. Sayle. Elastic Deformation in Ceria Nanorods via a Fluorite-to-Rutile Phase Transition. *ACS nano*, 4(2):879–886, 2010.

[35] T.X.T. Sayle, B.J. Inkson, A. Karakoti, A. Kumar, M. Molinari, G. Möbus, S.C. Parker, S. Seal, and D.C. Sayle. Mechanical Properties of Ceria Nanorods and Nanochains; the Effect of Dislocations, Grain-Boundaries and Oriented Attachment. *Nanoscale*, 3:1823, 2011.

[36] J.D. Gale and A.I. Rohl. The General Utility Lattice Program (GULP). *Molecular Simulation*, 29(5):291, 2003.

[37] W. Smith and T.R. Forester. DL_POLY_2. 0: A General-Purpose Parallel Molecular Dynamics Simulation Package. *Journal of Molecular Graphics*, 14(3):136–141, 1996.

[38] I.T. Todorov, W. Smith, K. Trachenkob, and M.T. Dove. DL_POLY_3: New Dimensions in Molecular Dynamics Simulations via Massive Parallelism. *Journal of Materials Chemistry*, 16:1911–1918, 2006.

[39] W. Humphrey, A. Dalke, and K. Schulten. VMD: Visual Molecular Dynamics. *Journal of Molecular Graphics*, 14(1):33–38, 1996.

Chapter 3

Ceria Nanoparticles, Doping, and Nanocomposites: Synthesis, Optimisation, and Characterisation

3.1 Introduction

With increasing surface area there are more reactive sites available, with nanoparticles having the most favourable volume to surface area ratio. This feature is one of the main reasons why nanoparticles have been used in so many areas of research.

The surface structure is also very important to activity and with different surface structures there are inherently different nanoparticle shapes, for example for ceria a truncated octahedron has a predominantly {111} surface, a polyhedron has a mixture of {111} and {100} surfaces, and a cuboid has a predominantly {100} surface with smaller {110} and {111} surfaces. With the {100} surface being the most reactive, cuboidal nanoparticle would be the preferred morphology, and this therefore gives rise to a need for controlling both the size and shape of nanoparticles.

Recently there has been increasing attention given to the development of new synthetic routes which are able to control the size and shape of nanoparticles [1, 2, 3]. In particular, great interest has been shown towards ceria nanomaterials [4, 5, 6], due to the extraordinary properties they exhibit in terms of reactivity [7]. Ceria has the capacity to store and release oxygen ions depending on the oxygen partial pressure of the environment, this originates from the labile and reversible redox cycle between Ce^{4+} and Ce^{3+}, generating the equilibrium given in Equation 3.1. Where the equilibrium lies further to the left, the ceria is more oxidised, and to the right, more reduced, where there is a higher concentration of oxygen vacancies. This means the ability of ceria to store and release oxygen is driven by the vacancies within the structure [8]. Here, $V_O{}^{xx}$ is a Kröger-Vink notation denoting the vacancy is on the oxygen site, with two null charges.

$$CeO_2 \rightleftharpoons (Ce^{3+}{}_{2x})(Ce^{4+}{}_{1-2x})O_{2-x} + \frac{x}{2}O_2 + xV_O{}^{xx} \tag{3.1}$$

The functionality of ceria is far more prevalent when reduced to the nanoscale, therefore the control of size and shape requires careful and rationalised thought in regards to the synthetic method. Thermal techniques, including hydrothermal [9] and solvothermal [10, 11] crystallization, and thermal decomposition [12] have been used for the synthesis of ceria nanoparticles, along with combustion [13], and spray pyrolysis [6, 14], among other techniques. These techniques have been used to synthesis nanoparticles of cuboidal [15], spherical [16], polyhedral [17], and truncated octahedral [6] shapes, along with nanorods [18], nanotubes [19], and various nanoporous materials [20].

Nanoceria can catalyse an oxidation/reduction reaction by capturing, storing, and releasing oxygen [8], making it a promising catalyst for industrial processes like three-way automobile exhaust catalysts [21]. The synthesis of ceria nanoparticles with the most reactive surface, e.g. cuboidal, generally requires the use of a surfactant, used as a capping agent, to control nanoparticle growth during the synthesis, Figure 3.1; this is due to the cuboidal shape being meta-stable. Without a capping agent the nanoparticles are able to form more stable shapes and are prone to aggregation, which hinders activity and reduces exposed surface area. Use of a capping agent results in the formation of a nanoparticle comprising of an inorganic core, i.e. CeO_2, coated with a layer of organic molecules, i.e. a fatty acid.

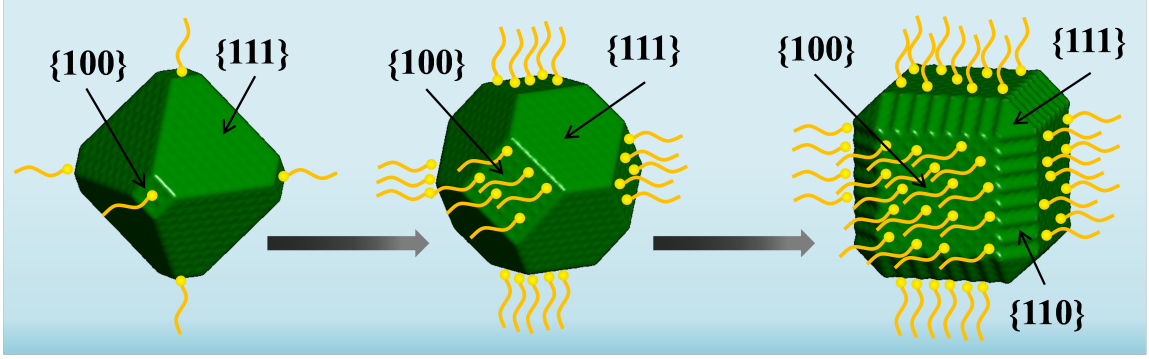

Figure 3.1: A representation of the growth of a ceria nanocube, with use of a surfactant/capping agent (oleic acid), showing the progressive change in surface area.

Using a surfactant does however have its limitations. Specifically, with the surface coated in an organic molecule, it limits the accessibility of the surface and therefore the reactivity of the nanoparticle. However if the surfactant is removed after the synthesis, such as through thermal treatment, the nanoparticles are then prone to aggregate and uncontrolled growth can occur. A potential solution to prevent aggregation of the nanoparticles is to disperse them in a host matrix. This host matrix must be able to act as a support for the ceria nanocubes, separating and stabilising them without hindering functionality or reacting with the nanoparticles. This would then allow us to fully exploit the surface of the ceria nanocubes for their reactivity in catalysis.

The characteristics of aerogels makes them particularly attractive as a host matrix, not only allowing the prevention of nanoparticle agglomeration/aggregation but also, due to the thermal properties, allows for the surfactant to be removed via thermal treatment, exposing the surface. Discussed previously were applications of silica aerogel as catalyst support [22, 23], but it can also been employed in thermal [24, 25] and acoustic [26, 27] insulation, and other applications such as pollutant traps [28, 29].

Another method for improving the reactivity of the ceria nanoparticles would be to change their chemical composition by use of a dopant. In crystalline materials dopants commonly take the place of elements within the crystal lattice for the desired result of altering their properties. In this case, the desired result would be to increase the oxidation/reduction properties of the ceria nanocubes. As this property is highly dependent on the formation of oxygen vacancies, the dopant must be able to assist in their formation, without inhibiting the oxidation. As the ceria is reduced from Ce^{4+} to Ce^{3+} with the formation of the vacancies, the ideal dopant would have an x^{3+} state, to replace some of the Ce^{4+}, which would subsequently introduce vacancies. The dopant would also require a similar atomic radius to cerium to allow it to sit in the cerium sites without changing the lattice structure. One such dopant is lanthanum. Lanthanum oxide is commonly found in the form La_2O_3, giving a La^{3+} state, which has an ionic radius of 0.110 nm in comparison to 0.0097 nm for Ce^{4+}. It has been successfully employed previously as a dopant for ceria based materials [30], with evidence showing the enhancement of CeO_2 oxidation [31].

In this chapter we present a synthesis route for the formation of ceria nanocubes, with focus on optimising the process. We investigate the use of silica aerogel as a host matrix for the pre-made ceria nanoparticles, characterising the formed nanocomposite, as well as synthesising and characterising the use of lanthanum as a dopant to improve catalytic activity.

3.2 Ceria Nanocubes - Synthesis Optimisation

The synthesis process used as a basis for optimisation was sourced from literature [15], with the procedure given in Appendix 1.1. Briefly, an aqueous cerium precursor solution is heated in an autoclave to 180 °C for an extended duration along with an organic solvent (toluene), a capping agent (oleic acid), and an oxidising agent (*tert*-butylamine). The organic layer containing the nanoparticles is then separated and purified by centrifugation, followed by the precipitation of the nanoparticles with a precipitating agent (EtOH).

The process of optimisation involved varying all aspects of the synthesis, which was long and tedious, with some aspects either completely preventing the formation of the nanoparticles and others not resulting in a noticeable difference. For this reason, only the most substantial parameters, which yielded change, will be discussed; these were the ceria precursor, the thermal treatment duration, and the capping agent. In each case, the resulting nanoparticles were characterised using TGA/DSC, XRD, and TEM, which allowed comparison of the yield, removal of the oleic acid, structure, and visualisation of the particle sizes and size distribution. For all presented data XRD was conducted using a 0-background silicon sample holder, where samples were deposited from a toluene solution onto the sample holder and allowed to dry before analysis. Ceria nanocubes have the ability to self-assemble on the sample holder, allowing the corresponding crystalline phases present in the XRD pattern to indicate the shape of the nanoparticles. The nanocubes should present a predominately {100} surface structure, as this is the preferential orientation. Differences in peak intensity, as opposed to internal peak ratio, is related to sample concentration, therefore some peaks may appear larger in different samples, however the composition will still be the same if the internal ratios are the same. For TGA/DSC analysis the temperature range investigated was 25-600 °C, with a ramp of 10 °C/min, and under a flow of air, which was conducted on the ceria nanoparticles after purification and (air) drying.

3.2.1 Precursor

Two ceria precursors were used for the synthesis of the ceria nanocubes; these were cerium(III) nitrate hexahydrate ($Ce(NO_3)_3.6H_2O$) and ammonium cerium(IV) nitrate ($Ce(NH_4)_2(NO_3)_6$). The reason these two precursors were chosen was to determine whether initiating the synthesis with Ce^{4+} or Ce^{3+} precursor would result in nanoparticles with differing morphologies, or different yields. A 16.7 mMol L^{-1} aqueous solution was used for each precursor.

3.2.1.1 XRD

In Figure 3.2 (top), the XRD patterns obtained from the nanoparticles synthesised with cerium(III) nitrate hexahydrate (red) and ammonium cerium(IV) nitrate (blue) are presented, along with a reference pattern for CeO_2 (black) which is labelled and reported at the bottom of the pattern. The first peak on the pattern is broad, and not associated with CeO_2, as it is related to the presence of oleic acid in the sample. The peak is broad as oleic acid is amorphous, and presents a superimposed contribution to the patterns in the 2θ range 15-25.

The XRD patterns present the main characteristic peaks for CeO_2, however not in the relative intensities presented in the reference pattern. With higher intensities given for the {200} peak in both syntheses, it presents evidence to suggest the presence of a higher surface area, which confirms the preferential orientation of the ceria nanocubes on the XRD sample holder. This is further evidenced by the increased {400} peak.

By comparing the relative intensities of the {111} and {200} peaks with the reference, it is clear that there is a higher presence of {200} surfaces in the nanoparticles synthesised with cerium(III) nitrate hexahydrate. This suggests the nanoparticles have a more cubic morphology in comparison to those synthesised with ammonium cerium(IV) nitrate. Further to this, adjacent to the {200} peak for the ammonium cerium(IV) nitrate synthesis there is a narrow peak which is not associated with the ceria structure, which is likely caused by an impurity.

3.2.1.2 TEM

TEM images of the ceria nanoparticles synthesised with cerium(III) nitrate hexahydrate (red outline) and ammonium cerium(IV) nitrate (blue outline) are presented in Figure 3.2. Here it can be observed that the nanoparticles synthesised with cerium(III) nitrate hexahydrate have a small size distribution, with all nanoparticles being of similar size, and a fairly large percentage of the nanoparticles appear to have a cubic morphology. In contrast, the nanoparticles synthesised with ammonium cerium(IV) nitrate have a large size distribution, some agglomeration of the nanoparticles, and a large variety of particle shapes.

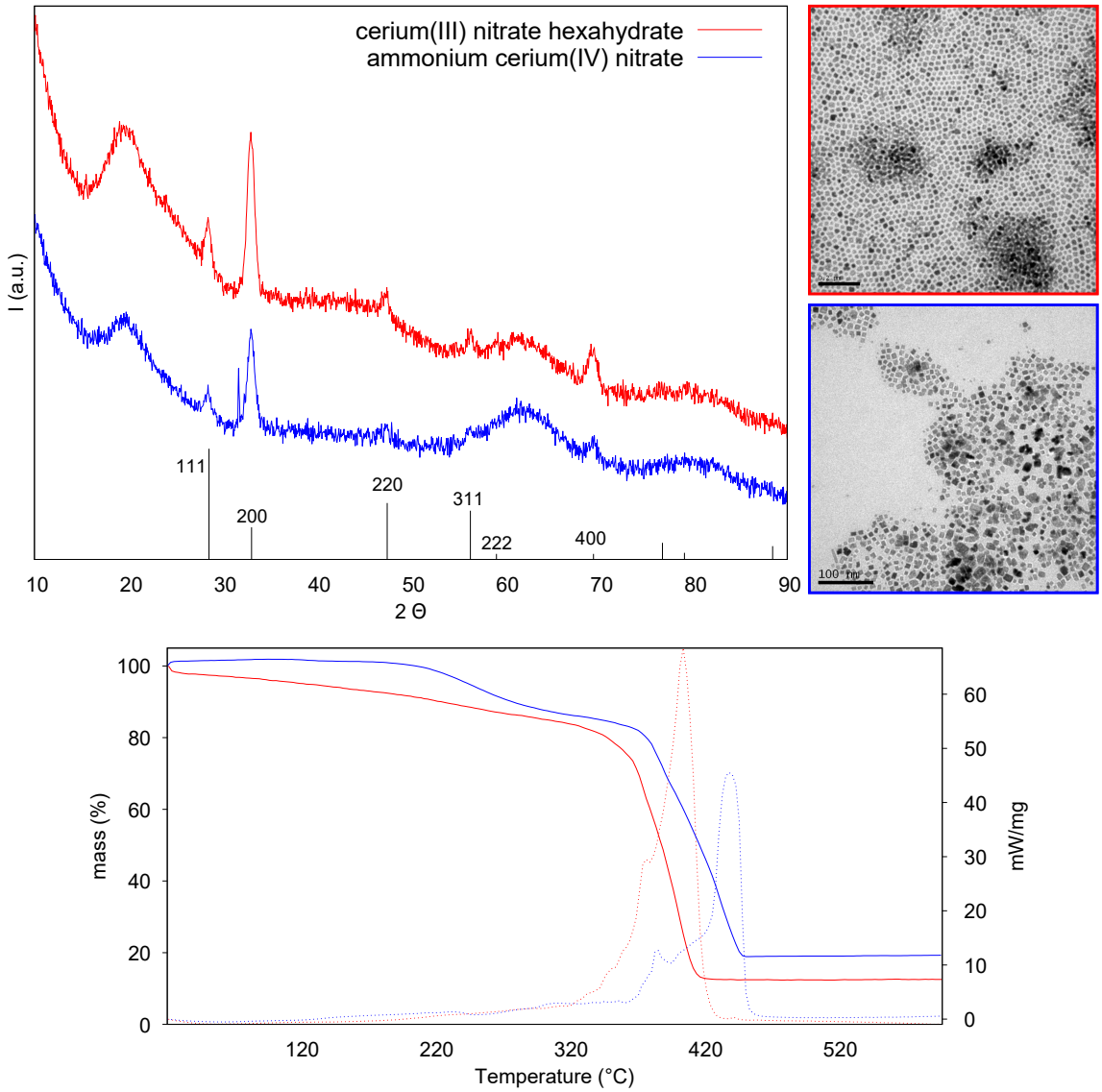

Figure 3.2: XRD patterns (top), TEM images, and TGA/DSC measurements (bottom) for nanoparticles synthesised with cerium(III) nitrate hexahydrate (red) and ammonium cerium(IV) nitrate (blue). An XRD reference pattern for CeO_2 is also given (black). For the TGA/DSC plot the solid lines relate to the mass axis and the dotted lines relate to the mW/mg axis.

3.2.1.3 TGA/DSC

Figure 3.2 (bottom) presents the TGA/DSC curves of the ceria nanoparticles obtained with the cerium(III) nitrate hexahydrate (red) and ammonium cerium(IV) nitrate (blue), with the results summarised in Table 3.1, reporting each DSC peak, temperature, and corresponding TGA mass change.

Table 3.1: TGA/DSC data relating to the synthesised nanoparticles using cerium(III) nitrate hexahydrate and ammonium cerium(IV) nitrate as precursors.

Precursor	**Peak**	**Temperature (°C)**	**Mass change (%)**	**Residual mass (%)**
Cerium(III) nitrate hexahydrate	1	377.7(1)	87.1(1)	12.9(1)
	2	405.3(1)		
Ammonium cerium(IV) nitrate	1	386.8(1)	80.9(1)	19.1(1)
	2	439.3(1)		

For nanoparticles synthesised with cerium(III) nitrate hexahydrate, the DSC curve shows its predominant exothermic peak centred at around 405 °C, with a lower and slightly extended exothermic activity from 370 °C, leading up to 405 °C. This exothermic activity is due to the decomposition of the oleic acid which is bound to the surface of the ceria nanoparticles. In contrast, for nanoparticles synthesised with ammonium cerium(IV) nitrate, the DSC curve shows its predominant exothermic peak centred at around 440 °C, which is around 35°C higher, with a lower and more extended exothermic activity from 380 °C, leading up to 440 °C, which is also related to the decomposition of the oleic acid.

The mass change measured by the TGA is significant due to the removal of the oleic acid. This residual mass, relating to the mass of the ceria nanocubes, is fairly similar between the syntheses, with around an 80% decrease in mass and slightly more oleic acid present for the nanoparticles synthesised with cerium(III) nitrate hexahydrate. This could be due to the differences in size and shape of the nanoparticles, were the cerium(III) nitrate hexahydrate particles have a more cubic morphology, resulting in a larger {100} surface for the oleic acid to bind to, but it could also be partially due to experimental errors, arising due to natural variations in the synthesis conditions, such as fluctuations in temperature and/or minor timing differences.

3.2.1.4 Discussion and Conclusion

In Figure 3.2, a comparison of the XRD, TEM, and TGA/DSC of the ceria nanoparticles synthesised with cerium(III) nitrate hexahydrate (red) and ammonium cerium(IV) nitrate (blue), can be observed. By combining these characterising techniques, it was possible to determine that cerium(III) nitrate hexahydrate is the more favourable precursor, as it resulted in a higher percentage of ceria nanocubes. The XRD of both syntheses are similar, with a more prominent {200} peak in comparison to the CeO_2 reference pattern, however this was more intense for the cerium(III) nitrate hexahydrate nanoparticles. Furthermore, the ammonium cerium(IV) nitrate nanoparticles appeared to contain an impurity in the pattern.

The difference in the size and shape of the nanoparticles was particularly evident in the TEM images. It was clear that there was extensive size distribution and irregular particle shapes for the ammonium cerium(IV) nitrate, which is undesirable, however the cerium(III) nitrate hexahydrate nanoparticles had more consistent cubic shape and distribution. This difference in structure was further confirmed by TGA/DSC, where the mass change was more significant for the cerium(III) nitrate hexahydrate nanoparticles, indicating a higher presence of oleic acid. With less oleic acid removed in the ammonium cerium(IV) nitrate nanoparticles, it suggests a smaller portion of {100} surfaces and therefore less cubic morphology.

The overall conclusion is that the cerium(III) nitrate hexahydrate presents a better precursor for the synthesis of the ceria nanocubes, and all syntheses following used this precursor.

3.2.2 Thermal Treatment Duration

Once the reactants are sealed in the autoclave it is placed in a binder oven at 180 °C, which subsequently increases the pressure in the vessel, forming the appropriate conditions for the synthesis to occur. The duration the vessel is under these conditions has a substantial influence on the formation and size distribution of nanoparticles.

Syntheses using the base procedure were used, varying only in thermal treatment duration (24, 48, and 72 hours). As observed through XRD (Figure 3.3), the duration change had significant effects on the nanocubes. The 24 hours synthesis presented a sharp and sizeable peak at the {200} position and the {400} peak position, indicating a highly cubic morphology. There are however two smaller peaks that sit either side of the prominent {200} peak, which are not attributed to CeO_2 fluorite structure. This indicates there is either contamination in the sample, or the crystal structure is no longer fluorite, therefore TEM imaging is needed to provide further information.

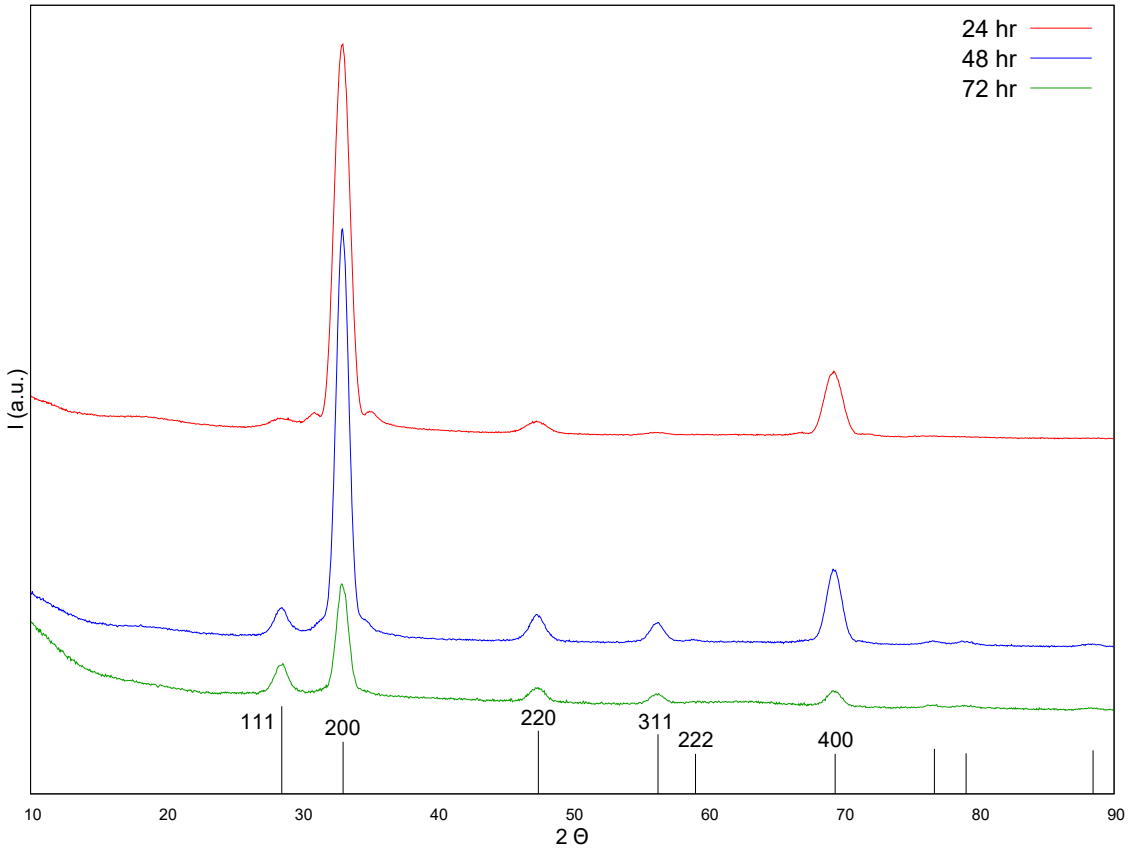

Figure 3.3: XRD patterns for nanoparticles thermally treated for 24 hours (red), 48 hours (blue), and 72 hours (green). An XRD reference pattern for CeO_2 is also given (black).

The XRD of the 48 hour thermal treatment gives sharp, clear ceria peaks, with no additional peaks present. The {200} is the most prominent, as should be expected for the cubic morphology, with a significantly lower {111} peak. This indicates that 48 hours is sufficient to seed and grow the nanocubes, with the narrow peaks indicating a fairly narrow range of crystallite size. This preliminarily suggests that the extended time period is preferable. This however does not seem to be a progressive trait, as the resulting XRD pattern of the 72 hour thermal synthesis indicates a reduction in cubic morphology due a reduction in {200} peak intensity and an increase in {111} peak intensity. The additional time seems to have allowed for particles to grow to larger sizes, while also seeding new particles, which is an undesirable result. The analysis of the XRD patterns can be further corroborated with the TEM images of the nanocubes.

The TEM images presented in Figure 3.4 give the resulting nanoparticles from the 24, 48,and 72 hour syntheses. The image of the 24 hour synthesis confirms the indications of the XRD patterns, with nanoparticles forming highly cubic morphologies, but also with the presences of smaller nanoparticle with non-cubic morphologies. These smaller nanoparticles indicate that the nanocubes have not fully formed in some parts, with growth on the seeds still occurring. This suggests that 24 hours is insufficient time to fully synthesis nanocubes in adequate quantity and size. The TEM image for the 48 hour synthesis shows a highly ordered self-assembly of nanocubes, with a fairly consistent size distribution, which is consistent with the XRD findings. The TEM image of the 72 hour synthesis confirms a larger particle size distribution, and the presence nanoparticles with non-cubic morphologies. With this comparison, it was determined that 48 hours thermal treatment is the most appropriate for the synthesis, with sufficient time to form nanocubes of consistent size distribution without forming new seeds.

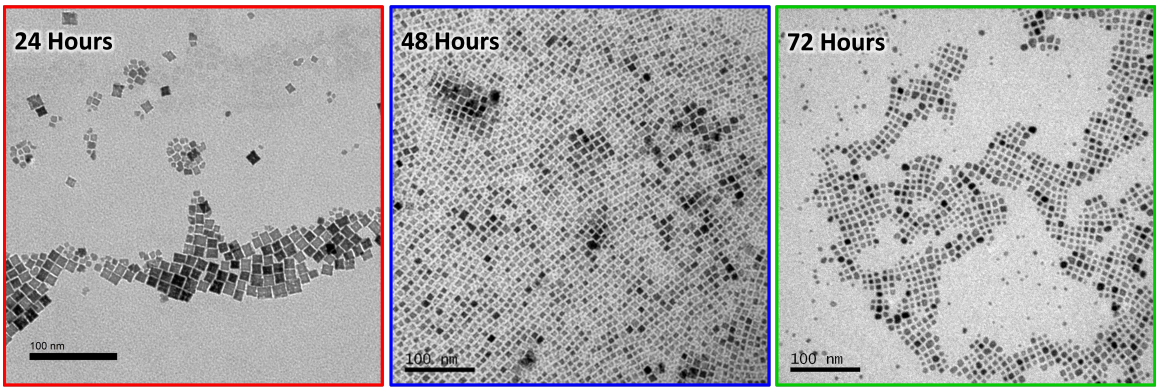

Figure 3.4: TEM images of nanoparticles thermally treated for 24 hours (red outline), 48 hours (blue outline), and 72 hours (green outline).

3.2.3 Capping agent

Oleic acid was used as a capping agent (surfactant) in the ceria nanocube synthesis. Oleic acid preferentially attaches to the {100} surface, 'capping' its growth but allowing the other surfaces to grow. As the other surfaces grow, it extends the {100} surface along the edges, which is capped as it appears. This is the mechanism which results in the cubic morphology; therefore the shape of the nanoparticle is highly dependent on the capping agent, making it a vital part of the synthesis. Previous work was carried out by a predecessor on the use of different capping agents, such as dodecanoic acid, where oleic acid was found to be the most suitable. In this investigation, oleic acid is used as the capping agent, with consideration for determining the most appropriate quantity (molar ratio in relation to the CeO_2) and purity.

3.2.3.1 Concentration by Quantity

In the original synthesis, 1.5 mL of 70% pure oleic acid was used, giving a molar ratio of 1:13.3 CeO_2:oleic acid. Here, two purities of oleic acid were investigated, 70% and 99%, which is discussed and compared in Section 3.2.3.2, however the change in purity also changes the molar ratio if the quantity is not adjusted. To determine whether changing the quantity of the oleic acid has an effect on the synthesis, the 99% pure oleic acid was employed in the original quantity, 1.5 mL, giving a higher CeO_2 to oleic acid ratio (1:18.8). The quantity of 99% pure oleic acid was also reduced to 1.06 mL to keep the 1:13.3 molar ratio.

XRD

Figure 3.5 (top), presents the XRD patterns obtained from the nanoparticles synthesised with 1.5 mL (red) and 1.06 mL (blue) oleic acid, along with an XRD reference pattern for CeO_2 (black). The broad oleic acid peak at 2θ range 15-25 is noticeably larger for the 1.5 mL of oleic acid. This suggests that a higher quantity of oleic acid being present in the synthesis process results in a higher amount bonding to the surface of the nanoparticles. The characteristic {200} peak is far more intense for the 1.5 mL oleic acid synthesis, as is the {400} peak, suggesting a highly cubic morphology, however there is also an extremely intense {220} peak, which although present in the nanocubic morphology, should not be as prominent; this could suggest the nanoparticles have not self-assembled on the XRD sample holder, and therefore have a different orientation. The 1.06 mL oleic acid synthesis contains fairly low intensity peaks, with the {200} being the most prominent, suggesting a high proportion of particles with cubic morphology.

From the XRD alone, it is not possible to determine which synthesis has yielded the most preferential results, therefore the visualisation of the nanocubes via TEM is essential to understanding the morphology and distribution in more detail.

TEM

TEM images of the ceria nanoparticles synthesised with 1.5 mL oleic acid (red outline) and 1.06 mL oleic acid (blue outline) are presented in Figure 3.5. Here it can be observed that the size distribution of the nanoparticles is fairly consistent, however there is a larger space between the nanoparticles of the 1.5 mL oleic acid synthesis, which is due to a thicker layer of oleic acid on the surface. In both syntheses there is a large percentage of nanoparticles with cubic morphology, with the 1.5 mL oleic acid synthesis being slightly higher. This suggests that the presence of more oleic acid in the synthesis causes a small improvement in the formation of the ceria nanocubes.

TGA/DSC

Figure 3.5 (bottom) presents the TGA/DSC curves of the ceria nanoparticles obtained with the 1.5 mL oleic acid synthesis (red) and 1.06 mL oleic acid synthesis (blue) with the results summarised in Table 3.2, reporting each DSC peak, temperature, and corresponding TGA mass change.

The major exothermic activity for both syntheses is similar, focusing around 420 °C. The slight differences here could be related to the thickness of the oleic acid coating of the nanoparticles, as a thinner layer will allow for the oleic acid to decompose slightly faster, therefore presenting an exothermic peak at a slightly lower temperature. The main difference however is in the TGA mass change. With less oleic acid on the surface of the nanoparticles for the 1.06 mL oleic acid synthesis, there is a smaller associated weight change (∼65%) in comparison to the 1.5 mL oleic acid synthesis (∼80%). This is fairly unsurprising, and further confirms the additional presence of the oleic acid aiding the formation of the nanocubes.

Table 3.2: TGA/DSC data relating to the synthesised nanoparticles using 99% pure oleic acid in quantities of 1.5 mL and 1.06 mL, giving molar ratios of 1:18.8 and 1:13.3 in relation to CeO_2.

Oleic acid quantity	**Peak**	**Temperature (°C)**	**Mass change (%)**	**Residual mass (%)**
1.5 mL	1	375.5(1)	80.1(1)	19.9(1)
	2	423.0(1)		
1.06 mL	1	384.0(1)	65.2(1)	34.8(1)
	2	419.0(1)		

Conclusion

By characterising the ceria nanoparticles synthesises with 1.5 mL and 1.06 mL oleic acid, using XRD, TEM, and TGA/DSC, it was concluded that the higher ratio of oleic acid (1.5 mL 1:18.8) produced better results. This is evidenced particularly by the intensity of the {200} and {400} peaks in the XRD and by the clear presentation of the nanoparticles in the TEM images. There is however a higher mass change given in comparison to the 1.06 mL oleic acid synthesis due to the presence of the additional oleic acid, though this seems fairly essential to cubic morphology of the nanoparticles.

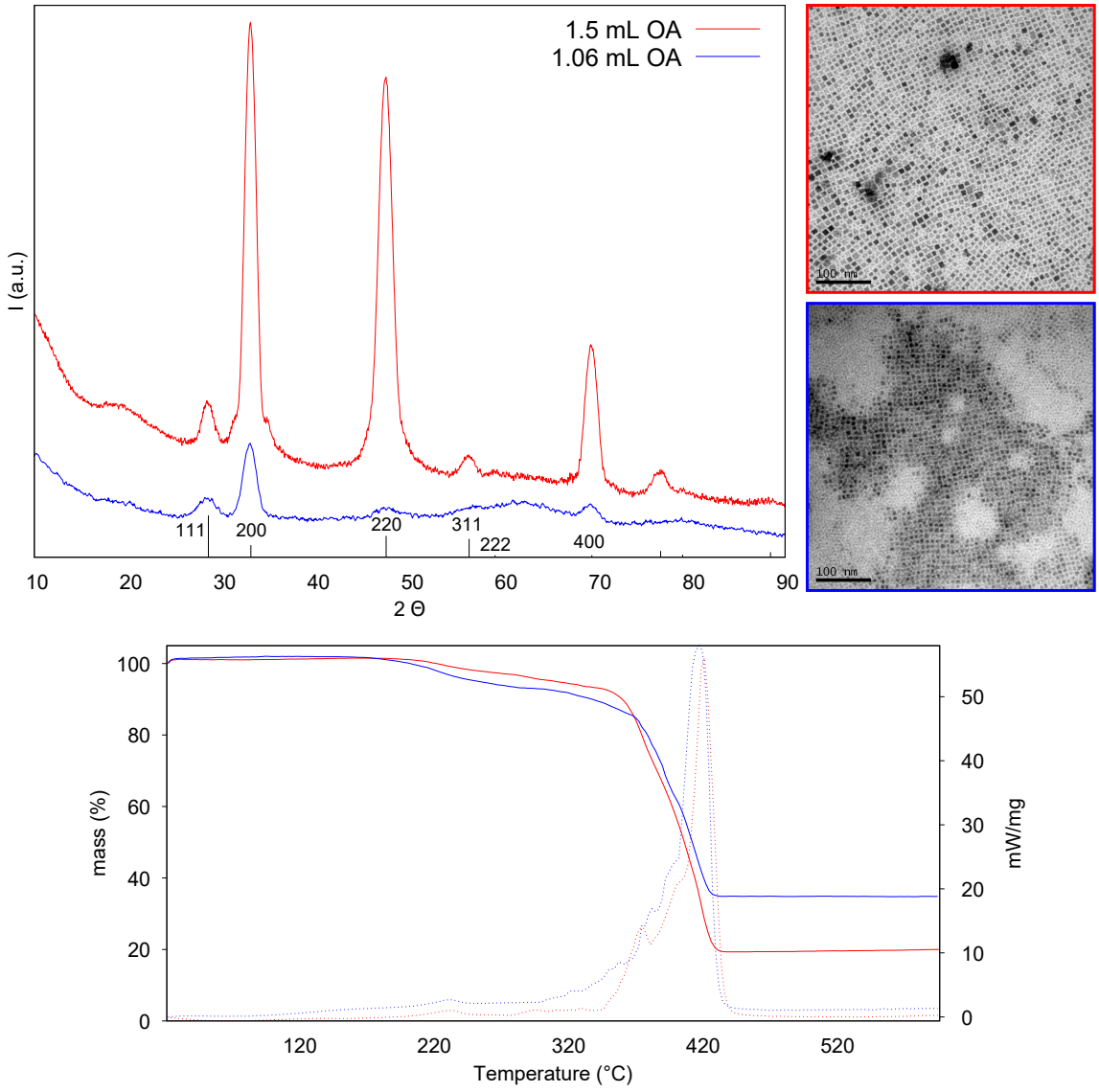

Figure 3.5: XRD patterns (top), TEM images, and TGA/DSC measurements (bottom) for nanoparticles synthesised with 1.5 mL (red) and 1.06 mL (blue) of oleic acid. An XRD reference pattern for CeO_2 is also given (black). For the TGA/DSC plot the solid lines relate to the mass axis and the dotted lines relate to the mW/mg axis.

3.2.3.2 Purity

Two purities of oleic acid, 70% and 99%, were investigated as although higher purity should produce higher quality results (in theory), the 99% pure oleic acid is also considerably more expensive and is very unstable, requiring specific storage conditions. This makes the handling fairly difficult, and it is believed that the lower purity could be a more sustainable alternative. 70% pure oleic acid was chosen as it was readily available in sufficient quantities and only required refrigerated storage, allowing easier handling and presenting higher thermal stability.

XRD

Figure 3.6 (top) presents the XRD patterns obtained from the nanoparticles synthesised with 1.5 mL (red) and 1.06 mL (blue) oleic acid, along with an XRD reference pattern for CeO_2 (black), which is labelled and reported at the bottom of the pattern. The characteristic {200} peak has high intensity for both purities, along with intense {400} peaks, which suggest they both contain particles with highly cubic morphology. The intensities of all the peaks are clear and well defined, with the only noticeable difference between the purities being the presence of a {311} peak in the 70% pure oleic acid synthesis, which is not in the 99% pure oleic acid synthesis. This suggests that although there is a prominent {200} peak, representing the cubic morphology, not all nanoparticles hold this shape. As the XRD patterns are so similar, the difference in morphology requires TEM to further determine/understand any differences in the nanoparticles.

TEM

TEM images of the ceria nanoparticles synthesised with 99% pure oleic acid (red outline) and 70% pure oleic acid (blue outline) are presented in Figure 3.6. Here it can be observed that the size distribution of the nanoparticles is fairly consistent, with a slightly larger size distribution for the 70%. The TEM images also confirm the indications given by the XRD that there is a difference in nanoparticle shape. The 99% synthesis appears highly orientated in a grid like packing, with nearly all nanoparticles holding a cubic morphology. The 70% synthesis, although containing a high percentage of nanoparticles of cubic morphology, also contains non-cubic morphologies, and is not arranged as orderly. This shows that the 99% oleic acid is more conducive to the synthesis of ceria nanocubes, however the 70% is adequate for basic analysis and parameter testing.

TGA/DSC

In Figure 3.6 (bottom) the TGA/DSC curves of the ceria nanoparticles obtained with the 99% pure oleic acid synthesis (red) and 70% pure oleic acid synthesis (blue) are presented, with the results summarised in Table 3.3, reporting each DSC peak, temperature, and corresponding TGA mass change.

Table 3.3: TGA/DSC data relating to the synthesised nanoparticles using 99% and 70% pure oleic acid.

Oleic acid purity	**Peak**	**Temperature (°C)**	**Mass change (%)**	**Residual mass (%)**
99%	1	375.7(1)	80.0(1)	20.0(1)
	2	423.5(1)		
70%	1	377.7(1)	87.5(1)	12.5(1)
	2	405.2(1)		

The major exothermic activity for both syntheses is fairly similar, focusing around 405-425 °C, with the 70% pure oleic acid synthesis being closer to the low end, and the 99% to the higher temperature end. The slight difference could be due to general variations in the experimental synthesis, as mentioned in previous section. There is however a difference in the TGA mass change, where the 99% synthesis results in a higher residual mass (20%) compared to the 70% synthesis (12.5%).

Conclusion

By characterising the ceria nanoparticles synthesised with 99% pure oleic acid and 70% pure oleic acid, using XRD, TEM, and TGA/DSC, it was concluded that the purer oleic acid produced more desirable ceria nanocubes of uniform shape and size. The 70% pure oleic acid however could be used as an alternative to the 99% pure oleic acid, at least for the optimisation process.

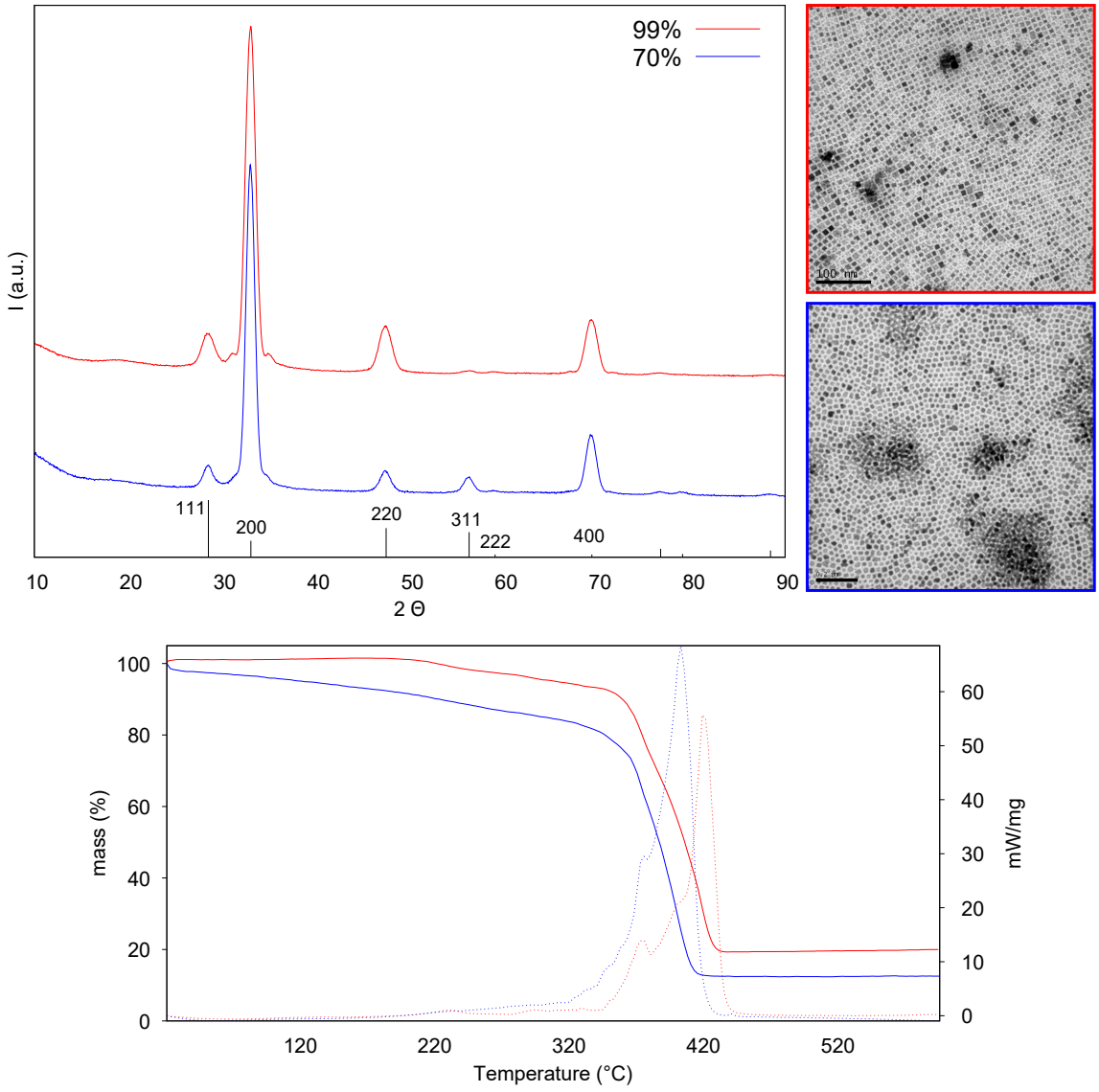

Figure 3.6: XRD patterns (top), TEM images, and TGA/DSC measurements (bottom) for nanoparticles synthesised with 99% (red) and 70% (blue) pure oleic acid. An XRD reference pattern for CeO_2 is also given (black). For the TGA/DSC plot the solid lines relate to the mass axis and the dotted lines relate to the mW/mg axis.

3.2.4 Conclusion

From the optimisation variables investigated, it was determined that cerium(III) nitrate hexahydrate is the more favourable cerium precursor, giving a more consistent size distribution and cubic morphology. The optimal thermal treatment duration is 48 hours, as 24 hours was not sufficient to grow all particle seeds, and 72 hours created new seeds late in the synthesis, resulting in a large size distribution. The oleic acid used in the synthesis as a capping agent/surfactant which should be in a higher molar ratio (1:18.8) to the CeO_2, giving a quantity of 1.5 mL for the 99% pure oleic acid. Although the 99% pure oleic acid is preferable for the synthesis, due to the delicate nature of the component, the more stable 70% pure oleic acid can be used.

3.3 La-doped Ceria Nanocubes

Use of dopants has been shown to strongly improve the catalytic performace of ceria by enhancing its ability to store and transfer oxygen [32, 33, 34, 35]. Here we investigate the use of Lanthanum as a dopant, determining the trend in doping concentration, the maximum doping concentration, and how this affects the morphology of the ceria nanocube.

It has been previously shown that incorporating La^{3+} into a ceria lattice can create defects due to a difference in the ionic radius between Ce^{4+} (0.097 nm) and La^{3+} (0.110 nm) [36]. These defects include the formation of oxygen vacancies which are desirable for improved catalytic activity. One concern with the process of doping the ceria nanocubes is a change in morphology, where loss of fluorite structure will change the shape and surface of the nanoparticles from the favourable cubic morphology. That being said, there are studies which show that the cubic fluorite structure of ceria remains with the incorporation of lanthanum [37], however the extend of the doping needs to be further investigated.

Lanthanum nitrate hexahydrate (99.99%) from Sigma-Aldrich was used as the lanthanum precursor. The same synthesis process was used as with the pure ceria nanocubes, with a given amount of Ce precursor substituted with La precursor. The lanthanum precursor was introduced into the synthesis by mixing a 16.7 mmol/L aqueous solution with the cerium precursor in the relative quantities in order to achieve dopings of 2.5, 5, 7.5, 10, and 15 mol%. The resulting nanoparticles were mainly characterised by XRD, TGA/DSC (though not discussed here), and different types of imaging including TEM, high-resolution TEM (HRTEM), aberration corrected TEM (AC-TEM), and scanning transmission electron microscopy - energy dispersive x-ray spectroscopy (STEM-EDS). HRTEM, AC-TEM, and STEM-EDS characterisation was conducted by a collaborative group at the King Abdullah University of Science and Technology (KAUST).

3.3.1 Characterisation

XRD is a useful technique for structural characterisation of the La-doped ceria nanocubes. With La introduced into the ceria lattice, increased ionic radius causes a shift in the XRD peaks, which is more easily distinguishable in the characteristic {200} peaks due to the higher intensity, and the extent of this shift is related to the doping level. XRD can also be used to calculate the lattice parameters where, for the cubic fluorite structure, a=b=c, can be used to determine a trend in the lattice accommodation of the lanthanum, and XRD can also give information to aid in estimating the crystallite size.

3.3.1.1 XRD Structural Analysis

Figure 3.7 gives the XRD patterns of the La-doped ceria nanocubes, in all stated doping quantities, with Table 3.4 presenting the calculated {200} peak positions, lattice parameters, and crystallite size. The post-precipitation XRD patterns of the La-doped ceria nanocubes and relating table of data is given in Appendix 2, Section 2.1. It is worth re-noting that the peak intensity is related to the sample concentration and therefore the intensity may vary between samples. This does not however impact the composition of the sample.

Table 3.4: Peak positions, lattice parameters, and estimated crystallite size of the pre-precipitated La-doped ceria nanocubes in 0, 2.5, 5, 7.5, 10, 12.5, and 15 %mol

%mol La	**{200} Peak position (2θ)**	**Lattice parameter (Å)**	**Crystallite size (nm)**
0	32.994(3)	5.425(3)	7±1
2.5	32.941(7)	5.443(7)	7±1
5	32.906(2)	5.439(2)	6±1
7.5	32.885(4)	5.443(4)	7±1
10	32.877(2)	5.444(2)	6±1
12.5	32.877(3)	5.444(3)	8±1
15	32.886(7)	5.443(7)	7±1

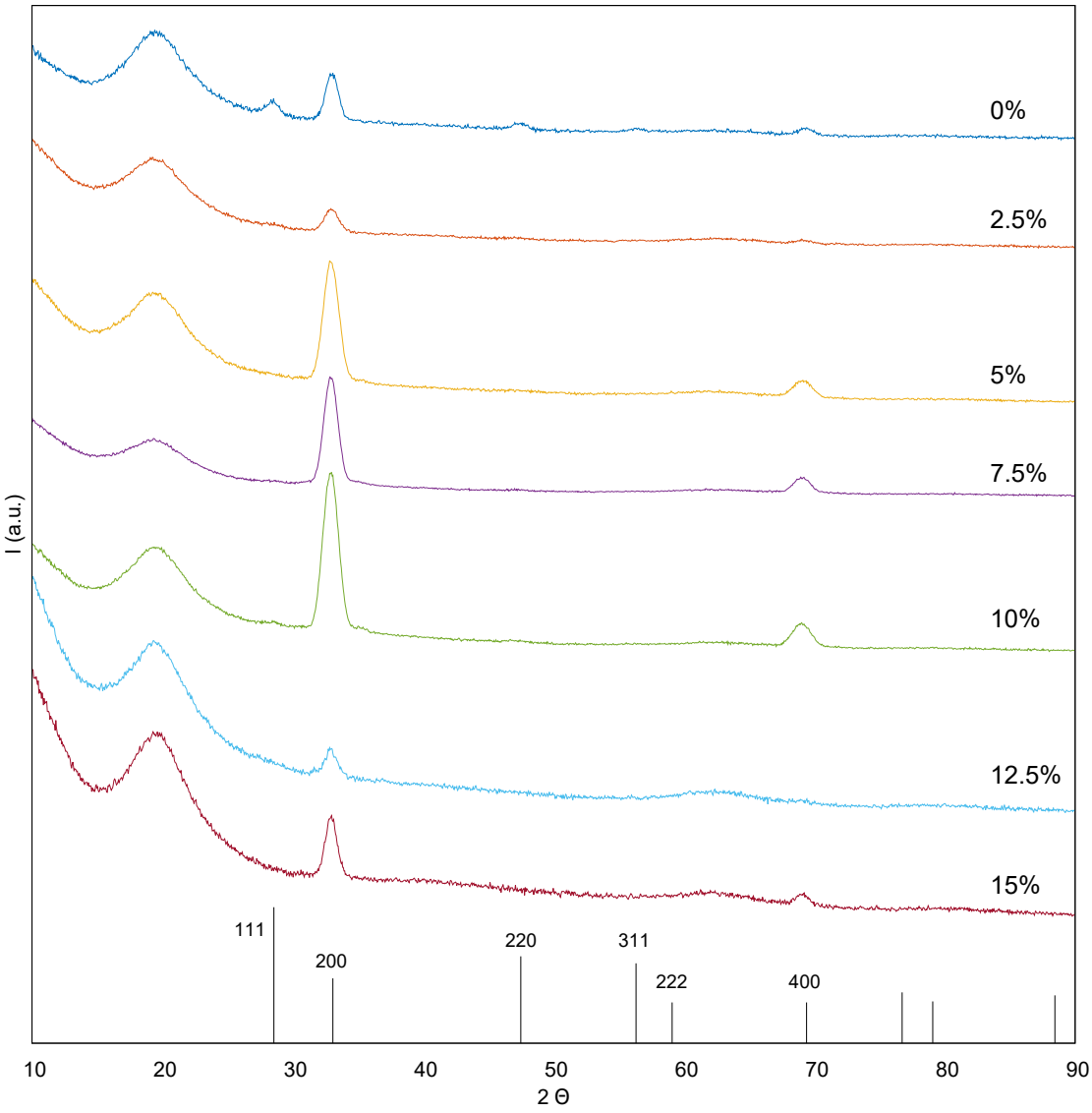

Figure 3.7: XRD patterns of the pre-precipitated La-doped ceria nanocubes, with 0 (dark blue), 2.5 (orange), 5 (yellow), 7.5 (purple), 10 (green), 12.5 (teal), and 15 (dark red) %mol of lanthanum. An XRD reference pattern for CeO_2 is also given (black).

It is not overly clear on the full size patterns that there is actually a shift of the peaks relating to the introduction of La into the ceria lattice, therefore the {200} section has been highlighted and presented in Figure 3.8. Here, it can be seen that the point of highest intensity for each peak decreases in 2θ position as the concentration of La increases. The values relating to the peak positions are given in Table 3.4 alongside the lattice parameters calculated from the patterns which show an increase with increasing %mol La. This is expected as the lattice must increase to accommodate the larger size of La.

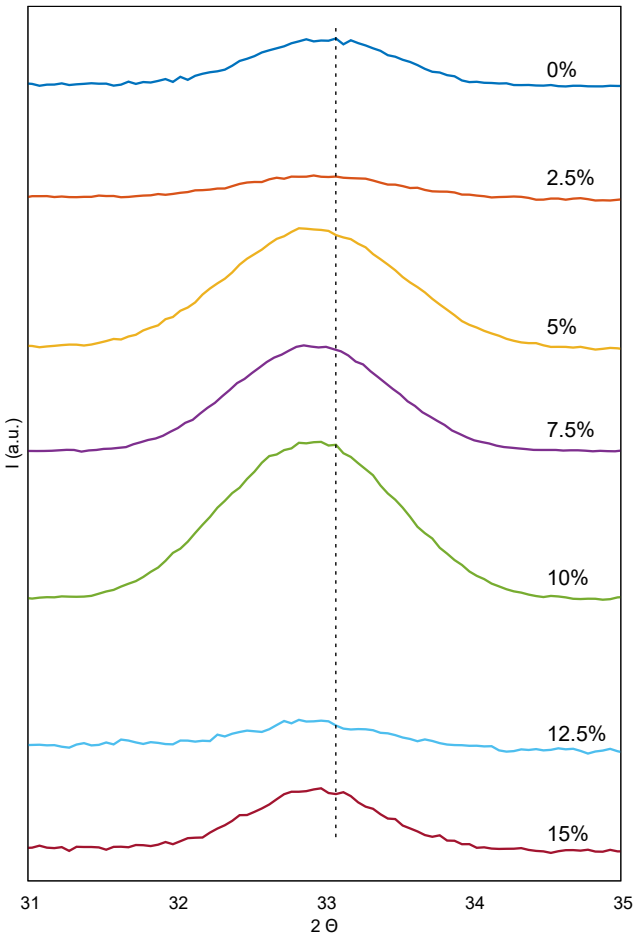

Figure 3.8: XRD patterns of the {200} pre-precipitated La-doped ceria nanocube peaks, with 0 (dark blue), 2.5 (orange), 5 (yellow), 7.5 (purple), 10 (green), 12.5 (teal), and 15 (dark red) %mol of lanthanum. A line representing the position of the reference CeO_2 {200} peak is also given (dotted black line).

Figure 3.9 shows an initial increasing linear trend which subsides into a concave form. The linear increase relates to the ceria lattice expanding for La, with the plateau indicating the lattice is no longer able to accommodate further expansion while holding the cubic fluorite structure. With the addition of more La into the ceria lattice, either the La will not incorporate into the structure, or the structure will change to a more favourable configuration, most likely the La_2O_3 hexagonal crystal structure. Therefore the maximum La-doping level, before the ceria nanocube changes structure, is between 7.5 and 10 %mol La.

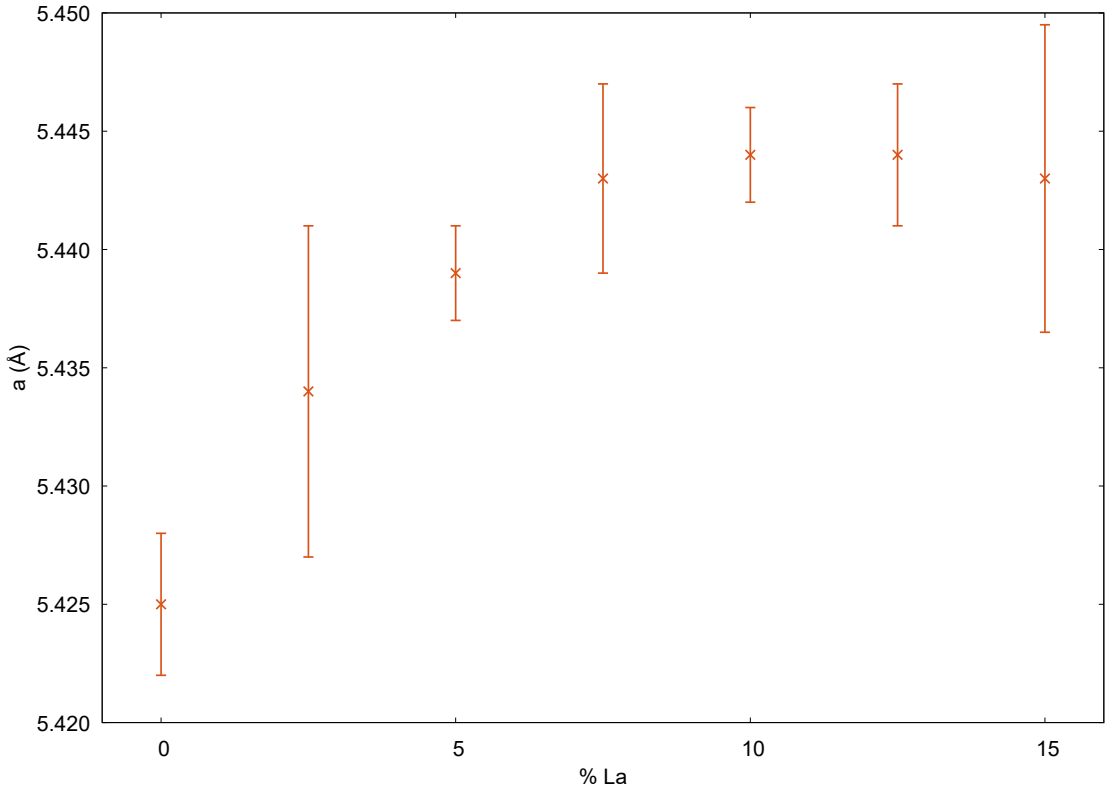

Figure 3.9: Trend of % La against lattice parameter (Å) for all La-doped ceria nanocubes.

3.3.1.2 TEM Analysis

Imaging of the La-doped ceria nanocubes is currently limited to 5% and 10%, due to access to required equipment, however future work will continue within the group to further analyse other concentrations. Figure 3.10 presents the TEM and AC-TEM images of the pre-precipitation 5% La-doped ceria nanocubes. Here, the highly ordered and cubic morphology can be seen, giving evidence that the fluorite structure has not been affected by the addition of La into the lattice. The post-precipitation 5% La-doped ceria nanocube images are presented in Appendix 2.2, showing the morphology is well retained after precipitation of the nanocubes.

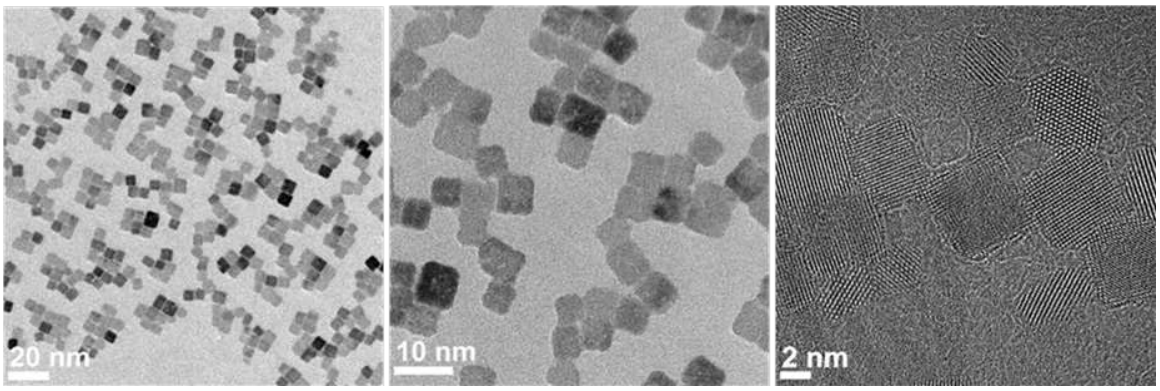

Figure 3.10: TEM images of pre-precipitation 5% La-doped ceria nanocubes at 20 nm (left), and 10 nm (centre), with an AC-TEM image at 2 nm (right).

Figure 3.11 presents the HR AC-TEM of a pre-precipitation 5% La-doped ceria nanocube, with the crystal planes highlighted, and an insert containing the projected diffraction pattern. This image is projected along the {100} direction, where the {200} and {220} crystal planes are identified. This confirms that the nanoparticle exposes mainly the most reactive {100} surface, and thus also confirming the cubic morphology. A HR AC-TEM of a post-precipitation 5% La-doped ceria nanocube is given in Appendix 2.3.

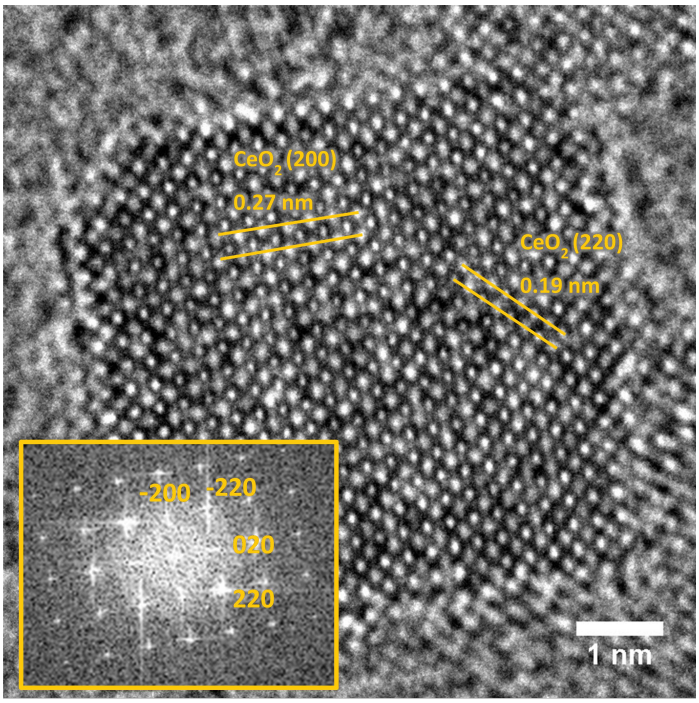

Figure 3.11: HR AC-TEM image of a pre-precipitation 5% La-doped ceria nanocube with crystal planes highlighted. The insert contains the projected diffraction pattern.

Figure 3.12 presents the TEM and AC-TEM images of the pre-precipitation 10% La-doped ceria nanocubes. Here, the highly ordered and cubic morphology can be seen, showing that even at this doping level the fluorite structure has not been affected by the addition of La into the lattice. The post-precipitation 10% La-doped ceria nanocube images are presented in Appendix 2.4, showing the morphology is still well retained after precipitation of the nanocubes.

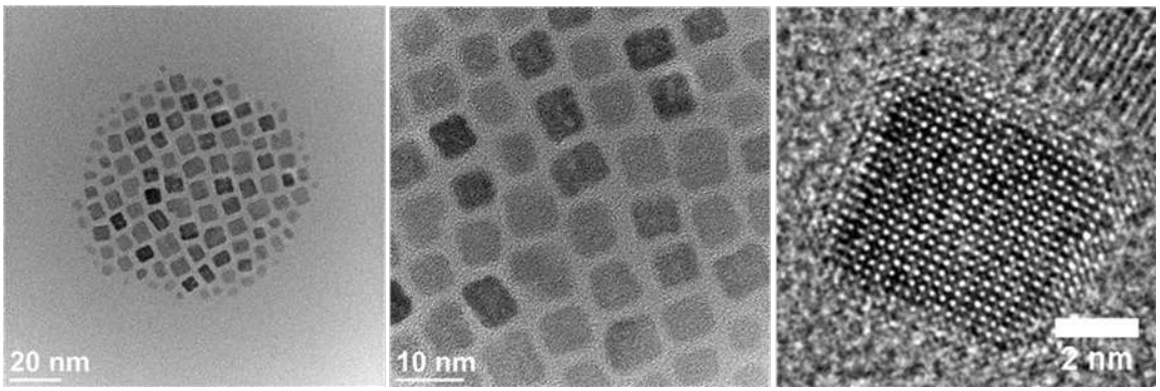

Figure 3.12: TEM images of pre-precipitation 10% La-doped ceria nanocubes at 20 nm (left), and 10 nm (centre), with an AC-TEM image at 2 nm (right).

Figure 3.13 presents the HR AC-TEM of a pre-precipitation 10% La-doped ceria nanocube, with the crystal planes highlighted, and an insert containing the projected diffraction pattern. This image is projected along the {100} direction, as with the 5% La-doped ceria nanocube, where the {200} and {220} crystal planes are identified. This again confirms that the nanoparticle exposes mainly the most reactive {100} surface, and thus also the cubic morphology. A HR AC-TEM of a post-precipitation 10% La-doped ceria nanocube is given in Appendix 2.5.

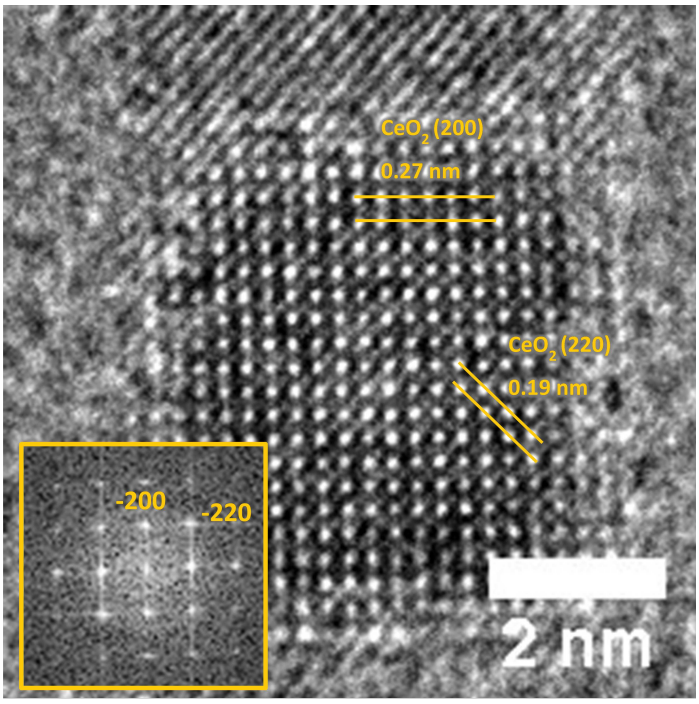

Figure 3.13: HR AC-TEM image of a pre-precipitation 10% La-doped ceria nanocube with crystal planes highlighted. The insert contains the projected diffraction pattern.

3.3.1.3 STEM-EDS Analysis

STEM-EDS is used to analyse the elemental composition of the nanocubes, which allows for further estimation of La uptake into the ceria lattice. Figure 3.14 presents three STEM-EDS images of the pre-precipitation 5% La-doped ceria nanocubes, with the first (left) a direct image of the nanocubes, the second (centre) giving the Ce elemental composition, and the last (right) giving the La elemental composition. It is clear that the majority of the Ce resides within the nanocubes, however due to the lower percentage (and concentration) of La in the sample, it is not immediately evident that La also mostly resides within the nanocubes. By analysing the chemical composition using TIA (Tecnai Imaging and Analysis) software, it was determined there is uniform distribution of the La throughout the ceria nanoparticles, comprising 96% Ce and 4% La. This is only slightly lower than the original 5 %mol La used in the synthesis.

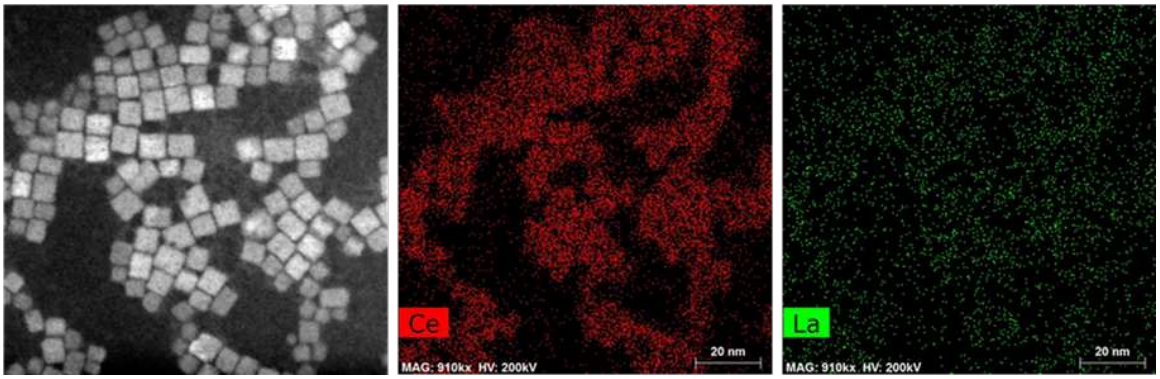

Figure 3.14: STEM-EDS images of the pre-precipitation 5% La-doped ceria nanocubes, with a standard STEM image (left), Ce elemental image (centre), and La elemental image (right) given.

Figure 3.15 presents three STEM-EDS images of the pre-precipitation 10% La-doped ceria nanocubes, and as with the 5%, the first (left) is a direct image of the nanocubes, the second (centre) gives the Ce elemental composition, and the last (right) gives the La elemental composition. Analysis of the chemical composition reveals that there is still uniform distribution of La throughout the nanocubes, which comprise roughly 93% Ce and 7% La. This is less than the targeted 10% La-doping, however as was shown with the lattice parameter change, the maximum doping level is between 7.5% and 10% and thus with experimental error this indicates that it has reached it maximum possible doping concentration, though further testing will need to be conduced to confirm this.

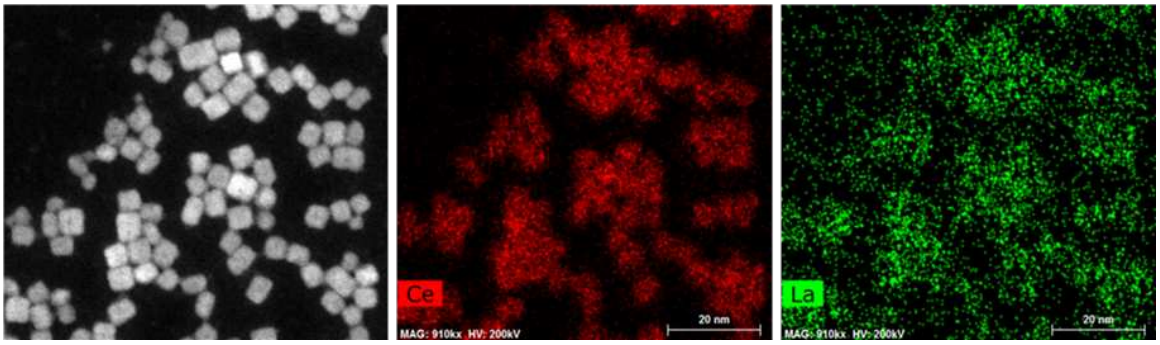

Figure 3.15: STEM-EDS images of the pre-precipitation 10% La-doped ceria nanocubes, with a standard STEM image (left), Ce elemental image (centre), and La elemental image (right) given.

3.3.1.4 Conclusion

XRD and TEM characterisation of the La-doped ceria nanocubes showed that the La was uniformly distributed throughout the ceria nanocubes, and the nanoparticles did in fact keep their cubic fluorite structure. XRD showed a visible shift in the {200} ceria peak with increased doping concentration, with the lattice parameters presenting a trend related to the increased doping concentration, providing evidence of a maximum doping quantity of between 7.5 and 10 %mol. TEM imaging shows the crystal structure is retained and provides information on the crystal planes, with STEM-EDS giving an elemental breakdown of the nanocubes, showing homogeneity of the La-doping both at 5% and 10%, and giving an estimated 4% and 7% (respectively) uptake of La into the ceria lattice.

3.4 Ceria-Silica Aerogel Nanocomposites

The synthesis method used for the aerogels is described in Chapter 2 Section 2.1.2, with the procedure given in Appendix 1.2. This is a two stage sol-gel process, followed by supercritical drying. An alcogel is formed in the two stage process; hydrolysis of an alkoxide Si precursor (TEOS) in an acid solution, followed by condensation in a basic solution to promote gelation. The nanoparticles are introduced into the aerogel synthesis following the hydrolysis step and before the condensation step. They are introduced while suspended in a toluene solution, in the desired percentage weight loading (wt%) of CeO_2 to SiO_2. High temperature supercritical drying (HT-SD) is then used to extract the solvent without collapsing the pores.

The majority of the embedment of nanoparticles into the aerogel presented in this chapter was conducted by Dr Danilo Loche as part of a collaboration. Previous embedment and aerogel syntheses were conducted by myself, however those results have not been included.

3.4.1 Characterisation

The CeO_2-SiO_2 aerogel nanocomposites were characterised using powder X-ray fluorescence (XRF), XRD, and TEM. XRF was used to determine the elemental composition of the nanocomposites, providing information related to the wt% of nanoparticles in the aerogel. Nanocomposites were made with targeted concentrations of 1, 3, and 5-6 wt% of CeO_2, with Table 3.5 presenting the targeted and XRF measured wt% of CeO_2. This indicates that the XRF measured wt% of CeO_2 is mostly similar to the targeted which was calculated from the concentration of the suspended toluene solution. However this is only an estimate and in the case of the targeted 1 wt%, the measured value was closer to 2 wt%. From this point on, the wt% will be referred to as their XRF measured concentrations rather than their targeted concentration.

Table 3.5: Comparison of the targeted wt% of CeO_2 in the nanocomposites to the XRF measured measured wt% of CeO_2.

Target wt% CeO_2	**XRF measured wt% CeO_2**
1	1.9
3	3.0
5-6	5.7

TEM and HAADF-STEM (high-angle annular dark-field STEM) analysis was conducted on the 2 wt% and 3 wt% aerogel nanocomposites to determine whether the nanoparticles were homogeneously dispersed within the aerogel matrix, and whether they retain their cubic morphology. The TEM images presented in Figure 3.16 show a low magnification image of the 2 wt% nanocomposite, with a higher magnification image highlighting an embedded nanocube. The two inserts present give the HR AC-TEM crystal planes of the nanocube and its projected diffraction pattern. Although fairly difficult to resolve, it is clear enough to indicate that the cubic morphology of the nanoparticles remain somewhat intact following embedment into the aerogel.

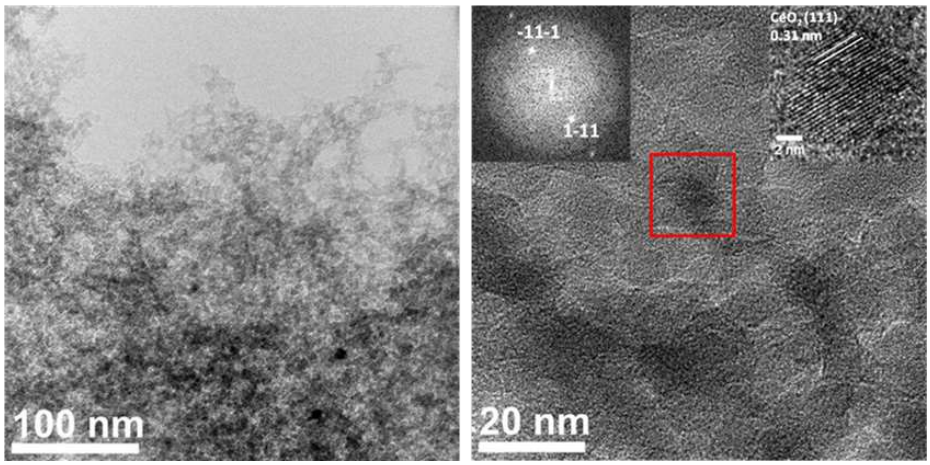

Figure 3.16: TEM images of the 2 wt% ceria nanocube - silica aerogel nanocomposite, with a low magnification TEM image (left), and a higher magnification image (right) with two inserts presenting the HR AC-TEM crystal planes of an embedded ceria nanocube and its projected diffraction pattern.

There is not high enough distinction between the nanoparticles and the aerogel for a standard TEM image to clearly display the dispersion of the nanoparticles in the aerogel matrix, which is partially due to the thickness of the sample. HAADF-STEM can be used to gain better z-contrast between the ceria and aerogel, highlighting the locations of the nanoparticles. Figure 3.17 presents two HAADF-STEM images of the 2 wt% aerogel nanocomposite, at low magnification, and a higher magnification section highlighting some of the individual positions of the ceria nanocubes. This clearly shows a fairly uniform distribution of the ceria nanoparticles throughout the aerogel composite. Analysis of the HAADF-TEM images indicate an average nanoparticle diameter of 4-8 nm.

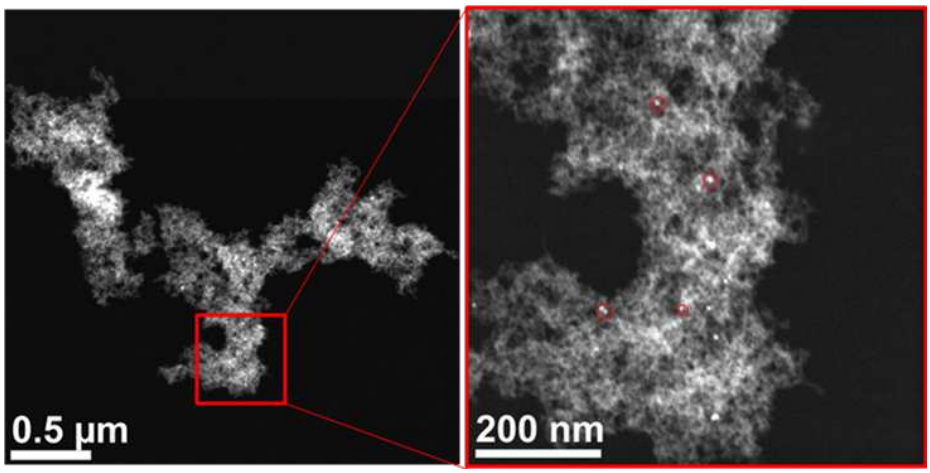

Figure 3.17: HAADF-STEM images of the 2 wt% ceria nanocube - silica aerogel nanocomposite, with a low magnification image (left), and a higher magnification image (right) with selected individual embedded ceria nanocubes highlighted.

The TEM image presented in Figure 3.18 gives a low magnification image of the 3 wt% nanocomposite, with darker regions indicating the presence of aggregated ceria nanoparticles. The sample used in this instance was too thick to identify and resolve the nanoparticle crystal planes. However as the same embedment process was used as for the 2 wt% nanocomposite, the cubic morphology of the nanoparticles may still have remained intact. However this can not be seen and further analysis is required.

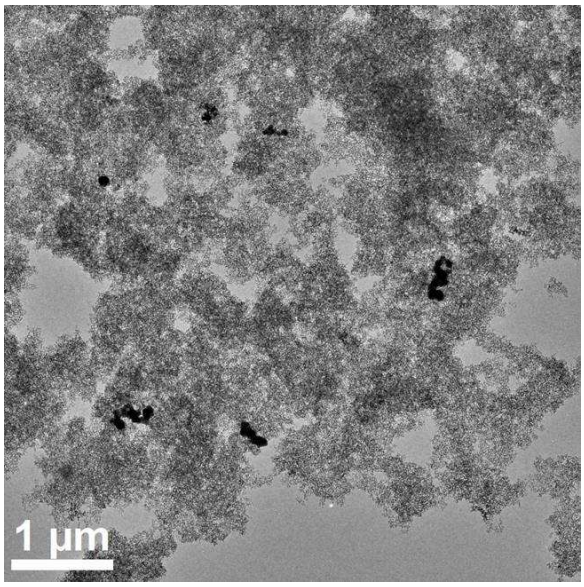

Figure 3.18: A low magnification TEM image of the 3 wt% ceria nanocube - silica aerogel nanocomposite. The darker regions are aggregated nanoparticles.

HAADF-STEM was used to gain better z-contrast between the ceria and aerogel, where Figure 3.19 presents a HAADF-STEM image of the 3 wt% aerogel nanocomposite, at low magnification, with an insert highlighting an area of intense aggregation of ceria nanocubes. This clearly shows there is no uniform distribution in the aerogel matrix.

The cause of this aggregation is most likely due to how the composite was prepared, where the nanoparticles were introduced into the aerogel synthesis process dispersed in toluene. As EtOH is used in the aerogel synthesis process and is also used to precipitate the particles from the toluene solution, the right ratio between the two needs to be found. This is fairly tricky as high concentrations of toluene could interfere with the aerogel synthesis and too low concentrations would result in particle precipitation. This nanocomposite was formed in the early stages of determining this ratio and presented inhomogeneous aerogel even on the macroscopic level. However, although the major factor that caused the nanoparticle aggregation is likely the synthesis process, other possibilities such as an effect of higher weight loading can not be ruled out and therefore further investigation is required.

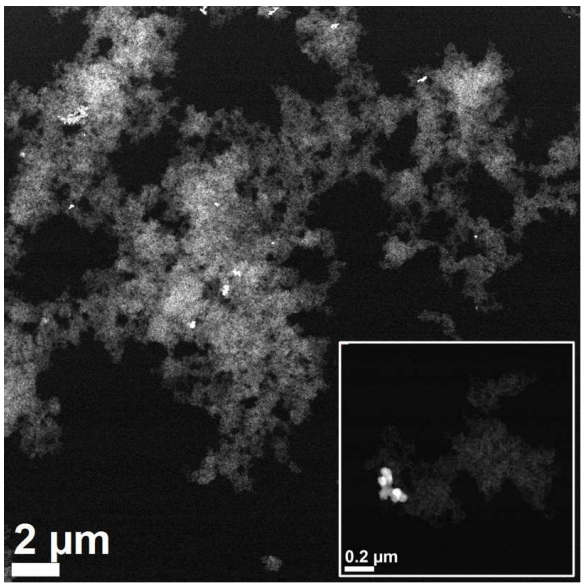

Figure 3.19: HAADF-STEM image of the 3 wt% ceria nanocube - silica aerogel nanocomposite, with an insert highlighting an area of intense aggregation of the ceria nanocubes.

3.4.2 Thermal Treatment

As ceria nanocubes are used as catalysts they need to be able to withstand relatively high working temperatures without structural degradation. To determine whether the ceria nanocubes are able to withstand higher working conditions when supported in an aerogel matrix, both the unsupported and aerogel supported ceria nanoparticles were thermally treated at 450 °C and 750 °C for a duration of 1 hour.

Figure 3.20 presents the XRD patterns relating the ceria nanoparticles both unsupported and aerogel supported, untreated, thermally treated at 450 °C, and thermally treated at 750 °C. Here it is evident that the unsupported ceria nanoparticles are stable with no thermal treatment, however when thermally treated at 450 °C there is an intensity reduction and a slight shift to a higher {111} peak and lower {200}, indicating that some of the cubic morphology is lost. When the unsupported nanoparticles were thermally treated at 750 °C the peaks become sharp and the ratios are similar to the CeO_2 reference pattern which indicates a complete loss in the cubic morphology. For the nanoparticles supported in the aerogel matrix, there is much lower intensity due to the wt% loading, however the peaks can be distinguished. From the XRD patterns presented, there are similar intensities and peak ratios for the untreated and both thermally treated nanocomposites, indicating the cubic morphology is stable up to 750 °C when supported in the aerogel matrix.

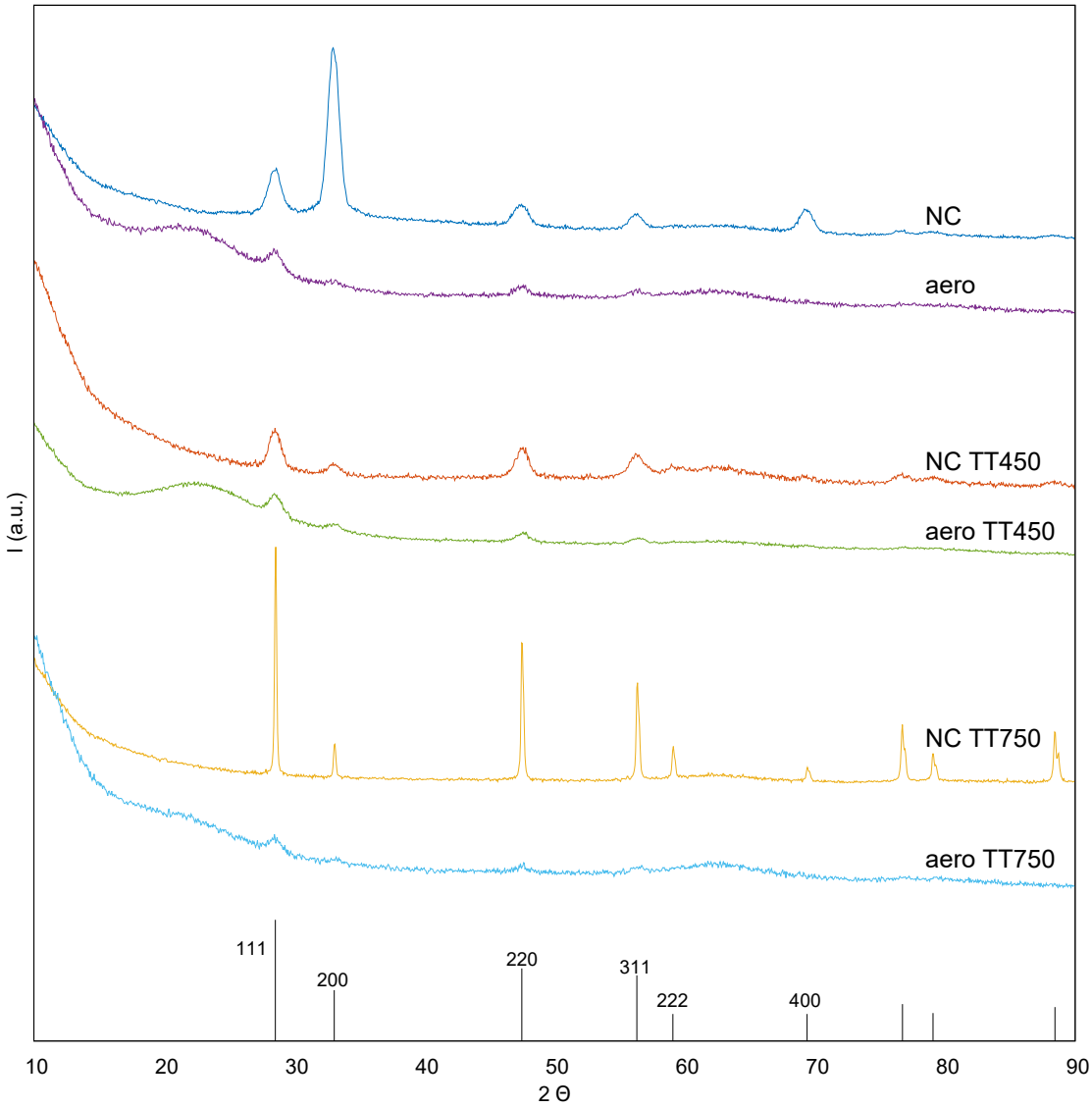

Figure 3.20: XRD patterns of the ceria nanocubes (NC) and the 2 wt% aerogel-supported ceria nanocubes (aero), with untreated NC (dark blue), NC thermally treated (TT) at 450 °C (orange), NC thermally treated at 750 °C (yellow), untreated aero (purple), aero thermally treated at 450 °C (green), and thermally treated at 750 °C (teal). A labelled XRD reference CeO_2 pattern is also given (black line).

3.4.3 Conclusion

Characterisation of the ceria-silica aerogel nanocomposites by XRF indicate the weight loading of ceria nanoparticles is fairly consistent with the targeted weight loading, and TEM images show that the cubic morphology of the nanoparticles is retained. HAADF-STEM analysis showed good dispersion of the ceria nanoparticles in the aerogel at 2 wt%, however aggregation of the nanoparticles appeared to occur at 3 wt%, with the reason not entirely clear. The aggregation could be due to the higher weight loading, however it could also be due to other synthesis conditions, as discussed above, and without further investigation, the cause can not be determined. Thermal treatment of the unsupported ceria nanoparticles and aerogel composites show that the aerogel supported nanoparticles are able to remain stable and retain their cubic morphologies up to 750 °C, where unsupported there is partial loss in cubic morphology at 450 °C, and complete loss at 750 °C. This gives strong indications that the nanocomposites are able to stabilise the ceria nanocube morphology, potentially enabling better catalytic activity under harsher conditions.

3.5 Future Work

One of the main challenges associated with the optimisation of the ceria nanoparticles was the instability of the oleic acid. The cause of this instability is still not entirely transparent; by most part it was due to the storage and handling conditions whereby requiring refrigeration and being frequently removed and replaced may have lead to degradation. This could have been a result of both change in temperature and also exposure to the air, causing oxidation. This challenge is one which the group will continue to investigate and address. Further to this, the group will continue to work with the ceria nanoparticles and nanocomposites, progressing into the use of different dopants, and possibly different aerogel matrices.

References

[1] L. Lisiecki. Size, Shape, and Structural Control of Metallic Nanocrystals. *Journal of Physical Chemistry B*, 109(25):12231–12244, 2005.

[2] K. An and G.A. Somorjai. Size and Shape Control of Metal Nanoparticles for Reaction Selectivity in Catalysis. *Special Issue: Synthesis of Nanocatalysts*, 4 (10):1512–1524, 2012.

[3] L. Qu, L. Dai, and E. Osawa. Shape/Size-Controlled Syntheses of Metal Nanoparticles for Site-Selective Modification of Carbon Nanotubes. *Journal of American Chemical Society*, 128:5523–5532, 2006.

[4] C. Sun, H. Li, and L. Chen. Nanostructured Ceria-Based Materials: Synthesis, Properties, and Applications. *Energy and Environmental Sciences*, 5(9):8475–8505, 2012.

[5] Q. Zhang, F. an Jin and S.W. Chan. Ceria Nanoparticles: Size, Size Distribution, and Shape. *Journal of Applied Physics*, 95:4319, 2004.

[6] X. Feng, D.C. Sayle, Z.L. Wang, S. Paras, B. Santora, A.C. Sutorik, T.X.T. Sayle, Y. Yang, Y. Ding, X. Wang, and Y. Her. Converting Ceria Polyhedral Nanoparticles into Single-Crystal Nanospheres. *Science*, 312(5779):1504–1508, 2006.

[7] N. Ta, J. Liu, and W. Shen. Tuning the Shape of Ceria Nanomaterials for Catalytic Applications. *Chinese Journal of Catalysis*, 34(5):838–850, 2013.

[8] E. Mamontov and T. Egami. Lattice Defects and Oxygen Storage Capacity of Nanocrystalline Ceria and Ceria-Zirconia. *J. Phys. Chem. B*, 104(47):11110–11116, 2000.

[9] T. Taniguchi, K. Katsumata, S. Omata, L. Okada, and N. Matsushita. Tuning Growth Modes of Ceria-Based Nanocubes by a Hydrothermal Method. *Crystal Growth & Design*, 11(9):3754–3760, 2011.

[10] C. Sun, H. Li, H. Zhang, Z. Wang, and L. Chen. Controlled Synthesis of CeO_2 Nanorods by a Solvothermal Method. *Nanotechnology*, 16(9):1454–1463, 2005.

[11] L. Qian, J. Zhu, W. Du, and X. Qian. Solvothermal Synthesis, Electrochemical and Photocatalytic Properties of Monodispersed CeO_2 Nanocubes. *Materials Chemistry and Physics*, 115(2–3):835–840, 2009.

[12] M. Kamruddin, P.K. Ajikumar, R. Nithya, A.K. Tyagi, and B. Raj. Combustion Synthesis of Nanocrystalline Ceria (CeO_2) Powders by a Dry Route. *Scripta Materialia*, 50(4):417–422, 2004.

[13] C. Hwang, T. Huang, J. Tsai, C. Lin, and C. Peng. Combustion Synthesis of Nanocrystalline Ceria (CeO_2) Powders by a Dry Route. *Materials Science and Engineering: B*, 132(3):229–238, 2006.

[14] S. Shih, Y. Wu, C. Chen, and C. Yu. Morphology and Formation Mechanism of Ceria Nanoparticles by SprayPpyrolysis. *Journal of Nanoparticle Research*, 14: 879, 2012.

[15] S. Yang and L. Geo. Controlled Synthesis and Self-Assembly of CeO_2 Nanocubes. *Journal of American Chemistry Society*, 128:9330–9331, 2006.

[16] T. Yu, J. Joo, Y. Park, and T. Hyeon. LargeScale Nonhydrolytic SolGel Synthesis of UniformSized Ceria Nanocrystals with Spherical, Wire, and Tadpole Shapes. *Angewandte Chemie*, 117(45):7577–7580, 2005.

[17] C. Paun, O.V. Safonova, J. Szlachetko, P.M. Abdala, M. Nachtegaa, J. Sa, E. Kleymenov, A. Cervellino, F. Krumeich, and J.A. van Bokhoven. Polyhedral CeO_2 Nanoparticles: Size-Dependent Geometrical and Electronic Structure. *Journal of Physical Chemistry C*, 116(13):7312–7317, 2012.

[18] K. Zhou, X. Wang, X. Sun, Q. Peng, and Y. Li. Enhanced Catalytic Activity of Ceria Nanorods from Well-Defined Reactive Crystal Planes. *Journal of Catalysis*, 229(1):206–212, 2005.

[19] K. Zhou, Z. Yang, and S. Yang. Highly Reducible CeO_2 Nanotubes. *Chemistry of Materials*, 19(6):1215–1217, 2007.

[20] J.C. Yu, L. Zhang, and J. Lin. Direct Sonochemical Preparation of High-Surface-Area Nanoporous Ceria and CeriaZirconia Solid Solutions. *Journal of Colloid and Interface Science*, 260(1):240–243, 2003.

[21] H.C. Yao and Y.F. Yu Yao. Ceria in Automotive Exhaust Catalysts: I. Oxygen Storage. *Journal of Catalysis*, 86(2):254–265, 1984.

[22] B.C. Dunn, P. Cole, D. Covington, M.C. Webster, R.J. Pugmire, R.D. Ernst, E.M. Eyring, N. Shah, and G.P. Huffman. Silica Aerogel Supported Catalysts for FischerTropsch Synthesis. *Applied Catalysis A: General*, 278(2):233–238, 2005.

[23] M.L. Anderson, R.M. Stroud, and D.R. Rolison. Enhancing the Activity of Fuel-cell Reactions by Designing Three-dimensional Nanostructured Architectures: Catalyst-modified CarbonSilica Composite Aerogels. *Nano Letters*, 2(3):235–240, 2002.

[24] D.M. Smitha, A. Maskaraa, and U. Boesb. Aerogel-Based Thermal Insulation. *Journal of Non-Crystalline Solids*, 225:254–259, 1998.

[25] M. Reim, W. Körner, J. Manara, S. Korder, M. Arduini-Schuster, H.P. Ebert, and J. Fricke. Silica Aerogel Granulate Material for Thermal Insulation and Daylighting. *Solar Energy*, 79(2):131–139, 2005.

[26] R. Baetens, B.P. Jelle, and A. Gustavsen. Aerogel Insulation for Building Applications: A State-of-the-Art Review. *Energy and Buildings*, 43(4):761–769, 2011.

[27] M. Gronauer and J. Fricke. Acoustic Properties of Microporous SiO_2-Aerogel. *Acta Acustica united with Auctica*, 59(3):177–181, 1986.

[28] S. Štandeker, Z. Novak, and Ž Knez. Adsorption of Toxic Organic Compounds from Water with Hydrophobic Silica Aerogels. *Journal of Colloid and Interface Science*, 310(2):362–368, 2007.

[29] A. Sayari, S. Hamoudi, and Y. Yang. Applications of Pore-Expanded Mesoporous Silica. 1. Removal of Heavy Metal Cations and Organic Pollutants from Wastewater. *Chemistry of Materials*, 17(1):212–216, 2005.

[30] T. Mori, J. Drennan, J. Lee, J. Li, and T. Ikegami. Oxide Ionic Conductivity and Microstructures of Sm- or La-Doped CeO_2-Based Systems. *Solid State Ionics*, 154–155:461–466, 2002.

[31] A. Bueno-López, K. Krishna, M. Makkee, and J.A. Moulijn. Enhanced Soot Oxidation by Lattice Oxygen via La^{3+}-Doped CeO_2. *Journal of Catalysis*, 230 (1):237–248, 2005.

[32] A. Suda, K. Yamamura, A. Morikawa, Y. Nagai, H. Sobukawa, Y. Ukyo, and H. Shinjo. Atmospheric Pressure Solvothermal Synthesis of CeriaZirconia Solid Solutions and their Large Oxygen Storage Capacity. *Journal of Material Science*, 43:2258–2262, 2008.

[33] J.G. Nunan, H.J. Robota, M.J. Cohn, and S.A. Bradley. Physicochemical Properties of Ce-Containing Three-Way Catalysts and the Effect of Ce on Catalyst Activity. *Journal of Catalysis*, 133(2):309–324, 1992.

[34] J. Kašpar, P. Fornasiero, and M. Graziani. Use of CeO_2-Based Oxides in the Three-Way Catalysis. *Scripta Materialia*, 50(2):285–298, 1999.

[35] X.B. Zhao, F. Chen, J. You, X.Z. Li, X.W. Lu, and Z.G. Chen. The Synthesis of Mesoporous $Ce_{1-x}Zr_xO_2$ by Modified Evaporation-Induced Self-Assembly Method. *Journal of Materials Science*, 45:3563–3568, 2010.

[36] X. Hou, Q. Lu, and X. Wang. Enhanced Catalytic Properties of La-doped CeO_2 Nanopowders Synthesized by Hydrolyzing and Oxidizing $Ce_{46}La_5C_{49}$ Alloys. *Journal of Science: Advanced Materials and Devices*, 2(1):41–44, 2017.

[37] S. Liang, E. Broitman, Y. Wang, A. Cao, and G. Veser. Highly Stable, Mesoporous Mixed LanthanumCerium Oxides with Tailored Structure and Reducibility. *Journal of Materials Science*, 46:2928–2937, 2011.

Chapter 4

Oxidation/Reduction Study Using HERFD–XANES

4.1 Introduction

The application of reducible oxides, such as ceria nanocubes, as catalysts is linked to the ability of the cations to quickly, and reversibly, change oxidation states. Therefore the inherent ability of ceria to oxidise/reduce between a Ce^{3+} and Ce^{4+} state is essential to its functionality as a catalyst. Within this chapter we investigate the electronic structure and local environment of the synthesised nanocubes and nanocomposites using High-Energy Resolution Fluorescence Detected (HERFD) - X-ray Absorption Near Edge Spectroscopy (XANES) at the Ce L_3 absorption edge. XANES is sensitive to the electronic configuration of the material, which is a consequence of its high energy resolution, and in ceria compounds the 4f and 5d levels will be the most affected. Here, we use both static oxidation state measurements in an ambient environment and in-situ measurements, which allowed the study of electronic structure evolution during the oxidation/reduction process in controlled environments, while utilising thermal treatment under 5% H_2 in He_2/ 5% O_2 in He_2 gas flows.

For reducible oxides it is essential to understand the dependence of reducibility on extrinsic variables. In this case, the use of a supporting substrate, aerogel, to prevent aggregation of the particles, and a doping species, La, were used to study the effects of proximity and dimensionality of the material, while thermal treatment was used to investigate the stability of the oxidation/reduction process at higher temperatures, and with the removal of the surfactant, oleic acid.

All measurements presented in this chapter were taken at the Diamond Light Source on the I20 beamline, using an emission spectrometer where an energy of 8480.7 eV for the emitted photons was selected, while scanning the incident photon energy close to the Ce L_3 absorption edge, in order to obtain High-Energy Resolution Fluorescence Detected (HERFD) - X-ray Absorption Near Edge Spectroscopy (XANES).

Data analysis was conducted using Athena–Demeter [1], which functions allowed for the normalisation of the data and a linear combination fitting function to estimate the proportion of Ce^{3+} and Ce^{4+} species within the samples. Normalisation was done to the second order (a linear polynomial function), using the higher energy region of the spectrum where there is a plateau in the spectrum. The post-edge line was positioned so as to fit to the plateau area, and also to intercept the centre of the smaller peaks at higher energy. Where multiple spectra of the same sample under the same conditions were obtained, producing equivalent spectra (i.e. no significant deviances), the spectra were merged to give an overall representation of the sample, and remove noise.

4.2 Sample Preparation

4.2.1 Pellet Preparation and Set-Up

Powder samples were prepared by homogenising 100 mg of Polyvinylpyrrolidone (PVP), a polymer used as a diluting agent/filler, with roughly 4 mg by weight of ceria within the sample (i.e. 4 mg CeO_2, 10 mg Ce(III)Nitrate, etc.). Once homogenised, the mixture is compacted using a press to form a pellet. Samples in solution were prepared by adding a solution of nanoparticles in toluene to 100 mg PVP and grinding in a mortar and pestle. The toluene evaporates, leaving a homogenised powder, which can be compacted into a pellet using a press. Once formed the pellet is then loaded into the sample stage vertically (Figure 4.1), with the flat surface placed 45° to the incident beam and to the detector.

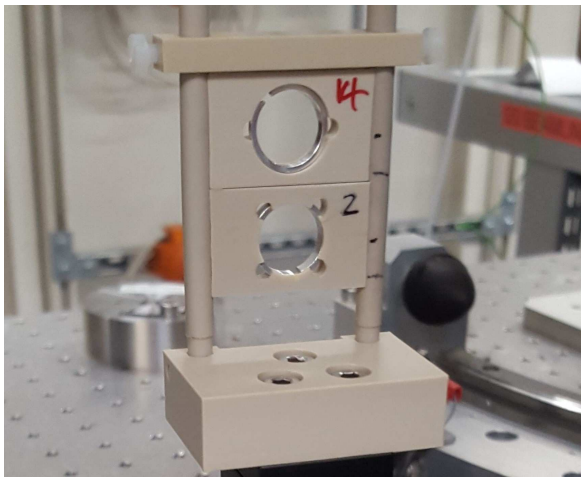

Figure 4.1: Pellet sample stage, where the pellets are loaded vertically into the spaces labelled 4 and 2, and placed at a 45° angle between the incident beam and the detector.

4.2.2 Kapton Capillary Preparation and Set-Up

Powdered samples (CeO_2 and aerogel) were prepared by homogenising the sample with a mortar and pestle. A small amount of quartz wool is placed into the capillary and pushed, using a rod, till almost centre. The capillary is then filled with 1 cm of the homogenised sample, which is pushed using two rods to the centre 1 cm of the capillary where the beam will hit. A small amount of quartz wool is then placed the other side of the powered sample to keep it in place; the positioning of this is shown in Figure 4.2.

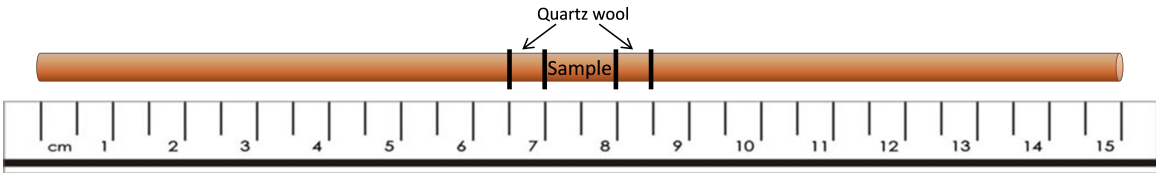

Figure 4.2: Labelled schematic of a Kapton capillary, showing the positioning of the sample and quartz wool.

Samples in solution were prepared by adding a toluene solution of nanoparticles to a small amount of quartz wool and allowing to dry in an oven at 40 °C. This method evaporates off the toluene, leaving the nanoparticles impregnated in the quartz wool. Once impregnated and dry, the quartz wool is placed into the centre of the capillary, with the aid of two rods, and pushed to the centre. As before, quartz wool is placed either side of the sample to ensure it is held in place (Figure 4.2).

Once prepared, the capillary is loaded into a mount which allows a chosen gas (N_2; 5% H_2 in He_2; 5% O_2 in He_2) to pass through the capillary and interact with the sample. A thermocouple is inserted into the capillary until in contact with the quartz wool, then the mount capillary is placed inside an open heating mantle. A labelled diagram of the capillary set-up is given in Figure 4.3.

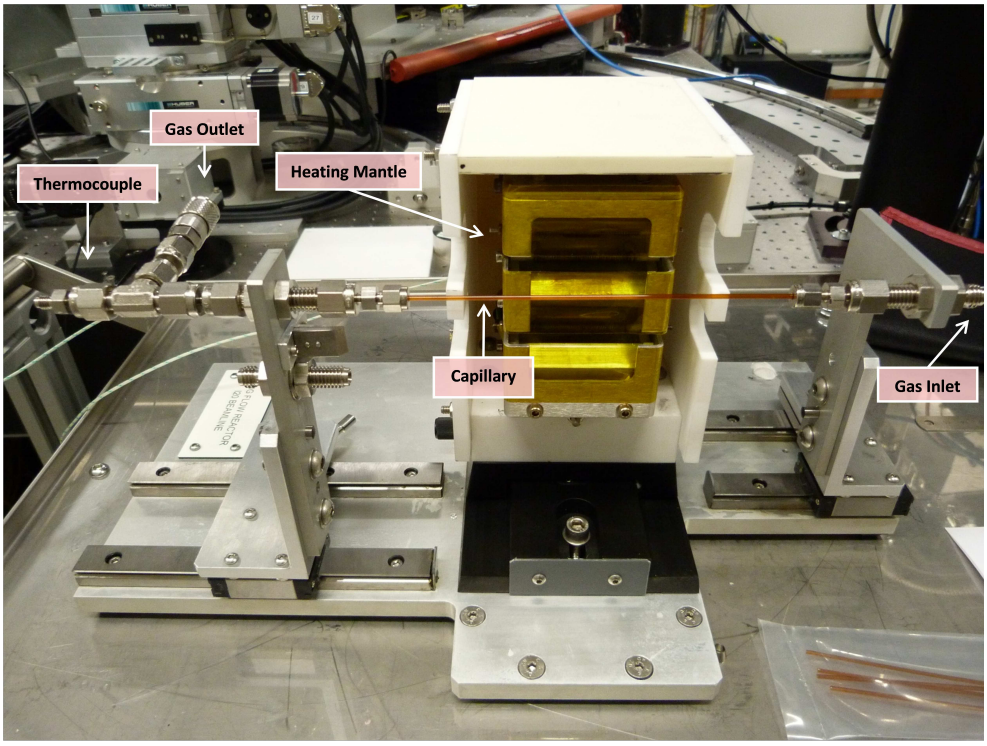

Figure 4.3: Labelled diagram of the capillary sample stage.

4.2.3 Investigated Samples

Table 4.1 gives a list of the samples investigated in this chapter, and their corresponding synthesis names used in the preparation (where appropriate).

Table 4.1: Samples investigated within this study, with their corresponding syntheses and consistency.

Sample	Consistency	Analysis form	Synthesis samples
Ce^{4+} standard	powder	pellet/capillary	Sigma Aldrich Cerium(IV) oxide 99.995%
Ce^{3+} standard	powder	pellet	Sigma Aldrich Cerium(IIII) nitrate hexahydrate 99.99%
Ceria nanoparticles	solution impregnated in wool	capillary	LM_NC_1 KL_NC_2 JVH_NC_3 JVH_NC_4
TT450 Ceria nanoparticles	powder	pellet	DL_TT450_NC_2b DL_TT450_NC_2c
7.5% La-doped Ceria nanoparticles	solution	pellet	DL_LaNC_1a DL_LaNC_1b DL_LaNC_2b
TT450 7.5% La-doped Ceria nanoparticles	powder	pellet	DL_TT450_LaNC_2a
5% Ceria Aerogel Nanocomposite	powder	pellet/capillary	KL_5%aero_1
TT450 5% Ceria Aerogel Nanocomposite	powder	pellet	KL_TT450_5%aero_1
2% Ceria Aerogel Nanocomposite	powder	pellet	DL_2%aero_1

4.3 Static Measurements

4.3.1 Standards (Ce^{4+}/Ce^{3+})

The standards used for comparison between the Ce^{4+} and Ce^{3+} states for the linear combination fitting were Sigma Aldrich Cerium(IV) oxide 99.995% and Sigma Aldrich Cerium (III) nitrate hexahydrate 99.99%. Cerium(IV) oxide has a fluorite structure, which is face-centred cubic (isometric) where a=b=c and $\alpha=\beta=\gamma=90°$. Cerium (III) nitrate hexahydrate however does not have a fluorite structure, and is in fact pinacoidal triclinic (anorthic), where $a\neq b\neq c$ and $\alpha\neq\beta\neq\gamma\neq90°$, so the fitting boundaries are not quite perfect. Large error margins are sometimes associated with this, however we are interested in the evolution, rather than an absolute value, therefore the fitting function is adequate. Additionally, when measuring along the near edge, the most prominent effect is due to the electronic structure, rather than the crystallographic structure, and therefore the standards are an adequate estimation for comparison in this analysis.

The fitting function used throughout this chapter to determine the relative percentage of Ce^{4+} and Ce^{3+}, can have sizeable errors associated due to the reasons stated. Therefore although differences to 1% are acknowledged, as obtained from the fitting, any differences less than 5%, or variations under this value, should be considered as equivalent. For example, if the percentage of Ce^{4+} is stated as 98% for one sample and 96% for another, there is not enough of a difference for it to be considered notable and therefore the composition of the two samples can be considered the same.

In Figure 4.4 the HERFD-XANES Ce L_3-edge spectra of the Ce^{3+}/Ce^{4+} standards, ranging 5715–5745 eV, are reported (full spectra are presented in Appendix 3.1). At a glance, one of the most notable differences between the standards, which is fairly expected as it also occurs in conventional XANES, is the shift in edge position. As the oxidation state increases, so does the energy, shifting the peak. There is also a reduction of peak intensity at 5727 eV, with an additional peak present in the Ce^{4+} standard at 5732 eV. The ratio between these two peaks can be used to quickly visualise the trend in the percentage of Ce^{3+} and Ce^{4+} within the sample. With close inspection of the pre-edge peak region (5720 eV), a shift in the position of the pre-edge peak can also be observed. This can be seen in greater detail in the enlarged inset in Figure 4.4. This shift in the pre-peak position is also an indication of the oxidation state, where the pre-peak lies at a lower energy for Ce^{3+}.

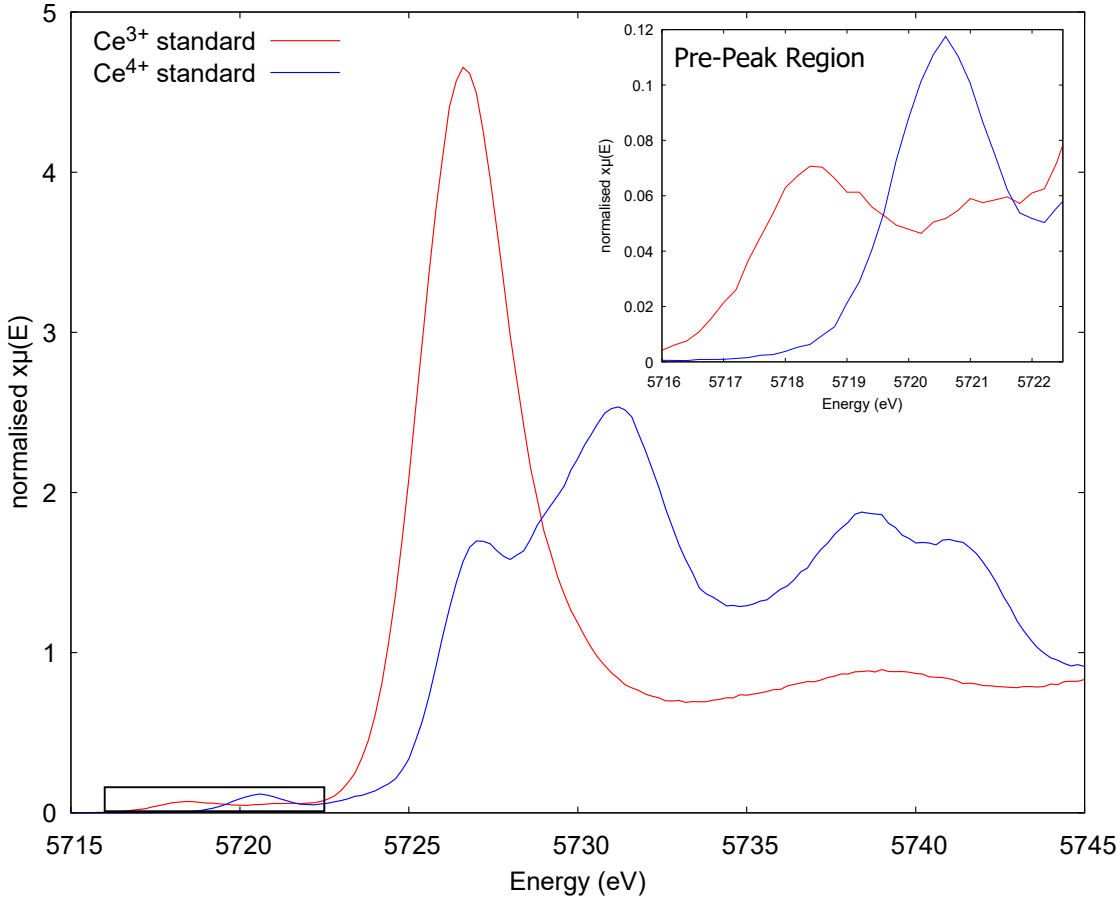

Figure 4.4: HERFD-XANES Ce L_3-edge spectra of Ce^{3+}/Ce^{4+} standards, in energy range of 5715–5745 eV, where the blue trace shows Ce^{4+} standard and the red trace Ce^{3+} standard. The inset shows the pre-edge in greater detail.

4.3.2 Ceria Nanocubes

4.3.2.1 Comparison to Standards

Ceria nanocubes hold the same fluorite structure (fcc) of Ce(IV)oxide, and in their 'perfect' composition should be fully oxidised to Ce^{4+}. In reality, microstructural features form during the synthesis process, which can create oxygen vacancies in the structure, leading to a mixture of Ce^{3+}/Ce^{4+}. Figure 4.5 gives the HERFD-XANES Ce L_3-edge spectra for the synthesised ceria nanocube at room temperature, along with the standards. Here, it can be seen that the ceria nanocubes contain both Ce^{3+} and Ce^{4+} species. This can be further evidenced by the pre-peak region (Figure 4.5 inset), where the ceria nanocubes present both pre-peaks associated with Ce^{3+} and Ce^{4+}.

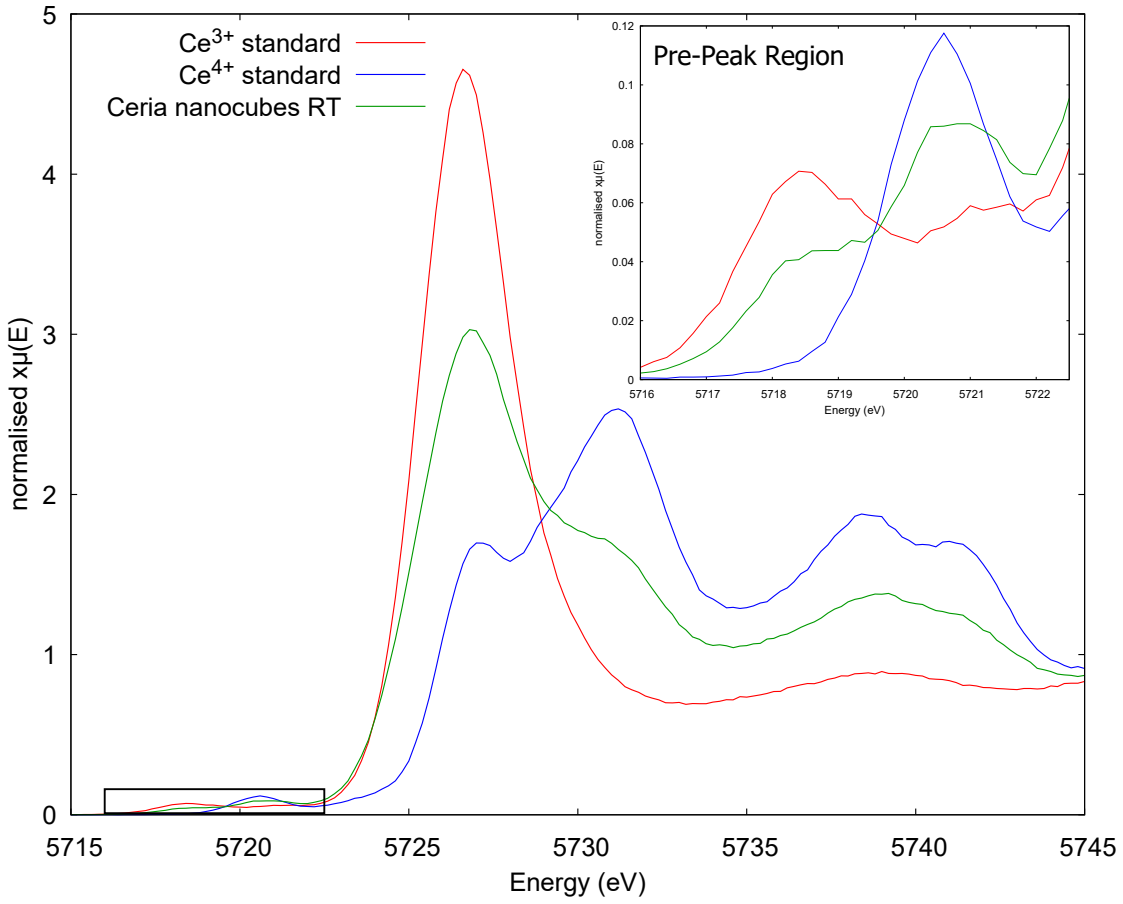

Figure 4.5: HERFD-XANES Ce L_3-edge spectra of ceria nanocubes at room temperature (green), Ce^{3+} standard (red), and Ce^{4+} standard (blue). The inset shows the pre-edge in greater detail.

Using the linear combination of standards fitting function, it was possible to determine an estimated percentage of Ce^{3+}/Ce^{4+}. For this sample of ceria nanocubes at room temperature, this was calculated as 52% Ce^{4+} and 48% Ce^{3+}. As two samples of the ceria nanocubes were prepared for in-situ measurement (see Section 4.4.2), a comparison of their static measurements was drawn. Curiously, there was a noticeable difference, with the first presenting an estimated 52% Ce^{4+} and 48% Ce^{3+} (subsequently referred to as A), and the second 74% Ce^{4+} and 26% Ce^{3+} (subsequently referred to as B). The exact cause of this difference is unknown, however there are known variables which could have contributed. During the measurements beam damage can occur, which can result in the reduction of ceria. Although this reduction is related to the time in the beam, which was consistent between A and B, the effect could be greater depending on sample concentration and conditions. Although the samples were prepared from the same synthetic products, due to the loading process onto the quartz wool they have different concentrations. By removing the normalisation on the data, and comparing the counts under the same time intervals, it was clear that B was more concentrated than A. This could suggest that the beam damage is more prevalent with lower concentrations. There may also be inhomogeneities in the loading of the nanocubes on the quartz wool, and the analysis of a different section could yield different oxidation ratios. For the purposes here, A will be used for the static measurement comparison, with both A and B discussed in-situ later in the chapter.

4.3.2.2 Ex-situ Thermally Treated Nanocubes

Under ambient conditions, ceria nanocubes are capped by oleic acid molecules as a surfactant. This controls the nanoparticle growth during the synthesis, allowing them to form their metastable cubic morphology, forming their more reactive {100} surface, and prevent the nanoparticles from aggregating. A negative effect of this is that the oleic acid also acts as a barrier on the surface, which can inhibit some of the activity, therefore removing the surfactant should allow improved surface activity. Oleic acid is an organic material which is thermally labile, and when reacted with air can decompose to CO_2 and water. Temperatures of around 250 °C, or above, should be sufficient to cause this decomposition, removing the oleic acid from the surface of the nanoparticles. Ceria nanocubes that underwent ex-situ thermal treatment at 450 °C resulted in almost complete oxidation of the ceria to Ce^{4+}, Figure 4.6, with an estimated 96% Ce^{4+} and only 4% Ce^{3+}.

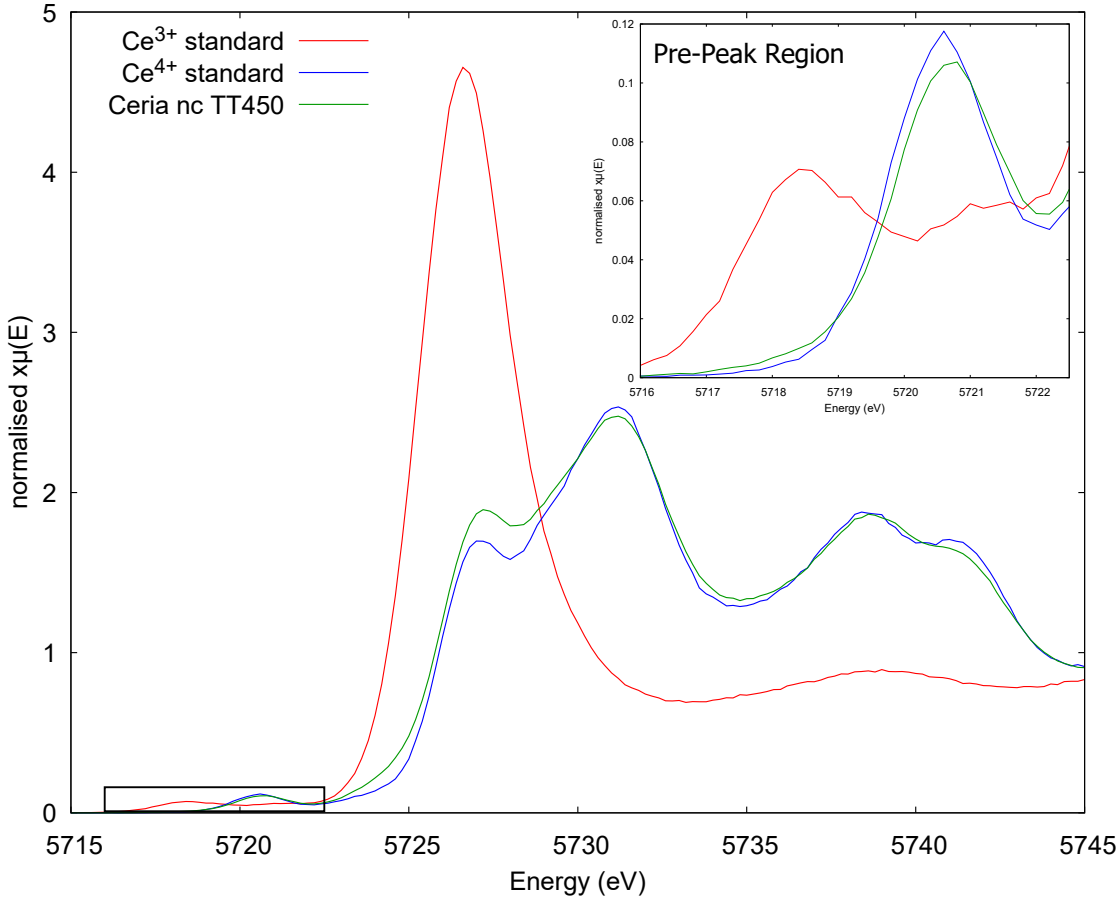

Figure 4.6: HERFD-XANES Ce L_3-edge spectra of ceria nanocubes ex-situ thermally treated at 450 °C (green), Ce^{3+} standard (red), and Ce^{4+} standard (blue). The inset shows the pre-edge in greater detail.

The difference between the untreated and ex-situ thermally treated (450 °C) nanocubes is fairly significant, with the untreated nanocubes retaining an even mix of charges, where thermally treated nanocubes are almost entirely Ce^{4+}. A direct comparison of the spectra is given in Figure 4.7. It is noted here that even with respect to sample B there is significant increase in Ce^{4+}/Ce^{3+} ratio.

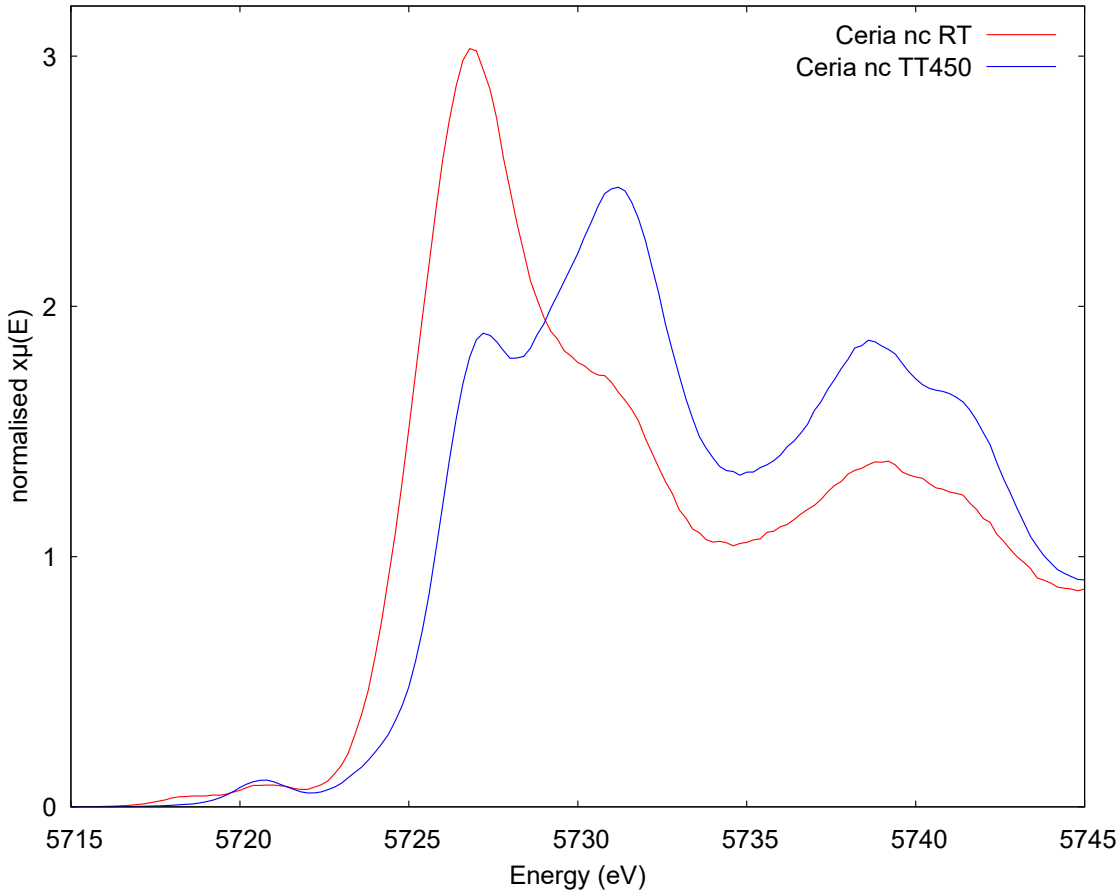

Figure 4.7: HERFD-XANES Ce L_3-edge spectra of ceria nanocubes (red) and ex-situ thermally treated nanocubes at 450 °C (blue).

4.3.3 La-doped Ceria Nanocubes

4.3.3.1 Comparison to Standards and Non-Doped Nanocubes

Lanthanum has a 3+ oxidation state, which promotes the formation of oxygen vacancies in the ceria nanocubes [2]. La^{3+} is most likely to occupy the vacant Ce^{3+} ion sites, which suggests the majority of the remaining Ce species, or a higher percentage of, should be in an oxidised (Ce^{4+}) state. 7.5% (La:Ce) La-doped Ceria nanocubes, Figure 4.8, gives an estimated 95% Ce^{4+} content, with only a 5% Ce^{3+} content.

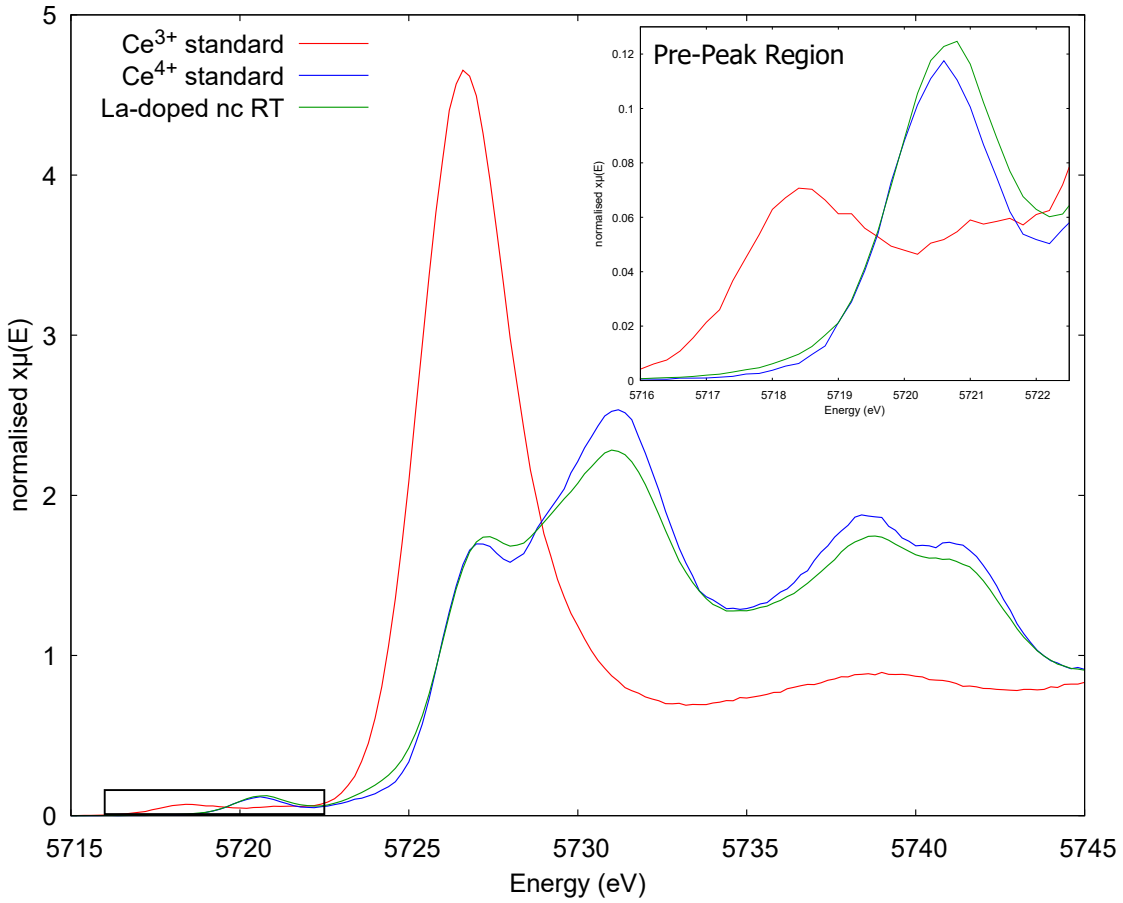

Figure 4.8: HERFD-XANES Ce L_3-edge spectra of La doped ceria nanocubes (green), Ce^{3+} standard (red), and Ce^{4+} standard (blue). The inset shows the pre-edge in greater detail.

The synthesised, non-doped, ceria nanocubes gave only 49% Ce^{4+} in comparison to the 7.5% La-doped ceria nanocubes, which gave 95% Ce^{4+} (XANES spectral comparison given in Appendix 3.2). The oxidation of the Ce in the ceria nanocubes, when doped, are similar to that of the non-doped ceria nanocubes after thermal treatment at 450 °C (96%).

When comparing La-doped with un-doped ceria nanocubes another consideration is the sample preparation. Although there is not enough data to determine what effect, if any, the way in which the sample is prepared, such as a pellet from a liquid or powder (see Table 4.1), it should be a consideration when discussing discrepancies or differences between the samples. Ideally, with more time, this would have been investigated further, and/or sample preparation would be made consistent.

4.3.3.2 Ex-situ Thermally Treated La-doped Nanocubes

The 7.5% La-doped ceria nanocubes underwent ex-situ thermal treatment at 450 °C to determine whether the removal of the surfactant would further affect the Ce oxidation. The thermal treatment resulted in an estimated 96% Ce^{4+} and 4% Ce^{3+}, therefore showing only a slight increase (1%) in oxidation of Ce (Figure 4.9). This is a similar estimated Ce^{4+} content to the non-doped ceria nanocubes ex-situ thermally treated at 450 °C. The remaining 4% Ce^{3+} may be an irreversible feature within the structure due to microstructural features which form during the synthesis, or could possibly be oxidised with a higher temperature thermal treatment, or a higher doping concentration.

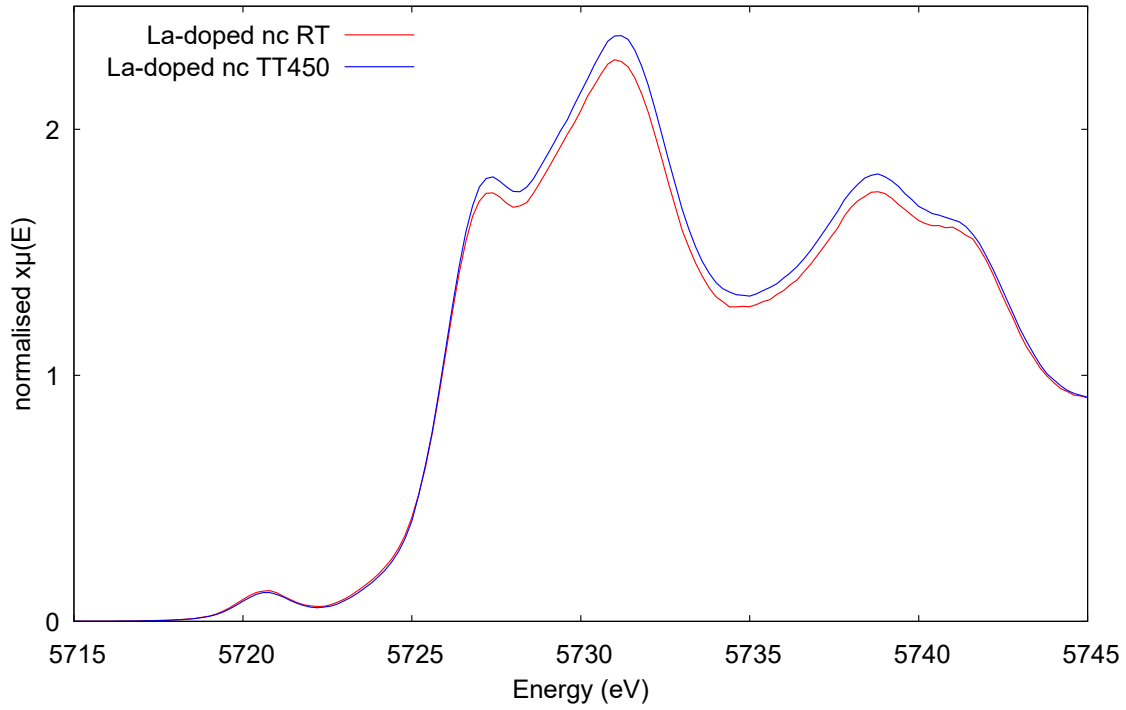

Figure 4.9: HERFD-XANES Ce L_3-edge spectra of La doped ceria nanocubes at room temperature (blue), and thermally treated at 450 °C (red).

4.3.4 Aerogel Nanocomposites

4.3.4.1 Weight Loading

Two aerogels of different weight loadings (2% and 5% of ceria nanocubes) were analysed via HERFD-XANES, Figure 4.10. Here it can be seen that the 5% weight loading is mostly Ce^{4+} (estimated 86%) with a small percentage of Ce^{3+}(14%), while the 2% weight loading is almost completely oxidised (∼100%). This is a fairly noticeable difference in oxidation state which is likely due to variances in the synthesis process of the ceria nanocubes. Although the same synthesis process was used, the resulting nanoparticles could have formed in different shapes and sizes, which will inherently affect the oxidation state and surface chemistry. Due to the scaling of the synthesis process, only small quantities of the nanoparticles can be synthesised at a time, therefore to achieve the desired weight loading into the aerogel, nanoparticles from multiple syntheses are used. For the higher weight loading of 5% there were more samples used than for 2% to get the desired loading. As the synthesis process is not accurately reproducible, although most successfully produce nanocubes, some are not as successful and result in a variety of different sized and shaped nanoparticles. Where a smaller number of synthesis products are used for the 2% weight loading, any issues with one of the synthesis will give a larger overall effect, in comparison, where a larger number of synthesis products are used, any issues with one will have less of an overall effect. There are other factors to consider to aid in explaining the cause of the oxidation state difference, including the effect of nanocube distribution within the aerogel, and also how loading affects the supercritical drying process.

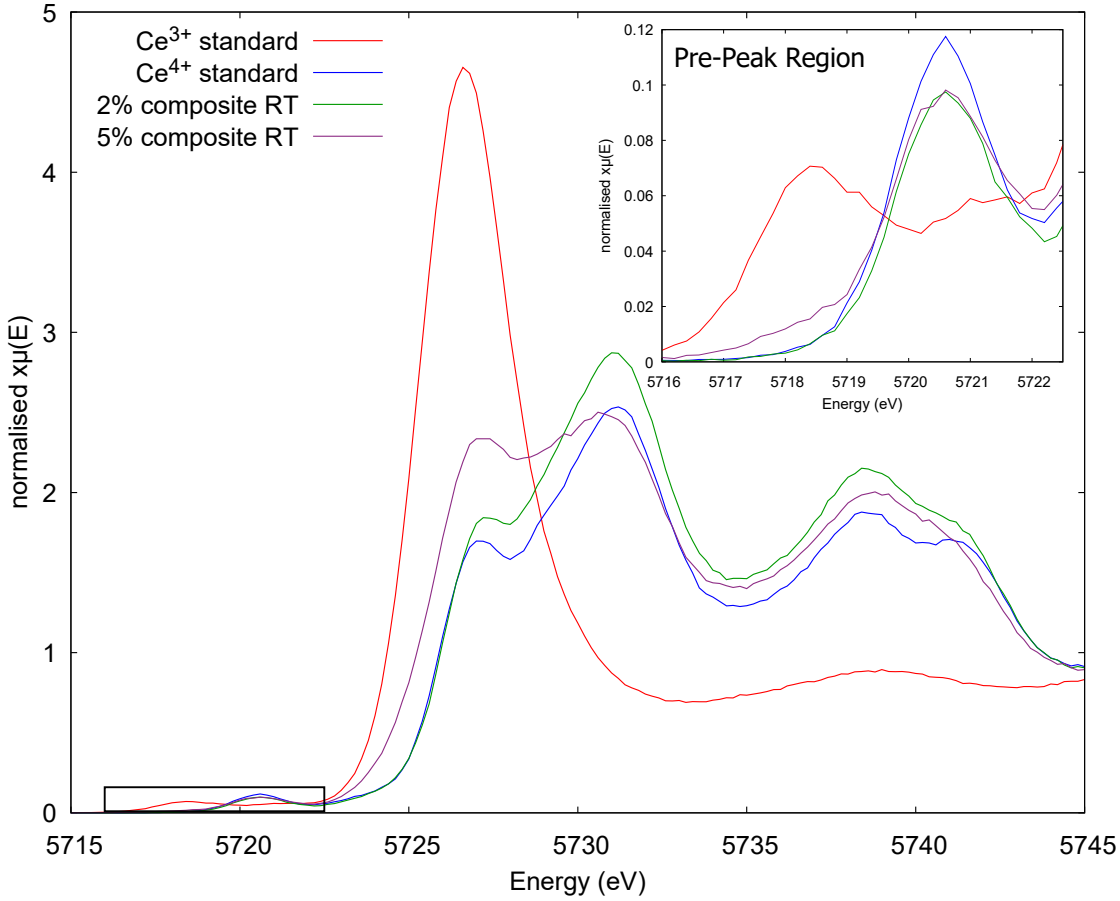

Figure 4.10: HERFD-XANES Ce L_3-edge spectra of 2% ceria nanocubes in aerogel (green), 5% ceria nanocubes in aerogel (purple), Ce^{3+} standard (red), and Ce^{4+} standard (blue). The inset shows the pre-edge in greater detail.

4.3.4.2 Ex-situ Thermally Treated Aerogel

Aerogel is used as a host matrix/supporting medium, which aids in preventing aggregation of the nanoparticles. When ex-situ thermal treatment is used to remove the surfactant, without aggregation, a higher percentage of the Ce^{3+} should be oxidised to Ce^{4+}. The 5% weight loaded ceria nanoparticles in aerogel were thermally treated at 450 °C, and also at 750 °C to determine whether higher temperatures will further oxidise the nanoparticles. As ex-situ thermal treatments are conducted in air, e.g. in the presence of O_2, some level of oxidation will occur naturally during this process, however this may differ between the different weight loadings.

Figure 4.11 presents the HERFD-XANES spectra for the untreated and thermally treated 5% Ce in aerogel, showing an increase in oxidation with thermal treatment. Untreated, the ceria is a mixture of oxidation states with 86% Ce^{4+}, where after thermal treatment at 450 °C this increases to ∼99%, with a further increase to ∼100% after thermal treatment at 750 °C.

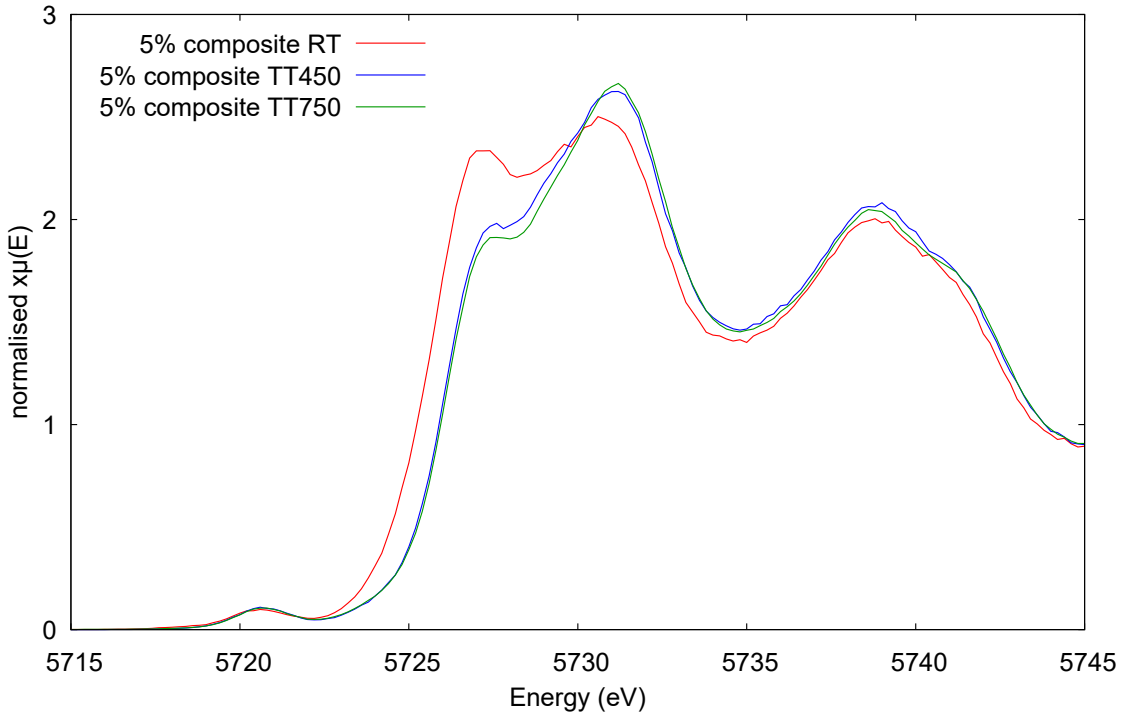

Figure 4.11: HERFD-XANES Ce L_3-edge spectra of 5% ceria nanocubes in aerogel untreated [RT] (blue), ex-situ thermally treated at 450 °C [TT450] (red), and ex-situ thermally treated at 750 °C [TT750] (green).

4.3.5 Conclusion

The capacity of metal oxides for oxidation/reduction is dependent on extrinsic variables, such as chemical composition and supporting substrates. Understanding these extrinsic variables is therefore essential for progressing in the use of oxides as catalysts. In this work a static HERFD-XANES study of the oxidation state of Ce within ceria nanocubes, 7.5% La-doped ceria nanocubes, and ceria nanocubes dispersed in a silica aerogel matrix, both before and after thermal treatment to remove the surfactant, was conducted.

Untreated ceria nanocubes present a fairly even mixture of Ce^{4+}/Ce^{3+}, where thermal treatment of the nanocubes, and use of La as a dopant increase the percentage of Ce^{4+} significantly, showing how the change in chemical composition affects the oxidation of the material. Similarly, the use of silica aerogel as a supporting substrate, preventing aggregation of the nanocubes, also increase the percentage of Ce^{4+}. These values are summarised in Table 4.2.

Table 4.2: Estimated percentage ratio of Ce^{4+}/Ce^{3+} species within the ceria nanocubes, 7.5% La-doped ceria nanocubes, and aerogel composites, both untreated (ambient) and thermally treated at 450 °C or 750 °C.

	Thermal Treatment	Ce^{4+}	Ce^{3+}
Ce nanocubes	-	52%	48%
	450 °C	96%	4%
La-doped Ce nanocubes	-	95%	5%
	450 °C	96%	4%
2% Ce in aerogel	-	∼100%	∼0%
5% Ce in aerogel	-	86%	14%
	450 °C	99%	1%
	750 °C	∼100%	∼0%

4.4 In-situ Measurements

4.4.1 Standard Ce^{4+}

The same CeO_2 standard (Ce^{4+}) used for the static measurements was also prepared in a capillary to test the temperature and gas flows of the in-situ set-up. The maximum temperature used for these measurements was 400 °C, as capillaries comprising Kapton, a polyimide, are unstable above this temperature. An N_2 gas flow was used to flush all air out of the capillary due to the dangers of the H_2/O_2 gas mixture igniting at high temperatures.

Firstly the Ce^{4+} standard was flushed with a flow of N_2 at 20 SCCM (Standard Cubic Centimetres per Minute) for 10 minutes and a measurement taken at ambient room temperature. The resulting spectrum, when compared to the static (pellet) measurement of the standards, gave an estimated 93% Ce^{4+} and 7% Ce^{3+} (XANES comparison given in Appendix 3.3). As a Ce^{4+} standard, the spectrum should theoretically be identical to the static measurement for the same material. The most likely reason for some of the Ce being reduced to Ce^{3+} is the flow of N_2. With a constant flow of gas over the sample, it is possible to remove some of the more energetically removable oxygen from the surface of the CeO_2.

The gas flow was then changed to H_2 (20 SCCM) and the Ce^{4+} standard heated to 400 °C at roughly 1 °C/s, which should cause the Ce^{4+} to reduce to Ce^{3+} for surface sites. The resulting spectrum, Figure 4.12, gave an estimated 91% Ce^{4+} and 9% Ce^{3+}, which is a 2% reduction from the room temperature measurement. The capillary was then flushed with N_2 for 10 minutes and the gas changed to O_2. The resulting spectrum gave an estimated 92% Ce^{4+} and 8% Ce^{3+}, which is a 1% oxidation from the previous measurement. The capillary was then again flushed with N_2 and the temperature reduced to ambient over the course of 1 hour, where a further measurement was taken. After the temperature was reduced to ambient, restoring the original conditions, the resulting spectrum gave an estimated 95% Ce^{4+} and 5% Ce^{3+}, which is slightly higher than the original percentage of Ce^{4+}.

A summary of the oxidation state percentages throughout the in-situ measurements of the CeO_2 standard is given in Table 4.3.

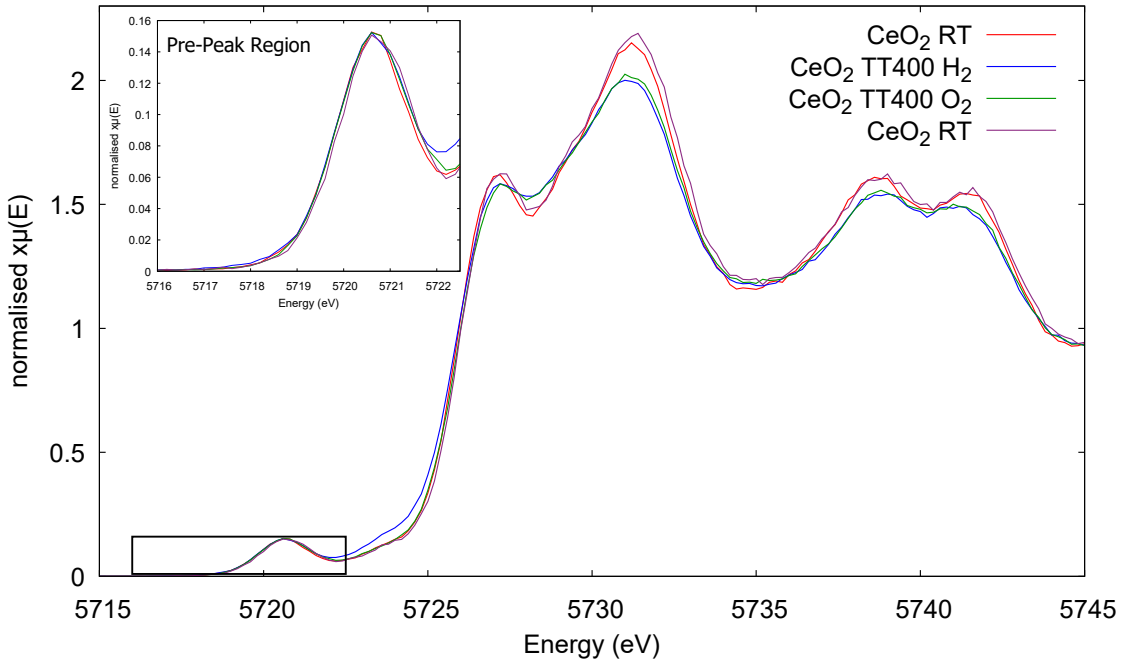

Figure 4.12: HERFD-XANES Ce L_3-edge spectra of the Ce^{4+} standard at room temperature under N_2 (red), at 400 °C under H_2 (blue), at 400 °C under O_2 (green), and at room temperature (after) under N_2 (purple). The inset shows the pre-edge in greater detail.

Table 4.3: Estimated percentage ratio of Ce^{4+}/Ce^{3+} species within the CeO_2 standard prepared in a capillary, and placed under a flow of gas at 20 SCCM.

CeO_2 standard	Gas flow	Ce^{4+}	Ce^{3+}
Ambient (before)	N_2	93%	7%
400 °C	H_2	91%	9%
400 °C	O_2	92%	8%
Ambient (after)	N_2	95%	5%

4.4.2 Impregnated quartz wool - Nanocubes

Two samples of ceria nanocubes, produced from the same syntheses mixtures, were analysed using two in-situ programs. The first program (in-situ program 1) involved reduction/oxidation steps at increasing temperatures: 150 °C, 275 °C, and 400 °C, while the second (in-situ program 2) looked more closely at reducibility at 275 °C and 400 °C, where each reduction/oxidation step was followed with another reduction step before increasing the temperature. For in-situ program 1, the ceria sample used was sample A, and for in-situ program 2 was sample B.

4.4.2.1 In-Situ Program 1, Sample A

The capillary was flushed for 10 minutes with N_2 gas, flowing at 20 SCCM, between changes of the gas type. Figure 4.13 gives the HERFD-XANES Ce L_3-edge spectra for the synthesised ceria nanocube for in-situ program 1, showing the initial measurements at ambient temperature and 150 °C. Here, there is a clear indication that the nanocubes reversibly reduce at 150 °C, evidenced by the increase in Ce^{3+} (48% $\rightarrow$ 72%) when H_2 is passed over the nanocubes, and a decrease in Ce^{3+} (72% $\rightarrow$ 56%) when O_2 is passed over the nanocubes. There appears almost complete reversibility of this reduction, with the estimated percentage of Ce^{3+}/Ce^{4+} returning close to those calculated for the ceria nanocubes at ambient temperature (See Table 4.4).

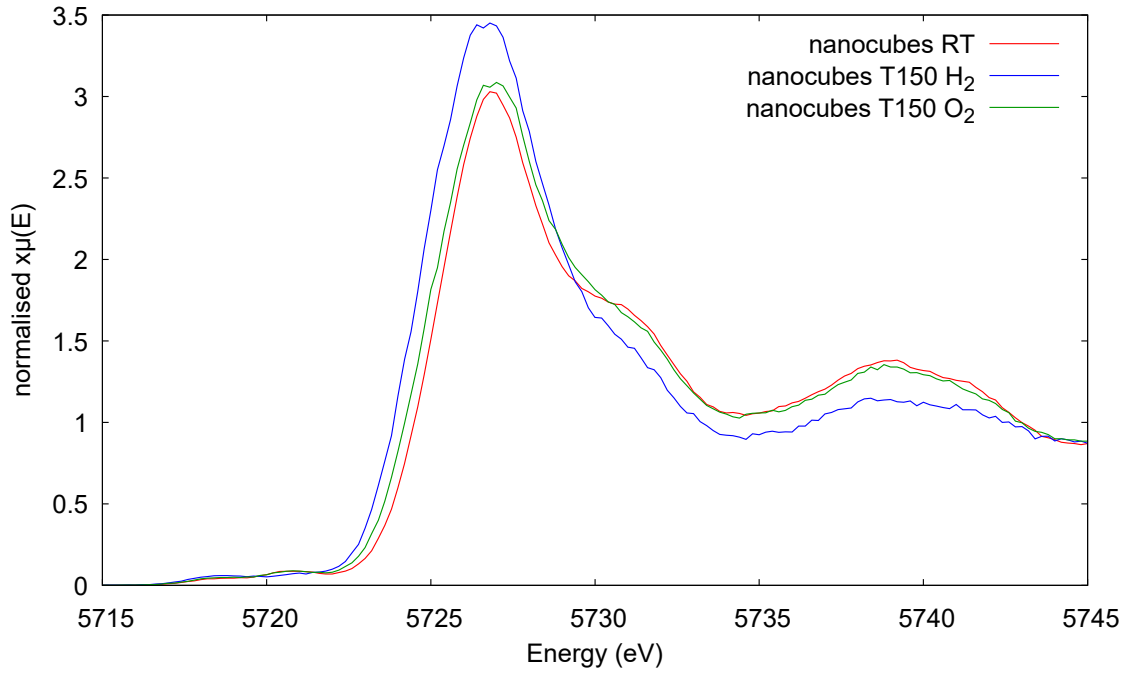

Figure 4.13: HERFD-XANES Ce L_3-edge spectra of the ceria nanocubes at room temperature under N_2 (red), at 150 °C under H_2 (blue), and at 150 °C under O_2 (green).

The next step was to increase the temperature to 275 °C under H_2, which resulted in partial re-reduction (69% Ce^{3+}) of the nanocubes, which is a reduction to a lesser extent than at 150 °C (72% Ce^{3+}). The XANES spectra showing this change can be found in Appendix 3.4. Once reduced, the nanocubes were oxidised at 275 °C with O_2, which did not occur instantaneously, but in fact was gradual over the course of 1 hour and 40 minutes, which can be seen in Figure 4.14. After 1 hour 40 minutes, the oxidation states stabilise with an estimated 96% Ce^{4+} oxidation, much higher than the 44% Ce^{4+} at 150 °C after oxidation, and the original ambient measurement of 49% Ce^{4+}.

The reason for this change in oxidation is most likely due to the removal of the oleic acid, which occurs due to the decomposition of the thermally labile oleic acid. This is supported by the process happening over a period of time. With the surfactant removed, the nanocube is more readily able to oxygenate, resulting in a higher percentage of Ce^{4+}. This does also have the implication that the nanocubes could have changed shape and/or suffered aggregation without the surfactant stabilising the meta-stable cubic morphology; this would however have to be further investigated, and is past the scope of this investigation.

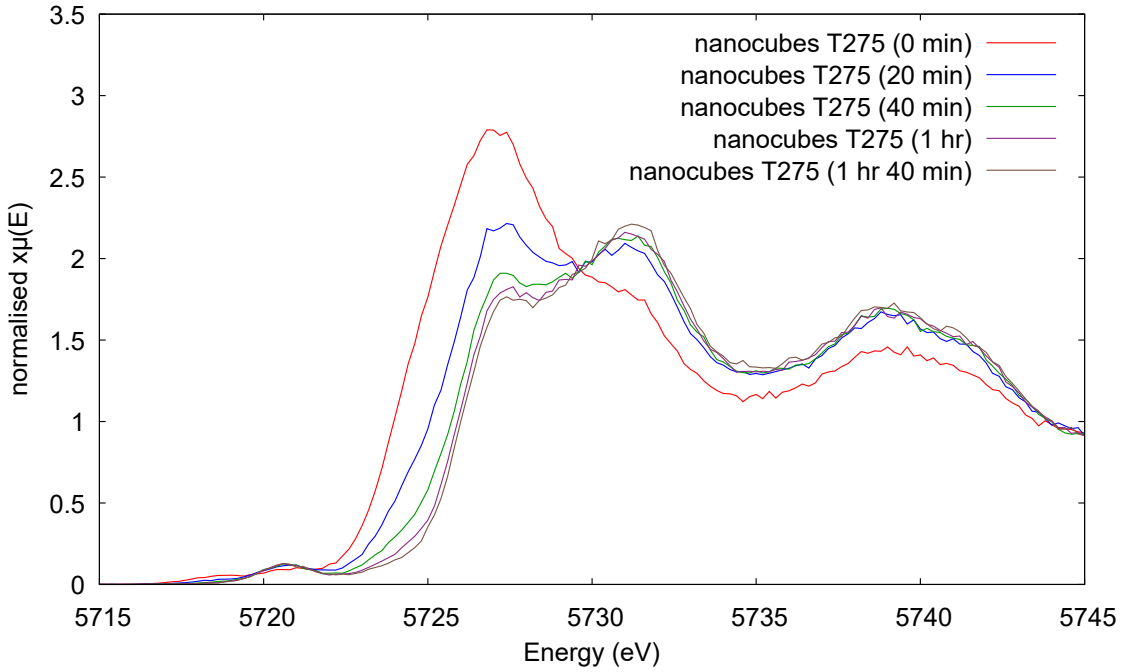

Figure 4.14: HERFD-XANES Ce L_3-edge spectra of the ceria nanocubes at 275 °C under O_2, showing the gradual oxidation at approximately 0 minutes (blue), 20 minutes (red), 40 minutes (green), 1 hour (purple), and 1 hour 40 minutes (brown).

The gas was then changed to H_2 and the temperature of the nanocubes increased to 400 °C to re-reduced the nanocubes, Figure 4.15. The reduction was shown to be partially reversible, with 33% Ce^{3+} in comparison to the 4% Ce^{3+} after oxidation at 275 °C. The nanocubes were then re-oxidised with O_2, resulting in 97% Ce^{4+}. The gas was changed to N_2 and the temperature reduced to ambient which surprisingly increased the oxidation to 99% Ce^{4+}. This could be due to a variety of factors such as temperature effects. At raised temperatures the atoms have a higher energy, allowing freer movement and could potentially introduce thermal ellipsoids, which is less evident at ambient temperature.

Table 4.4 contains a summary of the estimated percentage oxidation states for Ce within the ceria nanocubes at each stage of the program, calculated from the HERFD-XANES Ce L_3-edge spectra, using the standards within the Athena software. Here, it is clearly seen the notable increase in oxidation after 275 °C, and the effect on the reducibility of the nanoparticle.

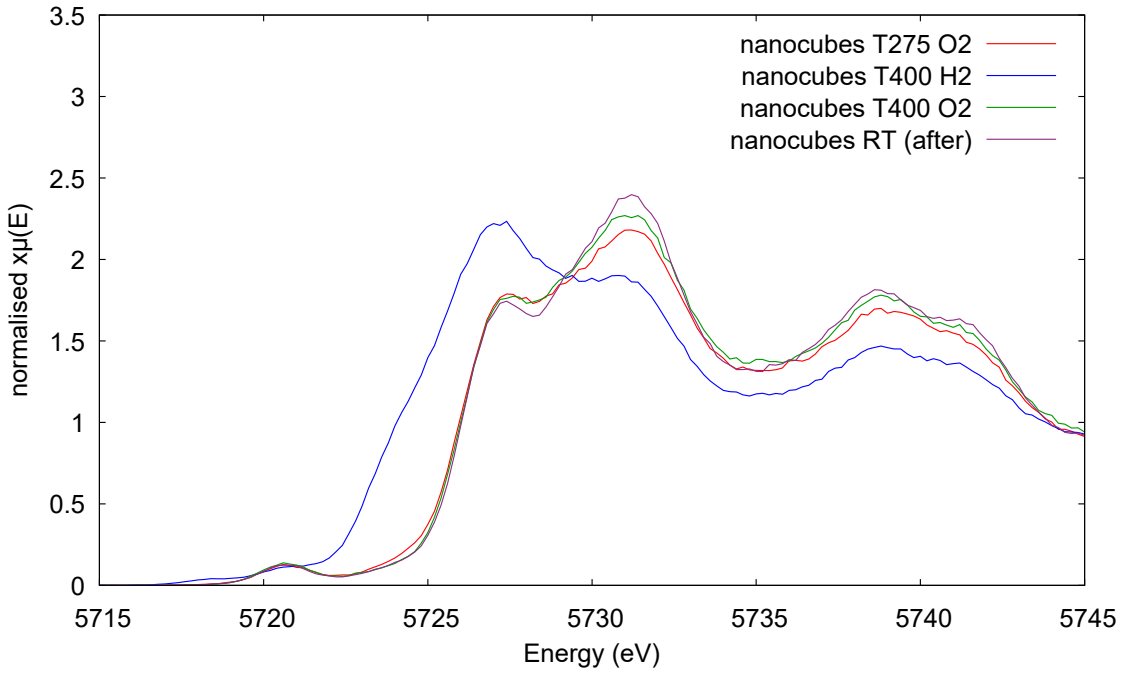

Figure 4.15: HERFD-XANES Ce L_3-edge spectra of the ceria nanocubes at 275 °C under O_2 (red), at 400 °C under H_2 (blue), at 400 °C under O_2 (green), and at ambient temperature under N_2 (purple).

Table 4.4: Estimated percentage ratio of Ce^{4+}/Ce^{3+} species within the ceria nanocube impregnated quartz wool prepared in a capillary (Sample A), and placed under a flow of gas at 20 SCCM.

Ceria nanocubes	Gas flow	Ce^{4+}	Ce^{3+}
Ambient (before)	N_2	52%	48%
150 °C	H_2	28%	72%
150 °C	O_2	44%	56%
275 °C	H_2	31%	69%
275 °C	O_2	96%	4%
400 °C	H_2	67%	33%
400 °C	O_2	97%	3%
Ambient (after)	N_2	99%	1%

4.4.2.2 In-Situ Program 2, Sample B

This in-situ program (2) was used to more closely study the reducibility of the ceria nanocubes at higher temperatures. At 275 °C the surfactant is removed from the nanoparticles, leaving the surface fully exposed and active to oxidation; however this could have negative effects on the morphology and reducibility of the nanoparticles. Oxidation seems to be more energetically favourable than reduction and without the protection of the oleic acid the reduction is likely to require additional energy to reduce the nanoparticles after oxidation.

Following the capillary being flushed with N_2 gas, and an ambient measurement taken, the gas was switched to H_2 and the temperature raised to 275 °C for reduction of the nanoparticles. This gave a reduction from 74% Ce^{4+} to 60% Ce^{4+}, which is a similar percentage reduction (∼13/14%) in comparison to program 1; with the temperature increasing from 150 °C under O_2. The actual percentage of Ce^{4+} however is much higher (60% in comparison to 31%) so it is practically speaking less reduced. As discussed in the static measurements section, there is already a difference between the initial measurements of samples A and B, so some differences are expected. The HERFD-XANES Ce L_3-edge spectra can be found in Appendix 3.5.

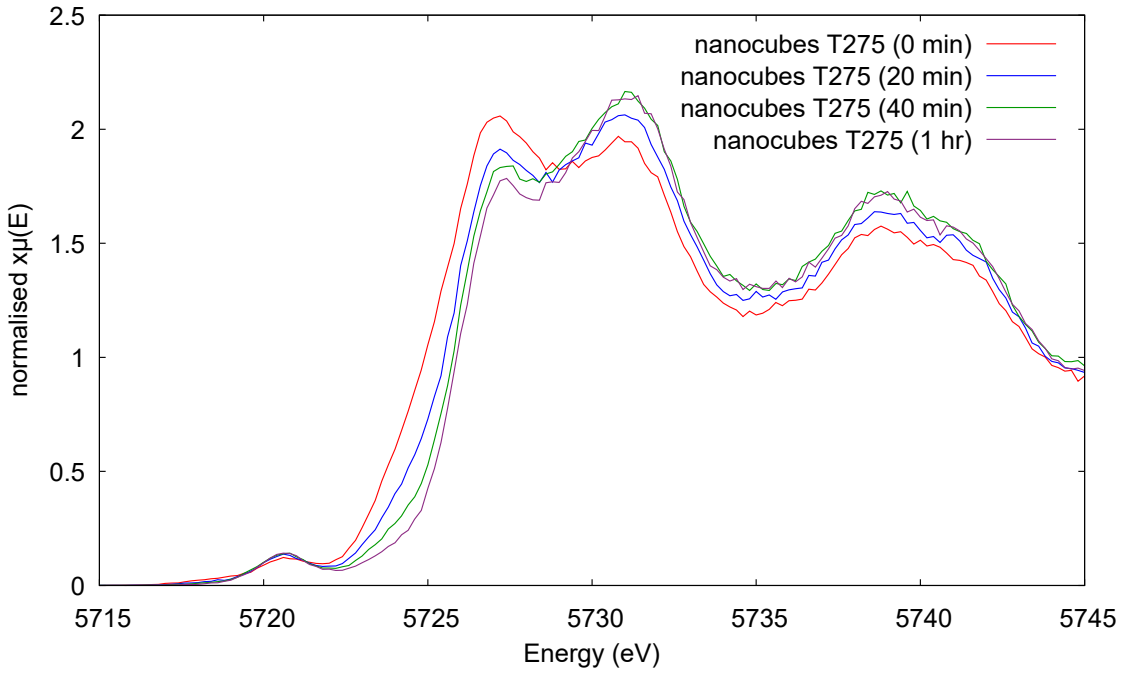

Figure 4.16: HERFD-XANES Ce L_3-edge spectra of the ceria nanocubes at 275 °C under O_2, showing the gradual oxidation at approximately 0 minutes (red), 20 minutes (blue), 40 minutes (green), and 1 hour (purple).

As observed with in-situ program 1, oxidation at 275 °C is gradual, occurring over the course of more than an hour, as presented in Figure 4.16. This process stabilises with an estimated 93% Ce^{4+}, which is similar to that previously measured in in-situ program 1 (96%). This is again due to the removal of the oleic acid from the surface, which allows full access to the surface of the nanoparticles, and a larger quantity of the vacancies are available to be filled, resulting in a higher percentage of Ce^{4+}. An observation made here is that the oxidation at 275 °C for both in-situ programs is gradual, where at 150 °C and 400 °C is fairly immediate in comparison. This is due to the oleic acid decomposing gradually: At 150 °C the temperature is too low for any decomposition to take place and at 400 °C it occurs very quickly.

After oxidation at 275 °C, the gas was returned to H_2 for re-reduction of the nanoparticles; however no evidence of reduction was observed, remaining with 93% Ce^{4+}, Figure 4.17 / Appendix 3.6. This is not entirely unexpected as introducing oxygen is more energetically favourable than removing oxygen, therefore, for reduction to occur more energy needs to be introduced. Consequently increasing the temperature to 400 °C (thermal energy), should aid in reduction, which is the effect observed, presenting a partially reversible process. Figure 4.17 shows how temperature increase gives enough energy to the nanoparticles, allowing a reduction of over 20%.

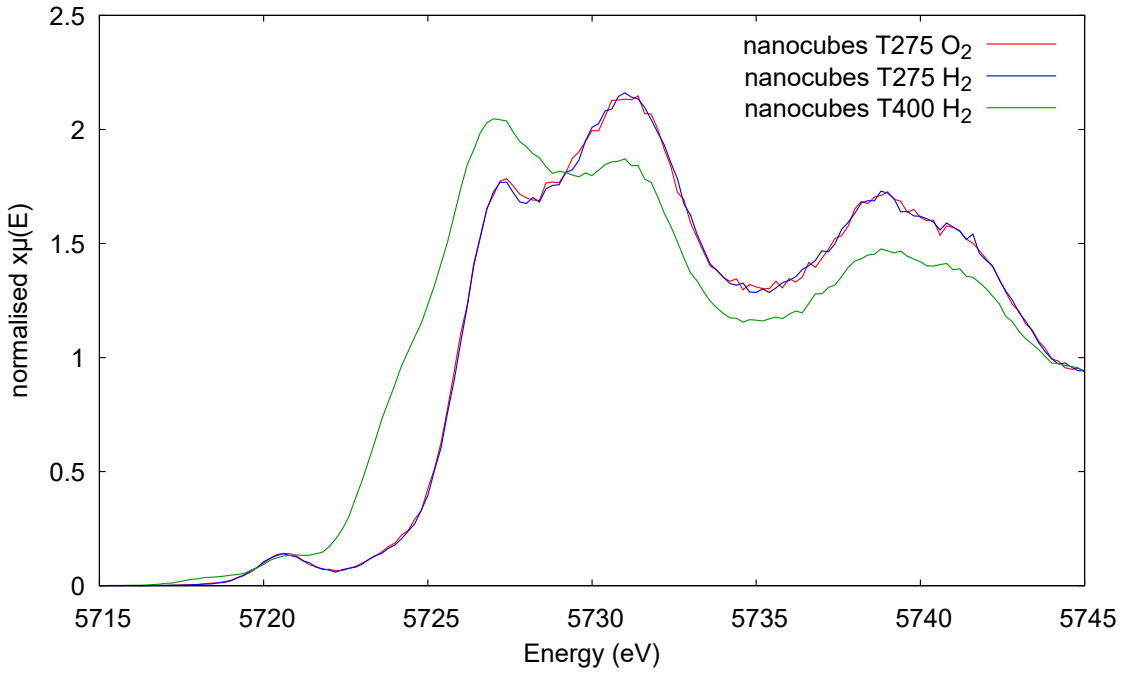

Figure 4.17: HERFD-XANES Ce L_3-edge spectra of the ceria nanocubes at 275 °C under O_2 (red), under H_2 (blue), and under H_2 after heating to 400 °C (green).

The nanoparticles were oxidised at 400 °C, resulting in 94% Ce^{4+}, similar to that for in-situ program 1 (97%), then re-reduced under H_2 which gave a partial reduction to 88% Ce^{4+}; the HERFD-XANES Ce L_3-edge spectra can be seen in Figure 4.18. After re-reduction, the gas was switched back to N_2 and the temperature reduced to ambient (Appendix 3.7). Curiously, this caused oxidation of the nanocubes to 97% Ce^{4+}, a fairly substantial increase, which is a similar effect to what we had observed previously with in-situ program 1 and the CeO_2 in-situ standard to lesser extent. This could still be attributed to temperature and vibrational interference, however other causes can not be excluded.

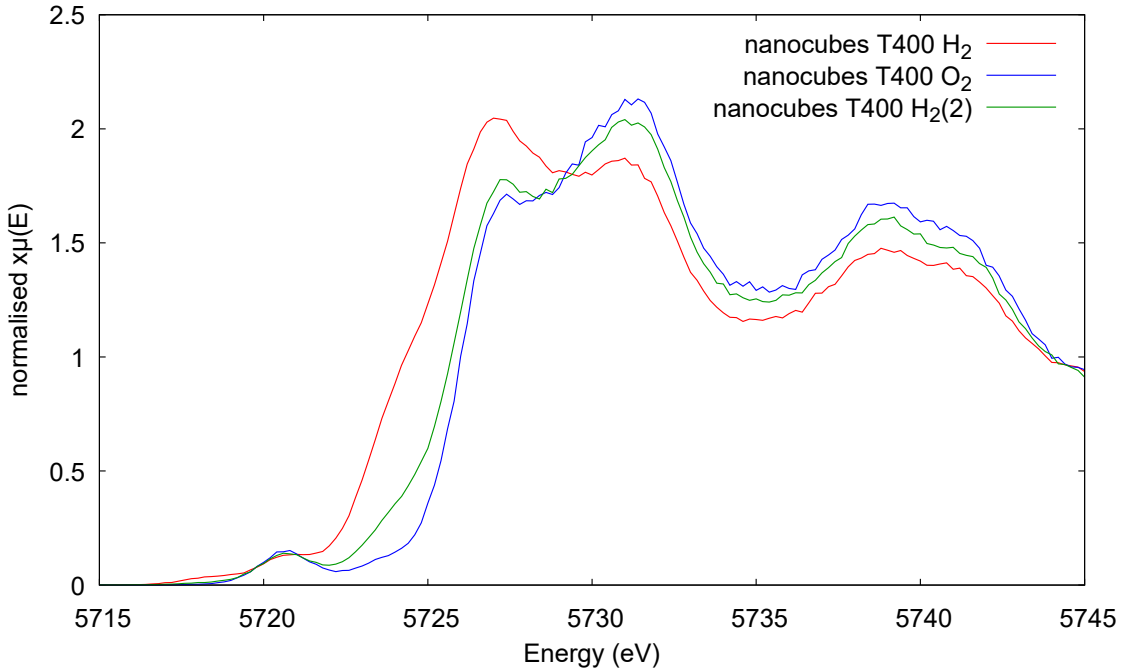

Figure 4.18: HERFD-XANES Ce L_3-edge spectra of the ceria nanocubes at 400 °C under H_2 (red), under O_2 (blue), and back under H_2 (green).

Table 4.5 contains a summary of the estimated percentage oxidation states for Ce within the ceria nanocubes at each stage of in-situ program 2, calculated from the HERFD-XANES Ce L_3-edge spectra, using the standards within the Athena software. Here, the notable increase in oxidation after 275 °C, attributed to the removal of the surfactant, can be observed, and the partial re-reducibility of the nanoparticle can be seen. It is evident that after oxidation at a certain temperature, more energy, thermal or otherwise, needs to be introduced for re-reduction of the nanoparticles to be practically significant.

Table 4.5: Estimated percentage ratio of Ce^{4+}/Ce^{3+} species within the ceria nanocube impregnated quartz wool prepared in a capillary (Sample B), and placed under a flow of gas at 20 SCCM.

Ceria nanocubes	Gas flow	Ce^{4+}	Ce^{3+}
Ambient (before)	N_2	74%	26%
275 °C	H_2	60%	40%
275 °C	O_2	93%	7%
275 °C	H_2	93%	7%
400 °C	H_2	71%	29%
400 °C	O_2	94%	6%
400 °C	H_2	88%	12%
Ambient (after)	N_2	97%	3%

4.4.3 Aerogel Nanocomposite

An aerogel nanocomposite comprising 5% ceria nanoparticles in SiO_2 aerogel was prepared in a capillary for in-situ measures. The measurements taken reflect the aspects of both in-situ programs 1 and 2 for the ceria nanocubes, where the temperature is increased in stages, at 150 °C, 275 °C, and 400 °C, while also incorporating the study into re-reducibility at 275 °C and 400 °C. This allows for a more efficient study of both the oxidation/reduction properties at temperatures below the removal of the surfactant and the re-reduction properties at higher temperatures.

Following the capillary being flushed with N_2 gas, and an ambient measurement taken, the gas was switched to H_2 and the temperature raised to 150 °C for reduction of the nanoparticles. This resulted in around a 10% reduction of the Ce^{4+} (74%→63%), a similar percentage reduction to that observed in the ceria nanocubes, however at a much higher oxidation value (i.e. 74%→63% Ce^{4+} instead of 49%→28% Ce^{4+}). The nanocomposite was then oxidised at 150 °C, resulting in 81% Ce^{4+}, which is a higher oxidation that the ambient measurement, and also a higher oxidation at 150 °C than seen for the ceria nanocubes. The HERFD-XANES Ce L_3-edge spectra for these measurements of the aerogel nanocomposite are presented in Figure 4.19.

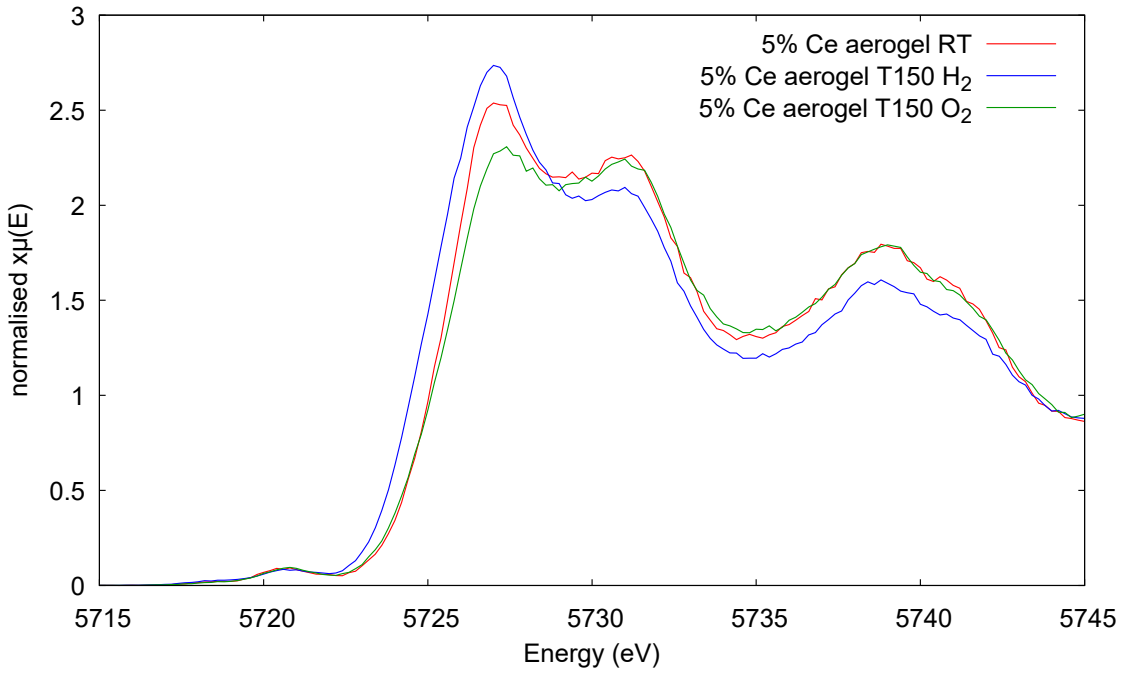

Figure 4.19: HERFD-XANES Ce L_3-edge spectra of the aerogel nanocomposite comprising 5% ceria nanoparticles in SiO_2 aerogel at room temperature under N_2 (red), at 150 °C under H_2 (blue), and at 150 °C under O_2 (green).

Following oxidation at 150 °C, the nanocomposite was reduced at 275 °C, giving an estimated 20% reduction; a similar percentage to that seen in the 150 °C reduction (62% in comparison to 63% Ce^{4+} respectively). This is a larger reduction in comparison to the ceria nanocubes which only reduced by an estimated 13% under the same conditions, however this occurred at a much lower oxidation (i.e. 81%→62% Ce^{4+} for the nanocomposite in comparison to 44%→31% Ce^{4+} for the nanocubes).

After reduction at 275 °C the nanocomposite was oxidised. In this case there are clear differences to the previous nanocube samples as the oxidation occurs mostly within the first 30 minutes, with oxidation occurring (to a lesser extent) up to 1 hour 30 minutes. This could be due to the oleic acid potentially being partially removed during the aerogel synthesis. The oxidation however is still attributed to the removal of the oleic acid on the surface of the nanoparticles. As the nanoparticles within the aerogel nanocomposite are already at a higher oxidation state (62% Ce^{4+}) than the ceria nanoparticles (31% Ce^{4+}), and the concentration of nanoparticles within the sample is much lower, the difference in oxidation between each measurement is smaller, but still notable. The HERFD-XANES Ce L_3-edge spectra showing the oxidation of the aerogel nanocomposite at 275 °C is given in Figure 4.20.

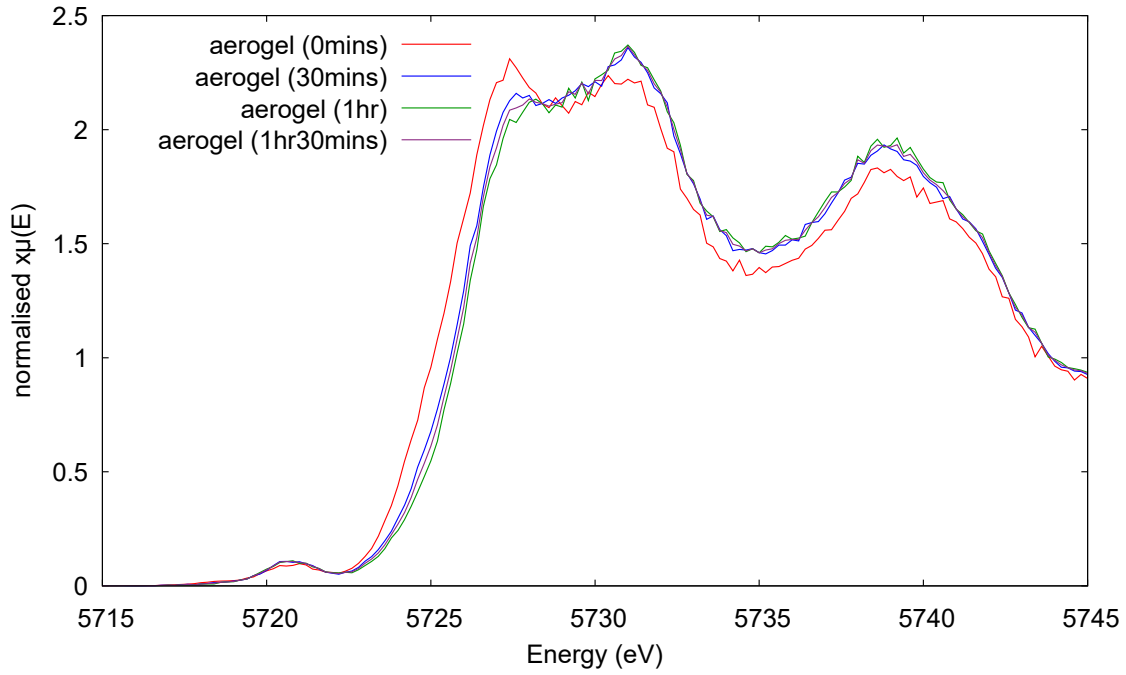

Figure 4.20: HERFD-XANES Ce L_3-edge spectra of the aerogel nanocomposite at 275 °C under O_2, showing the gradual oxidation at approximately 0 minutes (red), 30 minutes (blue), 1 hour (green), and 1 hour 30 minutes (purple).

Following oxidation, the nanocomposite was reduced at 275 °C to determine the re-reducibility of the nanoparticles within the aerogel matrix, without additional thermal energy. We observed an estimated 20% reduction (93%→73% Ce^{4+}) in the nanoparticles, presenting evidence that the oxidation is reversible, at least in part, at 275 °C without the requirement of additional energy. This suggests that the dispersion of nanoparticles within a host matrix, preventing aggregation of the nanoparticles, aids in stabilising the nanoparticles reduction/oxidation activity at higher thermal working conditions, after the removal of the surfactant. With the addition of thermal energy, increasing the temperature to 400 °C, the reduction is improved, with an additional ∼12% reduction to 61% Ce^{4+}.The HERFD-XANES Ce L_3-edge spectra showing the reduction of the nanoparticles within the aerogel nanocomposite at 275 °C and 400 °C under H_2 is given in Figure 4.21.

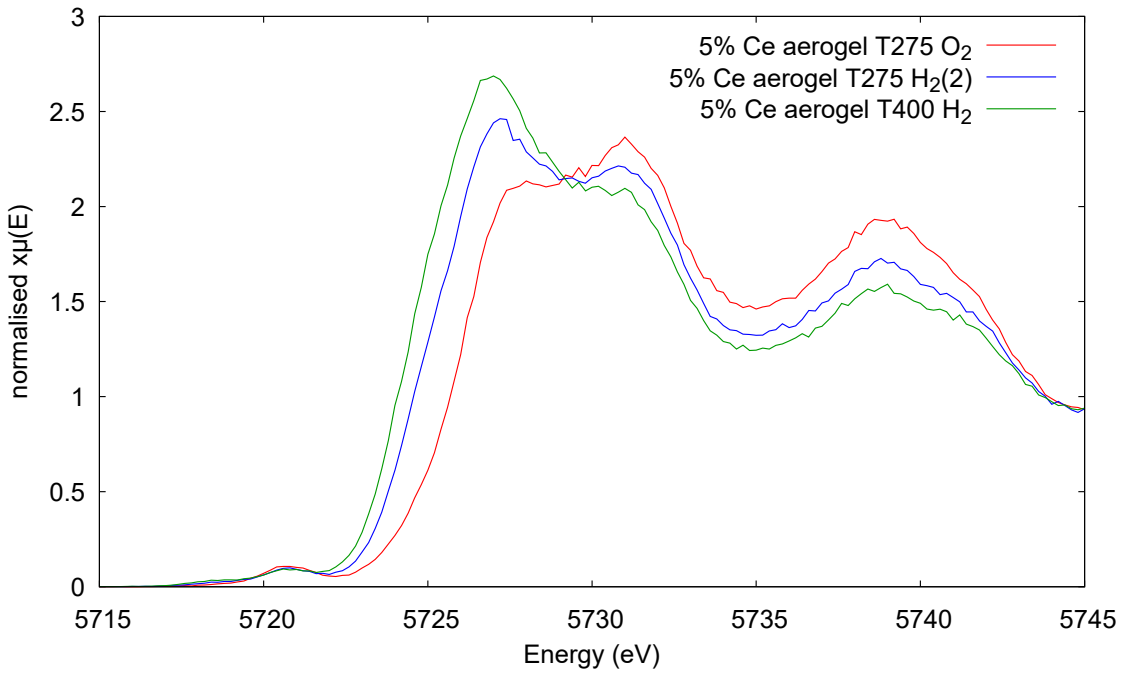

Figure 4.21: HERFD-XANES Ce L_3-edge spectra of the aerogel nanocomposite comprising 5% ceria nanoparticles in SiO_2 aerogel at 275 °C under O_2 (red), at 275 °C under H_2 (blue), and at 400 °C under H_2 (green).

The nanocomposite was oxidised at 400 °C under O_2, resulting in almost complete oxidation (∼99% Ce^{4+}), then re-reduced under H_2 by around 10% to 88% Ce^{4+}, Figure 4.22. This is a similar reduction to that seen for the ceria nanoparticles, which also gave 88% Ce^{4+}. The temperature was finally reduced to ambient under N_2 which, again, resulted in a slight increase in oxidation (95% Ce^{4+}). Comparing the final oxidation states to the starting oxidation states, at ambient temperature, within the aerogel nanocomposite, there is an estimated 20% increase in oxidation (76%→95% Ce^{4+}), which is similar to that seen for the nanocubes within in-situ program 2 (74%→97% Ce^{4+}).

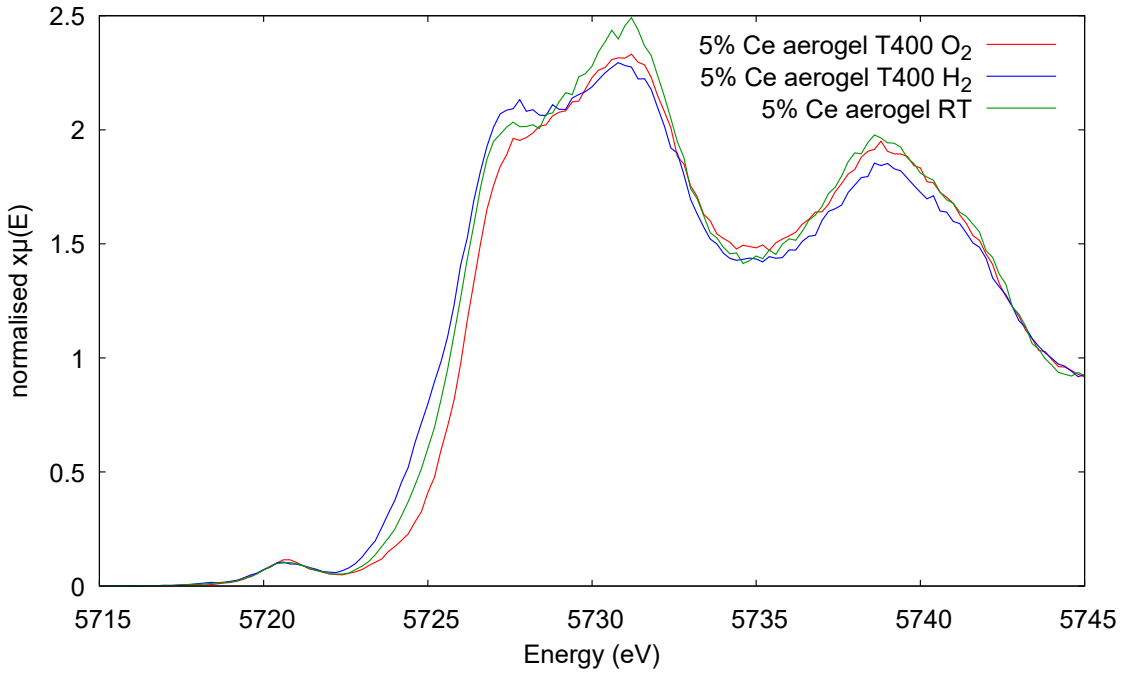

Figure 4.22: HERFD-XANES Ce L_3-edge spectra of the aerogel nanocomposite comprising 5% ceria nanoparticles in SiO_2 aerogel at 400 °C under O_2 (red), at 400 °C under H_2 (blue), and at ambient under N_2 (green).

Table 4.6 contains a summary of the estimated percentage oxidation states for Ce within the aerogel nanocomposite from these measurements, calculated from the HERFD-XANES Ce L_3-edge spectra, using the standards within the Athena software. Here, the notable increase in oxidation after 275 °C, attributed to the removal of the surfactant can be observed, and the improved re-reducibility of the nanoparticles in the nanocomposite, in comparison to the unsupported nanoparticles, can be seen.

Table 4.6: Estimated percentage ratio of Ce^{4+}/Ce^{3+} species within the 5% ceria nanocubes dispersed in aerogel. The sample was prepared in a capillary and placed under a flow of gas at 20 SCCM.

Nanocomposite	Gas flow	Ce^{4+}	Ce^{3+}
Ambient (before)	N_2	76%	24%
150 °C	H_2	63%	37%
150 °C	O_2	81%	19%
275 °C	H_2	62%	38%
275 °C	O_2	93%	7%
275 °C	H_2	73%	27%
400 °C	H_2	61%	39%
400 °C	O_2	99%	1%
400 °C	H_2	88%	12%
Ambient (after)	N_2	95%	5%

4.4.4 Discussion

When subjected to a concentrated radiation beam, the beam can cause some level of damage to the sample. This is commonly referred to as beam damage, and can cause different effects depending on the sample and intensity of the beam. A common effect seen for synchrotron radiation is the formation of point defects, which are known to occur in ceria [3]. In a study conducted by Winterstein el al [4], electron-beam damage from EELS resulted in a reduction of the oxide, which is due to the formation of oxygen vacancies and compensating Ce^{3+} defects. Therefore it is likely that some reduction within the ceria in this study will be a result of beam damage. However this will be a negligible amount and the oxidation steps should help to mitigate the effects of the beam damage.

In all samples, we observe an increase in oxidation state under N_2 after reducing the temperature back to ambient. The cause of this phenomenon is unknown, however there are some possible factors which could influence this. Intense ionising radiation can form trapped electrons within the subject lattice, which creates a non-stoichiometric structure. With greater thermal ellipsoids at elevated temperatures these electrons may be less 'trappable', however, when the temperature is reduced the effect is reduced, potentially causing more electrons to become trapped in the

structure. With proximity to the vacancies, these electrons could contribute to the charge increase on the cerium atoms.

Other theory, which is also related to the electrons, is the effect of polaron hopping [5]. Polaron hopping is a mechanism for electron transport which is prevalent at high temperature. At high temperatures this polaron hopping mechanism, along with higher vibration effects, could produce a masking effect on some of the oxygen. If the polaron is localised at an oxygen, its charge will attract the surrounding cerium atoms towards the oxygen, inducing a polarised state. This would effectively distort the charge on the oxygen, making it appear more positive, and therefore presenting as a 'vacancy'. When the temperature is lowered, there are less vibrational effects, and electrons travel by a band mechanism, which is a free movement of electrons. The effects of polaron hopping would no longer be present and the 'masked' oxygen would become visible to measurement, thus presenting higher oxidation. Another possibility is that, for some reason, the vacancies are more stable at higher temperatures. This would however need to be investigated further.

For catalysts to reduce/oxidise they need to form oxygen vacancies, a crucial parameter of which is energy. The oxygen formation energy needs to be as small as possible, but large enough to be energetically favourable to both create the vacancies and refill them. The electronic structure of the material is related to this ability, which has drawn wide interest to its study, and more specifically to ceria [6, 7, 8]. By analysing the oxidation state of the cerium under oxidation and reduction we are able to gain insight into how the formation and filling of oxygen vacancies evolve, and what effect temperature and removal of the surfactant has on this process.

The main concern with the stability of ceria nanoparticles as a catalyst is related to the surfactant used to control their growth. Working conditions will likely involve some level of thermal energy, so the ability to remain active at higher temperatures is crucial. Ceria nanocubes are the most reactive form of ceria nanoparticle, due to their more reactive {100} surface, forming with the use of a surfactant. This surfactant also prevents the aggregation of the nanoparticles, which would consequently reduce the active surface area. The surfactant, oleic acid, is an organic material, which is thermally labile and decomposes in air to CO_2 and water. This occurs at temperatures above $\sim$250 °C, which then gives way to potential aggregation. In an attempt to prevent aggregation the nanoparticles were separated by a supporting medium, silica aerogel, which should theoretically allow for continued activity at higher temperatures.

From the observations presented in this chapter, the aerogel was successfully able to increase the working temperature of the ceria nanoparticles. Notably, ceria in the aerogel nanocomposite was able to be re-reduced at 275 °C, after oxidation and without increasing the temperature, where the unsupported ceria nanocubes were unable to be. Oxidation is more energetically favourable in comparison to reduction, therefore reduction is improved by increasing the temperature of the ceria. With the ceria nanoparticles separated and supported in the aerogel, aggregation was prevented, allowing for the large surface area to be kept intact, and the surface oxygen available for reduction.

4.4.5 Conclusions

In this study, unsupported ceria nanoparticles, La-doped ceria nanoparticles, and ceria nanoparticles dispersed in a silica aerogel matrix were prepared and investigated using static and in-situ Ce L_3-edge HERFD-XANES, in order to observe the evolution of the ceria oxidation/reduction. The use of Lanthanum as a dopant had similar effects on the spectra to the use of ex-situ thermal treatment at 450 °C, increasing the oxidative state of the cerium. Dispersing the nanoparticles within a silica aerogel matrix prevented aggregation, improving the oxidation/reduction capacity of the ceria at higher temperatures, where the surfactant had been removed.

4.5 Future Work

With such success in measuring the oxidation and reduction of ceria in-situ, both unsupported and supported in aerogel, at a range of temperatures, the next step would be to take further measurements using the La-doped ceria nanoparticles. A new proposal for time at the Diamond Light Source I20 beamline is already under way, with the main aim of measuring the La-doped ceria nanocubes and nanocomposites, with future aims to do similar with different dopants.

References

[1] B. Ravel and M. Newville. ATHENA, ARTEMIS, HEPHAESTUS: Data Analysis for X-ray Absorption Spectroscopy using IFEFFIT. *Journal of Synchrotron Radiation*, 12:537–541, 2005.

[2] S. Liang, E. Broitman, Y. Wang, A. Cao, and G. Veser. Highly Stable, Mesoporous Mixed LanthanumCerium Oxides with Tailored Structure and Reducibility. *Journal of Materials Science*, 46:2928–2937, 2011.

[3] R. Sharma, P.A. Crozier, Z.C. Kang, and L. Eyring. Observation of Dynamic Nanostructural and Nanochemical Changes in Ceria-Based Catalysts during In-Situ Reduction. *Philosophical Magazine*, 84:2731–2747, 2007.

[4] J.P. Winterstein and C.B. Carter. Electron-Beam Damage and Point Defects Near Grain Boundaries in Cerium Oxide. *Journal of the European Ceramic Society*, 34: 3007–3018, 2014.

[5] J.J. Plata, A.M. Márquez, and J.F. Sanz. Electron Mobility via Polaron Hopping in Bulk Ceria: A First-Principles Study. *Journal of Physical Chemistry C*, 117 (28):14502–14509, 2013.

[6] F. Esch, S. Fabris, L. Zhou, T. Montini, C. Africh, P. Fornasiero, G. Comelli, and R. Rosei. Electron Localization Determines Defect Formation on Ceria Substrates. *Science*, 309:752–755, 2005.

[7] H.T. Chen, J.G. Chang, H.L. Chen, and S.P. Ju. Identifying the O_2 Diffusion and Reduction Mechanisms on CeO_2 Electrolyte in Solid Oxide Fuel Cells: a DFT + U Study. *Journal of Computational Chemistry*, 30(15):2433–2442, 2009.

[8] M. Nolan. Healing of Oxygen Vacancies on Reduced Surfaces of Gold-Doped Ceria. *Journal of Chemical Physics*, 130(14):144702, 2009.

Chapter 5

An MD Investigation into Protecting Mechanical Properties using Sacrificial Barriers

5.1 Introduction

Mechanical force applied to a nanomaterial can result in plastic deformation, which will irreversibly extinguish any desirable properties. It is therefore vital to understand the mechanical properties of functional nanomaterials, so the boundaries of working conditions, and improvement thereof, can be determined. For example, Huang *et al* showed that the intercalation of Li into SnO_2 nanowires, introduced considerable localized stress. This resulted in plastic deformation and pulverization of the material: 'such major mechanical effects plague the performance and lifetime of high-capacity anodes in lithium-ion batteries' [1]. With ceria being such an important catalytically functional nanomaterial it has been the subject of inense scrutiny, with remarkable properties such as high surface activity [2], oxygen transport [3], and redox chemistry [4]. For example, ceria, in nanoform, has been shown to be a highly active catalyst; CeO_2 nanocubes can catalyse CO to CO_2 at room temperature in contrast to the parent bulk material [5]. Currently, ceria is used as a component of three-way automobile exhaust catalysts [6] and if ceria is to be replaced by its nanostructured counterpart, it must resist damage under the harsh environmental conditions associated with its operation, such as extremes of temperature, impact, friction and wear.

Current composite catalysts include features such as expanding mats and enclosures to protect the active material in working conditions [7]. The design of the composite catalyst can therefore be informed by considering the sacrificial ability of some of the component materials of the composite catalyst. An additional consideration is that many nanosystems are comprised of multiple nanomaterials, for example, nanocomposites. Here, it is important to understand not only how each component responds individually to stress, but also in combination. For example, if stress is imposed upon a core-shell system, how does the system partition the stress? Does the shell accommodate some of the strain and then impose the residual stress upon the inner core? And if the shell is 'harder' than the core, would the partition of stress be different to the reverse? Such understanding will reveal insight into 'sacrificial' and protective nanomaterials.

Stress can originate from a variety of sources in addition to mechanical load, operational vibration, or friction. For example, the differences in the thermal expansion coefficients of two interfaced materials will induce stress when a system is exposed to high temperature fluctuations. Similarly, intercalation and substitution cause localised lattice expansion that will impart stress on neighbouring regions that have not (yet) any intercalated ions [8].

Some insight into this area is already available. In particular, during the mechanical testing of nanomaterials, the anvils, used to communicate pressure upon the test material, will likely themselves deform [9]; a soft anvil, such as a metal will likely suffer greater deformation than a hard anvil, such as diamond [10]. Accordingly, we question how anvil hardness influences the catalytic and mechanical properties, and deformation behaviour of a material measured using such anvils. The relationships between the mechanical properties and nanostructure have been investigated experimentally using nano-indentation [11], Transmission Electron Microscopy (TEM) [12], and Atomic Force Microscopy (AFM) [13]. Characterising the structural changes and time-resolved stress-strain properties is challenging experimentally [14]. Computer simulation can therefore play a key complementary role to gain insight into these changes at the atomistic level and track their progress.

Notwithstanding its remarkable properties and diverse range of applications, there is limited information pertaining to the mechanical properties of nanoceria reported in the open literature. This does not mean the mechanical strength of nanoceria has gone entirely unconsidered, though the research is not always in agreement. For example, simulating uniaxial force, Caddeo *et al* [15] determined a yield strength of 12 GPa at 0.20 strain for a ceria nanocube. In contrast, also using simulated uniaxial force, cubic nanoporous ceria reported by Sayle *et al* determined a yield strength range of 5.4-13.8 GPa at 0.06-0.08 strain, dependant on axial direction [16]. Although the reported yield strengths are of a similar magnitude, the strain of the porous material is less than half that of the nanocube. Comparatively the bulk material, measured via DFT was reported by Sakanoi *et al* has a yield strength 22.7 GPa at 0.09 strain [17].

The influence of the anvil structure such as the surface roughness [18] and indenter shape [19] have been investigated and shown to influence the measured strength of the subject material. This highlights the importance of including shape and surface defects in computational simulations. If a material contains surface steps and deformations it will have an impact on the measured hardness.

In this Chapter, and the following, we simulate a ceria nanocube under uniaxial compression between fixed and deformable anvils, and use MgO and BaO as systems representative of hard and soft anvils respectively. We explore the deformation within the nanoceria test material and deformation suffered by the anvils, as well as the effect this may have on the catalytic activity.

5.2 Method

5.2.1 Potential Models

The simulations presented in this Chapter were performed using Molecular Dynamics (MD) simulation utilising the Born model of the ionic solid. The energy of the system, E, is given by Equation 5.1.

$$E(r_{ij}) = \sum_{ij} \frac{Q_i Q_j}{4\pi\varepsilon_0 r_{ij}} + \sum_{ij} A \exp\left(\frac{-r_{ij}}{\rho}\right) - C r_{ij}^{-6} \tag{5.1}$$

Where the first term represents the Coulombic interaction between ions, i and j, of charge Q_i and Q_j at a distance of r_{ij}. The second two terms represent the Buckingham form with the potential values [20, 15] presented in Table 5.1 along with the atom mass and charges. All ion-ion interactions were set to zero.

Table 5.1: Buckingham potentials used for the MD simulations within this chapter, along with the atom mass and charges.

Atom i	Atom j	A/eV	ρ/Å	C/eV Å^{-6}
Ce	O	1986.83	0.3511	20.40
Mg	O	1428.50	0.2945	0.00
Ba	O	931.70	0.3939	0.00
O	O	22764.00	0.1494	27.88

Atom	Mass	Charge
Ce	140.12	4.00
Mg	24.30	2.00
Ba	137.33	2.00
O	16.00	-2.00

5.2.2 Atomistic Models

Simulated amorphization and recrystallization [21] was used to generate atom-level models of the anvils. This technique was used to enable microstructural features to evolve during the crystallisation step, such like the features which occur naturally in synthesis. The structural models are therefore more realistic in that they capture the structural features observed experimentally. These include: surface steps, vacancies (Figure 5.1), interstitials, dislocations, and grain-boundaries. This is important as the mechanical properties of a material are governed by its microstructure [22].

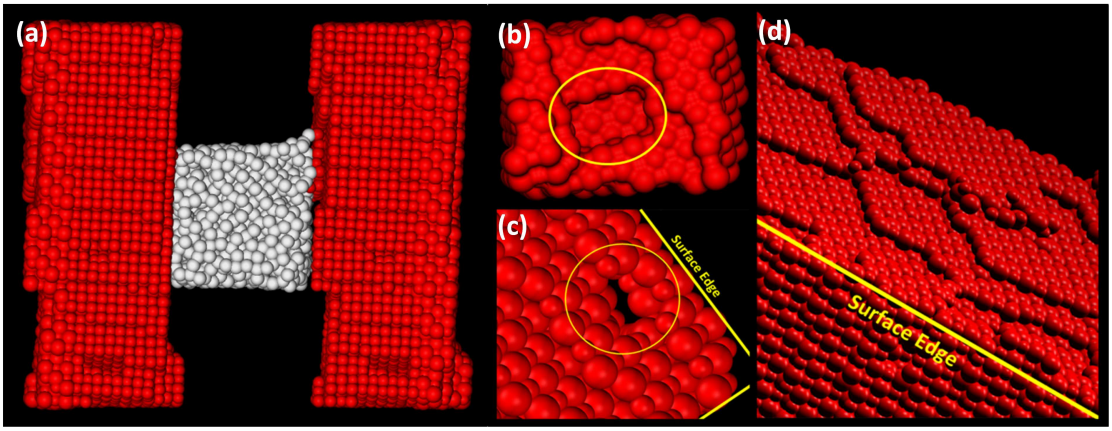

Figure 5.1: (a) Image showing the ceria nanoparticle, coloured white, sandwiched between two anvils, coloured red. The structural complexity of the anvil can be seen in (b, c and d). (b) shows a void on the surface of the anvil, (c) shows a void along the edge of the anvil and (d) shows a variety of steps on the anvil surface.

The atomistic structure of the model ceria nanocube comprises six {100} surfaces, with extensive surface relaxation along the edges in accord with the real nanomaterial [23]. The atomistic structures for the MgO and BaO anvils, comprise {100} surfaces with a variety of steps and edged stepped {100} surfaces, in accord with the real materials [24]. The generation of each structure, outlined below, was carried out using an NVT ensemble (Nosé-Hoover) with thermostat and barostat relaxation times of 0.1 and 0.5 ps respectively. The simulations were conducted with a time step of 0.002 ps and a cutoff at 10.00 Å. The electrostatics were calculated using an Ewald summation precision of $1d^{-3}$. An Ewald summation precision of $1d^{-6}$ was also used however with negligible improvement in the results and therefore $1d^{-3}$ was used to reduce computational expense.

5.2.2.1 CeO_2 Nanocube

To generate the atomistic model of the ceria nanocube a crystal, comprising 1800 atoms (600 Ce atoms and 1200 O atoms) and bound by six CeO_2 {100} surfaces, was instantaneously heated to 3750 K and left for 40 ps using MD. This did not cause complete amorphization; rather the high temperature allowed the atoms to move to a low-energy configuration while retaining the cubic shape. The simulation was then instantaneously cooled to 300 K and left for 50 ps. The final atomistic model is shown in Figure 5.2.

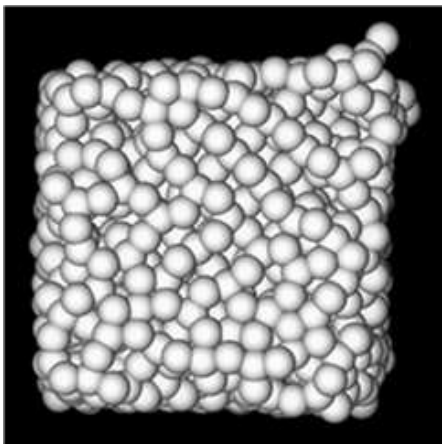

Figure 5.2: The atomistic model for the Ceria nanoparticle, formed using an amorphization–recrystallization technique.

5.2.2.2 MgO Anvil

To generate the atomistic model of the MgO anvil, Figure 5.3, a crystal comprising 16428 atoms (8214 Mg atoms and 8214 O atoms) was melted (amorphization) under constant volume MD simulation, performed at 5000 K. The temperature was then reduced; MD simulation was performed for 50 ps at 4500 K, 4000 K, 3500 K, and 3000 K. Finally, to induce crystallisation, MD simulation was performed for 200 ps at 2600 K, which resulted in a polycrystalline structure. The thermodynamic ensemble was then changed from constant volume to constant pressure to allow the structure to relax any residual stress emanating from the constant volume simulation. MD simulation was performed at 2600 K for 2000 ps to sinter the polycrystalline MgO into a single crystal together. Finally, constant pressure MD simulation was performed at 300 K for 50 ps. An MgO anvil was then placed either side of the ceria nanocube for the compression with a total of 32856 atoms (16428 of each Mg and O atoms) forming the anvils.

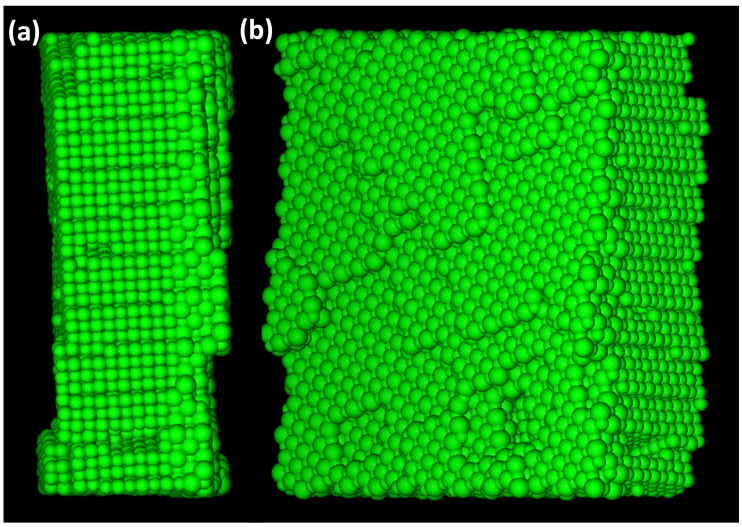

Figure 5.3: The generated atomistic model for the MgO anvils, where (a) shows the side view and (b) an angular view of the surface with stepping.

5.2.2.3 BaO Anvil

As both MgO and BaO have a rock salt structure, the MgO model was adapted to create the BaO anvils, Figure 5.4, by replacing the Mg with Ba and allowing the system to relax with BaO potentials, Table 5.1, using constant pressure MD simulation performed at 300 K for 200 ps. The final BaO (anvil) structure retained the microstructure of the MgO anvil to enable comparisons to be made between the two systems; the only difference being the lattice parameters of the two materials.

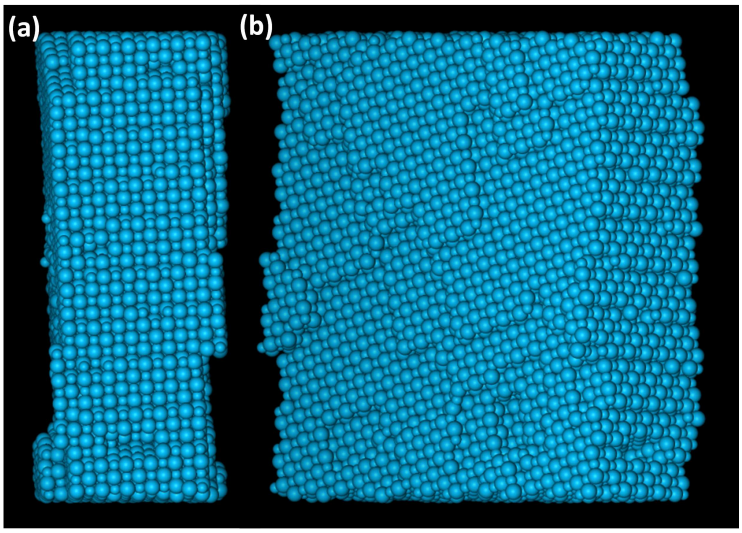

Figure 5.4: The generated atomistic model for the BaO anvils, where (a) shows the side view and (b) an angular view of the surface with stepping.

5.2.2.4 Fixed Anvil

Here, the MgO anvil model was used with the atom positions fixed in place, Figure 5.5. This therefore enables direct comparison between all three anvil types as the microstructural features are identical in all.

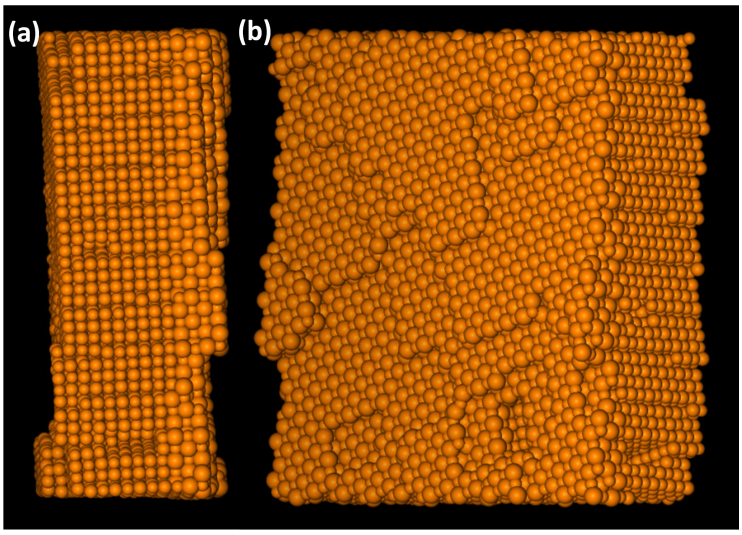

Figure 5.5: The generated atomistic model for the fixed anvils, where (a) shows the side view and (b) an angular view of the surface with stepping. This model was created using the MgO model with all atoms fixed in place.

5.2.3 Uniaxial Compression

Uniaxial compression was performed under constant volume (NVT) MD simulation. Atoms at the back of one anvil were then moved by 0.02 Å every 100 steps (step size $0.002ps$) to give a compression rate of 0.1 Å ps^{-1} (10 ms^{-1}). The strain within the system is expressed as:

$$\epsilon = \frac{(L_i - L_n)}{L_i} \tag{5.2}$$

Where ϵ is the strain, L_i is the initial distance between the anvils and L_n is the distance after each 100 steps of the compression (each movement of the anvil). As only uniaxial compression is considered, strain is reported as a positive value between 0 and 1.

5.2.4 Stress Partitioning

During the compressions, the total imposed stress is partitioned between the anvils and the ceria nanocube. It is therefore important to de-convolute the total stress to reveal how much stress is captured by the anvils and the subsequent residual stress imposed upon the nanoceria. The stress on the system was calculated using the system pressure which is output by DL_POLY. This is the stress (pressure) acting on the whole system. As this is a uniaxial compression, the stress of the system is used to calculate the directional stress. As pressure is equal to force over area, the stress acting in the direction of the compression can be calculated by:

$$P' = P\frac{A}{A'} \tag{5.3}$$

Where P' is the pressure in the direction of the compression, P is the system pressure, A is the surface area of the system cell, and A' is the surface area perpendicular to the line of compression, as depicted in Figure 5.6 by the two dotted lines ($y * z$ axis), where the compression is along the x axis ($\mathrm{D_T}$). An addition is then made to this equation to narrow the surface area to that which is acting on the surface of the nanoparticle, in this case where the nanoparticle is cubic, this would be the surface area of the two faces of the cube in direct contact with the anvils. This is given as:

$$P'' = P'\frac{A'}{A''} \tag{5.4}$$

Where P'' is the pressure in the direction of the compression acting on the anvil, P' is the system pressure, A' is the directional surface area as calculated in Equation 5.3, and A'' is the surface area the nanoparticle in direct contact with the anvils. Partitioning of the stress was done using the percentage of distance relating the anvil and particle in relation to the total distance. The percentage of the distance relating to the nanoparticle was calculated using:

$$\%D = \frac{D_n}{D_T}100 \tag{5.5}$$

Where D_n is the width of the nanoparticle and D_T is the total distance of the nanoparticle and anvils, as shown in Figure 5.6. This was used to calculate the percentage stress at each designated step section, by:

$$\%Stress = \frac{P_t}{100}\%D \tag{5.6}$$

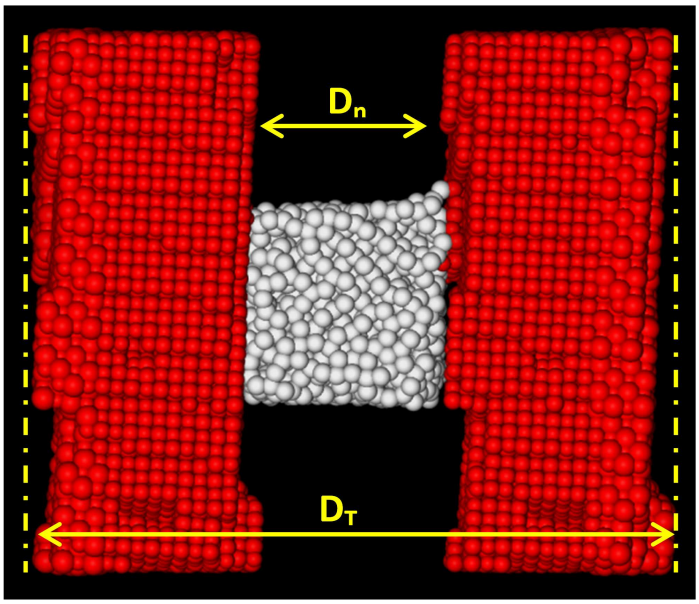

Figure 5.6: Image of the ceria nanoparticle sandwiched between the two anvils, where D_T is the total distance and D_n is the nanoparticle distance. The two dotted yellow lines are aligned with the back of the anvil.

5.3 Results

5.3.1 Stress-strain analysis

Stress-strain curves for the ceria nanocube using soft, hard, and non-deformable anvils are shown in Figure 5.7, showing the total stress (black), stress absorbed by the anvils (grey), and residual stress acting upon the nanocube (orange/green/blue), with highlighted events (numbered on the graphs) detailed in Table 5.2. These curves have been smoothed using a 10 data point moving average to reduce the noise in the baseline while keeping and highlighting the deformation events. The raw data curves are presented individually in Appendix 4, Section 4.1. The yield strength was determined when both of the following criteria were satisfied: Sudden system stress release (drop in the stress-strain curve) and corresponding plastic deformation event in the ceria nanoparticle. In particular, there are several occurrences of sudden system stress release, however, these events correspond to the sacrificial material capturing the stress, via a plastic deformation event, and not the nanoceria catalyst.

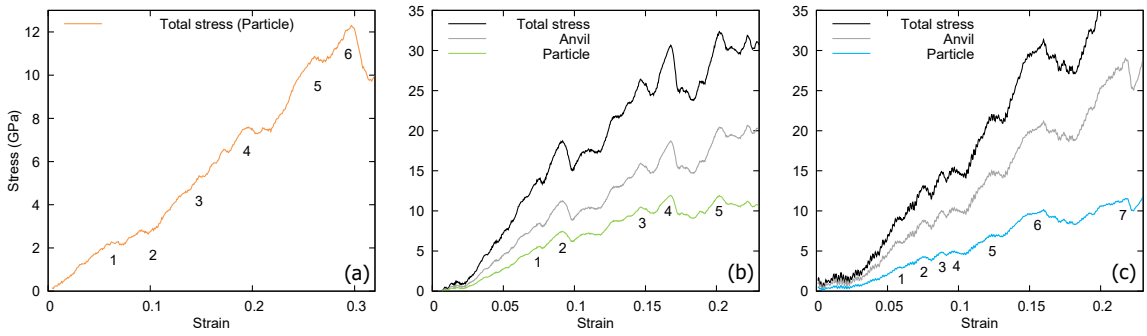

Figure 5.7: Smoothed stress-strain curves of nanoceria using: (a) fixed anvils, (b) MgO anvils, and (c) BaO anvils. In each stress-strain curve the total stress (black), stress on anvil (grey), and residual stress on nanoceria sample (orange/green/blue) are given. The numbers correspond to the data points highlighted in Table 5.2.

Experimentally, yield strength is based upon the total stress, without consideration of stress partitioning. Here the yield strength is calculated for the ceria nanocube using hard, soft and fixed anvils, as given in Table 5.3. Yield strength is the first point of irreversible plastic deformation and is referred to as a moderate/major deformation, and was determined by visual analysis. This is seen as a point of discontinuity in the stress-strains (i.e Figure 5.7(b)2). Minor deformations were considered to be potentially reversible through removal of the anvils and extended equilibration time, for example Figure 5.7(b)1, and therefore were disregarded when determining the yield strength.

Table 5.2: Details describing events during the deformation of the nanocube, at the locations given in Figure 5.7, as observed through visual analysis. Values in GPa, with emphasised data relating to the yield points.

	Fixed Anvils		Hard Anvils (MgO)		Soft Anvils (BaO)	
	Strain, Stress	Deformation Event	Strain, Stress	Deformation Event	Strain, Stress	Deformation Event
1	0.06, 2.2	Twist in the particle as a result of the particle adjusting to the stress places on it by the anvils	0.07, 5.6	Slight particle deformation while adjusting to the surface step on the anvil	0.06, 2.8	Anvil suffers minor deformation while adjusting to the particle pressing on step edge of one of the anvils
2	**0.10, 2.5**	**Moderate particle deformation as the particle releases stress to adjust to a step in the anvil surface**	0.09, 7.4	Both the anvil and particle deform while adjusting to the step in the surface on the other anvil	0.08, 4.2	Anvil suffers deformation while adjusting to the particle pressing on the edge of a step on the other anvil
3	0.15, 5.0	Particle deformation while again adjusting to the same step in the anvil surface	0.15, 10.6	Minor particle and anvil deformation as a final adjustment to the anvil steps	0.09, 4.9	Minor particle deformation occurs while adjusting to the steps in both surfaces of anvil
4	0.20, 7.8	Particle deformation while again adjusting to the step in the anvil surface	**0.17, 12.1**	**Major particle and anvil deformation caused by the compression of the particle**	0.095, 5.0	Minor deformation in the particle corner, which releases pressure caused by adjusting to the anvil surface steps
5	0.26, 10.7	Particle deformation caused by the stress while adjusting to a different step in the anvil surface	0.21, 12.1	Major deformation in the particle as a result of the compression	0.12, 7.2	Particle rotates slightly instead of deforming, as a measure to release the stress
6	0.30, 12.4	Deformation in particle due to the compression of the nanoparticle	-	-	0.16, 10.0	Minor deformation in anvil and particle, which on the stress-strain graph looks fairly major, however it is due to the deformation being split between both the anvil and particle
7	-	-	-	-	**0.22, 11.6**	**Major deformation of particle caused by the compression**

Table 5.3: Mechanical properties of a ceria nanocube, calculated using soft, hard and fixed anvils. Yield strength values are given in GPa.

	Soft Anvils (BaO)	Hard Anvils (MgO)	Fixed Anvils
Yield Strain	0.22	0.17	0.10
Particle Yield Strength [%]	11.6 [29%]	12.1 [46%]	2.5 [100%]
Anvil Yield Strength [%]	28.5 [71%]	14.4 [54%]	-
Total Yield Strength	40.1	26.5	2.5
Anvil Elastic Constants, C_{11}, C_{12}	122, 58	393, 164	∞, ∞

5.3.2 Microstructural Features

Microstructural features are formed in materials, which emanate from the synthetic protocol [25]. This includes differences in morphology, grain-boundaries, dislocations, and point defect concentrations. As mechanical properties are governed by the microstructure of the material [22], these 'real' materials can vary in measured values by orders of magnitude. For example, Sato *et al* determined a fracture strength of 0.25 GPa, measured using Vickers indentation [26], whereas Sakanoi *et al* [17] calculated a fracture strength of 22.70 GPa for the same material using DFT.

More recently, microstructural features have been introduced into model structures, enabling more realistic simulations of mechanical properties [15, 16]. By using a simulated amorphization and crystallisation technique to generate the atom-level models, microstructural features can evolve 'naturally' within the model, in an analogous way to their evolution during the crystallisation step in synthesis.

The structural models used here are therefore more realistic in that they capture the structural features observed experimentally. These include: surface steps, vacancies (Figure 5.1), interstitials, dislocations, and grain-boundaries.

5.3.3 Structure and Catalysis

Nanoceria can catalyse an oxidation/reduction reaction by capturing, storing and releasing oxygen [27]. Intuitively, the less energy required to extract the oxygen, the more active the catalyst. In addition, if oxygen is lost from the surface of the catalyst, it must be replenished. Accordingly, oxygen transport throughout the material is pivotal to the ability of ceria to catalyse a chemical reaction. In particular, oxygen vacancy formation energies reflect the energy required to extract the oxygen and can be gauged by calculating the Madelung energies of the surface oxygen ions. Similarly, calculated mean square displacements (MSD) of oxygen provides insight into oxygen transport within the material.

The catalytic activity is highly dependent upon the surface(s) exposed. In particular, ceria {111} surfaces are thermodynamically more stable than {100} surfaces, however, it is more energetically favourable to extract oxygen from the {100} surfaces. Therefore nanoceria, which exposes {100} surfaces is catalytically more active than nanoceria exposing {111}. The structure of the nanomaterial, RDF, MSD, and Madelung energies are therefore all indicators of catalytic activity.

5.3.3.1 Structure of the Nanoceria

Our model ceria nanocube exposes six {100} surfaces (Figure 5.8, bottom right) and therefore a key indicator of catalytic activity is the structural preservation of the fluorite crystal structure and {100} surfaces under uniaxial loading. Figure 5.8 shows the structure of the ceria nanocube under 20% compression with BaO (soft), MgO (hard) and no sacrificial material for protection. Inspection of the model ceria nanocubes, using molecular graphics, reveals that the structural integrity of the {100} surfaces and fluorite crystal structure is retained when protected by BaO and partially retained with MgO. Conversely, with no sacrificial material, the nanocube deforms plastically resulting in an almost amorphous particle, Figure 5.8 (orange).

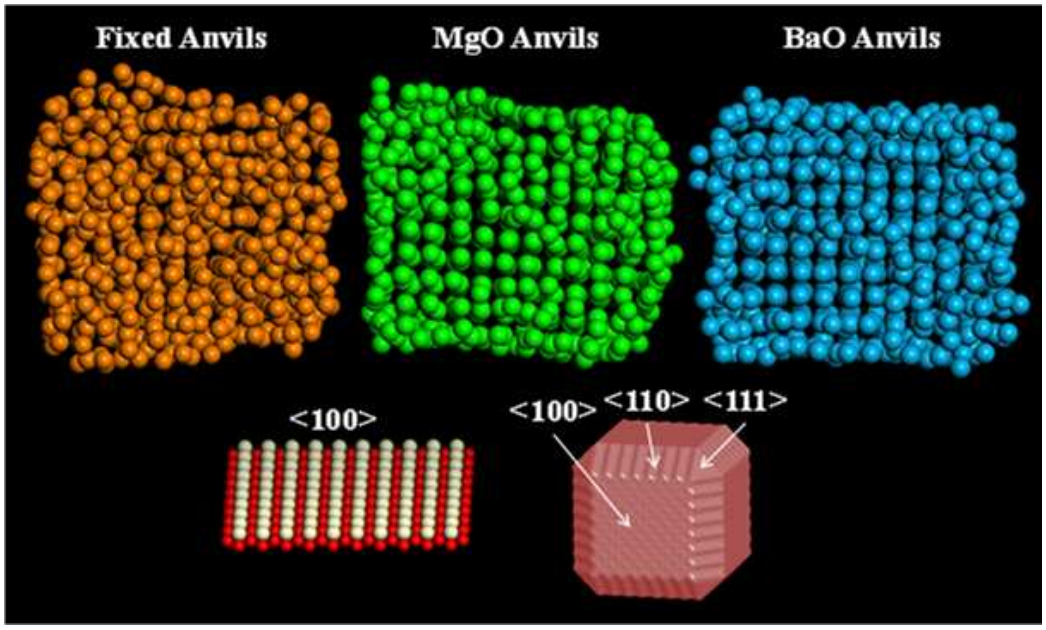

Figure 5.8: Cation structure of nanoceria at 20% compression using fixed anvils (top left), MgO anvils (top centre), and BaO anvils (top right). Here, the loss of ordered structure can be seen in varying degrees, with fixed anvils suffering the most loss of structure, and BaO the least. The atom-level structure of the perfect CeO_2 {100} surface and the morphology of the ceria nanocube is shown bottom left and bottom right respectively.

5.3.3.2 Mean Squared Displacement (MSD) and Madelung Energies

The MSD is given in Figure 5.9(a) for the ceria nanocube at 0% strain and protected by 'soft' BaO anvils and 'hard' MgO anvils at 20% strain. The Madelung energies for the oxygen species in the nanocube are given in Figure 5.9(b), calculated for 0% and 20% strain for the fixed anvil system. The Madelung energies were calculated by Dr Marco Molinari, from the University of Huddersfield, as part of a collaboration.

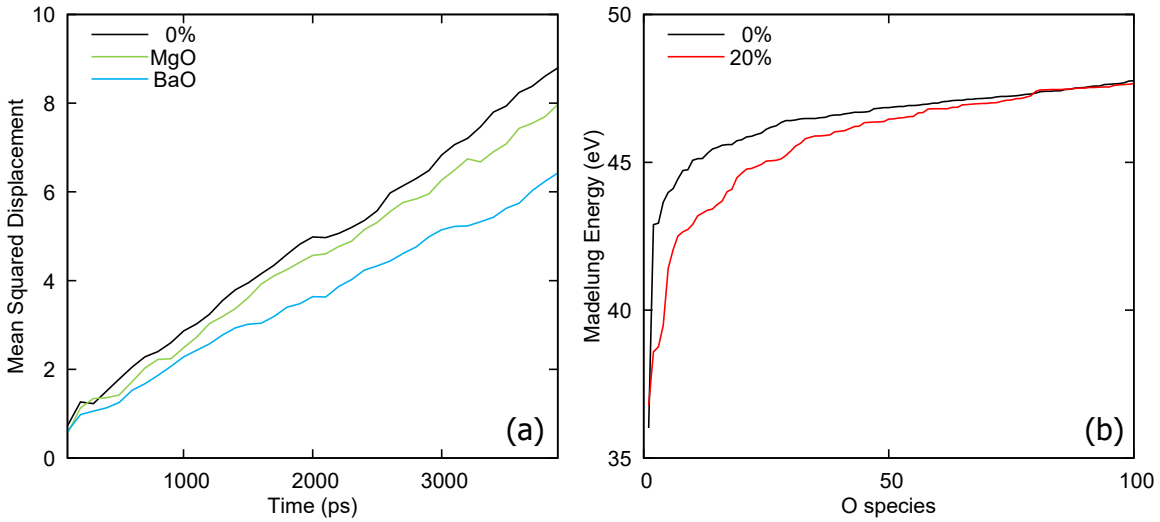

Figure 5.9: (a) Ceria oxygen mobility at 0% and 20% compression between MgO and BaO anvils, conducted at a simulated temperature of 3500 K, scaling roughly to a comparative experimental temperature of 2000 K., and (b) Madelung energy of the ceria nanocube under 0% and 20% compression by fixed anvils.

Analysis of the data reveals that under uniaxial pressure the catalytic properties of the nanoceria change. The compression impacts upon both the transport properties and the oxygen extraction. As expected, the soft (BaO) barrier protects the nanoceria better than the hard (MgO) barrier. This change however can be considered as fairly subtle, where detailed insight into the catalytic properties is not possible with the limited data. MSD and Madelung energies however can be used as an analytical tools, as the resulting data can indicate changes in catalysis.

5.3.3.3 Radial Distribution Function (RDF)

The calculated radial distribution functions provide additional insight into the structural deformations, Figure 5.10, with individual RDF given in Appendix 4.2. Inspection of the RDF reveal that when protected by BaO, the ceria nanocube retains long-range order. Specifically, the RDF trace is almost identical for the ceria nanocube under 0% and 20% strain, (blue). Conversely, when protected by MgO, the peaks start to broaden, (green), indicating some structural deformation. Unprotected, the long-range order is almost completely extinguished, (orange).

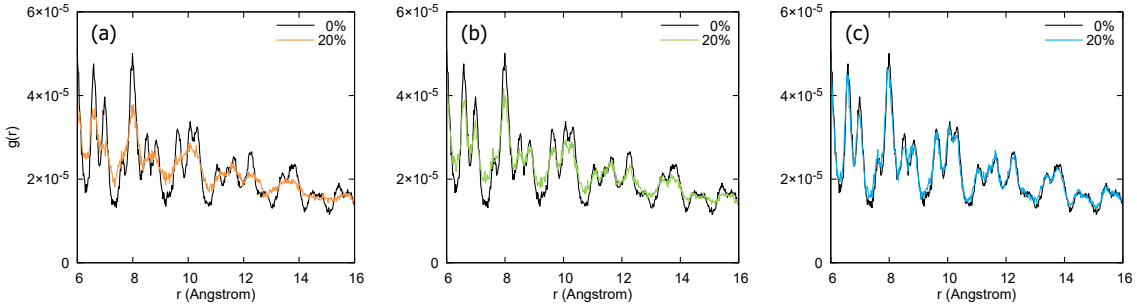

Figure 5.10: Radial Distribution Functions, RDF, within nanoceria using (a) fixed anvils, (b) MgO anvils, and (c) BaO anvils, at both 0% and 20% compression, highlighting the loss of long range order.

The atom level structures and calculated RDF both are consistent with the calculated yield strain of each system, as given in Figure 5.7, Table 5.2. At 20% strain we expect almost complete loss of structural integrity for the unprotected ceria nanocube (yield strain 10% at 2.5 GPa), partial loss for the MgO protected nanocube (yield strain 17% at 26.5 GPa), and minimal to no loss for the BaO protected nanocube (yield strain 22% at 40 GPa), Figure 5.10.

The BaO and MgO anvils therefore seem to act 'sacrificially', preserving the structure and hence catalytic activity of the nanoceria catalyst. The softer material (BaO) provides the greatest protection and can withstand uniaxial stresses of up to 40 GPa.

5.3.3.4 Oxygen Exchange

It was found that during the compression oxygen is exchanged between the nanoceria surface and MgO/BaO anvils. An example of the oxygen exchange occurring between the MgO anvils and the nanoparticle is shown in Figure 5.11, labelled (1)-(4). (1) shows the initial step, where there is no oxygen exchange, (2) highlights oxygen from the MgO anvil incorporating into the nanoparticle structure, (3) shows that the initial oxygen transferred onto the nanoparticle has returned to the anvil (indicated by the arrow) and in a different layer, a different oxygen from the anvil has transferred into the nanoparticle, and (4) shows the same oxygen has moved within the nanoparticle. This oxygen exchange also occurs for the BaO anvil, an example of which is shown in Figure 5.12.

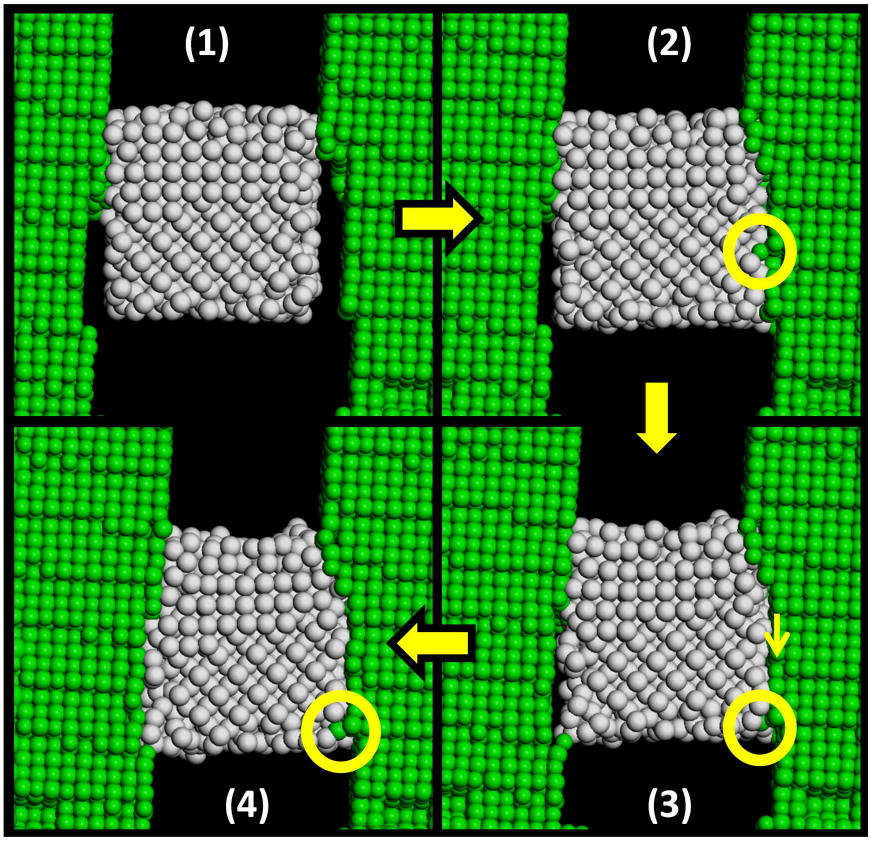

Figure 5.11: An example of the oxygen exchange occurring between the MgO anvils and the nanoparticle.

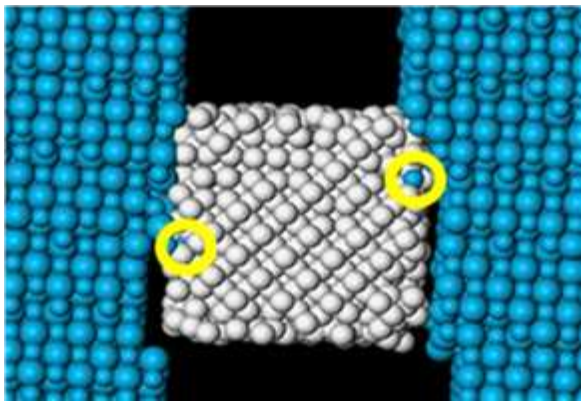

Figure 5.12: An example of the oxygen exchange occurring between the BaO anvils and the nanoparticle.

5.3.3.5 Structural Retention and Temperature

The morphological changes within the ceria nanocube are further affected by strain through changes in surface structure. The surface of cubic nanoceria is primarily the more reactive {100} structure, which is metastable. The structure transitions to polyhedral then truncated octahedral, over extended time periods, due to the more thermodynamically stable {111} surface, which is inherently less reactive. Comparison of the surface structure at 0% and 20% strain, while sandwiched between each anvil type revealed the 20% strain aids in preventing/slowing the structural change and thus retaining the cubic, {100}, surface structure for an extended time period. Further to this, the softer BaO anvils were more effective in retaining the {100} comparatively to MgO and fixed anvils, protecting the cubic nanoceria from structural transitioning as shown in Figure 5.13.

Further to this, the temperature at which the compression occurs affects the manner in which the nanocube deforms, thus the surface structure and activity of the material, as shown in Figure 5.14. This is a vital consideration for functional materials used in hostile environments, such as catalytic materials which need to function under high fluctuations in temperature.

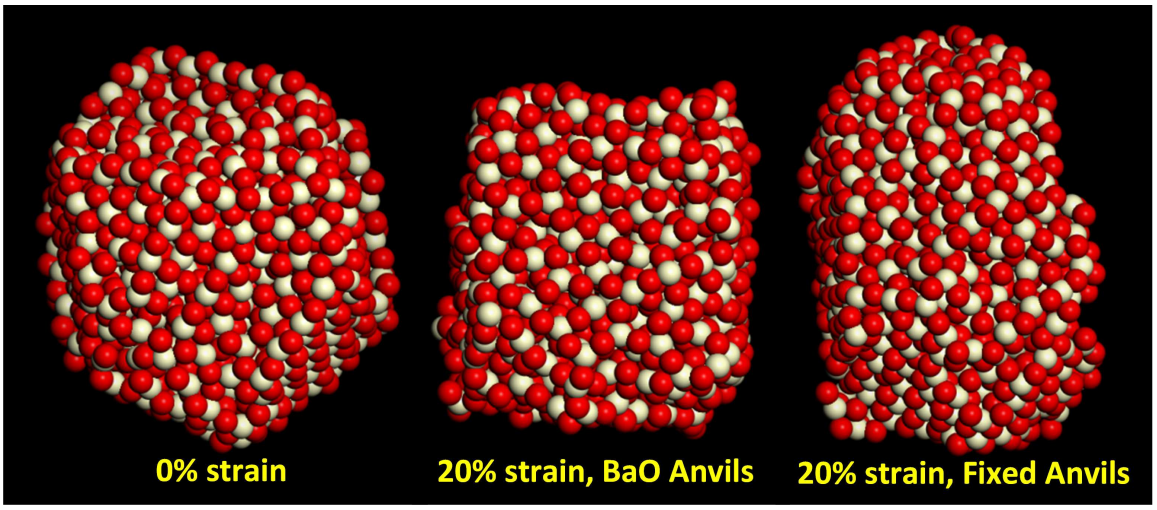

Figure 5.13: Ceria nanocube after an extended time period, highlighting the retention of the cubic {100} surface structure. Where 0% strain shows minimal retention (left), 20% strain using BaO anvils show high retention (centre), and 20% strain using fixed anvils shows moderate retention (right) of the {100} cubic surface structure.

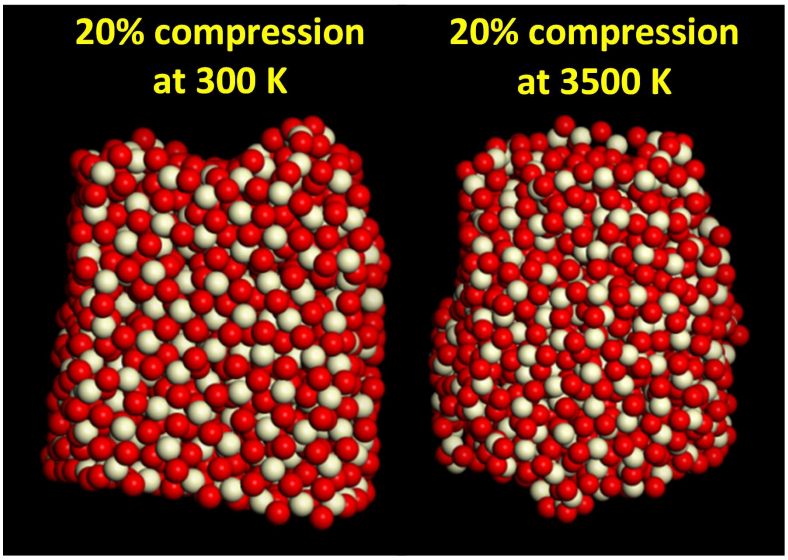

Figure 5.14: Comparison of the ceria nanocube at 20% compression with fixed anvils at 300 K and 3500 K.

5.3.4 Deformation Mechanisms

5.3.4.1 Deformation of the Ceria Nanocube

Under uniaxial compression, the ceria nanocube undergoes a crystalline to amorphous transition. This is a gradual process whereby the core of the nanocube retains its crystal structure while the 'shell' amorphises. Wang *et al* [28] rationalised this phenomenon by considering the structure as a core-shell system comprising a crystalline inner core surrounded by an amorphous shell. Under pressure, the shell transitions from a low- to high-density amorphous state. As the pressure increases, more of the inner core amorphises. Our simulations capture this process, which indicates that our methods capture the behaviour of the real material under load. This increases confidence in the reliability of data emanating from this study. The crystalline to amorphous transition is also linked to anvil hardness; complete amorphization occurs at strains of 0.42 (fixed anvils), 0.55 (hard anvils) and 0.71 (soft anvils).

Surprisingly, the surfaces of the ceria nanocube, which are not in contact with the anvils, appear more amorphous than the surfaces in contact with the anvils. Figure 5.15 shows the ceria nanocube under a system strain of 0.40 (40%), which reveals that nanoparticle deformation increases with anvil hardness.

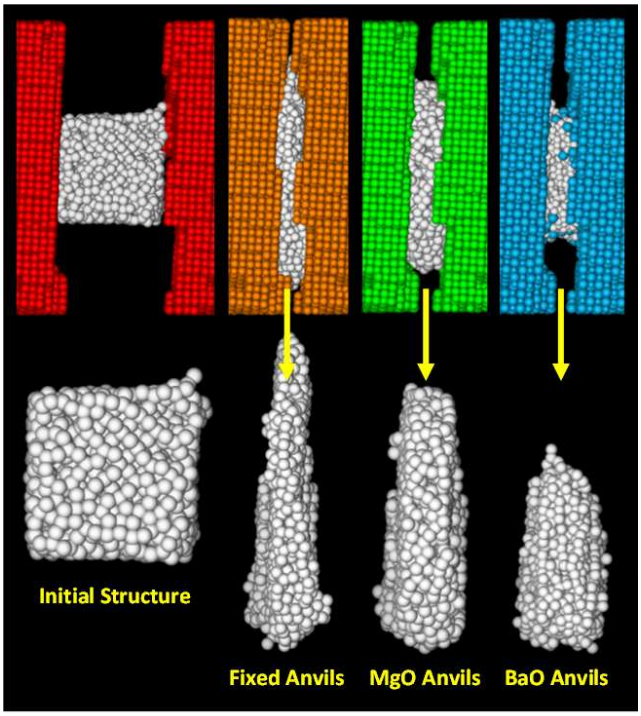

Figure 5.15: Compression of a ceria nanocube sandwiched between three anvil types. The bottom images show the initial and compressed states of the ceria nanocube.

5.3.4.2 Deformation of the Anvils

Plastic deformations in the anvils are shown in Figure 5.16. The figure reveals that the deformation, suffered by the soft (BaO) anvil is considerably higher than the hard (MgO) anvil, with higher penetration of the nanoparticle into the surface of the anvil. Conversely, when compressions were conducted with rotated nanoparticles, with opposing corners of the cube against the anvils, there is higher embedment into the anvils compared to the sides of the nanoparticle.

Anvil hardness is not the only consideration. In a study by Huang *et al* [18], the effects of smooth/rough anvil surfaces were investigated using High-Pressure Torsion (HPT). The study revealed that anvils with rough surfaces return higher hardness readings compared to anvils with smooth surfaces. In a study by Goel *et al* [19], the effects of indenter (anvil) shape and sample structure (single crystalline/poly crystalline) were investigated. It was found that spherical indenters returned higher load readings ($\sim$1200 nN) than pyramidal indenters ($\sim$200 nN) to a set depth.

In this study, we have designed (modelled) anvils that are not perfectly flat; rather they comprise surface steps, edges, and corners. Analysis of the deformation behaviour, using molecular graphics, reveals that the stress is concentrated along the step edge until the particle (or anvil) deforms to release the stress by 'wrapping' round the step. In particular, we find that anvil steps induce an initial deformation at 2.5 GPa, whereas a value of 12.4 GPa is calculated for complete deformation. Clearly, the 'roughness' of the anvil plays a key role in the calculated stress in accord with the findings of Huang *et al*.

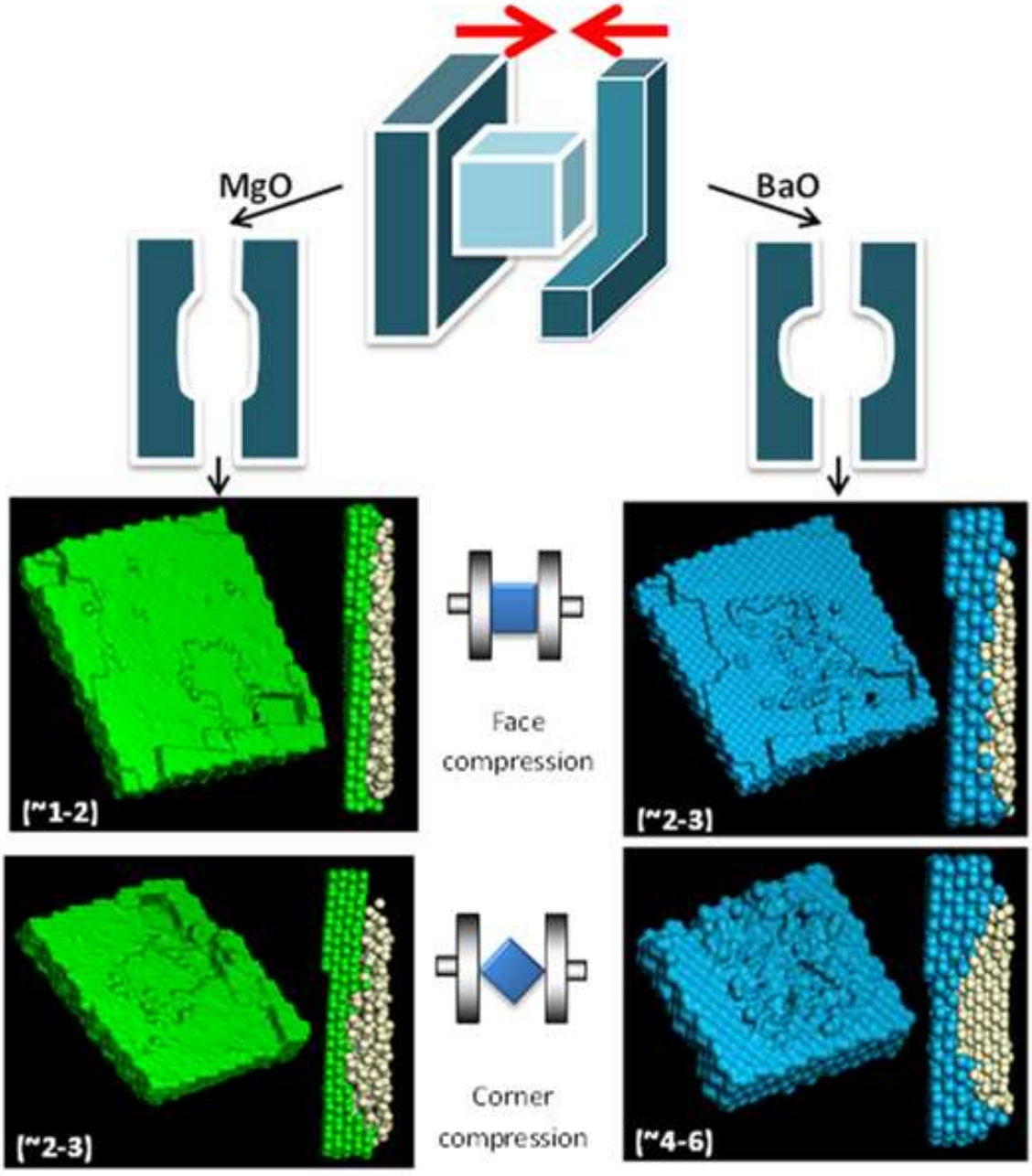

Figure 5.16: Deformation of MgO (hard) and BaO (soft) anvils. The values within the parentheses are the number of penetrated cation layers.

5.3.4.3 Accommodation of Anvil Surface Steps

During visual analysis it was noted that the anvil surface contains stepping, which creates highly localised stress on the nanocube. This results in the particle deforming to accommodate for the steps before deforming due to global strain placed on the particle. This can be seen for each anvil type, with different effects for each.

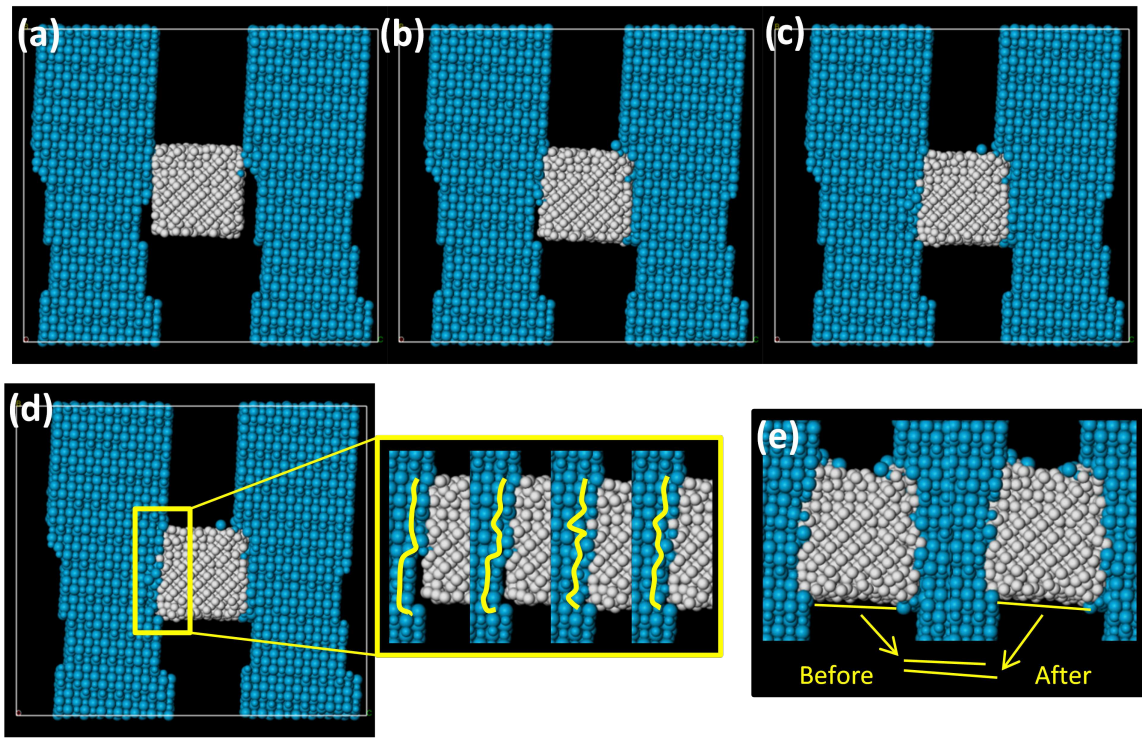

Figure 5.17: Deformation of a ceria nanocube by BaO anvils due to anvil stepping, where (a) is 0% compression of the ceria, (b) is the point the ceria wraps around the surface steps on one of the BaO anvils, and (c) is the point at which the ceria wraps around the surface steps on the other BaO anvil.(d) depicts the deformation in the BaO anvil, and (e) shows the tilting/twisting of the nanoparticle.

Figure 5.17 shows a series of images relating to (a) 0% compression of the ceria by BaO anvils, (b) the point at which the ceria 'wraps' around the surface steps on one of BaO anvils, and (c) the point at which the ceria 'wraps' around the surface steps on the other BaO anvil. Deformation within the nanoparticle and the anvil which occurs after this is caused by the compression. However between the initial stage and when both anvils are 'flat' against the nanocube, deformation occurs due to the stress 'overcoming' the step, which could be described as an obstacle in the compression.

As the BaO anvils are softer than the nanoparticle, the anvils also adjust to the localised stress on the step and 'wraps' around the particle to release the stress (d). The nanocube also suffers a level of deformation to aid in releasing pressure. Figure 5.17 (e) shows the tilt, or twisting, of the nanoparticle to accommodate the stress rather than it deforming. By drawing a line under the particle for the two steps, you can see how the angle of the line changes, which corresponds to the movement of the particle.

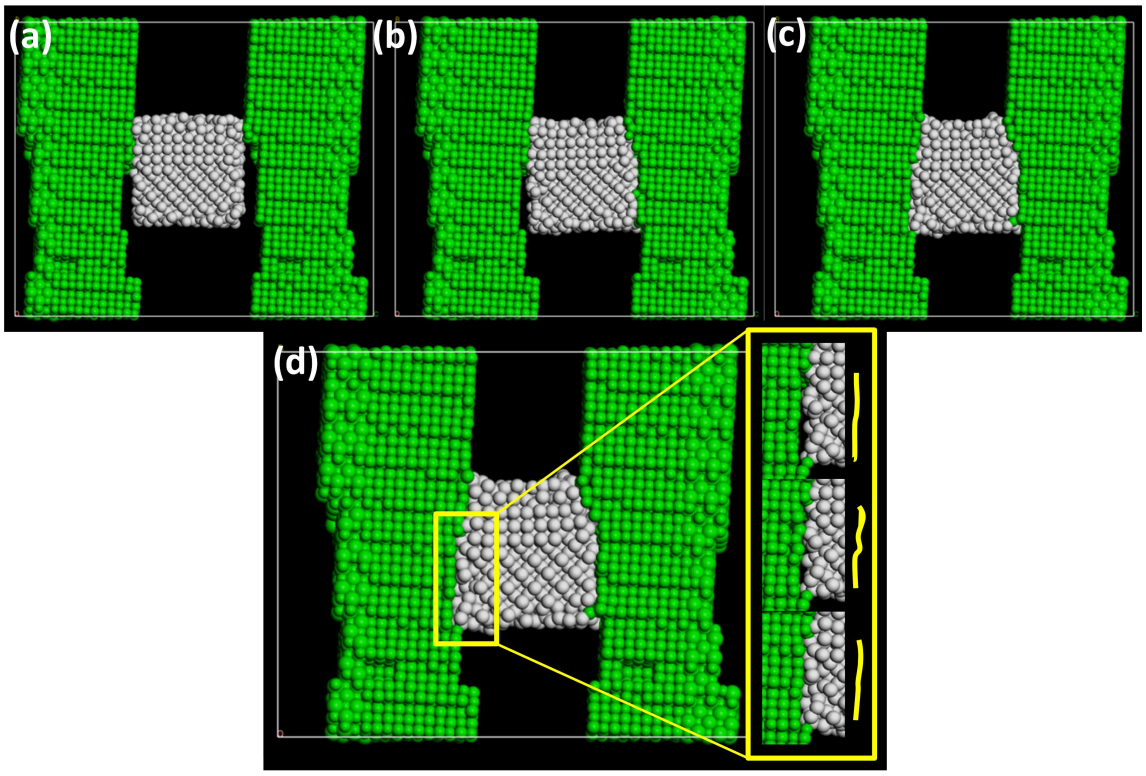

Figure 5.18: Deformation due to anvil stepping, where (a) is 0% compression of the ceria by MgO anvils, (b) is the point the ceria wraps around the surface steps on one of the MgO anvils, (c) is the point at which the ceria wraps around the surface steps on the other MgO anvil, and (d) depicts the deformation in the MgO anvil.

Figure 5.18 shows the structural effect of the surface stepping in the MgO anvils, where (a) is 0% compression, (b) the adjustment to the first anvil, and (c) the adjustment to the second anvil. Similarly to the BaO anvil compression, (d) depicts how the MgO anvil, being a hard yet still deformable anvil, deforms slightly to adjust for the particle. The nanoparticle deforms as well, and to a higher degree than in the BaO anvil compression.

Figure 5.19 shows the structure the effect of the surface stepping in the fixed anvils, where (a) is 0% compression, (b) the adjustment to the first anvil, and (c) the adjustment to the second anvil. This is similar to those shown for the BaO and MgO anvils. The main difference however is that only the nanoparticle deforms. (d) depicts the initial minor deformations within the nanoparticle, occurring before deformation as a result of the anvil steps. (e) shows the deformation of the particle as it wraps around the first step. The deformation is mostly localised at the top part of the nanoparticle, where the particle is already in contact with the anvil. The part of the particle which is not in contact with the anvil seems to hold its shape until in full contact with the anvil. (f) shows deformation of the nanoparticle as it wraps around the steps in the second anvil. Here, conversely to the first anvil, the part of the particle which is not initially in contact with the anvil appears to have the greater deformation, where the top of the anvil stays relatively undamaged.

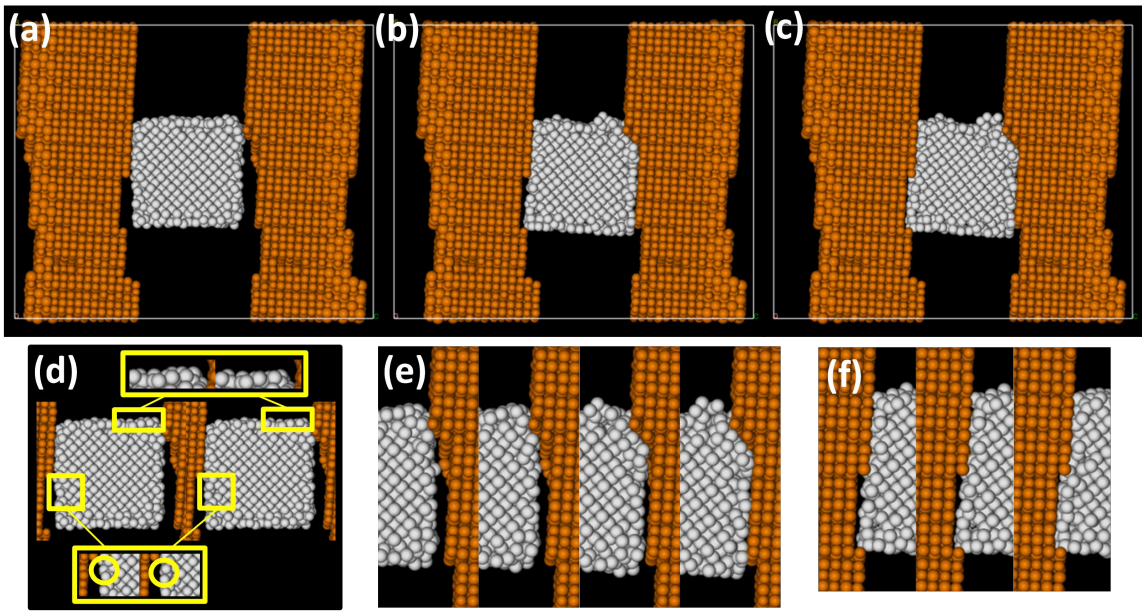

Figure 5.19: Deformation due to anvil stepping, where (a) is 0% compression of the ceria by fixed anvils, (b) is the point the ceria wraps around the surface steps on one of the fixed anvils, and (c) is the point at which the ceria wraps around the surface steps on the other fixed anvil. (d) the initial minor deformations within the nanocube before step deformation, (e) shows 4 stages of the nanocube deforming round the first anvil steps, and (f) shows 4 stages of the nanocube deforming round the second anvil steps.

5.4 Discussion

It is well known that anvil hardness affects measured stress, though not to what extent. Accordingly, (hard) diamond anvils are commonly used to ensure that the imposed stress is communicated almost completely to the sample. Conversely, measurements using more malleable anvils [9] may over report the yield stress because of load partitioning. Our calculations reveal that the soft (BaO) anvil can capture as much as 71% of the imposed stress. As expected, the harder anvil captures less of the imposed stress - in this case 54% (MgO anvil), Table 5.3.

The use of soft anvils makes it possible to gain insight into protective or 'sacrificial' materials. Here, stress partitioning is key to their performance. This is especially important for devices that comprise composite functional materials, such as batteries [8], fuel cells [29], CMP slurries [30], and catalysts [31].

It might appear that stresses of GPa magnitude are unlikely during operating conditions. However, for nanomaterials, where surface areas can be of the order of tens of nm^2, localised regions can easily suffer such high levels of stress. Examples may include: Li intercalation (charge cycling of batteries), friction [32], impact [33], and even temperature fluctuations [34] (relative expansion coefficients of composite nanomaterials). Caution must therefore be exercised in using documented information when designing devices that will be subject to high levels of operational stress.

Further to this, mechanical properties of a 'real' material contain microstructural features including differences in morphology, grain-boundary, dislocation, and point defect concentrations, which emanate from the synthetic protocol [25]. As mechanical properties are governed by its microstructure, measured values can therefore differ by orders of magnitude. For example, Sato *et al* determined a fracture strength of 0.25 GPa, measured using Vickers indentation, [26] whereas Sakanoi *et al* [17] calculated a fracture strength of 22.70 GPa for the same material using DFT.

More recently, microstructural features have been introduced into model structures, enabling more realistic simulations of mechanical properties [15, 16]. By using a simulated amorphization and crystallisation technique to generate the atom-level models, it enables microstructural features to evolve 'naturally' within the model, analogous to their evolution during the crystallisation step in synthesis.

5.5 Conclusions

An amorphization and re-crystallisation technique was used to generate the atomistic models of the CeO_2 nanocube, as well as the MgO and BaO anvils, with the atoms fixed in place for the fixed anvil system. Uniaxial compression was performed on each system in order to determine the mechanical behaviour of the nanoparticle.

We found that deformable anvils can act as a protective barrier for nanomaterials such as nanoceria, where it resists plastic deformation up to 40.1 GPa (BaO), 26.5 GPa (MgO) and 2.5 GPa (unprotected). Our simulations reveal that the soft anvils increase nanoparticle protection by absorbing more of the stress; the BaO and MgO anvils are able to capture 71% and 54% of the imposed stress respectively. Our simulations also show the importance of considering deformable anvils when simulating stress–induced plastic deformation. In particular, the yield strength of nanoceria, measured as the residual stress acting upon the nanoparticle just before plastic deformation, was calculated to be 11.6 GPa (Soft – BaO), 12.1 GPa (hard – MgO), and 2.5 GPa (no anvil).

Further work on this system is presented in Chapter 6, where the effects of temperature and compression rate are discussed, along side the introduction of a dynamic surface area into the analysis.

References

[1] J.Y. Huang, L. Zhong, C.M. Wang, J.P. Sullivan, W. Xu, L.Q. Zhang, S.X. Mao, N.S. Hudak, X.H. Liu, A. Subramanian, H. Fan, L. Qi, A. Kishima, and J. Li. In Situ Observation of the Electrochemical Lithiation of a Single SnO_2 Nanowire Electrode. *Science*, 330:1515, 2010.

[2] K. Zhou, X. Wang, X. Sun, Q. Peng, and Y. Li. Enhanced Catalytic Activity of Ceria Nanorods from Well-Defined Reactive Crystal Planes. *Journal of Catalysis*, 229(1):206–212, 2005.

[3] A. Holmgren, D. Duprez, and B. Andersson. A Model of Oxygen Transport in Pt/Ceria Catalysts from Isotope Exchange. *Journal of Catalysis*, 182(2):441–448, 1999.

[4] M. Mogensen, N.M. Sammes, and G.A. Tompsett. Physical, Chemical and Electrochemical Properties of Pure and Doped Ceria. *Solid State Ionics*, 129(1-4): 63–94, 2000.

[5] T.X.T. Sayle, M. Cantoni, U.M. Bhatta, S.C. Parker, S.R. Hall, G. Möbus, M. Molinari, D. Reid, S. Seal, and D.C. Sayle. Strain and Architecture-Tuned Reactivity in Ceria Nanostructures; Enhanced Catalytic Oxidation of CO to CO_2. *Chemistry of Materials*, 24(10):1811–1821, 2012.

[6] H.C. Yao and Y.F. Yu Yao. Ceria in Automotive Exhaust Catalysts: I. Oxygen Storage. *Journal of Catalysis*, 86(2):254–265, 1984.

[7] Z. Xie, Z. Liu, Y. Wang, Q. Yang, L. Xu, and W. Ding. An Overview of Recent Development in Composite Catalysts from Porous Materials for Various Reactions and Processes. *Int. J. Mol. Sci.*, 11(5):2152–2187, 2010. doi: 10.3390/ijms11052152.

[8] T.X.T. Sayle, K. Kgatwane, P.E. Ngoepe, and D.C. Sayle. 'Breathing-Crystals' the Origin of Electrochemical Activity of Mesoporous Li–MnO_2. *J. Mater. Chem. A.*, 4:6456, 2016.

[9] G.A. Crawford, N. Chawla, K. Das, S. Bose, and A. Bandyopadhyay. Microstructure and Deformation Behaviour of Biocompatible TiO_2 Nanotubes on Titanium Substrate. *Acta Biomater.*, 3:359, 2007.

[10] M. I. Eremets, I. A. Trojan, P. Gwaze, J. Huth, R. Boehler, and V. D. Blank. The Strength of Diamond. *Appl. Phys. Lett*, 87:141902–150, 2005. doi: 10.1063/1.2061853.

[11] G. Guillonneau, G. Kermouche, S. Bec, and J. Loubet. Determination of Mechanical Properties by Nanoindentation Independently of Indentation Depth Measurement. *J. Mater. Res.*, 27(19):2551–2560, 2012. doi: 10.1557/jmr.2012.261.

[12] S.P.S. Badwal, F.T. Ciacchi, and J. Drennan. Investigation of the Stability of Ceria-Gadolinia Electrolytes in Solid Fuel Cell Environments. *Solid State Ionics*, 121:253, 1999.

[13] S. Deville, H. Attaoui, and J. Chevalier. Atomic Force Microscopy of Transformation Toughening in Ceria-Stabilized Zirconia. *J. Eur. Ceram. Soc.*, 25:3089, 2005.

[14] T. Shokuhfar, G.K. Arumugam, P.A. Heiden, R.S. Yassar, and C. Friedrich. Direct Compressive Measurements of Individual Titanium Dioxide Nanotubes. *ACS Nano*, 3(10):3098, 2009.

[15] F. Caddeo, A. Corrias, and D.C. Sayle. Tuning the Properties of Nanoceria by Applying Force: Stress-Induced Ostwald Ripening. *Journal of Physical Chemistry C*, 120:14337–14344, 2016.

[16] T. X. T. Sayle adn B. J. Inkson, G. Mobus, S. V. Parker, S. Seal, and D. C. Sayle. Mechanical Properties of Mesoporous Ceria Nanoarchitectures. *Phys. Chem. Chem. Phys.*, 16:24899–24912, 2014. doi: 10.1039/c4cp03526g.

[17] R. Sakanoi, T. Shimazaki, Y. Higichi J. Xu, N. Ozawa, K. Sato, T. Hashida, and M. Kubo. Different Behaviour of Young's Modulus and Fracture Strength if CeO_2: Density Functional Theory Calculations. *J. Chem. Phys.*, 140:121102, 2014.

[18] Y. Huang, M. Kawasaki, A. Al-Zubaydi, and T. G. Langdon. Effect of Anvil Roughness on the Flow Patterns and Hardness Development in High-Pressure Torsion. *J. Mater. Sci.*, 49:6517–6528, 2014. doi: 10.1007/s10853-014-8203-6.

[19] S. Goel, N.H. Faisal, X. Luo, J. Yan, and A. Agrawal. Nanoindentation of Polysilicon and Single Crystal Silicon: Molecular Dynamics Simulation and Experimental Validation. *J. Phys. D: Appl. Phys.*, 47:275304, 2014.

[20] G.V. Lewis and C.R.A. Catlow. Potential Models for Ionic Oxides. *Journal of Physics C: Solid State Physics*, 18(6):1149–1161, 1984.

[21] T.X.T. Sayle, R.A. Catlow, R.R. Maphanga, P.E. Ngoepe, and D.C. Sayle. Generating MnO_2 Nanoparticles using Simulated Amorphization and Recrystallization. *Journal of the American Chemical Society*, 127(37):12828, 2005.

[22] T.X.T. Sayle, B.J. Inkson, A. Karakoti, A. Kumar, M. Molinari, G. Möbus, S.C. Parker, S. Seal, and D.C. Sayle. Mechanical Properties of Ceria Nanorods and Nanochains; the Effect of Dislocations, Grain-Boundaries and Oriented Attachment. *Nanoscale*, 3:1823, 2011.

[23] Y. Lin, Z. Wu, J. Wen, K.R. Poeppelmeier, and L.D. Marks. Imaging the Atomic Surface Structures of CeO_2 Nanoparticles. *Nano Letter*, 14(1):191, 2014.

[24] N.V. Skorodumova, K. Hermansson, and B. Johansson. Structural and Electronic Properties of the (100) Surface and Bulk of Alkaline-Earth Metal Oxides. *Physics Review B*, 72:125414, 2005.

[25] Y. Wang, K. Duncan, E. D. Wachsman, and F. Ebrahimi. The Effect of Oxygen Vacancy Concentration on the Elastic Modulus of Fluorite Structured Oxides. *Solid State Ionics*, 178:53–58, 2007.

[26] K. Sato, H. Yugami, and T. Hashida. Effect of Rare-Earth Oxides on Fracture Properties of Ceria Ceramics. *Journal of Material Science*, 39(18):5765–5770, 2004.

[27] E. Mamontov and T. Egami. Lattice Defects and Oxygen Storage Capacity of Nanocrystalline Ceria and Ceria-Zirconia. *J. Phys. Chem. B*, 104(47):11110–11116, 2000.

[28] Q. Wang, D. He, F. Peng, L. Lei, P. Liu, S. Yin, P. Wang, C. Xu, and J. Liu. Unusual Compression Behaviour of Nanocrystalline CeO_2. *Scientific Reports*, 4: 4441, 2014.

[29] L. Malavasi, C.A.J. Fisher, and M. Saiful Islam. Oxide-Ion and Proton Conducting Electrolyte Materials for Clean Energy Applications: Structural and Mechanistic Features. *Chemical Society Reviews*, 39:4370–4371, 2010.

[30] J. Harra, J. Mäkitalo, R. Siikanen, M. Virkki, G. Genty, T. Kobayashi, M. Kauranen, and J.M. Mäkelä. Size-Controlled Aerosol Synthesis of Silver Nanoparticles for Plasmonic Materials. *J. Nanopart. Res.*, 14:1, 2012.

[31] N. Ta, J. Liu, and W. Shen. Tuning the Shape of Ceria Nanomaterials for Catalytic Applications. *Chinese Journal of Catalysis*, 34(5):838–850, 2013.

[32] J. Fang, C.L. Bull, J.S. Loveday, R.J. Nelmes, and K.V. Kamenev. Strength Analysis and Optimisation of Double-Toroidal Anvils for High-Pressure Research. *Rev. Sci. Instrum.*, 83:93902, 2012.

[33] C. Anders, E.M. Bringa, G. Ziegenhain, G.A. Graham, J.F. Hansen, N. Park, N.E. Teslich, and H.M. Urbassek. Why Nanoprojectiles Work Differently than Macroimpactors: The Role of Plastic Flow. *Phys. Rev. Lett.*, 108(2):027601, 2012.

[34] Q. Li, Y. Yu, Y. Liu, C. Liu, and L. Lin. Thermal Properties of the Mixed n-Octadecane. Cu Nanoparticle Nanofluids during Phase Transition: A Molecular Dynamics Study. *Materials*, 10:38, 2017.

Chapter 6

Simulated Compression – Dynamic Surface Area, Temperature Variations, and Compression Rate

6.1 Introduction

As discussed throughout this thesis, ceria has been the subject of intense scrutiny due to its remarkable properties, including surface activity [1], redox and defect chemistry [2], and oxygen transport [3], with application in areas such as catalysis [4]. If ceria is to be replaced by its nanostructured counterpart it must resist damage under the harsh environmental conditions associated with its operation, such as extremes of temperature, impact, friction, and wear. It is therefore vital to understand the influence of working conditions on the real material. Working conditions, such as temperature, are an important factor to consider when selecting a catalyst. With many potential applications, the safe operating temperatures for catalysts is of high significance, and commonly results in long winded experimental studies [5, 6]. Computational studies of temperature, although not always directly comparable to experiment, can provide insight into how temperature affects catalysts, without the risks and time consumption associated with experiment.

Simulation poses many benefits to experimental investigation, and can complement experimental analysis to give greater understanding of the chemical and mechanical behaviour of a material. This is not to say that it does not also have its own shortfalls as well. Computational chemistry is an area of science that is still relatively new, and relies heavily on experimental data, advancement in technology, and new mathematics. It is therefore reasonable to anticipate the creation and use of non-ideal models in the founding years, which requires development and improvement. For example, in Chapter 2 Section 2.3.3, the use and development of computational compression techniques is discussed. The progress in technique development leads to the method of compression used in this thesis, however the technique could still be improved upon. A limitation of some of the compression methods discussed in Chapter 5 Section 5.2, is the assumption of a static surface area. As deformation occurs, the surface area of the material changes, and the contact area with the anvils can increase spreading the pressure load over a larger area. At the nanoscale even the slightest change in pressure distribution can have extreme effects, and therefore a dynamic surface area should be considered to give a more accurate representation.

In this chapter we continue our investigation into the mechanical properties of ceria, furthering the scope to consider the dynamics, specifically the dynamic surface area, to produce a more realistic representation of a ceria nanoparticle. Environmental conditions, namely temperature and compression rate, will also be explored to determine how they affect the properties of the material.

6.2 Basic Compression Method

6.2.1 Potential models

The simulations presented in this Chapter were preformed using Molecular Dynamics (MD) simulation utilising the Born model of the ionic solid. The energy of the system, E, is given by Equation 6.1.

$$E(r_{ij}) = \sum_{ij} \frac{Q_i Q_j}{4\pi\varepsilon_0 r_{ij}} + \sum_{ij} A \exp\left(\frac{-r_{ij}}{\rho}\right) - C r_{ij}^{-6} \tag{6.1}$$

Where the first term represents the Coulombic interaction between ions, i and j, of charge Q_i and Q_j at a distance of r_{ij}. The second term represents the Buckingham form with the potential values [7, 8] presented in Table 6.1 along with the atom mass and charges. All ion-ion interactions were set to zero.

Table 6.1: Buckingham potentials used for the MD simulations within this chapter, along with the mass and charges.

Atom i	Atom j	A/eV	ρ/Å	C/eV Å^{-6}
Ce	O	1986.83	0.3511	20.40
Mg	O	1428.50	0.2945	0.00
Ba	O	931.70	0.3939	0.00
O	O	22764.00	0.1494	27.88

Atom	Mass	Charge
Ce	140.12	4.00
Mg	24.30	2.00
Ba	137.33	2.00
O	16.00	-2.00

6.2.2 Atomistic models

As in Chapter 5, simulated amorphization and recrystallization was used to generate atom-level models. The same models and parameters were used for all simulations, with the exception of temperature and compression rate, where discussed.

6.2.3 Uniaxial Compression

As described in Chapter 5 Section 5.2, uniaxial compression was performed under constant volume (NVT) MD simulation. Anvils were moved at a rate of 10 ms^{-1} (unless stated otherwise). The strain within the system is expressed as:

$$strain = \frac{(L_0 - L_x)}{L_0} \tag{6.2}$$

Where L_0 is the initial distance between the anvils and L_x is the distance after each compressive movement.

6.3 Static VS Dynamic Surface Area

6.3.1 Theory and Method

Pressure (P) is applied perpendicular to the surface of the object, taking into account the per unit area (A) which that force (F) is distributed. This is described mathematically as:

$$P = \frac{F}{A} \tag{6.3}$$

When an object is under uniaxial compression, it will relieve pressure by expanding into the surrounding unoccupied space (Figure 6.1), creating an increase in surface area. This therefore results in the same applied force acting on a larger surface area, and thus producing a smaller overall pressure. Previously the pressure acting on the nanoparticle has been calculated using the system pressure output from DL_POLY. These values were adjusted to the pressure acting in the direction of compression, then to the surface area of the particle. The general expressions for these are:

$$A' = \frac{A_C}{A_D} \tag{6.4}$$

$$P' = P.A' \tag{6.5}$$

$$A'' = \frac{A_D}{A_P} \tag{6.6}$$

$$P'' = P'.A'' \tag{6.7}$$

Where A_C, is the surface area of the system cell, A_D is the surface area in the direction of compression, and A_P is the surface area of the particle which is in contact with the anvil. A' and P' are the area and pressure in the direction of compression, and A'' and P'' are the area and pressure applied to the surface of the nanoparticle.

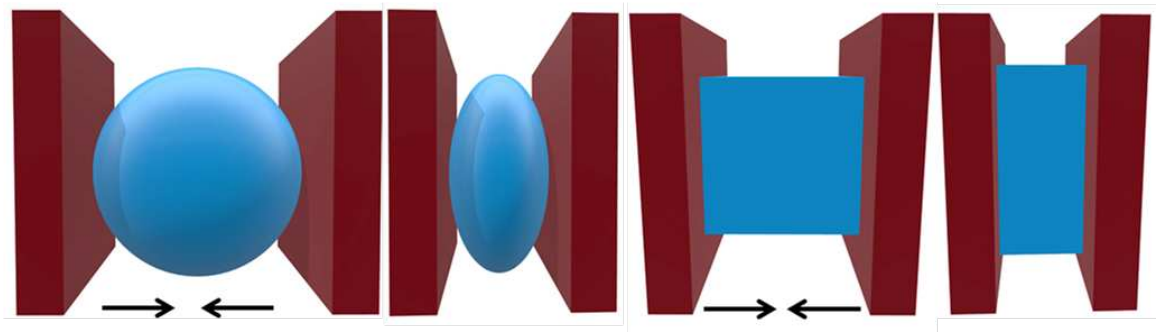

Figure 6.1: Diagrammatic representation of the uniaxial pressure causing an increase in the surface area contacting the anvils (green). The black traces show the 2-dimensional increase in size for a spherical object and cuboidal object.

This surface area is the initial surface area of the particle which is not recalculated as the compression continues, resulting in the pressure being overstated. Therefore the assumption of a constant surface area of the particle does not reflect the dynamic progression of the system. To determine whether the pressure could be more accurately measured, a new approach was developed where the surface area of the particle was recalculated with each restart of the compression.

With each movement of the anvil the co-ordinates of all atoms were corrected to the periodic boundaries (i.e. 0 to 100 rather than -50 to 50). The positions of the particle atoms in relation to the anvil were determined and those within a 4 Å distance were isolated. These atoms were used to determine the maximum and minimum co–ordinates in the perpendicular directions to the anvil, which form a basis for the surface area ($x * y$). Although this is not an accurate measurement of the surface area (excludes the potential for an irregular or spherical surface area, or the partial embedment of the particle into the anvil), it is a closer approximation of the surface area in comparison to the static surface, and a basis to work from.

6.3.2 Results

6.3.2.1 Surface Area Increase

The stress–strain curves presented in Figure 6.2 show the increase in surface area in relation to increasing strain. Within the first 20% of the compression, the surface area of the nanocube has increase by 9% (fixed), 18% (MgO), and 8% (BaO). This further increases to 70%, 45%, and 64%, respectively by 40% compression. This shows that not only does the surface area increase as the strain increases, but the surface area is dependent on anvil type. As the stress–strain curve shows, over the course of a full strain (100%) there is a trend showing that the softer the anvil, the smaller the change in the surface area. This is not however indicative of the initial 40% of the compression, where there is much overlap between the anvil types. The values and % increase in surface area for 0, 20, 40, 60, 80, and 100% are given in Table 6.2.

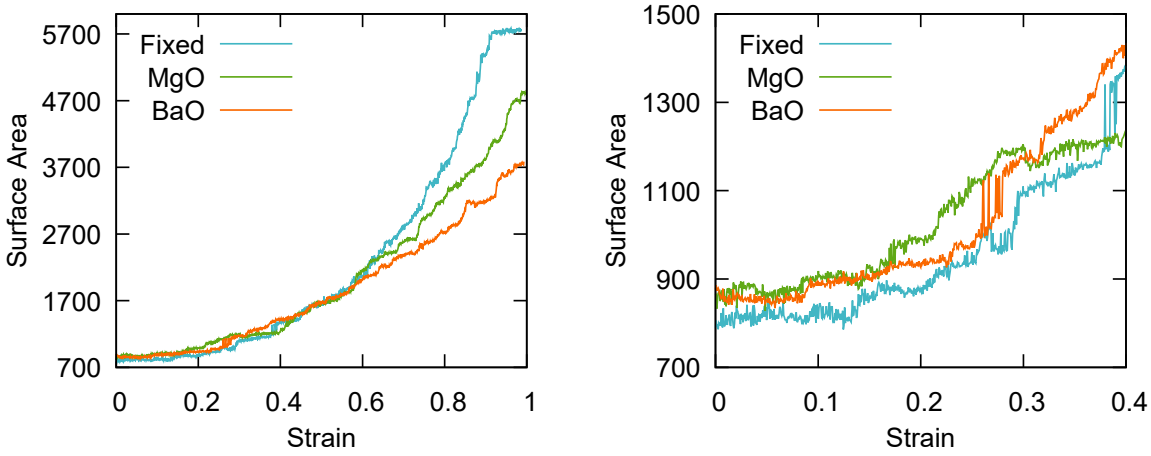

Figure 6.2: Strain curves of the surface area plotted against the strain for fixed, MgO, and BaO anvils, with the right curve highlighting the initial 0.4 strain.

This change in surface area is related to the deformation of the ceria nanocube, as described in Chapter 5. Softer anvils act as a protective shell around the nanoparticle, deforming themselves, which causes the nanoparticle to indent into the surface of the anvil, therefore reducing the overall surface area diameter. This effect is reduced with harder anvils, and is non–existent with fixed anvils. The change in surface area of the nanoparticle through the compression can be seen clearly in Figure 6.3, where the fixed anvil has the largest increase in surface area, followed by MgO, then BaO, as the stress–strain curve in Figure 6.2 shows.

Table 6.2: Surface area and relating % increase at set strains for each anvil type (BaO, MgO, and fixed)

Strain	BaO anvils Surface area (Å^2) [% increase]	MgO anvils Surface area (Å^2) [% increase]	Fixed anvils Surface area (Å^2) [% increase]
0%	867	864	789
20%	926 [6.8]	991 [14.7]	873 [10.6]
40%	1434 [65.4]	1234 [42.8]	1381 [75.0]
60%	2011 [131.9]	2162 [150.2]	2074 [162.9]
80%	2716 [213.3]	3254 [276.6]	3756 [376.0]
100%	3762 [333.9]	4803 [455.9]	5770 [631.3]

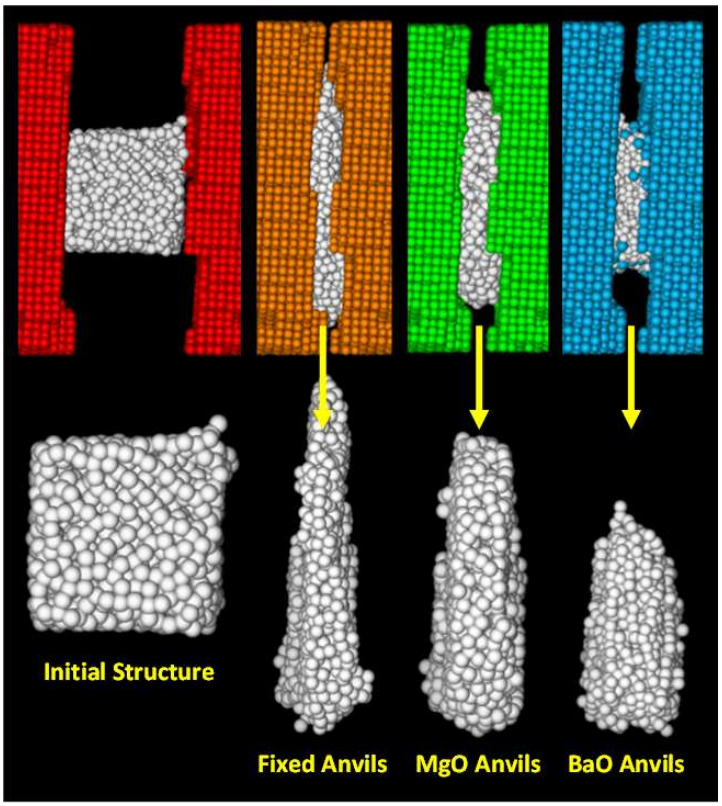

Figure 6.3: Compression of a ceria nanocube sandwiched between three anvil types. The bottom images show the initial and compressed states of the ceria nanocube.

6.3.2.2 Static vs Dynamic Stress–Strains

The stress–strain curves presented in Figure 6.4 show the difference between using a static (left) and dynamic (right) surface area for the calculation of stress. The dynamic surface area showed a significant effect on the measured strength, reporting substantially lower stress values for the same strain.

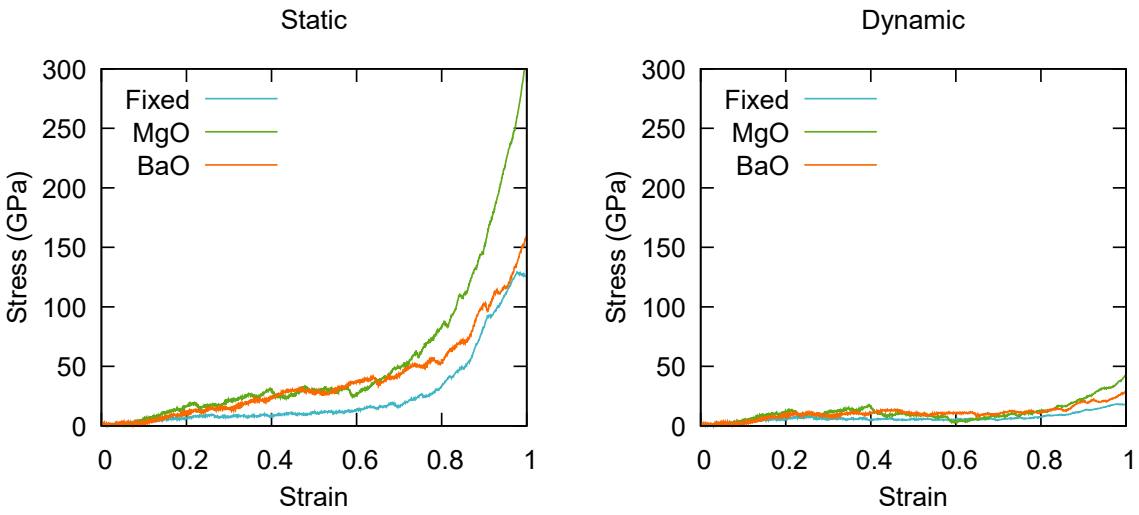

Figure 6.4: Stress–strain curves for fixed, MgO, and BaO anvils, with the left curve showing the static surface area and the right curve showing the dynamic surface area.

This reduction in stress however is not equivalent between the anvil types. Figure 6.5 shows the first 40% strain in better clarity. Here we can see that the reduction in stress is higher for the MgO anvils, in comparison to the BaO anvils. This is clearly highlighted between a strain of 0.2–0.3, where in the static curve, the MgO is higher than the BaO, however in the dynamic curve, the BaO is higher. Referring back to Figure 6.2, this same strain range shows a higher surface area increase in the MgO system, therefore this reduction in stress correlates to the surface area increase being comparatively higher at this strain. To better gauge the effect the surface area has, it is prudent to consider the differences between the static and dynamic surface areas for each anvil type separately.

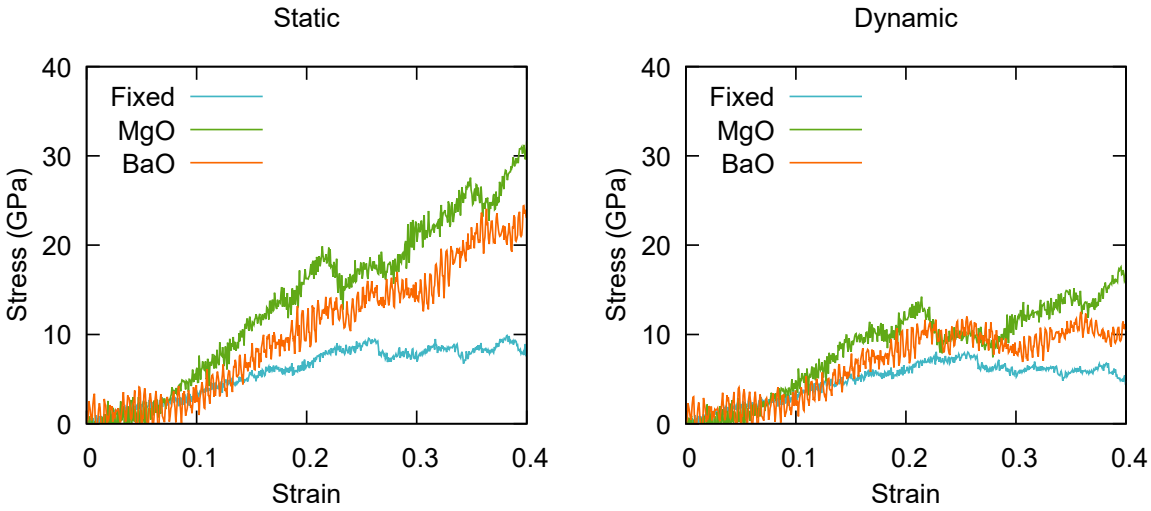

Figure 6.5: Stress–strain curves for fixed, MgO, and BaO anvils, with the left curve showing the static surface area and the right curve showing the dynamic surface area, up to 40% strain (0.4).

As presented in Chapter 5, the yield strengths for the ceria nanocube for each anvil type is 11.6 GPa at 0.2 strain for BaO anvils, 12.1 GPa at 0.17 strain for MgO anvils, and 2.5 GPa at 0.1 strain for fixed anvils. Figure 6.6 presents the stress–strain data for the BaO anvil system, left giving full strain (0–1) and right giving strain to 40% (0–0.4). Here, the yield strength of 11.6 GPa at 0.2 strain can be seen to have reduced to 8.7 GPa when a dynamic surface area is considered. This is a 2.9 GPa (25%) reduction in stress communicated to the nanoparticle. At a strain of 0.3, this difference increases to 6.2 GPa, which is a 45% reduction in measured stress (13.8 GPa for static and 7.6 GPa for dynamic).

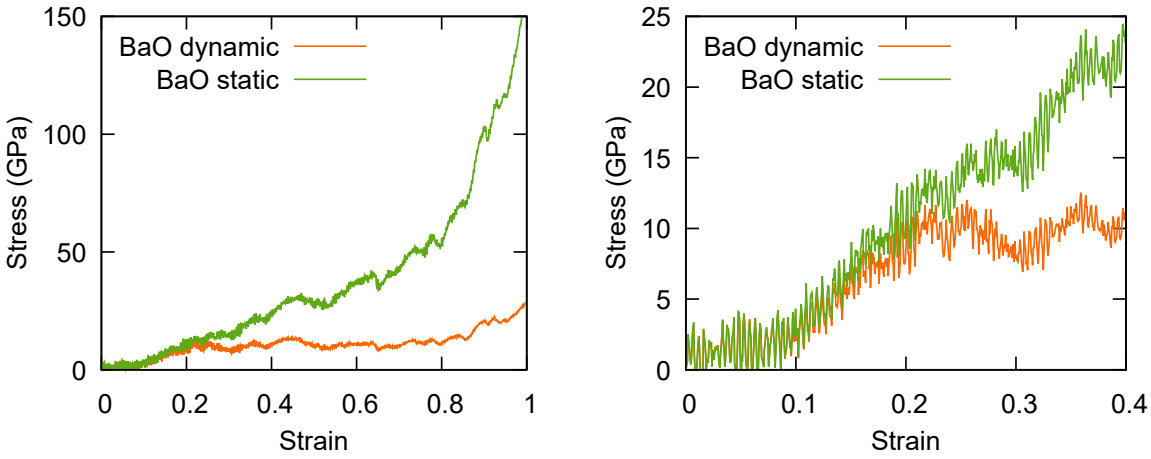

Figure 6.6: Stress–strain curve for BaO anvils, comparing the static and dynamic surface area methods of calculating stress.

Figure 6.7 presents the stress–strain data for the MgO anvil system, left giving full strain (0–1) and right giving strain to 40% (0–0.4). Here, the yield strength of 12.1 GPa at 0.17 strain can be seen to reduced to 9.1 GPa when a dynamic surface area is considered. This is a 3.0 GPa (25%) reduction in stress communicated to the nanoparticle, which is similar to that of the BaO anvil system. At a strain of 0.3 however, the difference between the static and dynamic surface area systems increases to 9.9 GPa, which is a 49% reduction in measured stress (20.4 GPa for static and 10.5 GPa for dynamic), which is a slightly higher reduction in measured stress compared to the BaO anvil system.

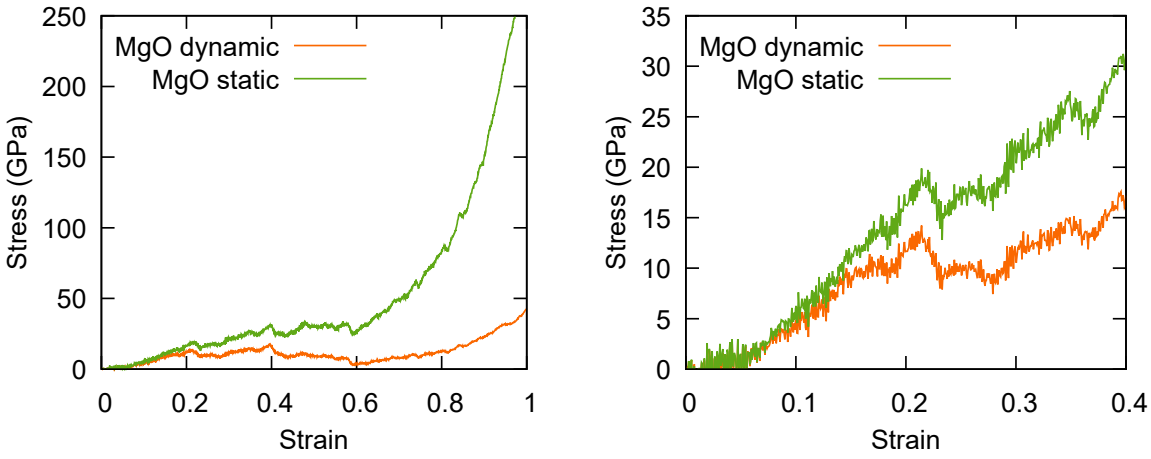

Figure 6.7: Stress–strain curve for MgO anvils, comparing the static and dynamic surface area methods of calculating stress.

Figure 6.8 presents the stress–strain data for the fixed anvil system, left giving full strain (0–1) and right giving strain to 40% (0–0.4). Here, the yield strength of 2.5 GPa at 0.1 strain can be seen to reduce (negligible) in the dynamic surface area system (2.47 GPa). At a strain of 0.3 however, the difference between the static and dynamic surface area systems is more prominent, increasing to a difference of 1.8 GPa, which is a 26% reduction in measured stress (7.0 GPa for static and 5.2 GPa for dynamic), this is almost half that of the BaO and MgO anvil systems.

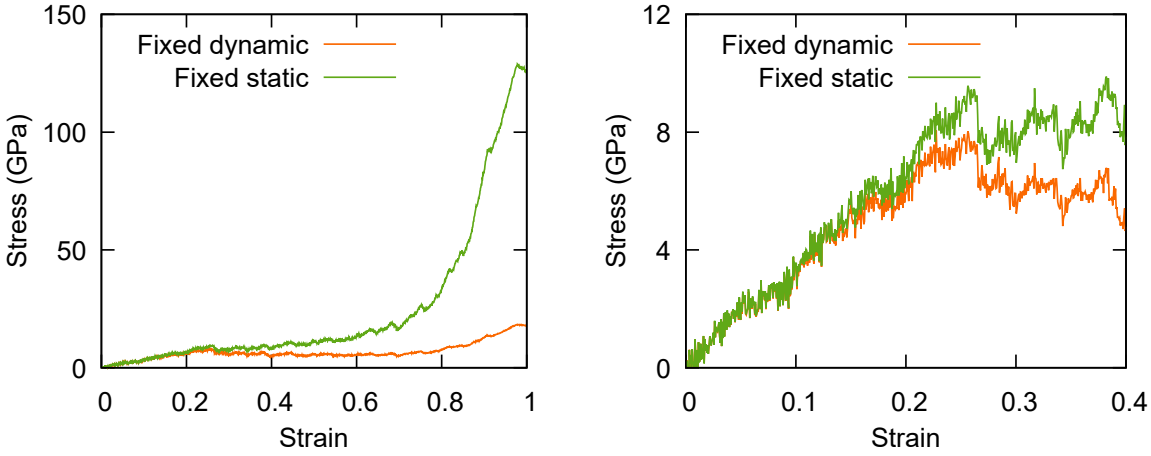

Figure 6.8: Stress–strain curve for fixed anvils, comparing the static and dynamic surface area methods of calculating stress

A comparison of the stress–strain values for the static and dynamic measurements with each anvil type is given in Table 6.3. In comparison to a study conducted by Sato *et al* [9] the fracture strength of nanoceria was determined as 0.25 GPa, which is one example of experimental measurements producing comparatively low stress values to simulation. With the introduction of a dynamic surface area measurement, the values produced from these simulations appear to correlate closer with experiment, giving more representative stress values.

Table 6.3: Comparison of the stress-strain data for static surface area and dynamic surface area systems, for BaO, MgO, and fixed anvils

Strain	BaO stress (GPa) static/dynamic	MgO stress (GPa) static/dynamic	Fixed stress (GPa) static/dynamic
0.1	2.4/2.0	6.3/4.8	2.5/2.5
0.2	11.6/8.7	16.2/11.7	6.4/5.9
0.3	14.4/8.1	20.4/10.5	7.0/5.2

6.3.3 Conclusions

A method of measuring the surface area of a ceria nanoparticle under pressure was developed and employed to incorporate a dynamic area into the measured stress. This dynamic method was compared to the already established static area measurement method. The results presented in this chapter reveal the vital role dynamic calculation of surface area has on the measured stress-strain properties. Initial measurements within the elastic region are similar to that of the static surface area measurements as the surface area had no significant increase. As the compression approached plastic deformation however the change in surface area had a significant impact. With the force distributed over a larger surface area, the pressure required to cause the plastic response is evidently lower. This is even more prominent when reaching the fracture strength of the ceria nanocube, where the surface area has increased exponentially.

The change in surface area of the nanoparticle also relates to the anvil type used in the compression, with fixed anvils communicating less stress onto the particle in comparison to the MgO and softer BaO anvils. Where at 100% strain, the surface area of the nanoparticle using fixed anvils is 631.3% larger than that of 0% strain. For MgO there is an increase of 455.9% and only 333.9% for BaO. The introduction of dynamic calculations of surface area has significantly reduced the measured stress on the nanoparticle, which closer aligns with measurements observed experimentally.

6.4 Simulated 'Temperature' Effects

6.4.1 Explanation of Simulated Temperature

DL_POLY provides the option for a range of ensembles (NVE, NVT, NPT, and N$\underline{\underline{\sigma}}$T), with a selection of different thermostats and barostats. Constant temperature is an important constraint for studying the behaviour of a system at different temperatures, therefore a constant number of particles, constant volume, and constant temperature ensemble, NVT, was employed. Constant temperature in MD is, in a sense, instantaneous. This means that if you change the system temperature from, for example, 300 K to 1000 K, the new temperature is instantly applied to all atoms in the system, rather than heat transferring from one atom to the next, such as in a heat bath. Constant temperature in MD is not actually instantaneous as the new temperature is ramped over a set duration time, known as the relaxation time and it is driven towards the desired temperatures by scaling the velocities. Temperature is based on kinetic energy and can be represented mathematically as given in Equation 6.8, where E_k is the kinetic energy, N is the number of particles, k_B is the Boltzmann constant, T is the desired temperature, and m_i and v_i are the mass and velocity of particle i.

$$E_k = \frac{3}{2} N k_B T = \sum_{i=1}^{N} \frac{1}{2} m_i {v_i}^2 \tag{6.8}$$

The available algorithms for an NVT ensemble are those of Evans [10] (a gaussian constraint), Berendsen [11], and Hoover [12]. A thermostat is used which couples the system to a heat bath to ensure that the average temperature of the system is maintained close to the desired temperature (T_{ext}). This modifies the equations of motion, where the system no longer samples the microcanonical ensemble, but instead the trajectories in the canonical NVT ensemble are generated. Of the three previously mentioned algorithms available for NVT, only the Nose–Hoover generates trajectories in the canonical NVT ensemble. This parameter is defined in the CONTROL file with the line: ensemble nvt hoover f. Where f is the relaxation constant (ps). Newton's equations of motion are modified in the Nose–Hoover algorithm as described below (Equations 6.9 and 6.10).

$$\frac{d\overrightarrow{r}(t)}{dt} = \overrightarrow{v}(t) \tag{6.9}$$

$$\frac{d\overrightarrow{v}(t)}{dt} = \frac{\overrightarrow{f}(t)}{m} - \chi(t)\overrightarrow{v}(t) \tag{6.10}$$

Here, t is the time, r is the position vector, $\overrightarrow{v}$ and $\overrightarrow{f}$ are the velocity and force, m is the mass of the particle, and χ is the friction coefficient. The friction coefficient is controlled by the first order differential equation, Equation 6.11.

$$\frac{d\chi}{dt} = \frac{N_f k_B}{Q}(\tau(t) - T_{ext}) \tag{6.11}$$

Where $Q = N_f k_B T_{ext} {\tau_T}^2$ is the effective mass of the thermostat, τ_T is a time constraint (specified by the user, in this case 0.1 ps), N_f is the system's degrees of freedom, and $\tau(t)$ is the instantaneous temperature of the system at time t. $\frac{N_f k_B}{Q}$ can also be expressed as α to denote the rate at which the system is scaled to drive the system.

Although the NVT ensemble controls the temperature to a specified value, simulated temperature is not always representative of experimental temperature. The potentials and charges placed on the atoms affect their interactions and energy, and therefore also affect simulated temperature. We therefore consider temperature as a function of the melting temperature. For example, the experimental melting temperature of cerium (IV) dioxide is approximately 2400 °C, however it does not melt in the simulated system until closer to 6000 °C. This deviation can be coarsely scaled to experimental temperatures as given in Equation 6.12

$$T_s = \frac{T_w}{T_m} T_w \tag{6.12}$$

Where T_s is the scaled temperature, T_w is the simulated working temperature, and T_m is the simulated melting temperature.

The simulated temperature is greatly affected by the potentials used in the modelling. For example, use of partial charges will produced different simulated melting temperatures to full charges, and use of Buckingham potentials compared to Morse potentials will also have differences. The choice of which potentials to use is determined by the purpose of the simulation, and the other potentials they have to interact with. After choosing appropriate potentials for the task, there is a level of trial and error in determining the melting temperature of the particles by running the simulation at different temperatures until the particle melts.

A point worth noting is how the initial temperature of the system is generated and the differences in the equilibration stage. The CONFIG is the input file which can contain co–ordinates, velocities, and forces for each atom in the system, with co–ordinates being the only compulsory parameter. This is the case of many simulations where only the co-ordinates are provided. DL_POLY therefore employs a Gaussian distribution of velocities which would give an average temperature towards the desired temperature. As most input files do not produce systems which have been adjusted to their parameters, including the temperature, an equilibration is performed. This involves scaling the temperature (and pressure) every step rather than over a relaxation time, resulting in a finer transition of the random (Gaussian) distribution of velocities to a more stable and favourable range.

6.4.2 Method

The method used for the simulations presented here is described in Chapter 5, Section 5.2. The only modification to this method is the change in temperature, as set by the CONTROL file. The compressions were conducted at simulated temperatures of 300 K, 700 K, 1000 K, 1300 K, 2300 K, 3000 K, and 3500 K.

6.4.3 Results

The raw stress–strain curves for the compression of the ceria nanocube at each temperature is given in Appendix 5.1. As the temperature increases, the data curves becomes overwhelmed with noise, thus clouding the finer details. For this reason the data presented in this section uses averaged data. This is done by averaging each data point with the surrounding 4 points (5 including the data point in question) to reduce the noise, resulting in higher clarity of the events occurring within the stress–strain curves.

The averaged stress–strain curves for the ceria nanocube compression at 300 K, 700 K, 1000 K, and 1300 K, are shown in Figure 6.9. Initial results show that with an increase in temperature, the stress on the nanoparticle is lower, indicating the particle deforms plastically at lower stress when the temperature increases. This is not unexpected since materials generally become more pliable with the addition of heat. The stress–strain curves however also indicated a threshold between 700 K and 1000 K where the stress difference is substantially reduced.

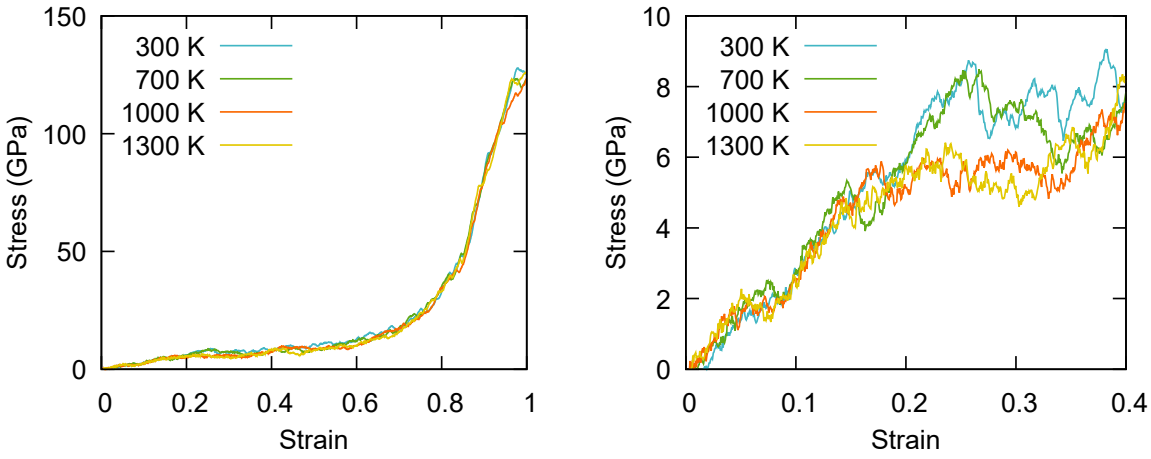

Figure 6.9: Averaged stress–strain curves for the ceria nanoparticle compression using fixed anvils at temperatures of 300 K, 700 K, 1000 K, and 1300 K, with the right curve highlighting the initial 0.4 strain.

When the temperature is increased above 2000 K there is another substantial drop in the stress, as presented in Figure 6.10, with a further reduction in stress after 3000 K. A possible reason for the sudden shift in stress could be due to the temperature introducing enough energy into the CeO_2 structure to overcome a discrete energy level. When the atoms within the CeO_2 overcome this energy barrier there is greater movement of the atoms within the system, and therefore less imposed stress would be needed to reconfigure or deform the structure. This is only one possible explanation for the shifts in stress at certain temperature ranges, and there are other factors which need to be considered.

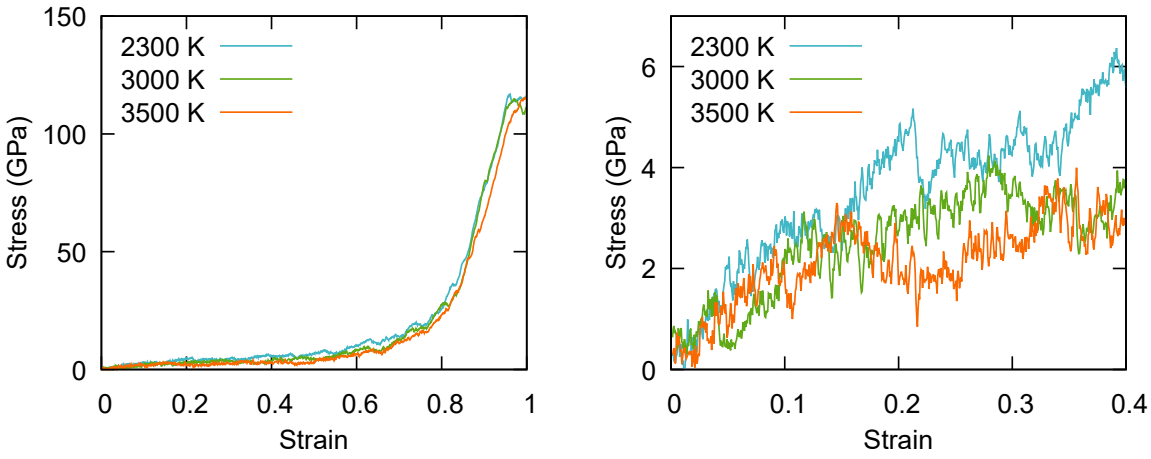

Figure 6.10: Averaged stress–strain curves for the ceria nanoparticle compression using fixed anvils at temperatures of 2300 K, 3000 K, and 3500 K, with the right curve highlighting the initial 0.4 strain.

A comparison of the lowest (300 K), highest (3500 K), and midrange (1300 K) temperatures for this system is given in Figure 6.11. Here the reduction of measured stress as a result of increase in temperature can be clearly seen. Not only is the measured stress reduced, but the strain at which plastic deformation occurs is also affected.

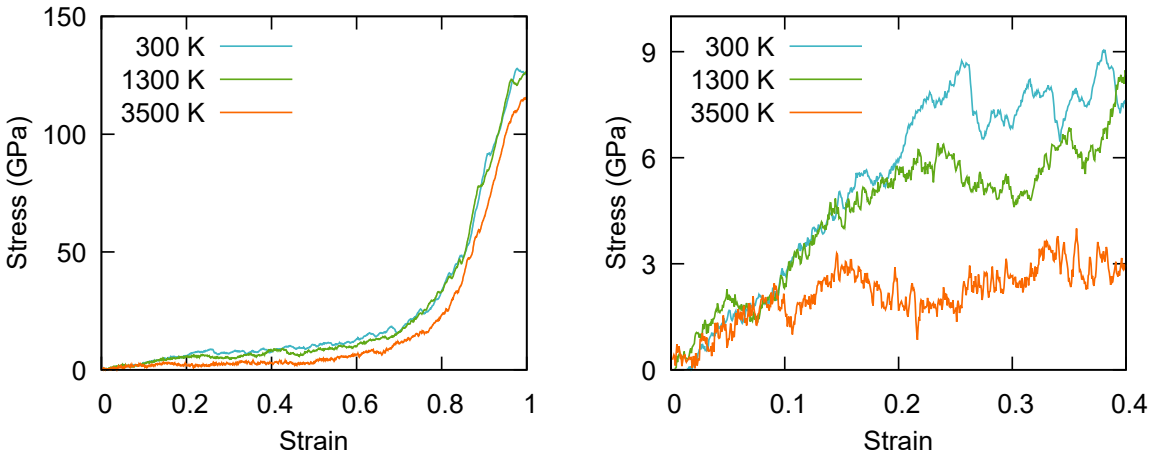

Figure 6.11: Comparison of averaged stress–strain curves for the ceria nanoparticle compression using fixed anvils at temperatures of 300 K, 1300 K, and 3500 K, with the right curve highlighting the initial 0.4 strain

6.4.4 Conclusions

The temperature of a ceria nanoparticle compression was carried out was varied to determine the effect of temperature on the system. The results presented in this chapter reveal that increasing the temperature of the system cause a reduction in measured stress. Furthermore the strain at which plastic deformation within the nanoparticle occurs is also affected. There are significant shifts in the stress within certain temperature ranges. Where below 1000 K, measured stress is in the range of 8 GPa for a strain of 0.2. For temperatures between 1000 K and 2000 K, the stress is reduced to roughly 5–6 GPa for a strain of 0.2, and temperatures above roughly 3000 K, the stress is further reduced to roughly 2–3 GPa for the same strain. This phenomenon could be caused by reaching a temperature threshold, where enough heat is added to the system for atoms to overcome discrete energy barriers and cause vibrations.

6.5 Compression Rate Effects

6.5.1 Velocity–Strain Relationship

The rate, or velocity, at which a material is compressed affects the stress–strain properties of a material. Variation in the rate of compression affects the reaction time of the material to the additional strain. In the previous compression simulations presented in this chapter, the anvils were moved at a rate of 10 ms^{-1}. This was done by fixing the atoms at the back of the anvil (or all atoms in the anvil) and moving those atoms by 0.02 Å every 100 steps, with a time step of 0.002 ps, which can be expressed mathematically using Equation 6.13.

$$V = \frac{d}{t_s n_s} \tag{6.13}$$

Where V is the velocity, d is the distance, t_s is the time step, and n_s is the number of steps between each movement. The steps between each anvil movement were included to reduce the computational expense, as well as to allow for a relaxation period, where the strain caused by the updated co-ordinates could be communicated to the particle (and to the rest of the anvil). Without a relaxation period the resulting stress–strain data would be more erratic with less defined information.

Experimentally, compression rate measurements can vary, depending on equipment and subject material. Similar materials to cubic nanoceria are closer to 1 ms^{-1}. In this section, the simulated compression rate is investigated to determine the effect on the measured stress–strain properties.

6.5.2 Method

The method used for the simulations is described in Chapter 5, Section 5.2, where only fixed anvils were considered for this section. The modifications made to this method were: the distance the anvil atoms moved (d), and the number of steps between each movement (n_s). These were modified to give compression rates of 0.5, 1, 5, 10, and 15 ms^{-1}, in accordance with Equation 6.13, where t_s was kept at 0.002 ps. These modified values are given in Table 6.4.

Table 6.4: Modified values to the fixed anvil compression simulation, as described in Chapter 5 Section 5.2, along with the resulting compression rates.

Compression Rate (ms^{-1})	Number of Steps [n_s]	Distance (Å)
0.5	1000	0.01
1	1000	0.02
5	100	0.01
10	100	0.02
15	100	0.03

6.5.3 Results

The raw stress–strain curves for the compression of the ceria nanocube for each compression rate is given in Appendix 5.2, Figure 5.3. At the lower compression rates, more data points were collected and the plot becomes noisy, therefore the data presented in this section uses averaged data. This is done by averaging each data point with the surrounding 4 points (5 including the data point in question).

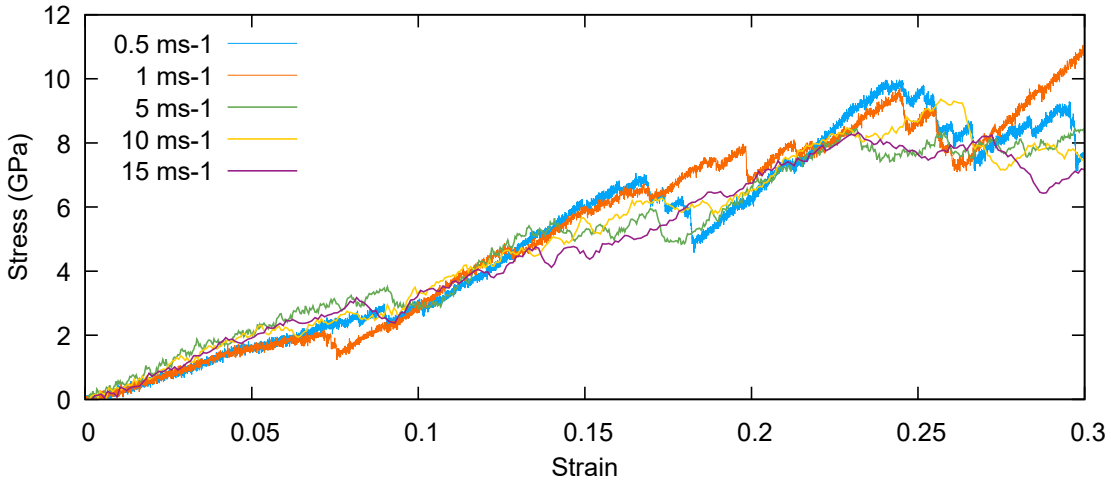

Figure 6.12: Comparison of averaged stress–strain curves for the ceria nanoparticle compression using fixed anvils at compression rates of 0.5, 1, 5, 10, and 15 ms^{-1}.

The averaged stress–strain curve, presenting a comparison of each compression rate, is given in Figure 6.12. At first glance, there appears to be little difference between compression rates, however when separated and compared individually, differences become more apparent. Appendix 5.3 , figures 5.4 to 5.8 give individual stress–strain curves for compression rates of 0.5, 1, 5, 10, and 15 ms^{-1}, respectively. Figure 6.13 gives the individual stress–strain curves for 0.5 and 15 ms^{-1} for comparison.

The most notable difference is the sharpness of the plastic deformation. The faster the compression, the shorter the time period for communicating the applied strain caused by the movement of the anvil to the particle, i.e. the relaxation time. This results in higher localised stress in comparison to global stress across the particle, thus more frequent smaller events. With slower compressions there are longer relaxation periods where the localised stress can be communicated to the rest of the particle, giving a higher global stress and minimal localised stress. This is reflected in the stress–strain curves, where 15 ms^{-1} presents smaller, more frequent, reductions in stress, and 0.5 ms^{-1} presents larger, less frequent, reductions in stress.

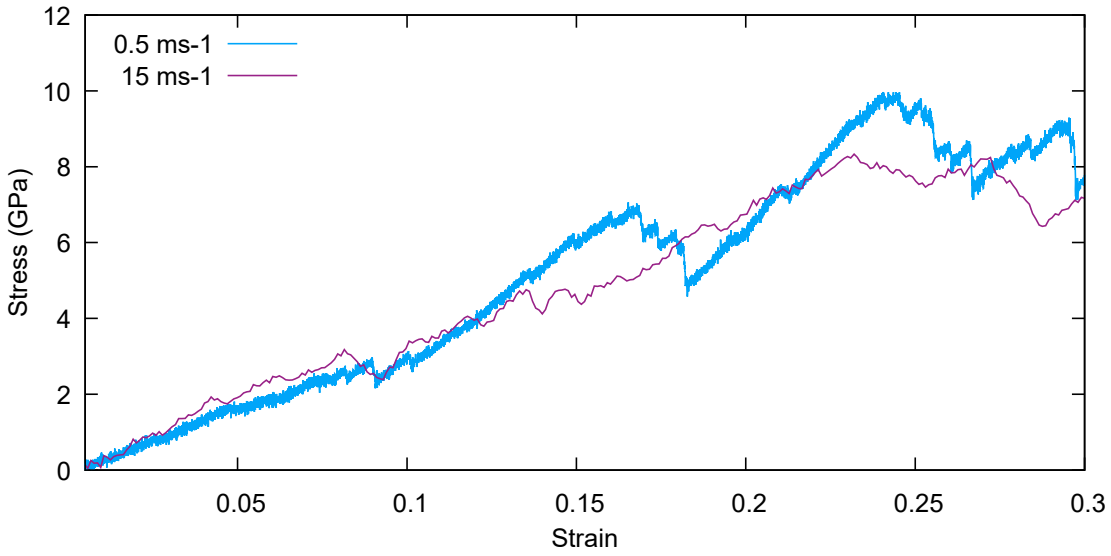

Figure 6.13: Comparison of averaged stress–strain curves for the ceria nanoparticle compression using fixed anvils at compression rates of 0.5 and 15 ms^{-1}.

The elastic moduli for the compressions is given in Table 6.5, with the relating curves presented in Appendix 5.4, Figures 5.9 to 5.13. There is no specific trend relating the compression rate to the elastic modulus, however there is an arguably notable increase in the elastic modulus between 1 ms^{-1} and 5 ms^{-1}, and a general increase as the compression rate increases. To fit a trend between the compression rate and elastic modulus, more data points would be needed. However it could be speculated that the increase in the elastic modulus as the compression rate increases is due to higher localised stress, as the particle has a lower relaxation time to distribute the stress more globally throughout the particle.

Table 6.5: Elastic modulus data relating to each compression of the ceria nanoparticle at compression rates of 0.5, 1, 5, 10, and 15 ms^{-1}.

Compression Rate (ms^{-1})	Regression Equation	Elastic Modulus
0.5	$y = 32.719x - 0.055$	32.719
1	$y = 31.309x - 0.013$	31.309
5	$y = 41.404x + 0.095$	41.404
10	$y = 37.740x - 0.051$	37.740
15	$y = 42.634x - 0.146$	42.634

6.5.4 Conclusions

The compression rate of the ceria nanoparticle was varied to determine what, if any, effect this would have on the compression of the system. The compression rates compared were 0.5, 1, 5, 10, and 15 ms^{-1}. The results presented in this chapter reveal that in the investigated range there is no specific overall effect on the measured stress–strain data. Lower compression rates however have more defined plastic deformation events, and arguably lower elastic moduli. With a more substantial difference in the compression rate, both the elastic modulus and the plastic deformations would suffer a greater effect, as indicated in the stress–strain at 15 ms^{-1}, where the yield point has the most substantial difference. Here, there are indications that reduced relaxation periods affect the distribution of stress globally throughout the particle, and instead the particle has higher regions of localised stress which resulted in less defined stress–strain curves. Compressions below 10 ms^{-1} have clear points of plastic deformation, with the yield point varying slightly, but within a negligible region.

There is a global relationship between increasing compression rate with increasing elastic moduli, however this is not linear and more data points would be required for a full deduction as to the relationship.

6.6 Discussion

6.6.1 Surface Area Measurement

Using a dynamic surface area for calculating stress acting on the particle is more natural and analogous to experiment. The results presented here reveal how vital dynamics surface area calculations are to measured stress–strain properties of a particle, more so as it reaches initial plastic deformation. The specific method employed here, although an improvement over use of a static surface area, is not optimal and requires refinement. Here, dynamic surface area is estimated using a 'box fit', where the surface area is considered uniformly square (i.e. $x * y$). This is a good estimate for the maximum surface area at each measurement, however in actuality, the surface area will be smaller and not uniform after the initial compression steps.

A more accurate method therefore needs to be developed to determine a better fit for the surface area. This would need to be considered in three dimensional space, as with deformable anvils there is a level of embedment into the anvil itself. As there are many factors to consider when calculating the surface area, including the non–uniform shape and the partial embedment into the anvil, as well as factors such as surface structure of the anvil (i.e. steps), oxygen exchange, and shortening of bond distances, it is conceivably more prudent to express the surface area as a range. This could be achieved by taking the minimum surface areas for each data point, and plotting the resulting stress–strain curve, and the same with the maximum surface area for each data point. As there are many factors which affect the stress–strain, it is likely that the real stress-strain properties will sit within this range, therefore predicting experimental properties could be more refined.

6.6.2 Working Conditions - Temperature Considerations

When working with any active material, the activity of the material under different working conditions must be considered. This includes mechanical properties such as strain and impact, as well as environment considerations such as temperature. At higher temperatures plastic deformation can occur at lower strains, therefore a working temperature range which has minimal effect on the activity of the material should be considered. The results presented in this chapter suggest the presence of discrete energy levels, where the increase in temperature has given the atoms enough thermal energy to surpass an energy barrier, affecting the mechanical properties. The temperatures at which these occur therefore need careful consideration.

6.6.3 Computational Trade-off

Computational simulations generally have some level of trade off between clarity/accuracy in the results with computational expense and/or overhead time. In this case, the overhead time is switching between running DL_POLY (for n number of steps), and the scripts which control the movement of the anvil. The number of steps which DL_POLY runs in each iteration is therefore critical to the overhead time, and to some degree, also the computational expense. With a lower value of n the overhead time becomes exceptionally high, however it allows for smaller, more frequent, movements of the anvil, resulting in a smoother and more consistent velocity. The derived stress-strains would therefore contain lower noise/fluctuation in the curve. For high values of n the overhead time is significantly reduced, however it requires larger, less frequent, movements of the anvil. This can lead to a more 'stop–start' motion in the anvil, where the velocity varies, resulting in stress–strains which contain high noise/fluctuations and can mask some of the features of the curve.

A middle ground is therefore needed to reduce the overhead without loss of clarity in the resulting data. This can be difficult to balance, and is dependent on factors such as the materials within the system, the computation facilities available, and the data being analysed.

6.7 Future Work

The work presented in this chapter is further work conducted from Chapter 5. These however are not the only considerations which can be given to this system. Further research could be conducted into varying the shape, size, and orientation of the nanoparticle, as well as use of different materials comprising the nanoparticle and/or anvils. A study into varying the microstructural features, i.e. the surface steps and voids, could also be further researched, as they play a vital role in the mechanical properties of a material. This work however would require an extended project, and in places would be challenging, and therefore was not possible here.

References

[1] K. Zhou, X. Wang, X. Sun, Q. Peng, and Y. Li. Enhanced Catalytic Activity of Ceria Nanorods from Well-Defined Reactive Crystal Planes. *Journal of Catalysis*, 229(1):206–212, 2005.

[2] M. Mogensen, N.M. Sammes, and G.A. Tompsett. Physical, Chemical and Electrochemical Properties of Pure and Doped Ceria. *Solid State Ionics*, 129(1-4): 63–94, 2000.

[3] A. Holmgren, D. Duprez, and B. Andersson. A Model of Oxygen Transport in Pt/Ceria Catalysts from Isotope Exchange. *Journal of Catalysis*, 182(2):441–448, 1999.

[4] N. Ta, J. Liu, and W. Shen. Tuning the Shape of Ceria Nanomaterials for Catalytic Applications. *Chinese Journal of Catalysis*, 34(5):838–850, 2013.

[5] G. Méli, J.M. Léger, C. Lamy, and R. Durand. Direct Electrooxidation of Methanol on Highly Dispersed Platinum-Based Catalyst Electrodes: Temperature Effect. *Journal of Applied Electrochemistry*, 23(3):197–202, 1993.

[6] R.V. Pindoria, A. Megaritis, A.A. Herod, and R. Kandiyoti. A Two-Stage Fixed-Bed Reactor for Direct Hydrotreatment of Volatiles from the Hydropyrolysis of Biomass: Effect of Catalyst Temperature, Pressure and Catalyst Ageing Time on Product Characteristics. *Fuel*, 77(15):1715–1726, 1998.

[7] G.V. Lewis and C.R.A. Catlow. Potential Models for Ionic Oxides. *Journal of Physics C: Solid State Physics*, 18(6):1149–1161, 1984.

[8] F. Caddeo, A. Corrias, and D.C. Sayle. Tuning the Properties of Nanoceria by Applying Force: Stress-Induced Ostwald Ripening. *Journal of Physical Chemistry C*, 120:14337–14344, 2016.

[9] K. Sato, H. Yugami, and T. Hashida. Effect of Rare-Earth Oxides on Fracture Properties of Ceria Ceramics. *Journal of Material Science*, 39(18):5765–5770, 2004.

[10] D.J. Evans and O.P. Morriss. Non–Newtonian Molecular Dynamics. *Computer Physics Reports*, 1(6):297–343, 1984.

[11] H.J.C. Berenden, J.P.M. Postma, W.F. van Gunsteren, A. DiNola, and J.R. Haak. Molecular Dynamics with Coupling to an External Bath. *The Journal of Chemical Physics*, 81:3684, 1984.

[12] W.G. Hoover. Canonical Dynamics: Equilibrium Phase-Space Distributions. *Physical Review a*, 31:1695, 1985.

Chapter 7

Silica Aerogel: A Computational Study

7.1 Introduction

Silica Aerogels, though widely used experimentally, are somewhat unused in computational studies. Attributing factors to this include high volume to atom ratio, the computational power requirement, and formation of interconnecting repeat cells. With such a low density material and the scale in which MD operates, capturing the amorphous and interlinking structure is challenging. There has been a few instances where models of aerogel have be used in molecular dynamics [1, 2, 3], however the scope of the investigation was limited to specific aspects due to the way in which the aerogel models were formed.

One of the main issues when using nanoparticles is the tendency for particle aggregation, forming larger macromolecules, and leading to a extensive reduction in surface area. This is particularly problematic in the field of catalysis where the reduced surface area will significantly reduce the reactivity of the particle [4]. The use of aerogel as a host matrix will allow the nanoparticles to be dispersed into the pores, preventing (at least in part) the aggregation and growth of the particles. Subsequently, the nanoparticles could also affect the mechanical properties of the aerogel, strengthening the structure, or causing weaknesses in the networked pores.

In this chapter, a newly developed approach to creating the SiO_2 aerogel model is presented. Nanoparticles comprising CeO_2, MgO, and BaO were embedded into the aerogel pore system and the resulting compression data also presented.

7.2 Method

All simulations presented in this chapter are based upon the Born model of the ionic solid. The energy of the system, E, is given by Equation 7.1

$$E(r_{ij}) = \sum_{ij} \frac{Q_i Q_j}{4\pi\varepsilon_0 r_{ij}} + \sum_{ij} A \exp\left(\frac{-r_{ij}}{\rho}\right) - C r_{ij}^{-6} \tag{7.1}$$

Where the first term represents the Coulombic interaction between ions, i and j, of change Q_i and Q_j, at a distance of r_{ij}. The second term represents the Buckingham form, with the model parameters given in Table 7.1 [5, 6]. A three-body potential was used alongside the Buckingham potentials for SiO_2 to control the bond angle within the structure, details of which are also given in Table 7.1.

Table 7.1: Potentials and parameters used for the MD simulations within this chapter, along with the mass and charges. [5, 6]

Atom i	Atom j	A(eV)	ρ(Å)	C(eV Å^{-6})
O	O	22764.0000	0.1494	45.8300
O	Si	1283.9070	0.3020	10.6615
O	Ce	1986.3000	0.3510	20.4000
O	Mg	1428.5000	0.2945	0.0000
O	Ba	931.7000	0.3939	0.0000

Atom i	Atom j	Atom i	Key	K (eV rad^{-2})	θ_0 (deg)	a	ρ (Å)	
O	Si	O	bvs2	2.09	109.4667	1.2	2.6	3.45

Atom	Mass (amu)	Charge (e)
O	15.9940	-2.00
Si	28.0860	4.00
Ce	140.1200	4.00
Mg	24.3050	2.00
Ba	137.3300	2.00

All simulations presented in the chapter were carried out using an NVT ensemble (Nosé-Hoover) with thermostat and barostat relaxation times of 0.5 and 0.5 ps respectively. The simulations were conducted with a time step of 0.001 ps and a cutoff at 10.00 Å. The electrostatics were calculated using an Ewald summation precision of $1d^{-3}$.

7.2.1 Formation of the Atomistic Models

7.2.1.1 SiO_2 Aerogel

Due to the nature of aerogel, consisting of a network of SiO_2 strands interconnecting between cells, the generation of SiO_2 aerogel was not conducted using a known or previously used method. The density of the aerogel was controlled by preselecting the cell volume (150 Å * 150 Å * 150 Å) and number of atoms in their stoichiometric ratio (6000 Si and 12000 O atoms), giving a density of 0.2 g cm^{-3}. Initially, a selected number of small SiO_2 clusters were placed in arbitrarily selected positions covering the volume of the cell. Individual atoms were then placed pseudo-randomly using a number-generator to determine acceptable co-ordinates within the cell; criteria for which enforce a minimum spatial distance of 4 Å between atoms. A constant volume and temperature (NVT) MD simulation was performed at 3000 K for 15 ps. This allowed for the randomly placed atoms to attach to the clusters. Clusters which formed chain like structures were selected and arbitrarily placed into a new cell of equal volume. These atoms were then fixed in position to promote chain growth, and new individual atoms were placed in pseudo-random positions as before, and an NVT MD simulation was repeated for 15 ps. This process was repeated four times, allowing the chain clusters to grow and merge, removing smaller unconnected clusters to make space for individual atoms, and promoting interconnecting cells. The final stage was extended to 50 ps to allow all atoms to attach, then the temperature was reduced to 300 K for 58 ps. The final atomistic model is given in Figure 7.1, along with images of the clusters/chains at the start of each of the four stages of chain growth.

The use of pseudo-random sampling for the initial placement of atoms is a well-practised method, widely utilised in simulation algorithms such as Monte Carlo. Monte Carlo relies on repeated random sampling to obtain numerical results, which are often used to solve difficult physical and mathematical problems, including three distinct problem classes: optimization, numerical integration, and probability distribution. Here, the use of pseudo-random sampling is utilised to place atoms in unoccupied locations within the unit cell, for a sizeable number of atoms. The actual position of the atoms is arbitrary, with the concern focused on preventing any overlap. Thus random seeds were used to generate a series of random numbers within the range of the cell parameters (i.e. 0–150), to use as x,y,z coordinates. These coordinates were then compared to all other atoms within the cell; those in an unoccupied space were accepted, and those within 4 Å of another atom were rejected. This process was then repeated until the total number of required atoms were accepted.

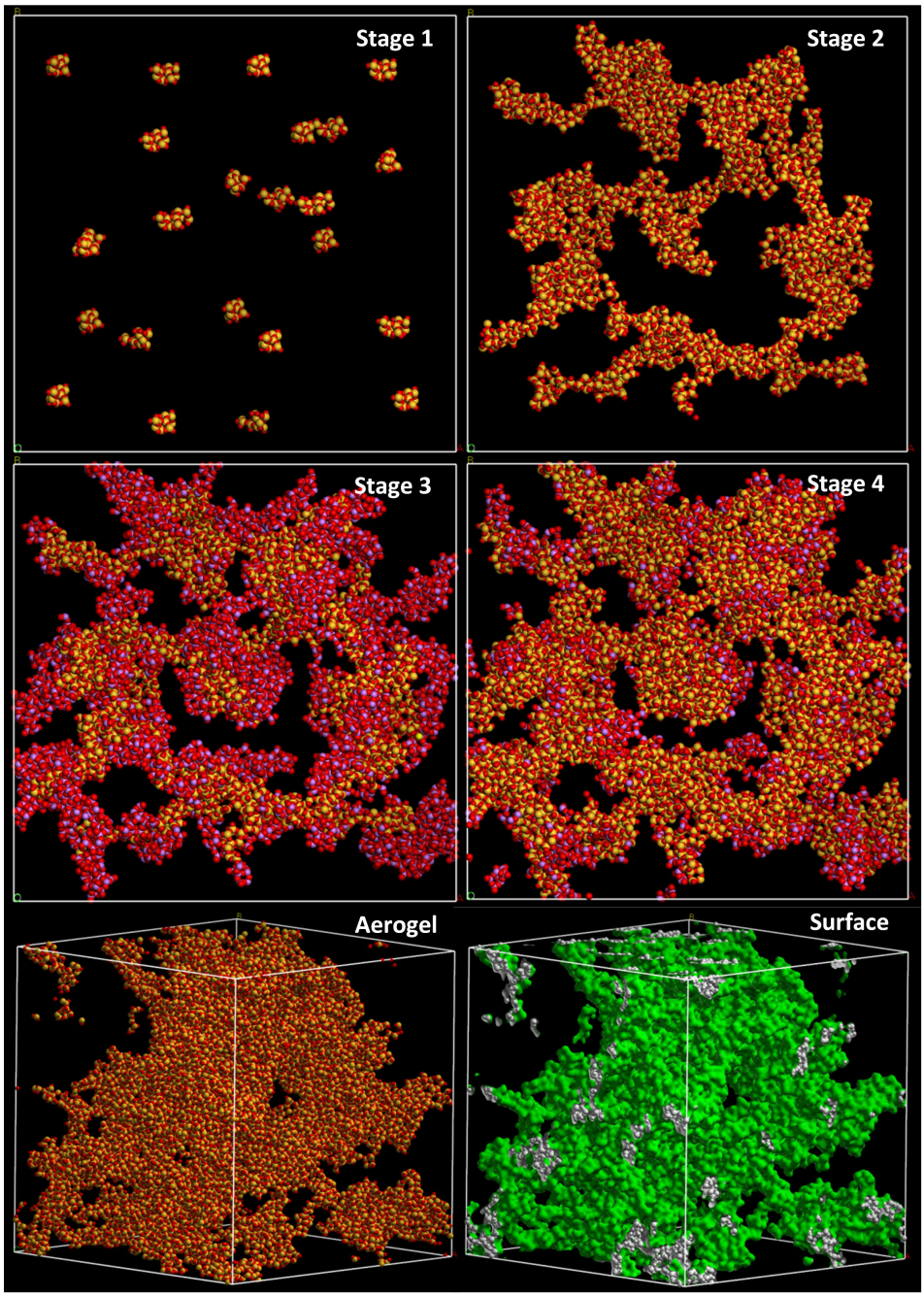

Figure 7.1: The four main stages in the formation of the SiO_2 aerogel atomistic model. Stage 1 – initial SiO_2 clusters, stage 2 – chains formed from the clusters and individual atoms, placed into a new cell and fixed, stage 3 – fixed clusters (yellow and red) with the individual atoms (purple and red) attached onto them, all fixed for the next stage, and stage 4 – new fixed frame work with the newly connected individual atoms (purple and red) attached onto them. The completed aerogel is given (labelled aerogel) forming a 0.2 g cm^{-3} density. The aerogel surface is shown in green, with the white sections indicating links to the repeating cells.

7.2.1.2 CeO_2 Nanoparticle

The ceria nanoparticle model was generated from a perfect crystal structure of CeO_2 comprising 1008 atoms (336 Ce atoms, 672 O atoms) and amorphization re-crystallisation was conducted by melting the ceria nanoparticle in a NVT MD simulation at 3750 K for 9714 ps. To re-crystallise the particle the temperature was reduced to 300 K for 10 ps under the same conditions. The final atomistic model is given in Figure 7.2.

7.2.1.3 MgO/BaO Nanoparticles

The MgO nanoparticle was formed using the same method as used for the CeO_2 nanoparticle, by melting the MgO particle, comprising 5832 atoms (2916 Mg atoms, 2916 O atoms) in a NVT MD simulation at 5000 K for 10 ps, then reducing the temperature to 300 K for a further 10 ps. The final atomistic model is given in Figure 7.2.

The BaO nanoparticle was formed in the same way, by melting the BaO particle, comprising 3054 atoms (1527 Ba atoms, 1527 O atoms) in a NVT MD simulation at 3500 K for 30 ps, then reducing the temperature to 1800 K for a further 30 ps, and finally 300 K for 10 ps. The final atomistic model is given in Figure 7.2.

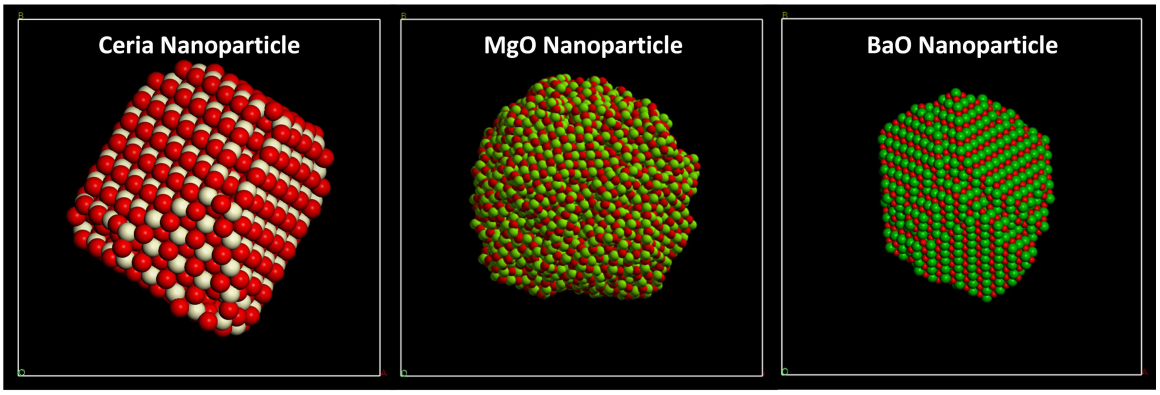

Figure 7.2: Full atomistic models of a CeO_2 nanoparticle (left), a MgO nanoparticle (centre), and a BaO nanoparticle (right), comprising of 1008, 5832, and 3054 atoms respectively.

7.2.2 Embedding Nanoparticles

Each nanoparticle was embedded in the same manner, by manually placing the particle into a spatial gap in which it was not overlapping with any neighbouring atoms; an equilibration was then conducted to settle the system.

7.3 Results

7.3.1 CeO_2/SiO_2 – Issues Surrounding the Potentials

Once the CeO_2 nanoparticle was place into the SiO_2 matrix and left to equilibrate, the mixture of the potentials seemed to cause the oxygen to uniformly retract into the Si atoms until close enough to repel. This caused a catastrophic collapse of the system, where the total extended system energy (engcns) increased from $-1.6e^{+06}$ to $4.2e^{+22}$. The specific cause of this problem was not immediately evident; therefore the parameters of the MD simulation were methodically tested to determine the cause. Here the modifications to the simulation parameters are discussed individually.

7.3.1.1 Temperature

Increasing the temperature of the system gives energy to the atoms, allowing freer movement. The temperature was increased to 2800 K, selected as it was lower than the melting temperature but high enough to provide the greater energy/movement to the atoms. This allowed for a more constant engcns value of $-1.6e^{+06}$, however increased the configurational energy (engcfg) by 2 orders of magnitude (OM), the Van der Waals/Tersoff energy (engsrp) by 3 OM, and the electrostatic energy by 2 OM. The total, Van der Waals, and electrostatic virial were also largely changed, and the mean squared displacement of the atoms decreased by 3 OM. This resulted in the O being drawn more slowly into the Si but also inhibited any other movement of the atoms, effectively appearing as if all atoms were fixed in place.

7.3.1.2 Temporary Fixation of SiO_2 / CeO_2 Atoms

Fixing atoms within the system allows un–fixed atoms to adjust to a more energetically stable configuration without interference from the fixed atoms. With this in mind, SiO_2 and CeO_2 atoms were independently fixed to allow the others to adjust to more energetically favourable states. Firstly, as the matrix host, the SiO_2 atoms were fixed, allowing the 'guest' particle to adjust accordingly into the pore space available. This was successful, presenting movement in the CeO_2 nanoparticle and a lower engcns. The configurational (engcfg), Van der Waals/Tersoff (engsrp), and the electrostatic energies only increased by 1 OM. The total, Van der Waals, and electrostatic virial were more consistent, as were the mean squared displacement values. Upon closer inspection however the directional stress tensors had changed by +/- 3 OM, which suggested there may still be an imbalance/problem within the system.

From this the SiO_2 atoms were released from their fix position and allowed to move, which allowed for the simulation to complete a great number of steps, however the O atoms were still sinking into the Si atoms and causing a spike in the system energy and collapse of the system.

With the same reasoning of fixing part of the system to allow for less-hindered adjustment, the CeO_2 atoms were independently fixed and the SiO_2 atoms allowed free movement. This unfortunately had minimal effect and the system energy soon increased and caused the collapse of the system as with the previous attempts. As the oxygen atoms appear to sink into the silicon atoms uniformly across the system, it suggests that the impediment is not with the settling of the system and in fact related to the potentials themselves.

7.3.1.3 Three–Body Potential

As the Buckingham potentials have been widely and successfully used for a variety of simulations, and the issue appears to be the interactions between the O and Si atoms, the three-body potential was considered the most likely source of the problem, therefore this was chosen as the first potential to alter. There were options to either change the bond angle or use a different potential. However as the structure of the aerogel had already been formed with the correct bond angles and had stabilised, there was the additional option to remove the three-body potential entirely.

The bond angle was first changed from 109 ° to 151 °, resulting in a faster collapse of the system, not due to the increased system energy, which only increase by 2 OM, but due to the deviation in the directional stress tensors, varying by up to 6 OM.

A new three-body potential for O-Si-O was then introduced [7], Table 7.2. This potential was chosen as it has previously been used in a system which also contained cerium and other oxides. The introduction of this potential caused a significant increase in the system energy, leading to a catastrophic collapse, and an even greater deviation in the directional stress tensors (up to 54 OM). This could partially be due to the aerogel formation not being conducted with these potentials, however as the oxygen was still being pulled into the silica atoms, this was not likely the cause of this particular issue.

7.3.1.4 Setting Potentials to Zero

As changing the three-body potential seemed to have a negative effect on the system stability, did not improve the problem of the oxygen-silica interaction, and worked

Table 7.2: Three body potential used to replace the original three-body potential used in the SiO_2–CeO_2 simulation.

Atom i	Atom j	Atom i	Key	K (eV rad^{-2})	θ_0 (deg)	a	ρ (Å)	
O	Si	O	bvs2	100.00	109.4667	1.0	2.5	3.45

successfully when the ceria nanoparticle was not present, it was determined that the bond angle and three-body potential were appropriate and the source must lie elsewhere. To determine if the interactions between the Buckingham potentials could be causing the issue, the final two terms (ρ and C), given in Table 7.1, were set to zero. This allowed for more time steps to be completed before the system collapsed, however still produced the same issue with the O and Si atoms; therefore the first term (A) was adjusted. This value was independently lowered to roughly half its value (642.0000) and raised to roughly double its value (2568.0000), both producing similar results where the total system energy caused catastrophic collapse and subsequent movement of the oxygen towards the silica.

7.3.1.5 Replacing Buckingham with Morse Potentials

As both the three-body potential and the Buckingham potentials were modified without successful improvement, the Buckingham potentials for the Ce–O and O–O were replaced with Morse potentials [8], Table 7.3, to see if they gave a more successful interaction. These potentials were chosen as they have been previously used within the group for studying ceria within different systems, and more particularly for investigating at redox chemistry and reactivity. Although there was not as significant increase in the total system, the problem with the oxygen atoms still persisted.

7.3.1.6 Increasing SiO_2 Oxygen Mass

As changing the potentials themselves did not merit any success, and considering they work correctly in separate systems, a different approach was taken. This involved changing the mass of the SiO_2 related oxygen atoms by increasing their mass in hope that the it would aid in preventing the pull of the Si atoms. This resulted in a catastrophic collapse in the total system energy and system temperature, with no improvement in the Si–O interactions.

Table 7.3: Buckingham, Morse, and Three–body potentials used to replace the original potential used in the SiO_2–CeO_2 simulation.

Atom i	Atom j	Key	A(eV)	ρ(Å)	C(eV Å^{-6})
O	Si	Buck	1283.9070	0.3020	10.6615

Atom i	Atom j	Key	E_0	R_0	K	
O	Ce	Morl	0.098362	2.930147	1.848592	1.000
O	O	Morl	0.041730	3.189367	1.886824	22.000

Atom i	Atom j	Atom i	Key	K (eV rad^{-2})	θ_0 (deg)	a	ρ (Å)	
O	Si	O	bvs2	2.09	109.4667	1.2	2.6	3.45

7.3.1.7 Discussion

With further consideration, and discussion with various academics familiar with Molecular Dynamics, the likely cause of the system collapse is due to the interaction of the oxygen potentials within the two species. This could potentially be rectified by extensive research into recalculating the potentials from first principles, however there are no guarantee this would have any affect.

7.3.2 SiO_2 Compressions

The stress–strain curves reported in Figure 7.3 reveal that the direction of compression, whether along the x, y, or z axis of the aerogel, has minimal variance. The only noticeable differences between the axial compressions occurs after 40% strain (-0.4), where the deviations occur due to multiple simultaneous plastic deformations occurring in the aerogel structure. Although noticeable, the differences are still minimal, and arise due to the amorphous nature of the aerogel. The key area of interest, where differences are more significant, is a strain below 40%.

Plastic deformation within a material usually causes a sudden drop of the stress in the stress–strain curve. This attribute is not presented within the stress-strain curves of the aerogel. This is due to the unique structure of the aerogel, where the low density and extensive pore network mask this feature. When the aerogel is placed under stress, the thin pillars of silica take the strain. These pillars, to a certain point, are able to take elastic deformation, whereby the pillars will bend and flex to relieve some of the stress imposed. Once the silica's stress tolerance is exceeded, it succumbs to plastic deformation, where the pillars will break. As these pillars are all interconnected, they share the stress load. When the stress in one section exceeds the silica's tolerance and deforms plastically, the stress is redistributed to the connected sections. This redistribution of the stress prevents a sudden drop in stress on the stress–strain curve. It is only once the aerogel suffers multiple simultaneous plastic deformations, where the stress is so high that the network of pillars is unable to compensate, that the characteristic drop in the stress–strain curve is seen.

An average stress of the x, y, and z axis was taken and the resulted in the plot presented in Figure 7.3 (right). This gives a better representation of the aerogel's overall stress–strain properties, compared to using just one of the directional data points.

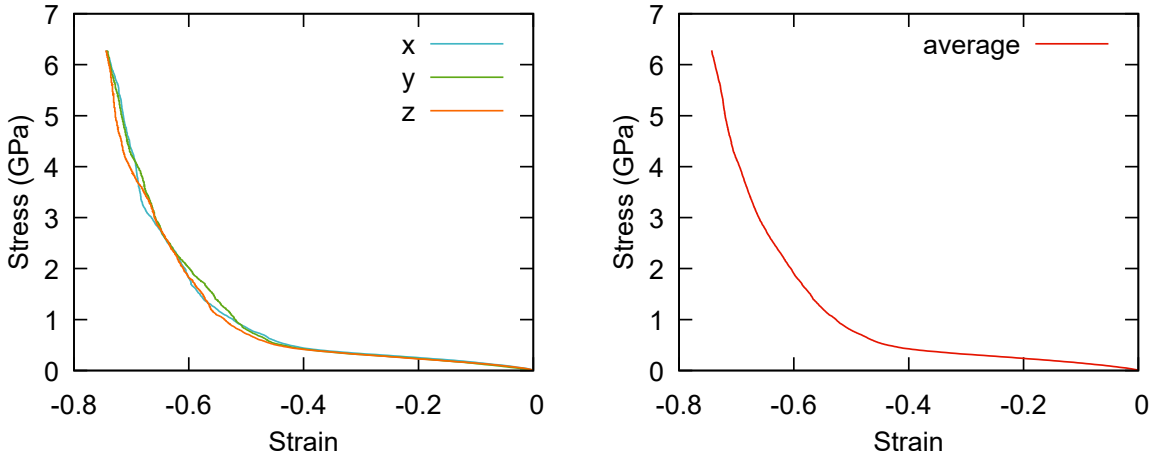

Figure 7.3: Stress–strain relationships of the aerogel, uni-axially compressed along the x, y, and z axis (left), and the average of the stress–strains (right)

7.3.3 MgO/SiO_2 Compressions

The stress–strain curves reported in Figure 7.4 reveal that the direction of compression, whether along the x, y, or z axis of the aerogel containing the MgO nanoparticle, has minimal variance. The only noticeable differences between the axial compressions occurs after 30% strain (-0.3), which is lower in comparison to the aerogel independently. An average stress of the x, y, and z axis was taken and resulted in the plot presented in Figure 7.4 (right).

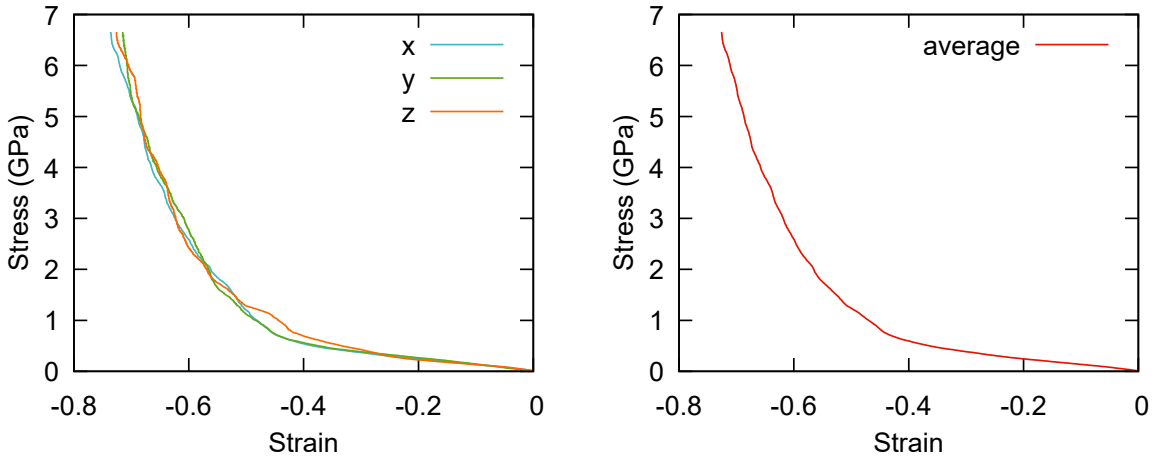

Figure 7.4: Stress–strain relationships of the aerogel containing an MgO nanoparticle comprising 5832 atoms, uni-axially compressed along the x, y, and z axis (left), and the average of the stress–strains (right)

7.3.4 BaO/SiO_2 Compressions

The stress–strain curves reported in Figure 7.5 reveal that the direction of compression, whether along the x, y, or z axis of the aerogel containing the BaO nanoparticle, has minimal variance. The only noticeable differences between the axial compressions occurs after 35% strain (-0.35), which is lower in comparison to the aerogel independently, but higher than the aerogel containing the MgO nanoparticle. An average stress of the x, y, and z axis was taken and the resulted in the plot presented in Figure 7.5 (right).

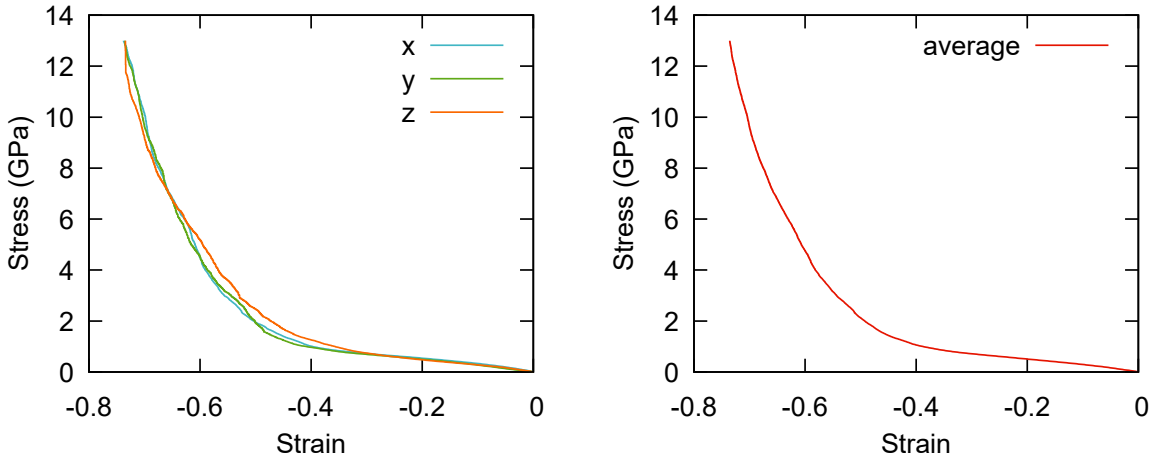

Figure 7.5: Stress–strain relationships of the aerogel containing a BaO nanoparticle comprising 3054 atoms, uni-axially compressed along the x, y, and z axis (left), and the average of the stress–strains (right)

7.3.5 SiO_2, MgO/SiO_2, and BaO/SiO_2 Comparison

A comparison of the averaged stress–strain curves for the compression of the aerogel, BaO nanoparticle in aerogel, and the MgO nanoparticle in aerogel are presented in Figure 7.6. This plot reveals the presence of a nanoparticle within the aerogel causes higher stresses on the aerogel under compression, as one might expect. Unexpectedly however, the data shows that the softer BaO atom produces higher stress–strains than the harder MgO atom. At 20% compression (-0.2) the stress on the system for the aerogel and the MgO nanoparticle in aerogel are almost indistinguishable, with the aerogel at 0.238 GPa, and the MgO nanoparticle in aerogel at 0.244 GPa. The BaO nanoparticle in aerogel at 20% compression in comparison gives over twice this stress at 0.506 GPa.

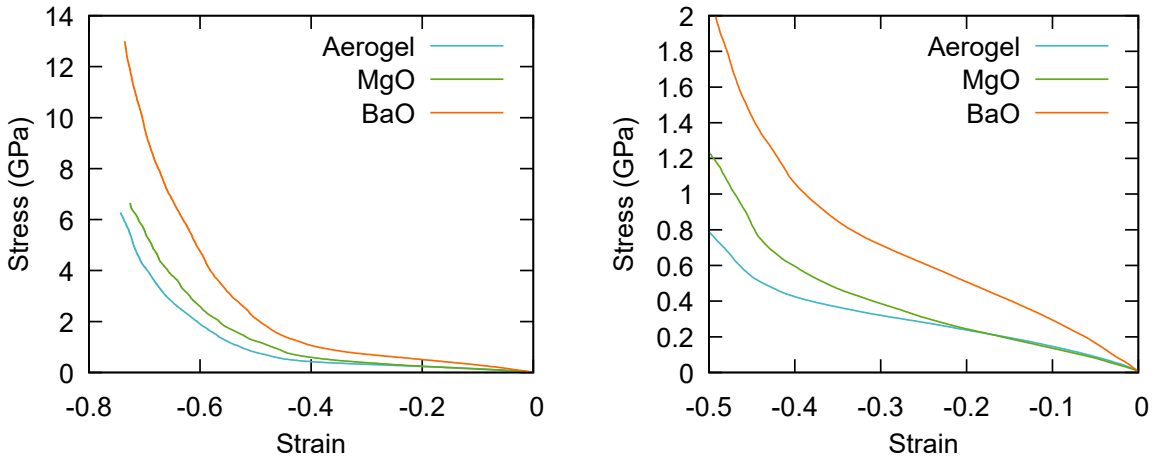

Figure 7.6: Stress–strain curves of the averaged compressions of aerogel, MgO nanoparticle in aerogel, and BaO nanoparticle in aerogel(left), with an enlarged plot of the initial stage of compression (right)

There are many factors to consider when comparing the mechanical properties of materials. One such factor, which has a major influence is the nanoparticle's shape. The shape governs the surface structure of the nanoparticle which influences many properties including the ionic conductivity [9], the magnetic properties [10], and the mechanical properties [11]. Here, although the size of the MgO and BaO particles are similar, the shapes of the particle are different. MgO is spherical in structure, whereas BaO is cubic in structure, as shown in Figure 7.2.

The spherical shape of the MgO nanoparticle has no sharp facets or protrusions, however the cubic shape of the BaO nanoparticle does, in the corners and along the edges. These sharp corners/edges can cause high localised stress on the aerogel,

whereas the spherical surface of the MgO has a larger surface contact to distribute the same stress over a larger area. The spherical structure therefore allows the aerogel to sustain an elastic response for a longer period than the cubic structure. A representation of this is shown in Figure 7.7.

There are other factors to consider within the aerogel system, however the shape of the nanoparticle, having such a major influence on not just its own mechanical properties, but also on the surrounding aerogel is a potential cause for large difference in stress values for the BaO and MgO nanoparticle systems.

Although not directly comparable, the yield strengths present in Chapter 6 for the BaO and MgO anvils were 28.5 GPa and 14.4 GPa respectively (at 22% and 17% compression). Here the strength of the BaO and MgO at 20% compression are 0.506 GPa and 0.244 GPa respectively. This suggests that the aerogel acts as a protective shell round the nanoparticle, significantly reducing the stress placed on the nanoparticle.

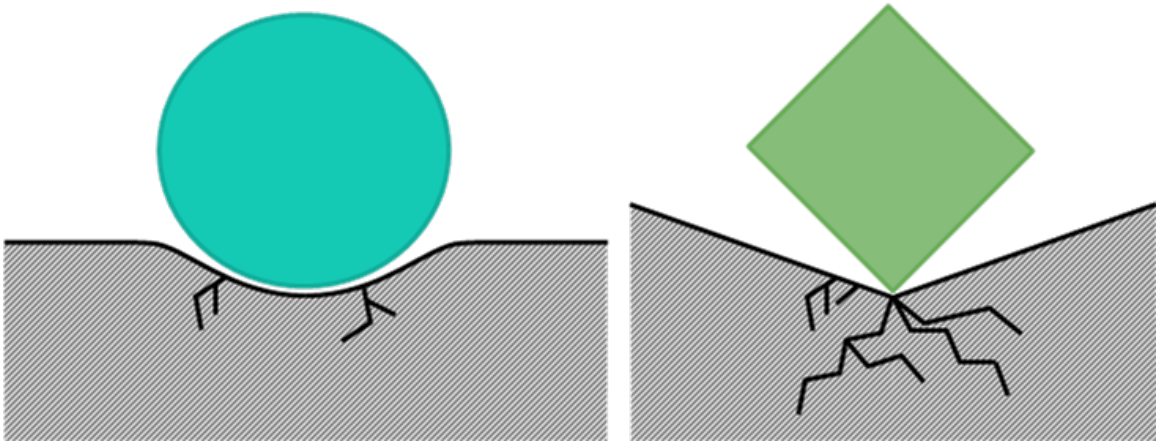

Figure 7.7: Graphical representation of the difference between a cubic and spherical nanoparticle in contact with a surface

7.4 Conclusions

An amorphization and re–crystallisation technique was used to generate the atomistic models of the CeO_2, MgO, and BaO nanoparticles, alongside a cluster–growth method utilising a pseudo–random co–ordinate generator to form the SiO_2 aerogel. Uniaxial compression was performed on the aerogel system as well as aerogel systems containing MgO and BaO nanoparticles in order to determine the mechanical behaviour of each system.

We found that the potentials for the CeO_2 and SiO_2 are unable to exist within the same system. The likely cause of this is the oxygen potentials, which would require extensive research and recalculation of the potentials to potentially rectify. Our simulations of aerogel show that the unique redistribution of stress by the network of SiO_2 channels prevent the characteristic sharp drops in the resulting stress–strain curves. The presence of nanoparticles in the aerogel when compressed has a negative effect on the mechanical properties of the aerogel system, dependent on the nanoparticle composition and shape, alongside other factors contributing to the effect. Finally we show that aerogel has an excellent potential to act as a protective shell for the nanoparticle, protecting its mechanical (and catalytic) properties from plastic deformation.

7.5 Future Work

Additional work could be carried out on this system in a variety of different ways. Firstly, if time permitted, the issue with the CeO_2 and SiO_2 potentials would be further investigated to determine the cause, and ideally find a solution so compressions on a ceria catalyst within this system could be conducted. Further to this, larger aerogel systems could be formed, with nanoparticles of different shapes and materials embedded into a variety of pore positions to determine the affect on the mechanical properties.

References

[1] P.I. Pohl, J. Faulon, and D.M. Smith. Molecular Dynamics Computer Simulations of Silica Aerogels. *Journal of Non-Crystalline Solids*, 186:349–355, 1995.

[2] J.S. Rivas Murillo, M.E. Bachlechner, F.A. Campo, and E.J. Barbero. Structure and Mechanical Properties of Silica Aerogels and Xerogels Modeled by Molecular Dynamics Simulation. *Journal of Non-Crystalline Solids*, 356:1325–1331, 2010.

[3] T.Y. Ng, J.J. Teo, and Z.S. Liu. A Molecular Dynamics Study of the Thermal Conductivity of Nanoporous Silica Aerogel, Obtained through Negative Pressure Rupturing. *Journal of Non-Crystalline Solids*, 358:1350–1355, 2012.

[4] S. Hoo Joo, J. Young Park, C.K. Tsung, Y. Yamada, P. Yang, and G.A. Somorjai. Thermally Stable Pt Mesoporous Silica CoreShell Nanocatalysts for High-Temperature Reactions. *Nature Materials*, 8:126–131, 2009.

[5] T.X.T. Sayle, M. Cantoni, U.M. Bhatta, S.C. Parker, S.R. Hall, G. Möbus, M. Molinari, D. Reid, S. Seal, and D.C. Sayle. Strain and Architecture-Tuned Reactivity in Ceria Nanostructures; Enhanced Catalytic Oxidation of CO to CO_2. *Chemistry of Materials*, 24(10):1811–1821, 2012.

[6] G.V. Lewis and C.R.A. Catlow. Potential Models for Ionic Oxides. *Journal of Physics C: Solid State Physics*, 18(6):1149–1161, 1984.

[7] J. Du, L. Kokou, J.L. Rygel, Y. Chen, C.G. Pantano, R. Woodman, and J. Belcher. Structure of Cerium Phosphate Glasses: Molecular Dynamics Simulation. *Journal of American Ceramic Society*, 94(8):2393–2401, 2011.

[8] T.X.T. Sayle, M. Molinari, S. Das, U.M. Bhutta, G. Möbus, S.C. Parker, S. Seal, and D.C. Sayle. Environment-Mediated Structure, Surface Redox Activity and Reactivity of Ceria Nanoparticles. *Nanoscale*, 5:6063–6073, 2013.

[9] D. Pergolesi, E. Fabbri, S N. Cook, V. Roddatis, E. Traversa, and J.A. Kilner. Tensile Lattice Distortion Done Not Affect Oxygen Transport in Yttria-Stabilized Zirconia–CeO_2 Heterointerfaces. *American Chemistry Society – ACS Nano*, 6:10524–10534, 2012.

[10] R. Evans, U. Norwak, F. Dorfbauer, T. Shrefl, O. Mryasov, R.W. Chantrell, and G. Grochola. The Influence of Shape and Structure on the Curie Temperature of Fe and Co Nanoparticles. *Journal of Applied Physics*, 99(8):08G703, 2006.

[11] F. Caddeo, A. Corrias, and D.C. Sayle. Tuning the Properties of Nanoceria by Applying Force: Stress-Induced Ostwald Ripening. *Journal of Physical Chemistry C*, 120:14337–14344, 2016.

Appendix 1

1.1 Procedure for the Hydro-Solvo-Thermal Synthesis of Cubic Ceria Nanoparticles

1. Place 15 mL of 16.7 mMol L^{-1} cerium (III) nitrate water solution into a stainless steel autoclave lined with a Teflon container.
2. Add to this a solution of 15 mL toluene, 1.5 mL oleic acid [capping agent], and 0.15 mL *tert*-butylamine, **do not stir**.
3. Seal and heat the autoclave to 180 °C for 48 h then cool to room temperature naturally.
4. Separate the organic (toluene) layer and centrifuge at 8000 rpm for 10 mins.
5. Pipette the purified toluene solution to a new container.
6. Precipitate the nanoparticles by adding an equal volume of ethanol.

1.2 Procedure for the Synthesis of Aerogel

Step 1

1. Prepare the hydrolysing acidic solution by mixing 80.00 mL of ethanol, 129.52 mL of H_2O, and 2.00 mL of HNO_3.
2. Prepare an ethanoic solution of TEOS by mixing 3.00 mL of EtOH and 7.90 mL of TEOS in a 100.00 mL conical flask.
3. Add 3.965 mL of the hydrolysing solution slowly to the TEOS solution.
4. Heat the solution to 50 °C under reflux for 30 minutes to promote the hydrolysis of the TEOS.
5. Prepare a 7.5 mL solution of EtOH contain the appropriate amount of metal nitrates (if used) and add to the solution while cooling the solution to room temperature.

Step 2

6. Prepare a solution of urea by dissolving 3.513 g of urea in 4.92 mL of distilled water and 9.00 mL of EtOH.
7. Add the dissolved solution to the TEOS solution and leave to stir for 10 minutes.
8. Heat the solution to 85 °C under reflux until the solution viscosity starts to change.
9. Transfer the solution to an appropriate vial and close vial before placing into an oven at 40 °C overnight in order to complete the gelation.

1.3 Summary of the High Temperature Supercritical Drying (HT-SD) Procedure

1. Place 50 mL EtOH into the autoclave chamber followed by the sample container/s.

2. Place the gauge on top being careful not to put the prongs into the sample container and seal.

3. Flush the chamber with N_2 gas at 1 atm for a minimum of 3 minutes.

4. Close the outlet valve followed by the inlet valve then turn off the N_2 gas supply.

5. Set the end temperature of the first ramp to 250 °C, with a ramp rate of 5 °C min^{-1}, followed by a dwell of 1 minute.

6. Set the end temperature to 330 °C, with a ramp rate of 1 °C min^{-1}, followed by a dwell of 10 minutes.

7. Monitor the pressure, checking it does not exceed 90 atm.

8. Once the program has finished (or the pressure has reached 90 atm) vent the chamber very slowly.

9. Once the pressure is close to zero, open the valve fully and carefully remove from the heating mantle.

10. Turn on the N_2 gas supply to 3 atm, open the inlet valve followed by the outlet valve and flush the chamber for a minimum of 5 minutes.

11. Close the outlet valve, followed by the inlet valve then turn off the gas supply and leave to cool to room temperature.

Appendix 2

2.1 Post-Precipitation XRD Patterns and Data Table of La-doped Ceria Nanocubes

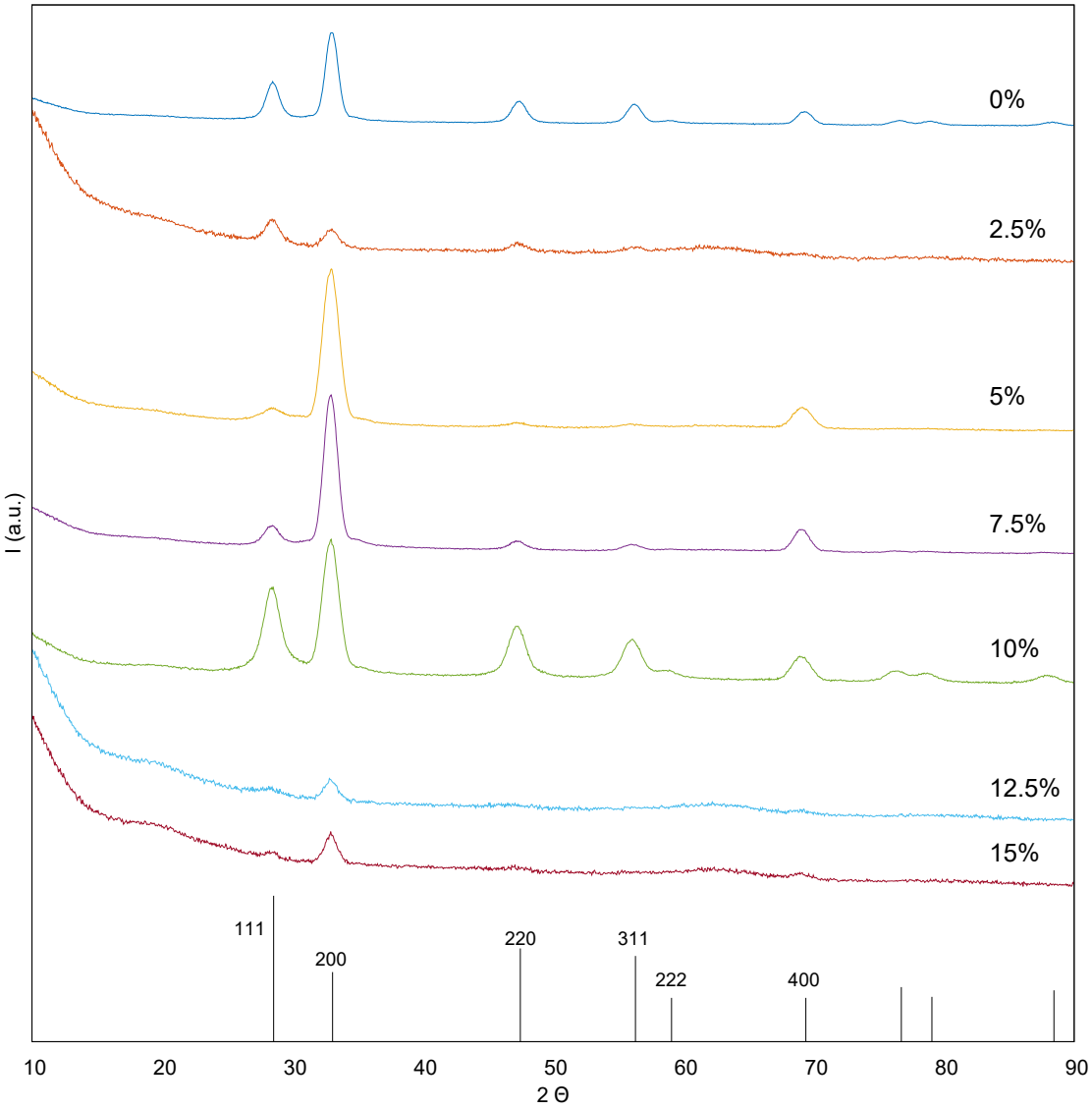

Figure 2.1: XRD spectra of the post-precipitation La-doped ceria nanocubes, with 0 (dark blue), 2.5 (orange), 5 (yellow), 7.5 (purple), 10 (green), 12.5 (teal), and 15 (dark red) mol% of lanthanum. A reference pattern for CeO_2 is also given (black).

Table 2.1: Peak positions, lattice parameters, and estimated crystallite size of the post-precipitated La-doped ceria nanocubes in 0, 2.5, 5, 7.5, 10, 12.5, and 15 %mol.

% mol La	**{200} Peak position** (2θ)	**Lattice parameter** ($\AA$)	**Crystallite size (nm)**
0	33.000(2)	5.424	7
2.5	32.94(2)	5.434	7
5	32.923(1)	5.437	6
7.5	32.90(1)	5.440	7
10	32.912(1)	5.439	6
12.5	32.877(3)	5.443	8
15	32.88(3)	5.443	7

2.2 Post-Precipitation TEM/AC-TEM Images of 5% La-doped Ceria Nanocubes

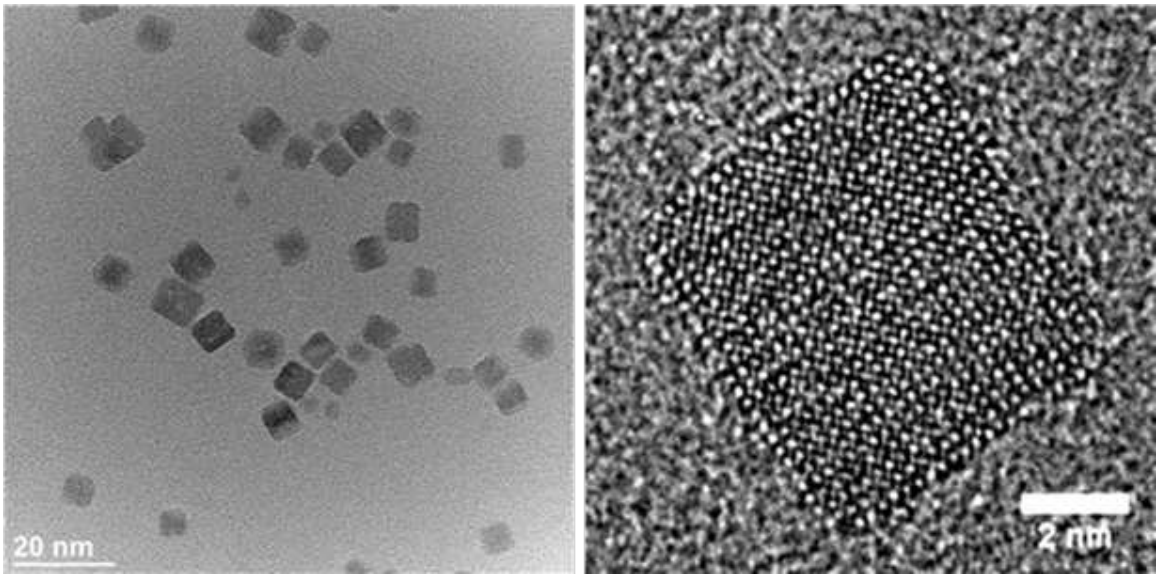

Figure 2.2: TEM image of post-precipitation 5% La-doped ceria nanocubes at 20 nm (left) with an AC-TEM image at 2nm (right).

2.3 Post-Precipitation HR AC-TEM Image and Projected Diffraction Pattern of 5% La-doped Ceria Nanocubes

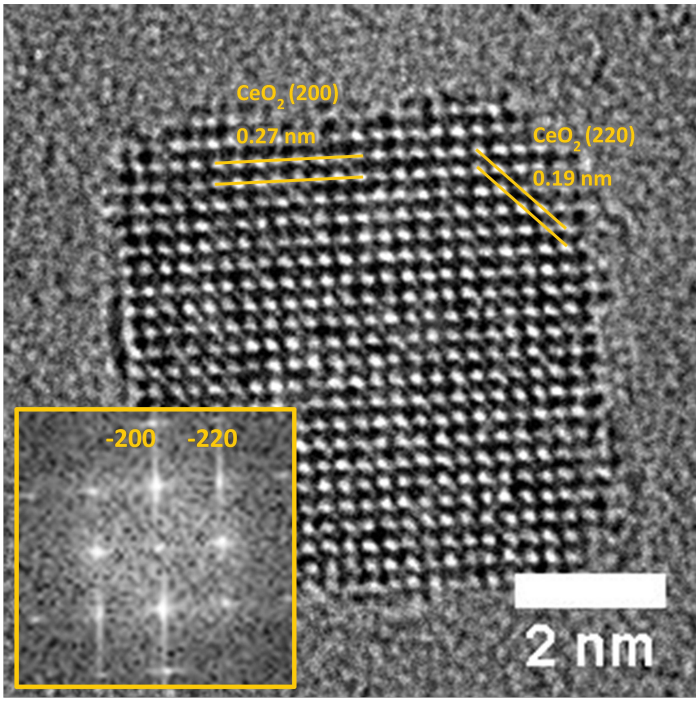

Figure 2.3: HR AC-TEM image of a post-precipitation 5% La-doped ceria nanocube with crystal planes highlighted. The insert contains the projected diffraction pattern.

2.4 Post-Precipitation TEM/AC-TEM Images of 10% La-doped Ceria Nanocubes

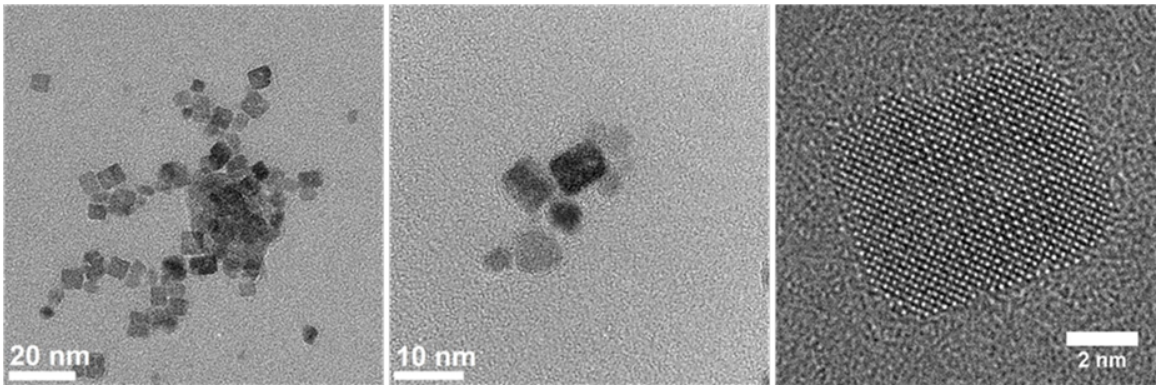

Figure 2.4: TEM images of post-precipitation 10% La-doped ceria nanocubes at 20 nm (left), and 10 nm (centre), with an AC-TEM image at 2nm (right).

2.5 Post-Precipitation HR AC-TEM Image and Projected Diffraction Pattern of 10% La-doped Ceria Nanocubes

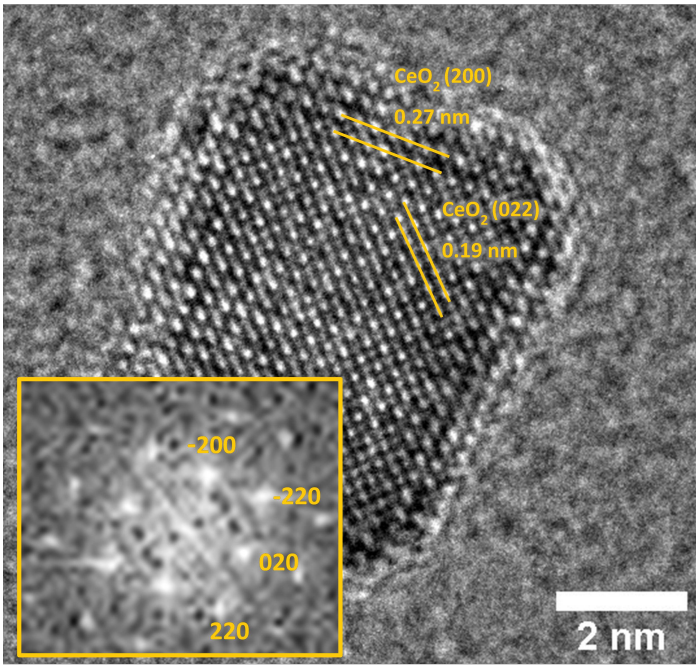

Figure 2.5: HR AC-TEM image of a post-precipitation 10% La-doped ceria nanocube with crystal planes highlighted. The insert contains the projected diffraction pattern.

Appendix 3

3.1 Static Standards

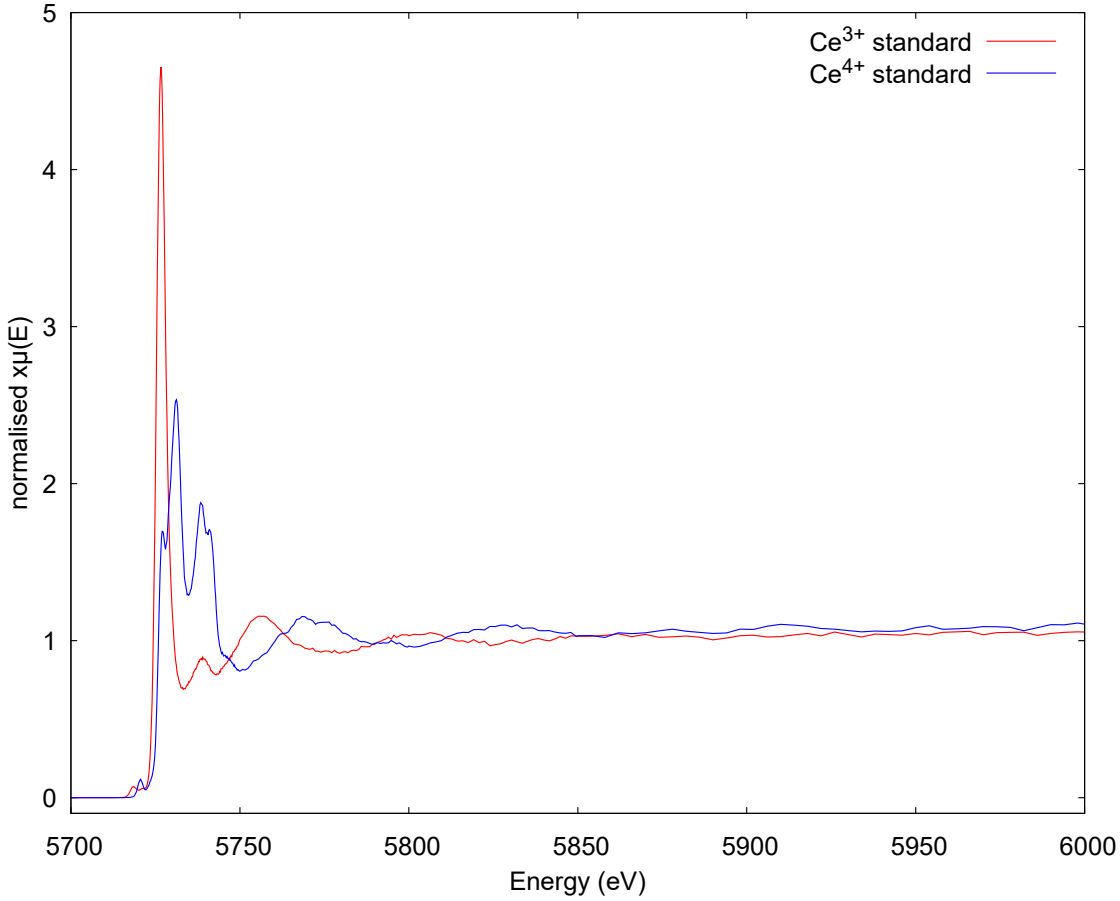

Figure 3.1: HERFD-XANES Ce L_3-edge spectra of Ce^{3+}/Ce^{4+} standards, where the blue trace shows Ce^{4+} standard and the red trace Ce^{3+} standard.

3.2 La-doped and Non-doped Ceria Nanocubes

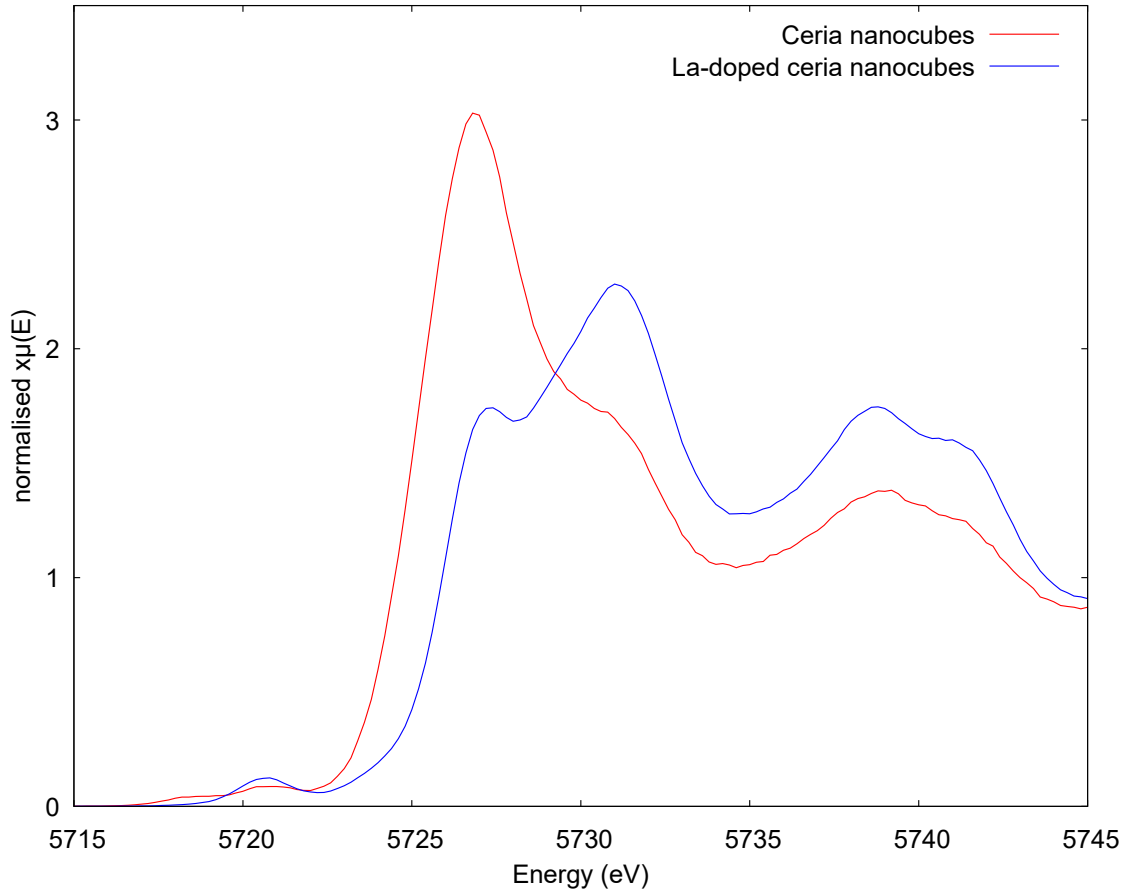

Figure 3.2: HERFD-XANES Ce L_3-edge spectra comparison of Ceria nanocubes (red) and 7.5% La-doped ceria nanocubes (blue).

3.3 Ce^{4+} Standard In-situ and Static

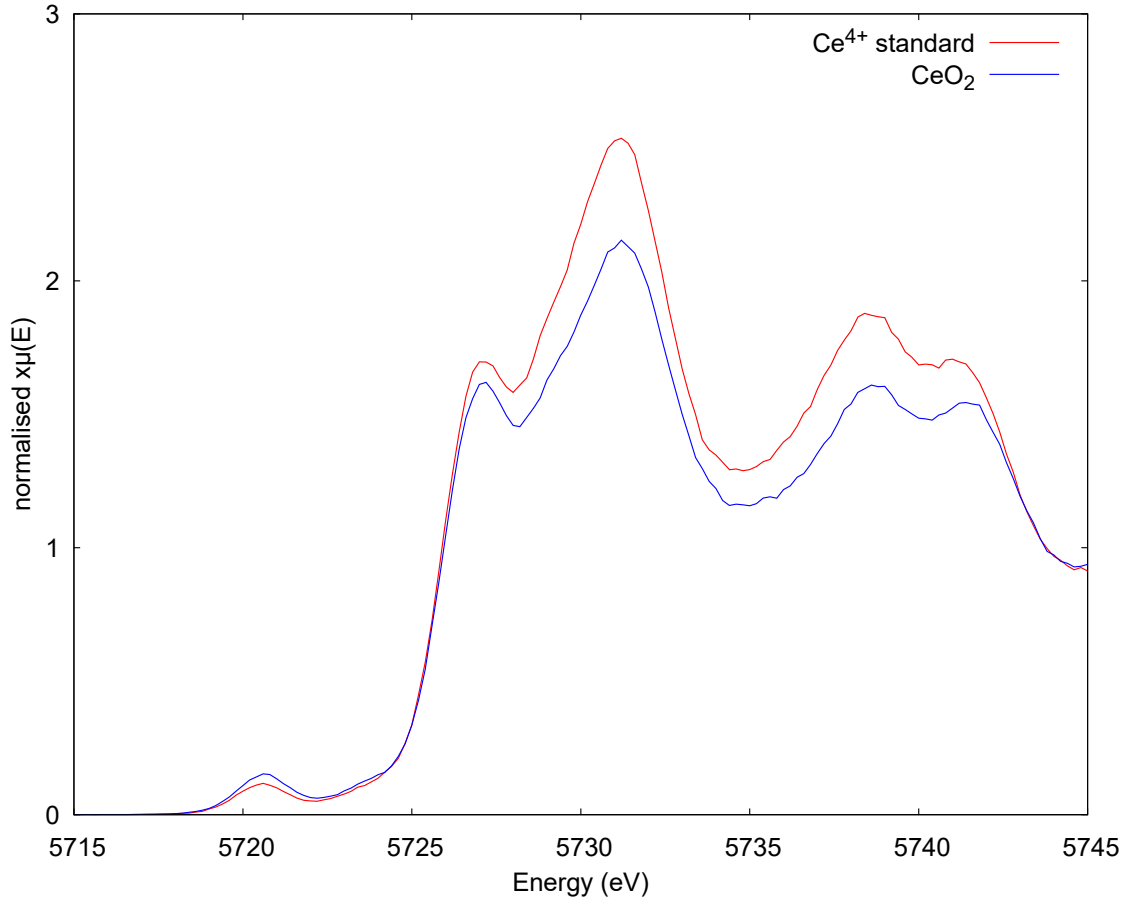

Figure 3.3: HERFD-XANES Ce L_3-edge spectra comparison of the Ce^{4+} standard static measurement (red) and in-situ measurement under a flow of N_2 gas (blue).

3.4 Ceria Nanocubes In-situ at 150 °C and 275 °C

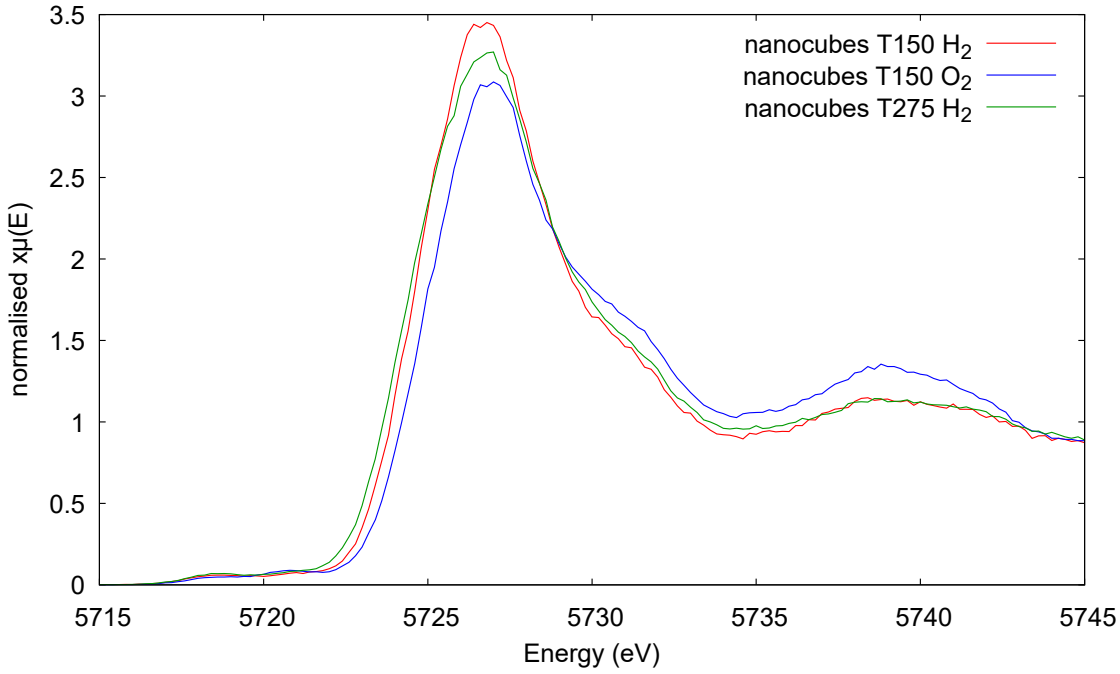

Figure 3.4: HERFD-XANES Ce L_3-edge spectra of the ceria nanocubes at 150 °C under H_2 (red), at 150 °C under O_2 (blue), and at 275 °C under H_2 (green).

3.5 Ceria Nanocubes In-situ (Program 2) at Ambient and 275 °C

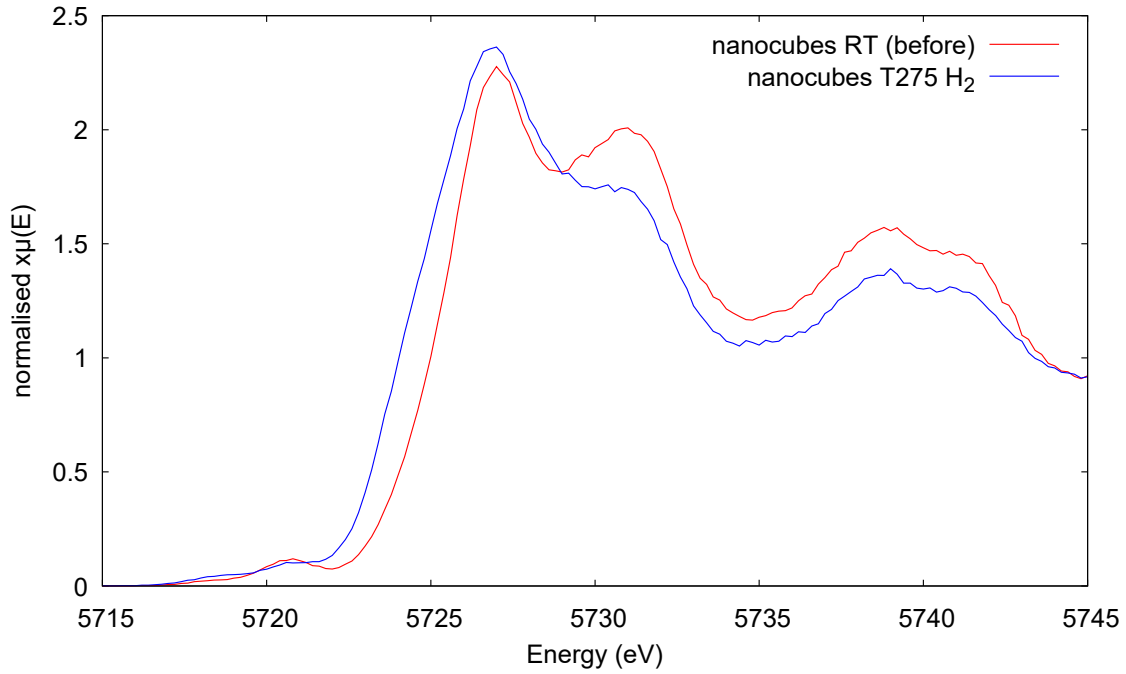

Figure 3.5: HERFD-XANES Ce L_3-edge spectra of the ceria nanocubes at ambient temperature under N_2 (red), and at 275 °C under H_2 (blue).

3.6 Ceria Nanocubes In-situ (Program 2) at 275 °C After Oxidation and Re-Reduction

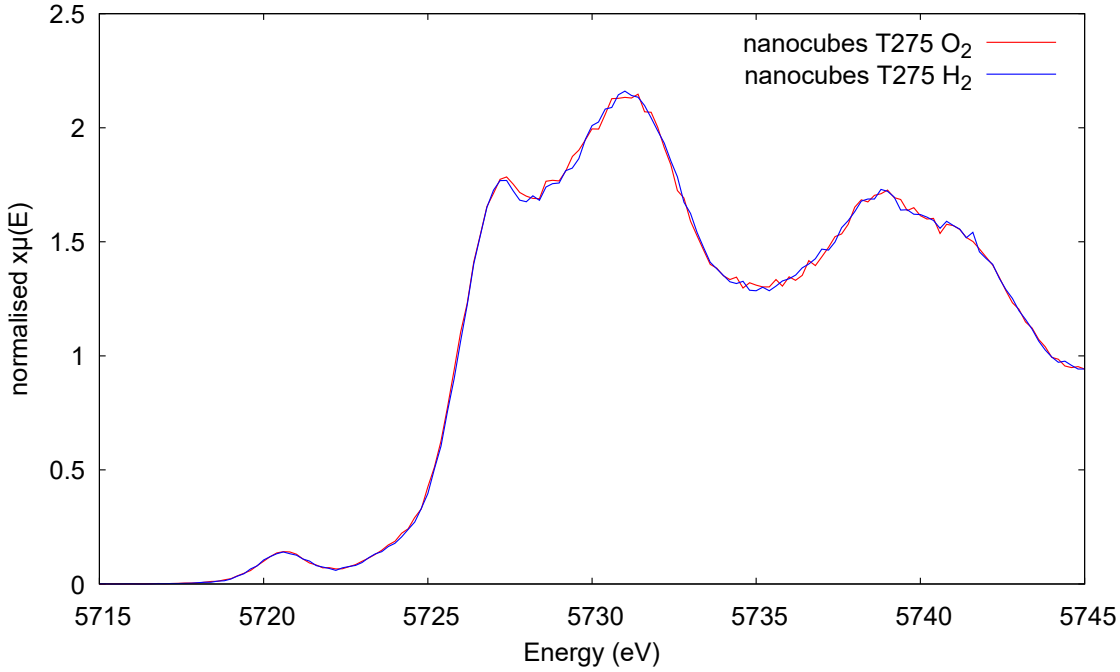

Figure 3.6: HERFD-XANES Ce L_3-edge spectra of the ceria nanocubes at 275 °C under O_2 (red), and under H_2 following the oxidation (blue).

3.7 Ceria Nanocubes In-situ (Program 2) at Ambient Temperature After Re-Reduction at 400 °C

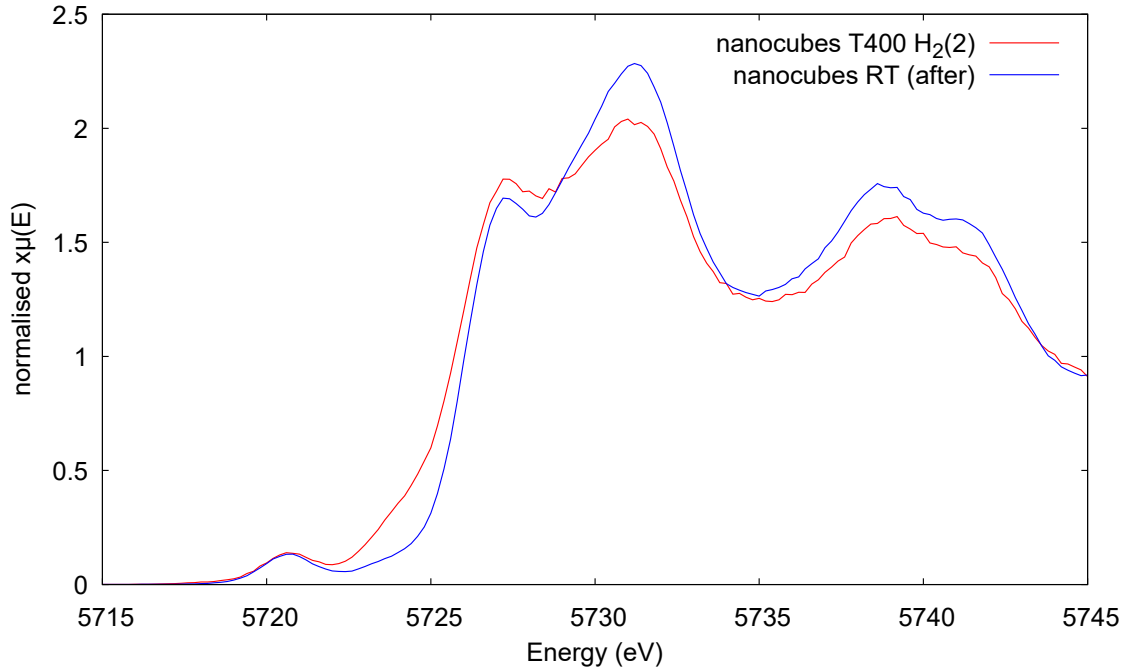

Figure 3.7: HERFD-XANES Ce L_3-edge spectra of the ceria nanocubes at 400 °C under H_2 (red) and at ambient temperature under N_2 following cooling (blue).

Appendix 4

4.1 Stress-Strain Graphs

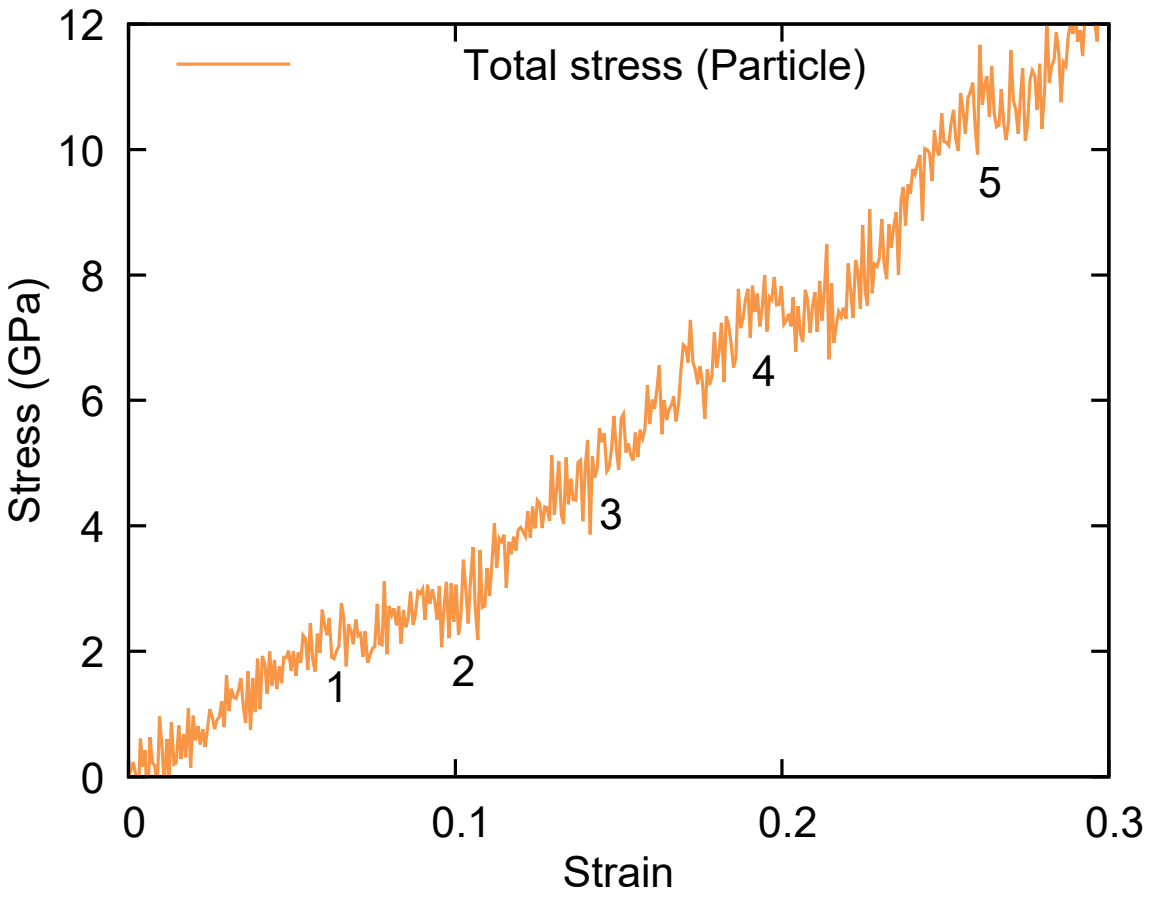

Figure 4.1: Stress-strain curves of nanoceria compressed by fixed anvils, where the total stress (black), stress on anvil (grey), and residual stress on nanoceria sample (orange) are given. The numbers correspond to the data points highlighted in Chapter 5, Table 5.2, and represent major events during the deformation process

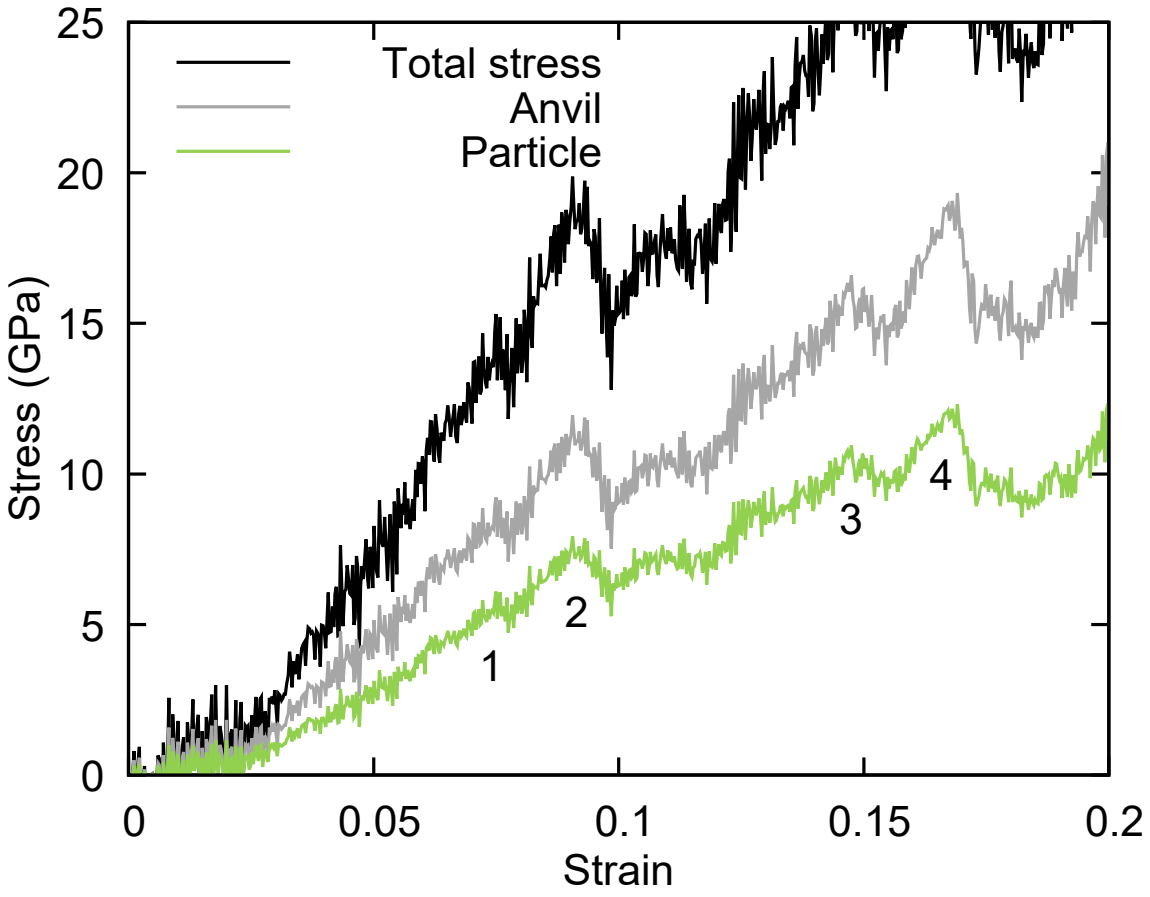

Figure 4.2: Stress-strain curves of nanoceria compressed by MgO anvils, where the total stress (black), stress on anvil (grey), and residual stress on nanoceria sample (green) are given. The numbers correspond to the data points highlighted in Chapter 5, Table 5.2, and represent major events during the deformation process

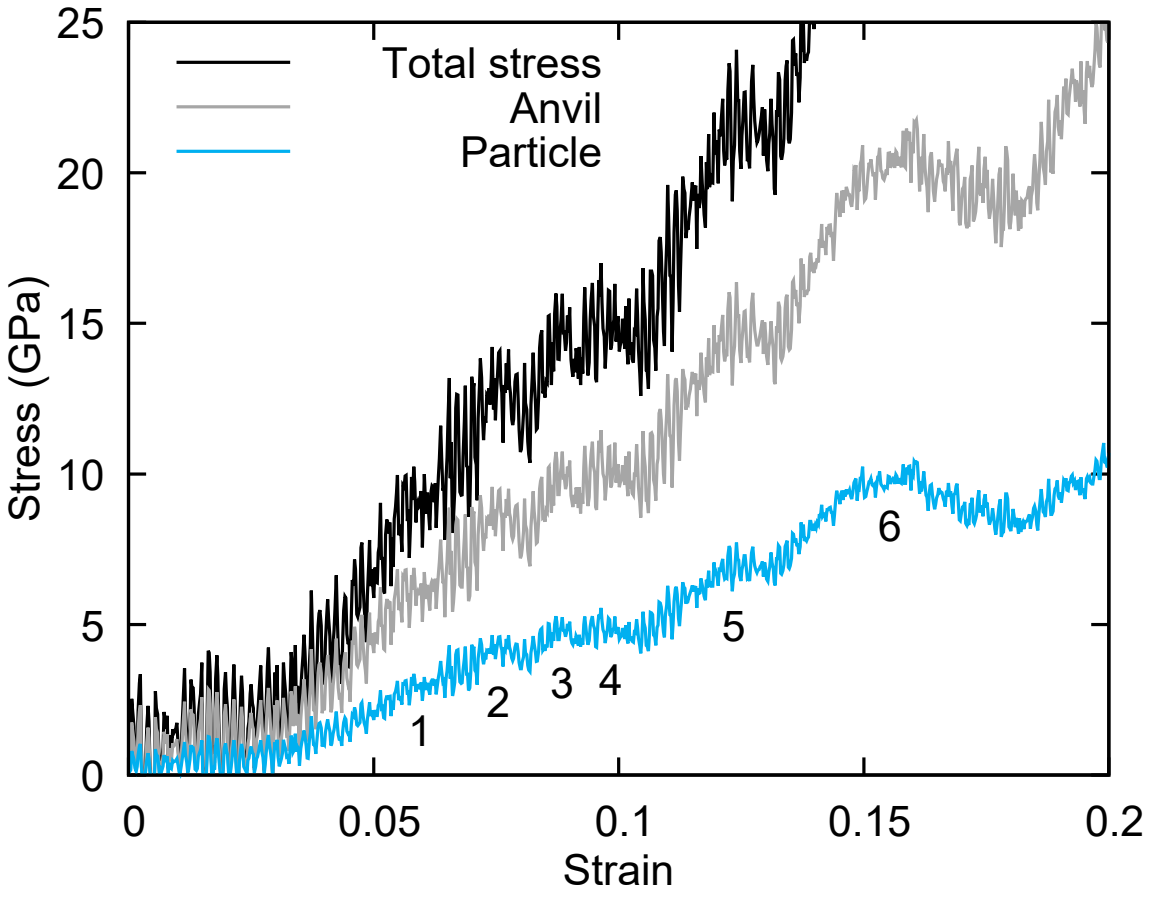

Figure 4.3: Stress-strain curves of nanoceria compressed by BaO anvils, where the total stress (black), stress on anvil (grey), and residual stress on nanoceria sample (blue) are given. The numbers correspond to the data points highlighted in Chapter 5, Table 5.2, and represent major events during the deformation process

4.2 Radial Distribution Functions (RDF)

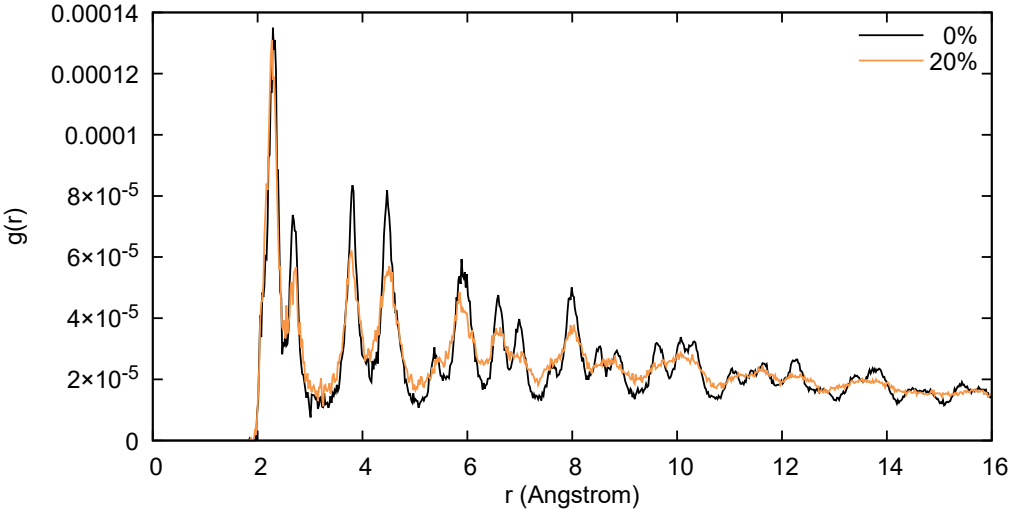

Figure 4.4: RDF plots of Ce-O and Ce-Ce within the nanoceria using fixed anvils at both 0% and 20% compression.

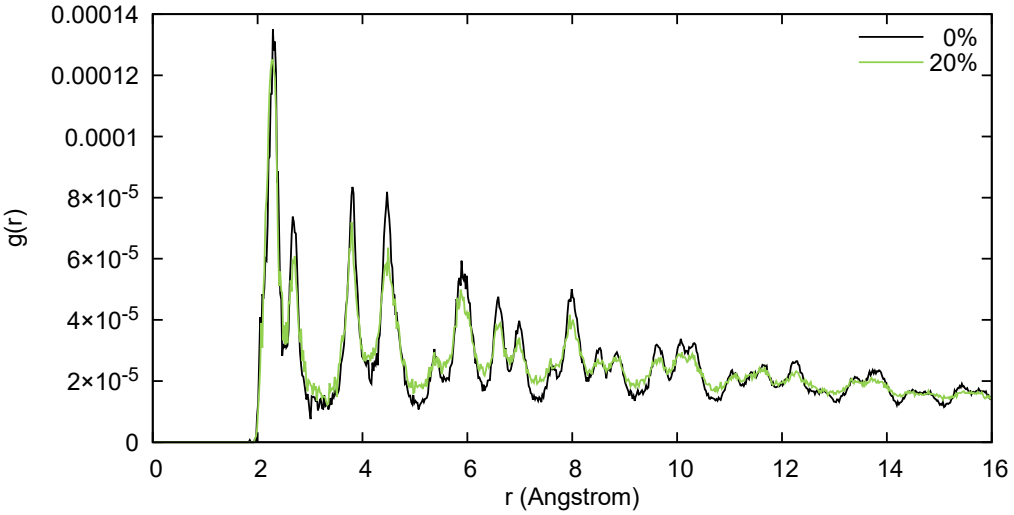

Figure 4.5: RDF plots of Ce-O and Ce-Ce within the nanoceria using MgO anvils at both 0% and 20% compression.

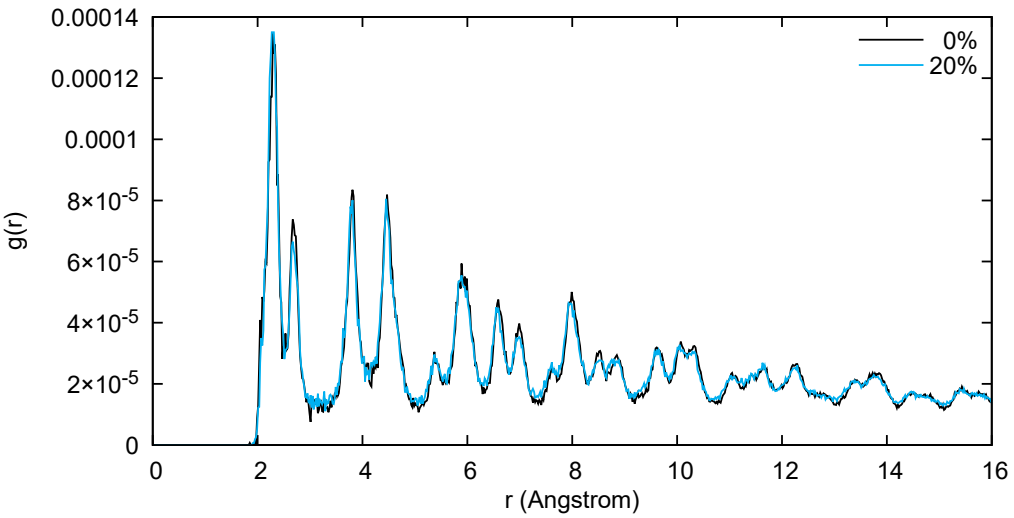

Figure 4.6: RDF plots of Ce-O and Ce-Ce within the nanoceria using BaO anvils at both 0% and 20% compression.

Appendix 5

5.1 Raw Temperature Stress–Strain Curves

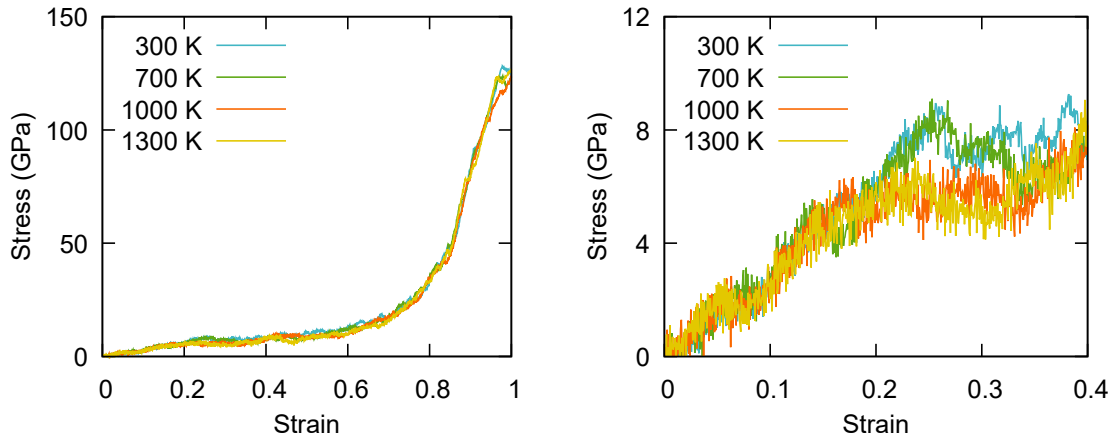

Figure 5.1: Stress–strain curves for the ceria nanoparticle compression using fixed anvils at temperatures of 300 K, 700 K, 1000 K, and 1300 K.

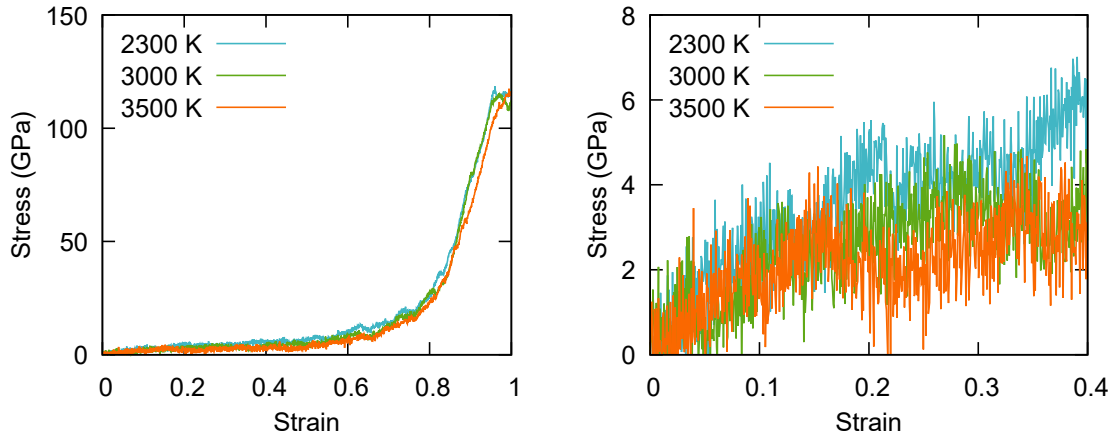

Figure 5.2: Stress–strain curves for the ceria nanoparticle compression using fixed anvils at temperatures of 2300 K, 3000 K, and 3500 K.

5.2 Raw Compression Rate Stress–Strain Curves

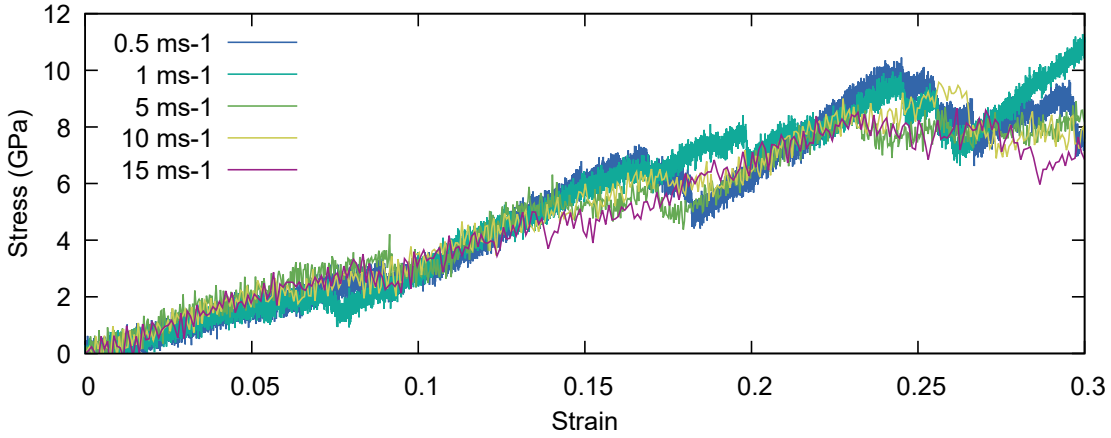

Figure 5.3: Stress–strain curves for the ceria nanoparticle compression using fixed anvils at compression rates of 0.5, 1, 5, 10, and 15 ms^{-1}.

5.3 Averaged Compression Rate Stress–Strain Curves (Individual)

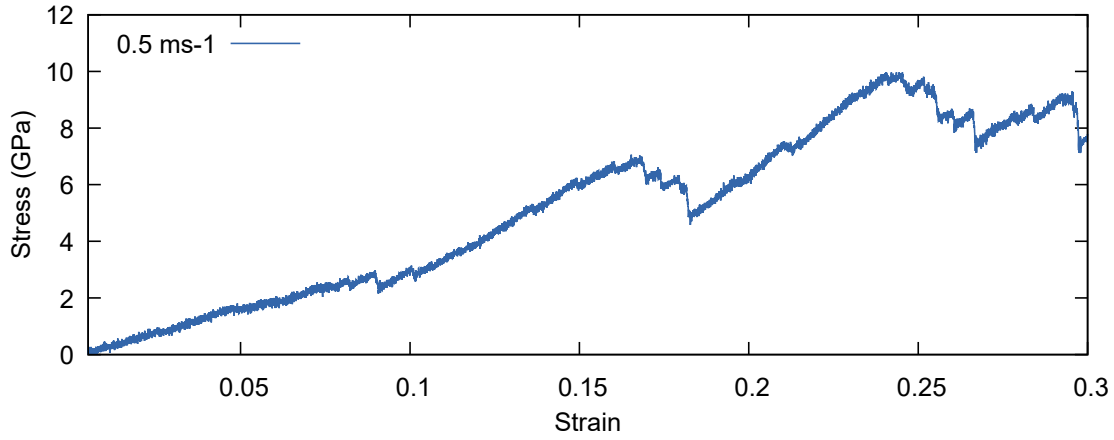

Figure 5.4: Averaged stress–strain curves for the ceria nanoparticle compression using fixed anvils at a compression rate of 0.5 ms^{-1}.

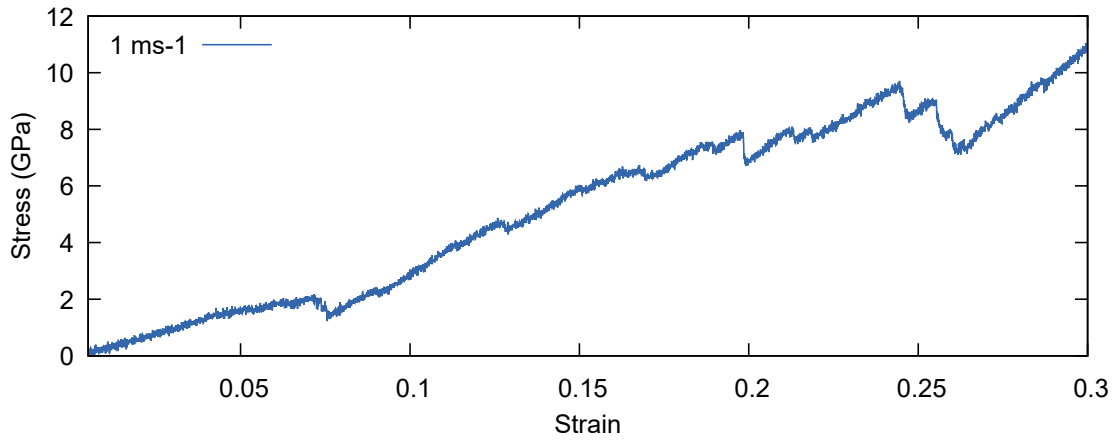

Figure 5.5: Averaged stress–strain curves for the ceria nanoparticle compression using fixed anvils at a compression rate of 1 ms^{-1}.

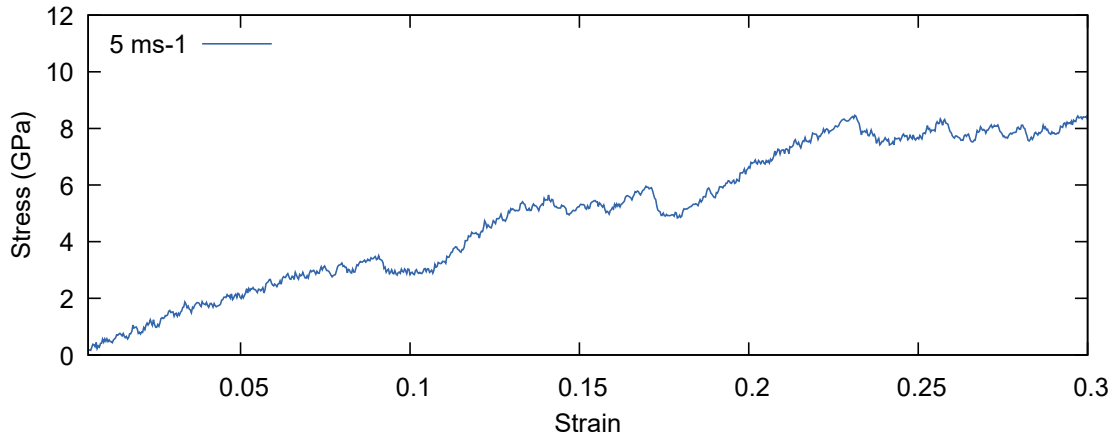

Figure 5.6: Averaged stress–strain curves for the ceria nanoparticle compression using fixed anvils at a compression rate of 5 ms^{-1}.

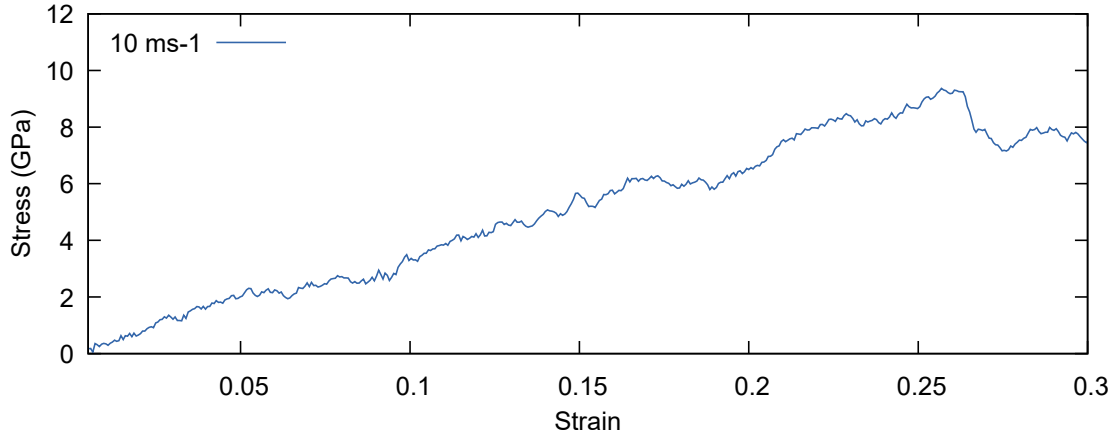

Figure 5.7: Averaged stress–strain curves for the ceria nanoparticle compression using fixed anvils at a compression rate of 10 ms^{-1}.

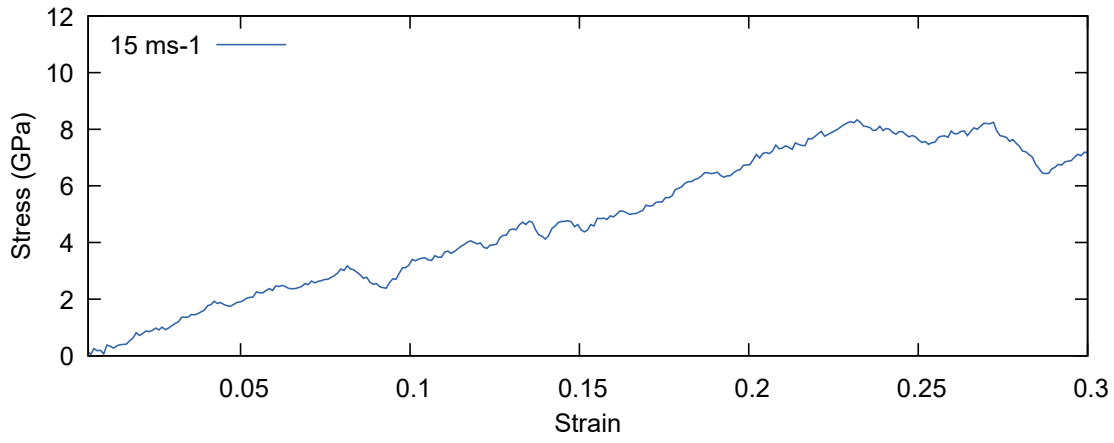

Figure 5.8: Averaged stress–strain curves for the ceria nanoparticle compression using fixed anvils at a compression rate of 15 ms^{-1}.

5.4 Elastic Moduli Stress–Strain Curves of the Individual Averaged Compressions

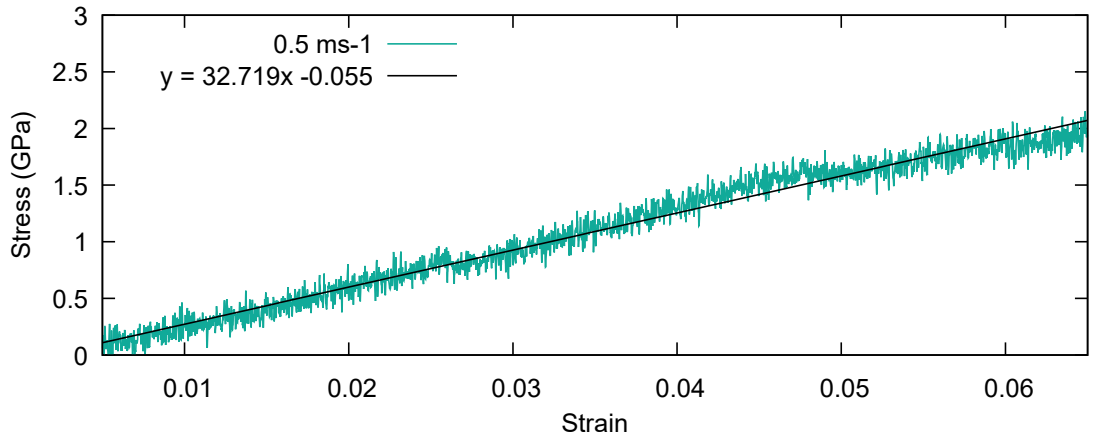

Figure 5.9: Averaged stress–strain curves for the ceria nanoparticle compression using fixed anvils at a compression rate of 0.5 ms^{-1}, with a linear trendline for calculating the elastic modulus

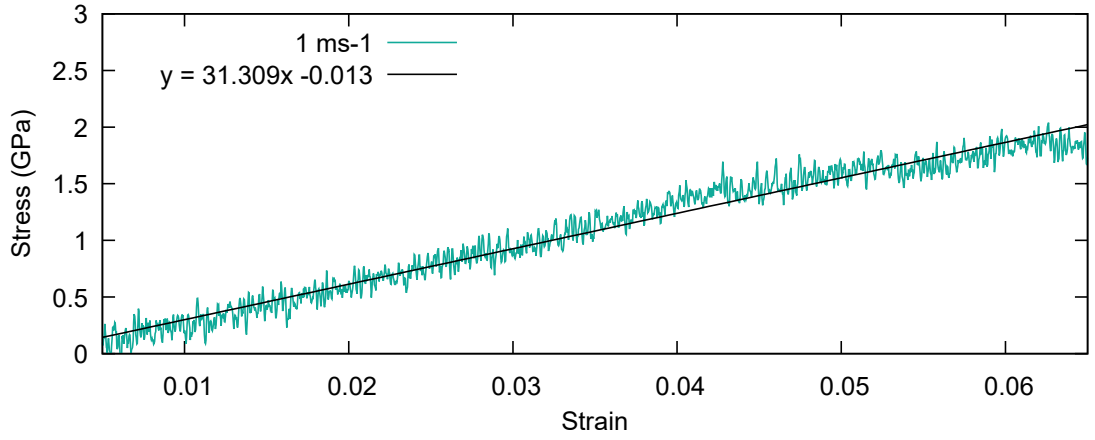

Figure 5.10: Averaged stress–strain curves for the ceria nanoparticle compression using fixed anvils at a compression rate of 1 ms^{-1}, with a linear trendline for calculating the elastic modulus

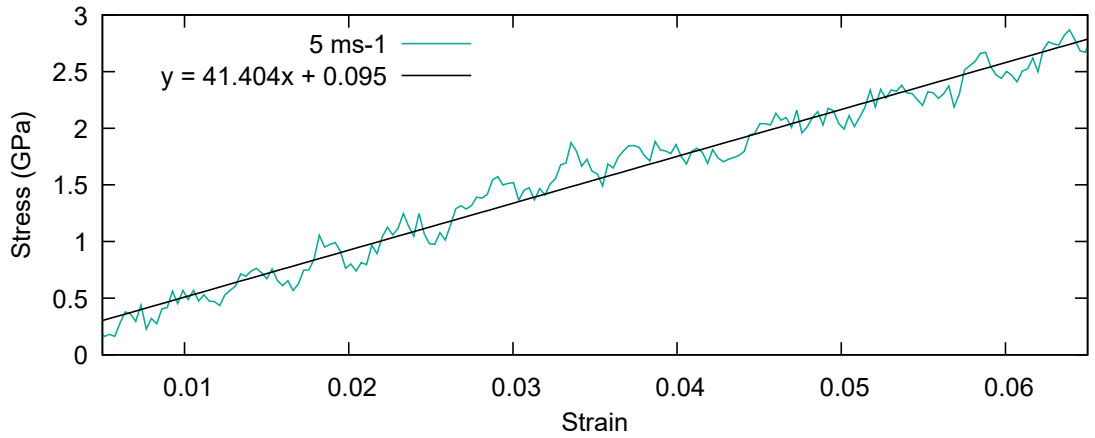

Figure 5.11: Averaged stress–strain curves for the ceria nanoparticle compression using fixed anvils at a compression rate of 5 ms^{-1}, with a linear trendline for calculating the elastic modulus

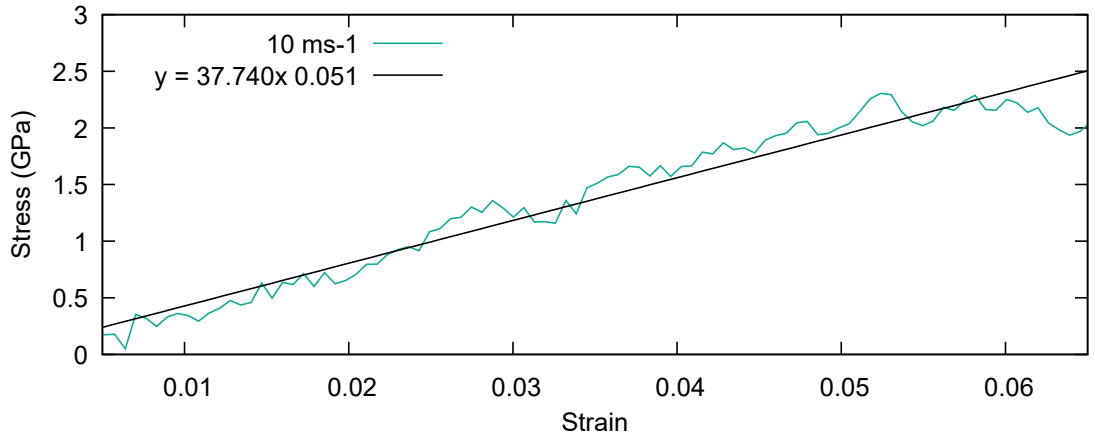

Figure 5.12: Averaged stress–strain curves for the ceria nanoparticle compression using fixed anvils at a compression rate of 10 ms^{-1}, with a linear trendline for calculating the elastic modulus

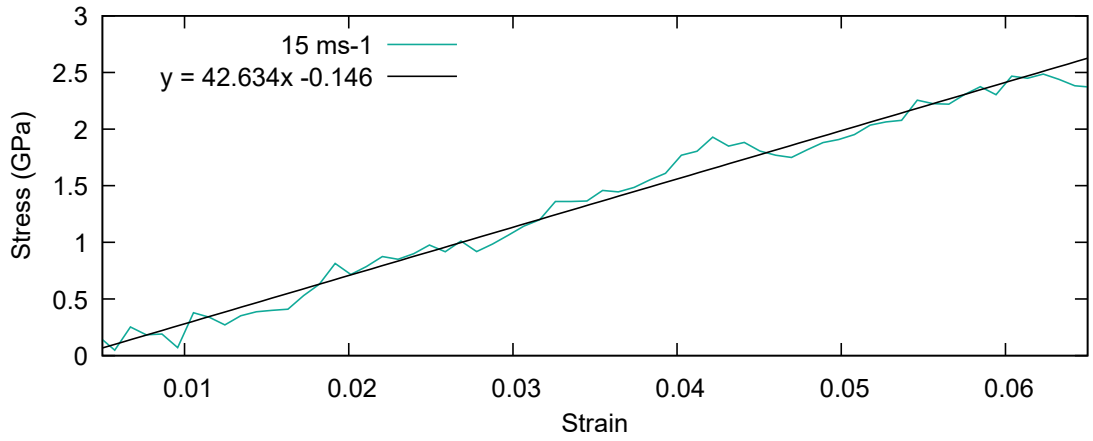

Figure 5.13: Averaged stress–strain curves for the ceria nanoparticle compression using fixed anvils at a compression rate of 15 ms^{-1}, with a linear trendline for calculating the elastic modulus